Gas-phase electronic spectroscopy of cold molecular cations of astrophysical interest

Inauguraldissertation
zur
Erlangung der Würde eines Doktors der Philosophie
vorgelegt der Philosophisch-Naturwissenschaftlichen Fakultät
der Universität Basel

von

François-Xavier Hardy
aus Frankreich

Basel, 2016

Genehmigt von der Philosophisch-Naturwissenschaftlichen Fakultät

auf Antrag von

Prof. Dr. John P. Maier und Prof. Dr. Markus Meuwly

Basel, 18/10/2016

Prof. Dr. Jörg Schibler

.

CONTENTS

1. THE INTERSTELLAR MEDIUM (ISM)

13.8 billion years after the Big-Bang, the universe contains ~ 100 billion galaxies, containing ~ 100 billion stars, each one containing $\sim 10^{57}$ atoms, making up a total of $\sim 10^{79}$ atoms in the observable universe. The Milky Way, a rather large but typical spiral galaxy, is composed of 84.5% dark matter, 14% stars, and 1.5% ISM by mass. Hydrogen (H) and helium (He) make up 99% of the ISM. Therefore, all heavy elements only account for 0.01% of the mass of the galaxy. Despite these very low proportions, these heavy elements are a focus of attention of astronomers for the following reasons: chemistry, and for an even more interesting though speculative reason, life in the universe. The elemental composition of Earth's biosphere exemplifies well the importance of elements such as carbon (C), oxygen (O), and nitrogen (N).

Stars are far too hot to allow any chemistry, and it is only by going far away enough from them that appropriate physical conditions can be met. There, molecules, clusters, crystals, ices and dust grains start to form and are the focus of interstellar chemistry. Inside a galaxy, interstellar clouds (ISCls) fill inhomogeneously the volumes between the stars, forming filaments, sheets or bubbles of various sizes and densities. With its specific physical properties and history, each local environment has a unique chemistry and composition. However, in the larger scales of the galaxy, the density of ISCls is well correlated with the density of stars for the reason that all stars are born from, and die into gas clouds.

Until the 20^{th} century, astronomers thought that the ISM was void of matter and of little interest. The interstellar matter was first discovered at the beginning of the 20^{th} century through observations of atomic absorption lines that did not belong to the stars under scrutiny.[1,2] In the middle of the 20^{th} century, it became clear that these atoms were indeed deep in the ISM. It was still assumed, however, that molecules could not form and survive in the ISM. The advance of radio astronomy enabled the next step forward, that is, the discovery of the presence of a multitude of molecules in interstellar and circumstellar environments.

Given this line of discoveries made over the 20^{th} century, what could now be the next step forward? Could complex or large biological molecules be present in the ISM? As of 2016, we do have the evidence that a variety of large molecules form, and even thrive in particular circumstellar and interstellar environments. However, their compositions and the extent of their complexity is still unknown.

1.1 General aspects

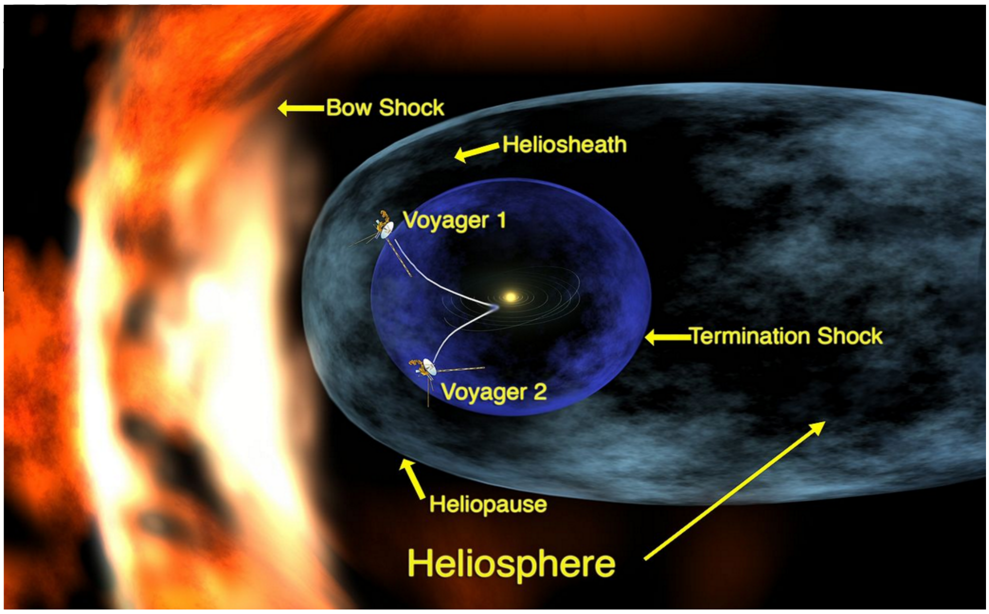

Fig. 1.1: A way to introduce the ISM is to show how the solar system, or more precisely, the solar wind, is interacting with the ISM. The solar wind, made of photons, energetic particles, and magnetic fields is pushing away the ISM, creating a shock wave called termination shock. The Sun is traveling through the local ISM at a speed of $20\,\mathrm{km\,s^{-1}}$. Also, we see in this illustration the Voyager probes actual locations, close to reaching the ISM[3]

The ISM is not all the space between the stars in the universe. The ISM is the space between stars exclusively within galaxies, and excluding the vicinity of the stars (circumstellar space). These intergalactic and circumstellar spaces both have unique physical conditions. For instance, within the circumstellar space, the radiation field is much higher than several light-years (ly) away from the star, deeper in the ISM.[4] As a consequence, pressures are characteristically lower (as within the blue sphere in Figure 1.1) than in the ISM because of the radiation pressure sweeping away most particles coming from the ISM. The boundary between the planetary system and the ISM consists of a shock wave caused by the radiation pressure from the star keeping away the ISM material and called ”termination shock” (Figure 1.1). The ISM then appears to be, in comparison, a milder environment than the interplanetary space. If life, as we know it on Earth, has been possible despite our proximity to the Sun, it is because Earth has a thick atmosphere protecting the fragile chemistry that makes us, from UV radiation and cosmic rays. In the same fashion, if a complex chemistry is possible in some ISCls, it is because these clouds are either protected by other layers of gas or because they are far away enough from surrounding stars.

ISCls have various shapes, structures, physical properties and chemical compositions. Before describing the main types of interstellar environments, we can first point out a few characteristics that they share and that constrast with terrestrial references. These are densities, volumes, timescales, and compositions.

Densities. There are $\sim 2\times10^{19}$ molecules.cm^{-3} in the air we breathe, and $\sim 10^{6}$ molecules.cm^{-3} in the best laboratory vacuums. Interstellar densities range from $\sim 10^{6}$ particles.cm^{-3} in the core dense clouds, to $\sim 10^{-4}$ cm^{-3} in very hot media.

Volumes. ISCls span over extremely large distances, measured in light years (ly) $\sim 10^{16}$ m; from $\inf 1$ ly for dense clouds to $\sup 100$ ly for the largest and more diluted ones.

Timescales. Unlike a star, an ISCl is rarely one proper unit. Nevertheless, their evolution typically ranges from tens to hundreds of millions of years, while most stars live for several billions of years. ISCls have much shorter lives because they are much more fragile and are regularly blown away by energetic events, such as supernovas, occurring in the neighborhood.

Compositions. Finally, they follow rather closely the cosmic elemental abundances, pictured in Figure 1.2. This logarithmic scale shows that 99.8% of this gas is merely H and He. He being chemically non-reactive, is not as relevant in astrochemistry, as O, C, and N. These, along with H, are the building blocks of organic molecules on Earth, as well as of most molecules discovered so far in the ISM. Less abundant, but still to be accounted for in the chemistry of the ISM, are elements like silicon, iron, manganese, magnesium, sulfur or phosphorus. However, heavy elements in the ISM are often hidden in grains, such as as silicates which constitute by mass a large portion of the interstellar matter.

In short, long timescales and large volumes are compensating for low densities

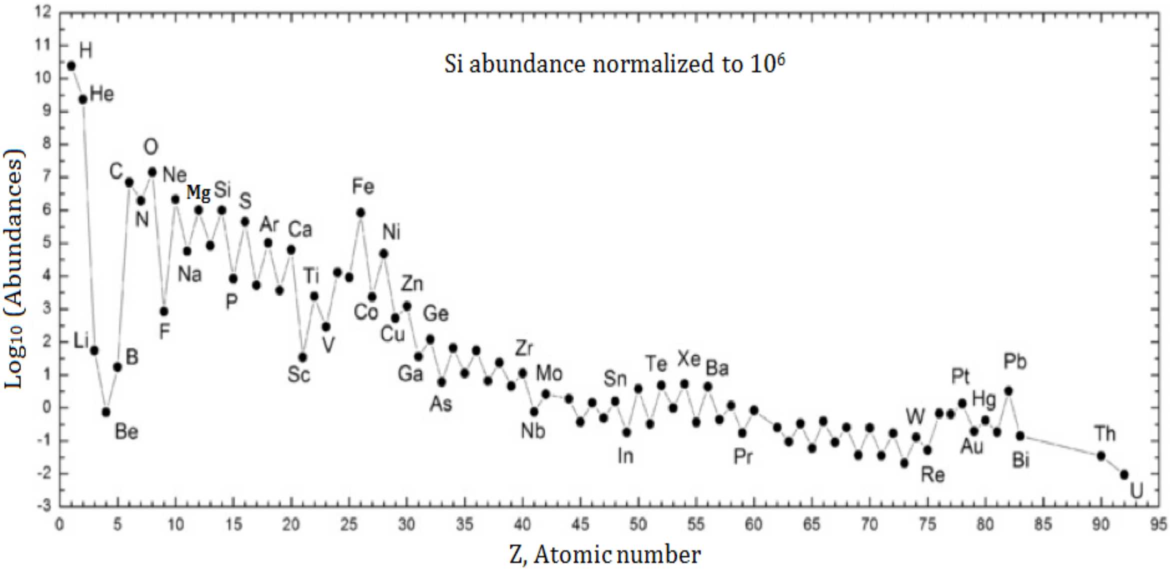

Fig. 1.2: Elemental abundances of the interstellar medium.[5] Though C is the central element in astrochemistry, the most abundant heavy element is O. These abundances are calculated from observation of atomic lines.

and allow rare chemical events to be overall consequential. One can see here the challenges of approaching a chemistry occurring in conditions so extraordinarily different from to the ones known on Earth.

Astronomers realized that the ISM was not void when observing some dark patches in the sky that hide the stars within and behind them. These patches are ISCls which do not let short wavelengths pass through (typically ultraviolet and visible (UV-Vis)) because of Rayleigh scattering by dust particles. On the other hand, one can see these clouds through infrared (IR) or millimeter (mm) wavelengths which are not scattered by the dust particles. In the early 20th century, Edward Barnard made a list of several hundred such dark patches[6,7] leading to the conclusion, for the first time, that "masses" of matter were present between the stars, obstructing the light. In a 1919 paper,[7] Barnard stated: "It would be unwise to assume that all the dark places shown on the photographs of the sky are due to intervening opaque masses between us and the stars. In a considerable number of cases, no other explanation is possible, but some of them are doubtless only vacancies". Barnard 68, shown in Figure 1.3 at different wavelengths, is a good example of a dark interstellar cloud. It is so close to the solar system (400 ly) that not a single star lies in between. UV-Vis light is scattered by dust particles, however, by observing this cloud at longer wavelengths, one can learn about its composition

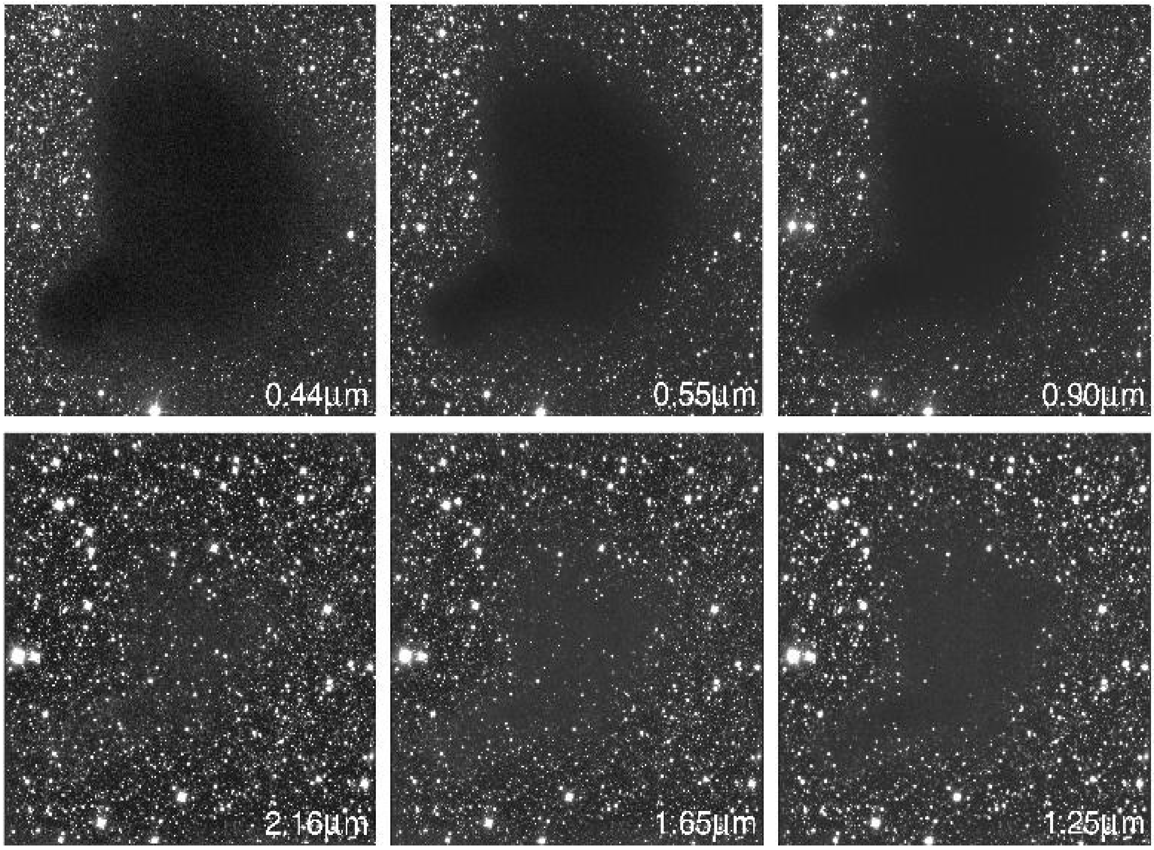

Fig. 1.3: Barnard 68 is a dark cloud not far away from our solar system. UV-Vis light is scattered by dust particles and does not pass through, whereas longer wavelengths do. Photos are taken from the European Southern Observatory.

through absorption or emission lines of molecules and atoms. Before astronomers had the telescopes for observing these "patches" in the IR or mm regions, we were not aware that many molecules were present in the ISM. In the second half of the 20^{th} century, with the advent of radio astronomy, pioneered by Karl Jansky in the 1930's, astronomers discovered that molecules were readily formed in dense clouds. By comparing astronomical data to laboratory spectra of rotational transitions of cold molecules, dozens of interstellar species have been identified to date[8] in dense clouds, such as the Taurus molecular cloud 1.

1.2 The three phases of the ISM

As elements can be found in different phases depending on the pressure and temperature, the ISM can also be described by three thermal phases, depending on the density and temperature of the gas. From the coolest to the hottest, they are described as follows:

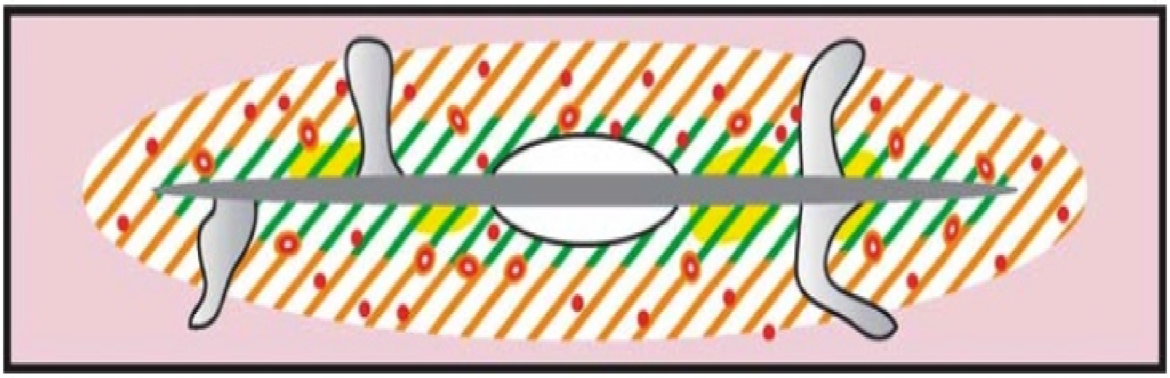

Fig. 1.4: Conceptual view of the Milky Way's ISM.[9] It is deconstructed into three phases: the cold neutral medium and warm neutral medium are in hatched green, and the hot ionized medium is in hatched orange. The red hot spots are young supernova remnants.

Cold neutral medium (CNM). Molecular clouds (H_2): In these clouds, hydrogen is mostly in the molecular form, at the lowest temperatures of the ISM of 10 - 20 K, and the highest densities of $\geq 10^3\,\text{cm}^{-3}$. Molecular clouds make up to $\sim 30\%$ of the mass of the ISM, but only occupy $\sim 0.05\%$ of its volume. Most molecular clouds are gravitationally bound, and the core of the densest ones may soon collapse to form a star. The main tracers are mm-wavelength molecular emissions which can pass through the cloud (mostly belonging to CO).

Cold neutral atomic hydrogen gas, on the other hand, is not distributed the same way than molecular cloud. Gravitation does not play such an important role and it forms sheets or filaments. It occupies roughly 1 - 4% of the ISM, has temperatures of ~ 80 - 100 K and densities of $\sim 50\,\text{cm}^{-3}$. The main tracers are UV and optical absorption lines seen towards bright sources.

Warm neutral and warm ionized media. Warm neutral atomic hydrogen makes up to $\sim 30\%$ of the volume of the ISM and is mainly located in photodissociation regions, on the boundaries of HII regions and molecular clouds. It has temperatures of $\sim 8\,000$ K and densities of $\sim 0.5\,\text{cm}^{-3}$ and the tracer is the HI 21 cm emission.

The warm ionized medium is responsible for HII emissions. Diffuse gasses with temperatures of 6 000 to 12 000 K, and densities $\sim 0.1\,\text{cm}^{-3}$ occupy about $\sim 25\%$ of the volume of the ISM. Nearly 90% of the H^+ in the galaxy resides in the warm ionized medium.

Hot ionized medium. The hot ionized medium is extremely low-density gas heated by supernovae (orange phase in Figure 1.4). It has temperatures $\geq 10^6\,\mathrm{K}$ and densities $\geq 0.003\,\mathrm{cm}^{-3}$, occupying $\sim 50\%$ of the ISM. This gas is called the hot corona of the galaxy since it is as high $\sim 100\,000\,\mathrm{ly}$ above the galactic plane.

Dust and ices. Mixed within all phases except the hottest phase where they do not survive, particles of dust and ice are an important component of the ISM. These particles range in size from a couple of nanometers (nm) to several micrometers (μm), that is, anything bigger than common molecules and smaller than little rocks. Dust grains plays a disproportionate role compared to their share of the mass of the ISM, for the following reasons. They are the primary source of interstellar extinction; they scatter short wavelengths. They account for gas-phase elemental depletion because they embed selectively some elements which cannot be detected when the dust grain is too large. Finally, they are the cradle and the catalyst of a chemistry which, otherwise, would not happen in the gas phase. However, the composition of grains along with the chemistry occuring on their surface is harder to probe than gas-phase molecules showing distinctive signatures.

In conclusion, the CNM is the coolest part of the galaxy despite being its inner part. The densities are high enough for ISCls to be sufficiently massive to shield themselves. On the other hand, the tenuous hot ionized medium is fully exposed to energetic radiation. Thus, only the CNM is characterized by temperatures and radiation fields low enough for molecules or dust particles to form.

1.3 The interstellar radiation field (ISRF)

The ISRF is the most crucial parameter to determine the physical and chemical state of a given interstellar environment. The ISRF causes ionization and ejection of electrons, dissociation or acceleration of atoms, molecules, and dust grains. It sets, along with the particle density, the balance between atomic and molecular gasses, neutrals and ionic species, and cold and hot environments. Six types of radiation are dominating the ISRF, and are listed in Figure 1.5, from longer to shorter wavelengths. Cosmic rays are worth mentioning although are not only radiation.

Synchrotron radiation is produced by relativistic charged particles which are deflected from their trajectories by magnetic fields. These relativistic particles, mostly electrons, spiral along the field lines emitting synchrotron radiation. The

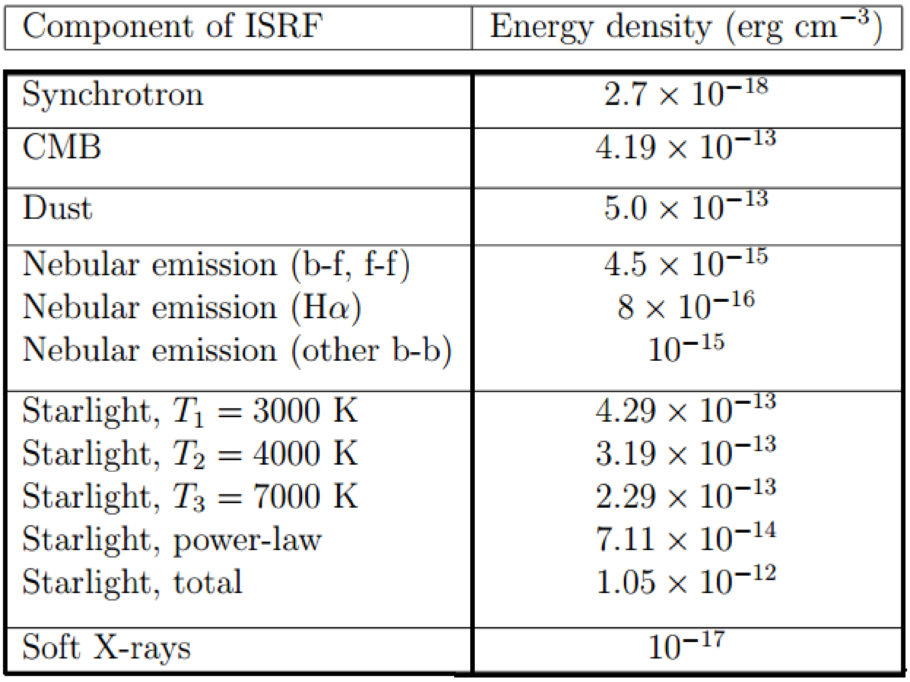

Component of ISRF	Energy density (erg cm^{-3})
Synchrotron	2.7×10^{-18}
CMB	4.19×10^{-13}
Dust	5.0×10^{-13}
Nebular emission (b-f, f-f)	4.5×10^{-15}
Nebular emission (Hα)	8×10^{-16}
Nebular emission (other b-b)	10^{-15}
Starlight, $T_1 = 3000$ K	4.29×10^{-13}
Starlight, $T_2 = 4000$ K	3.19×10^{-13}
Starlight, $T_3 = 7000$ K	2.29×10^{-13}
Starlight, power-law	7.11×10^{-14}
Starlight, total	1.05×10^{-12}
Soft X-rays	10^{-17}

Fig. 1.5: Energy densities of the different interstellar radiation field components.

total energy density of galactic synchrotron radiation is small (Figure 1.5 and 1.6). However, for wavelength $\lambda < 30\,\text{cm}$, it dominates over the cosmic microwave background radiation (CMBR) and is the main form of galactic emission in the long radio waves.

The CMBR is a nearly perfect plank spectrum with a temperature of 2.73 K. It is not displayed in Figure 1.6 but would be on the left of dust grains emissions with a similar energy density as shown in Figure 1.5. It dominates the ISRF for $600\,\mu\text{m} < \lambda < 30\,\text{cm}$, but the gas and dust being generally warmer, the CMBR does not play such an important role in the energy balance of the ISM.

IR emissions from dust dominates the ISRF between $5\,\mu\text{m} < \lambda < 600\,\mu\text{m}$. These emissions can be divided into emissions from hot PAHs in the near-IR (middle part of the magenta curve in Figure 1.6), and emissions from dust grains in the mid- and far-IR (left part of the magenta curve in Figure 1.6). Most of the power is radiated by dust grains $> 50\,\mu\text{m}$ and resembles the emission from a black body at 17 K. The rest of the power is radiated by PAHs through a series of discrete peaks, mainly between 3.3 and $12.7\,\mu\text{m}$ corresponding to IR emissions. Compared to the dust grains, PAHs emit at much shorter wavelengths when being subjected to the same incoming radiation because they distribute the photon energy over much less internal degrees of freedom. A UV photon absorption sets the internal temperature

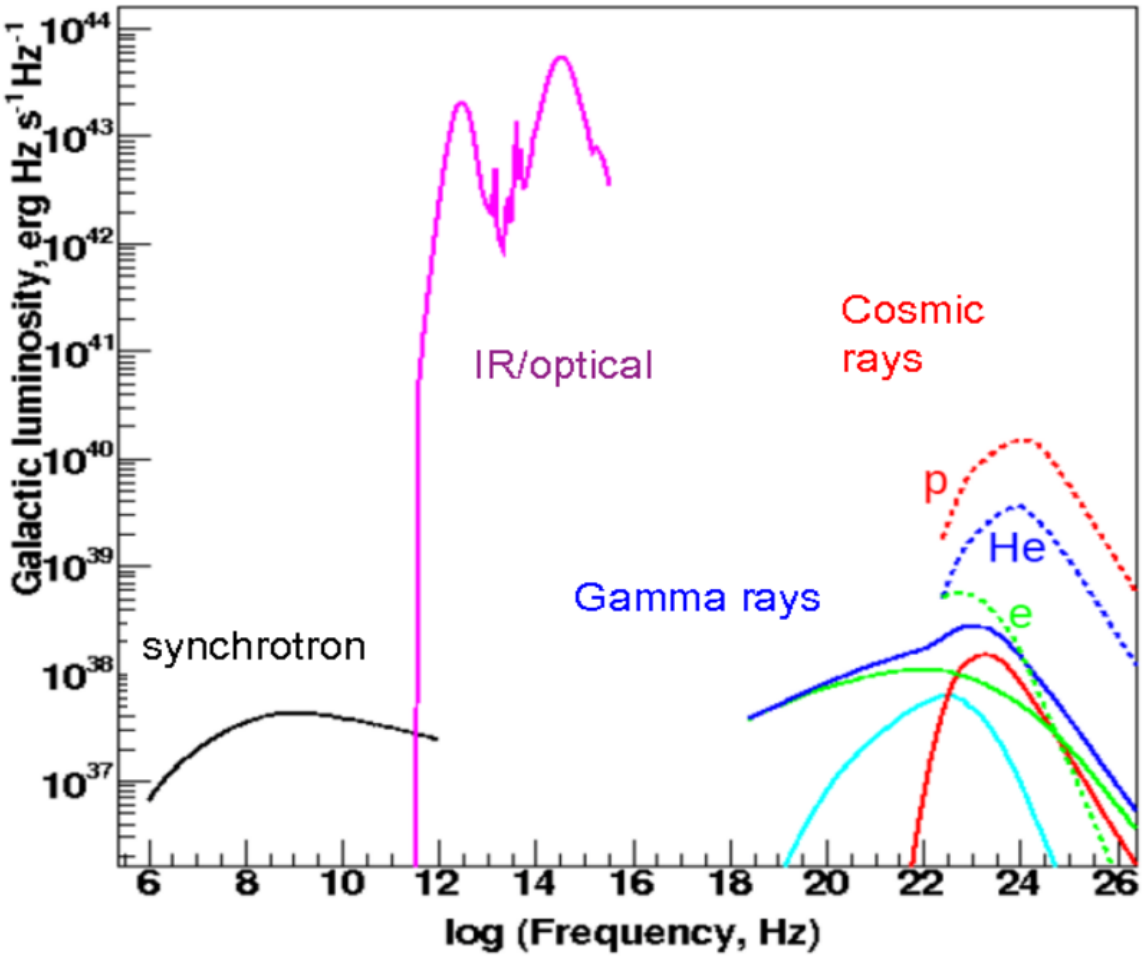

Fig. 1.6: Overview of the different components of the interstellar radiation field complementing Figure 1.5.[10] Only the cosmic microwave background is missing.

of a PAH to thousands of kelvins, but the same UV photon will set the internal temperature of a dust grain to much lower temperatures. Besides, the PAH will quickly cool down through IVR and IR emission, while the dust grain will do so much more slowly and at higher wavelengths.

Starlight is mostly from the near-IR to the soft-UV (right part of the magenta curve in Figure 1.6). It sharply drops above the ionization energy of hydrogen at 13.6 eV. A common estimate of starlight component of the ISRF at $\lambda < 2\,450$ nm is a sum of three blackbody spectra, shown in Figure 1.7, at 3 000, 4 000, and 7 500 K.[11]

Thermal X-rays are produced by highly energetic events, though localized in space and time. Hot ionized gasses with temperatures of more than 10^6 K cool via emissions of extreme UV or X-ray photons, but their total energy density is small (Figure 1.5).

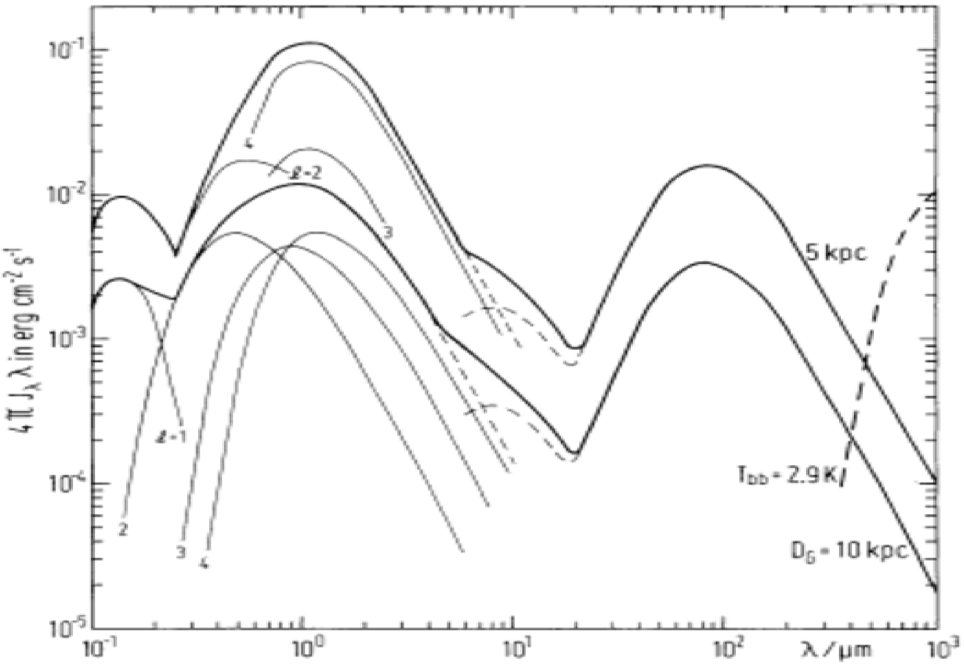

Fig. 1.7: Two sets of starlight and dust emission components of the interstellar radiation field (thicker curves), equivalent to a zoom-ins of the magenta curve of Figure 1.6. At wavelengths below 8 μm, the starlight takes over dust emissions, and can be approximated as a sum of several blackbody spectra[11] (thinner curves). The thick solid line is the sum. The upper set of curves is for a lower galactic latitude (5 kparsec).

Nebular emission comes from ionized regions heated by a nearby massive star to temperatures of 10^4 to 10^8 K. These are classified into free-free, free-bound and bound-bound emission, as any of the collision partners can be a free particle or a particle bound to another, like in an atom. Free-free emission is electromagnetic radiation emitted from the charged particles in a plasma continuously colliding with each other. The typical range of temperatures of this plasma will give rise to emission from the near-IR to X-rays for plasma as hot as 10^8 K. It cannot be seen in Figure 1.6 since the emission spans over a very large portion of the spectrum and has a lower energy density than most other components.

Cosmic rays act on interstellar gasses much like very energetic photons. Cosmic rays are baryonic particles which follow the comic elemental abundances meaning that 90% are protons, 10% alpha particles, and 1% metal nuclei (Figure 1.6). Their energy ranges from 100 MeV to 1 TeV. The energy density of cosmic rays is $\sim 2\,\mathrm{eV.cm^{-3}}$ to be compared to $0.65\,\mathrm{eV.cm^{-3}}$ of the total energy density generat-

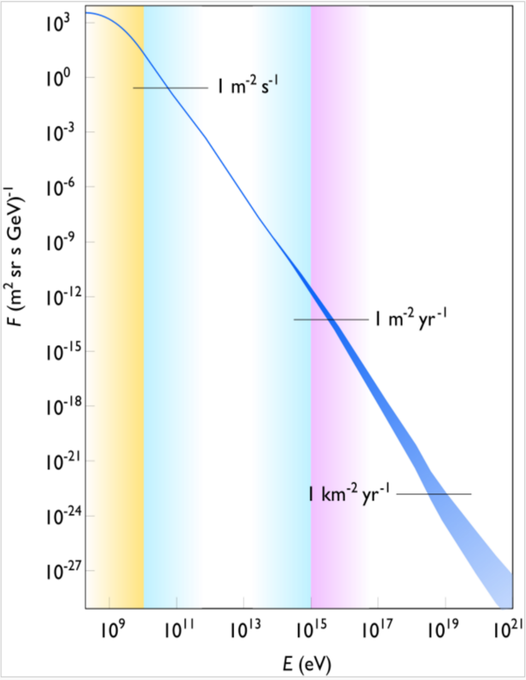

Fig. 1.8: Galactic, but mostly extra-galactic cosmic ray flux as a function of their energy. A large majority are free protons. They are observed by instruments mounted on balloons, satellites, and space crafts since most cosmic rays do not reach Earth's surface (Image credit: Wikimedia Commons user Sven Lafebre).

ed from starlight: They therefore play an important role in the energy balance of interstellar gasses. Most of the cosmic-ray-induced heating of interstellar gasses is provided by the least energetic ones ($\sim 100\,\mathrm{MeV}$), since they are much more numerous, as seen in Figure 1.8.

1.4 The cold neutral medium (CNM): cradle of interstellar molecules

Despite its name, the CNM described in Section 1.2, is still a harsh environment subjected to energetic radiation and violent shocks. It holds its name from H atoms being mostly neutral. However, heavier atoms, molecules, and dust grains, requiring less energetic photons, are ionized in significant proportions. The CNM comprises virtually all the types of clouds that contain molecules. These are atomic clouds, diffuse molecular clouds, translucent clouds and dense clouds. H is mostly neutral because the CNM receives little amount of photons with energies $> 13.7\,\mathrm{eV}$.

In diffuse clouds, C atoms are all ionized, and, as very reactive species, play a key role in the chemistry of these clouds. Table 1.9 divides the CNM into four components where diffuse atomic clouds are the hottest phase and dark clouds the coldest. The working definition for the CNM is that H is mostly neutral. The same way, the defining characteristics for differentiating the four types of clouds is the ratio of ionized over neutral, and atomic over molecular H and C. As a general trend, the hotter the cloud, the more diluted, the more transparent, and the more ionized it is. Within the CNM, dense clouds account for 30% of the mass, and hotter media for 99% of the volume.

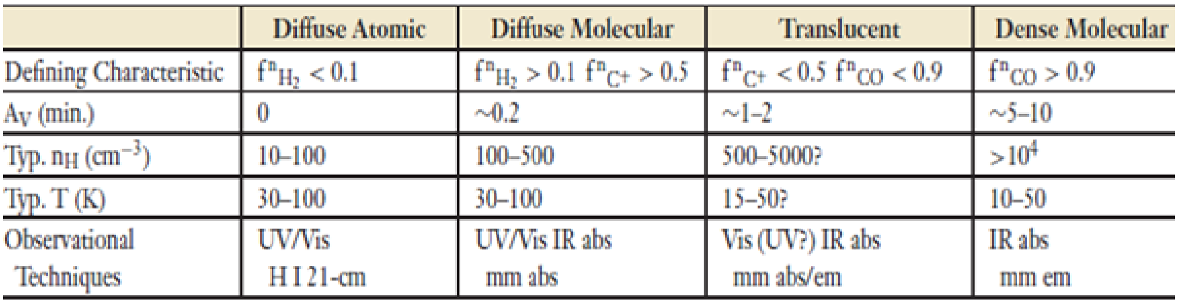

	Diffuse Atomic	Diffuse Molecular	Translucent	Dense Molecular
Defining Characteristic	$f^n{}_{H_2} < 0.1$	$f^n{}_{H_2} > 0.1$ $f^n{}_{C+} > 0.5$	$f^n{}_{C+} < 0.5$ $f^n{}_{CO} < 0.9$	$f^n{}_{CO} > 0.9$
A_V (min.)	0	~0.2	~1–2	~5–10
Typ. n_H (cm^{-3})	10–100	100–500	500–5000?	$>10^4$
Typ. T (K)	30–100	30–100	15–50?	10–50
Observational Techniques	UV/Vis H I 21-cm	UV/Vis IR abs mm abs	Vis (UV?) IR abs mm abs/em	IR abs mm em

Fig. 1.9: These four types[12] of environments all belong to the hatched green phase in Figure 1.4 and constitute the CNM, the coldest part of the ISM. $f^n{}_{H_2}$ and "$f^n{}_{CO}$" are the fractional abundances of H_2 and CO compared to the total amount of H and C atoms, respectively. "A_V" is the opacity of the cloud, decreasing with increasing density and volume. "n_H" is the typical density of hydrogen atoms, roughly equal to the total density. The observation technique depends on the transparency of the cloud.

Diffuse atomic clouds are the hottest phase of the ISM where H is still neutral. However, C is a particular case, since it undergoes chemical reactions leading to a production of C^+. This process is so efficient that the density of free electrons is approximated to the C density (see Figure 1.10). On the other hand, O and N are significantly less ionized. In diffuse atomic clouds, extinction is very low, meaning that the entirety of the cloud is exposed to the ISRF. All gas-phase molecules which are not resistant to UV radiation are quickly dissociated. Most small molecules known to be present in denser clouds do not survive there. Strickingly though, large molecules populate atomic clouds. These large molecules have not yet been identified and are the topic of the next chapter.

Diffuse molecular clouds are often shielded from the ISRF to some extent, typically by a diffuse atomic cloud. An important aspect of the shielding of molecular

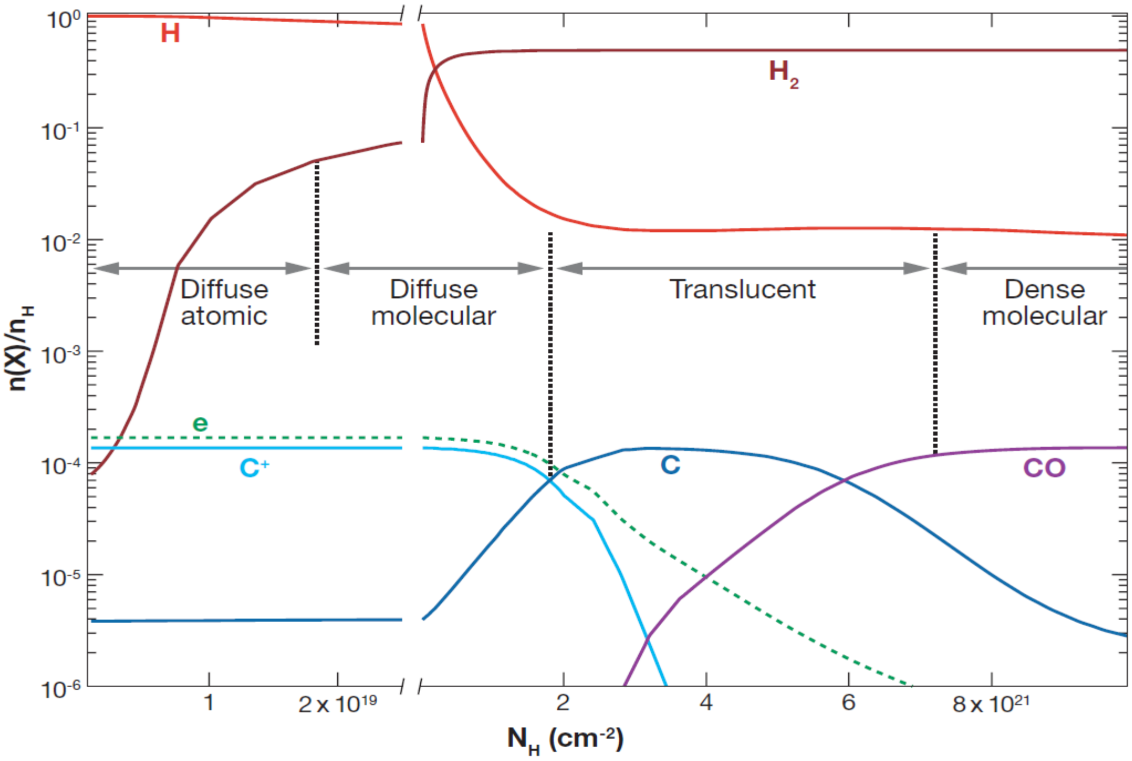

Fig. 1.10: Illustration of the CNM composition[12] as a function of the column density. As in the table above, the four types of cloud presented here all belong to the hatched green phase in Figure 1.4. The defining characteristic for a cloud is not the column density, and this illustration represents the local conditions, or an ideal case where one would probe a sightline with strictly only one type of cloud.

clouds is selective spectral shielding. The attenuation of the ISRF in the outer layer of a cloud will be strong at the absorption wavelengths of H and H_2, while there will be much less shielding at all other wavelengths since no other species have high enough densities to have such an effect. For instance CO cannot shield itself from the wavelengths of the ISRF where it has absorption bands. It is important, therefore, to understand that, despite the fact that the CO bond is much stronger than the H_2 bond, CO will be systematically dissociated in diffuse molecular clouds and will be mostly in the form of C^+. Higher column densities will be necessary for CO to shield itself, as seen in Figure 1.10. Molecules like CH, H_3^+, CO, nevertheless, are detected in diffuse molecular clouds, but this is due to a series of chemical reactions with the omnipresent H_2. Because C is mostly ionized, it allows an efficient ion-molecule chemistry to occur. However, again, all these simple species are short-lived in diffuse clouds since they do not shield themselves.

Translucent clouds must be surrounded by more diffuse clouds to allow C to be shield itself and be mostly neutral. Few translucent clouds have been observed but their chemistry is thought to be radically different from that of diffuse clouds since the very reactive C^+ is disappearing. Their molecular population constitutes indeed a transition between the many small molecules of dense clouds and the large photostable molecules of diffuse clouds.

Dense clouds have several orders of magnitude of extinction, densities of at least $10^4\,\mathrm{cm}^{-3}$, and temperatures down to $10\,\mathrm{K}$. These are the highest densities of the ISM and the lowest temperatures of the galaxy. They constitute the last stage of a typical cloud evolution before it starts a gravitational collapse to become a protostar. Most interstellar molecules have been identified only in dense clouds, starting with CH in 1937[13,14] and then OH in 1963.[15] Dense molecular clouds are always shielded from the ISRF by their outer layers, and hence, it is impossible to probe a sightline where only a dense molecular cloud will contribute. On the contrary, diffuse atomic clouds might very well be found to be the only contributors in a specific sightline, which makes their characterization easier.

In conclusion, a counterintuitive trend governs the chemistry of the CNM as we go from diffuse to dense clouds: despite that the fact the ISRF is getting milder and the densities higher in denser clouds, the chemistry actually gets slower in terms of reaction rates. The very reactive C^+ present in diffuse clouds is replaced by the moderately reactive C in translucent clouds, itself replaced by the non-reactive CO in denser clouds. If many simple molecules are found in dense clouds, this is because the much higher densities cope with lower reactivities. On the contrary, and to introduce the next Chapter, the presence of large molecules in diffuse media seems not to be related to the presence of reactive species, since these molecules likely originate from circumstellar envelopes (CSEs), and seem to merely survive in the ISM.

1.5 Thesis outline

This thesis, which is the core of a project started in 2010, is aimed at developing an experimental technique suitable for the measurement of the electronic spectra of cold, large, gas-phase molecular cations. Two approaches were initially targeted: photoinduced charge transfer and photodissociation of ionic complexes with He atoms. Since the latter is both the simplest of the two and a universal method, most efforts would be put toward its implementation. The project included the design and assembly of a new apparatus, a tandem mass spectrometer centered on a 22-pole trap. When this thesis was initiated, the apparatus was partially assembled and as a first major task, the assembly had to be completed and characterized. For this reason, chapters 4 and 6 treat some aspects of the obtained electronic spectra that are not novel, but which are part of the characterization of the apparatus and the method. Chapter 2 presents the several types of spectroscopic features that prove that large molecules do form interstellar and circumstellar media. Observations and laboratory experiments are used to put constraints on the responsible molecules. The experimental apparatus and the procedure to obtain the electronic spectra are detailed in Chapter 3, and some aspects of the characterization of the apparatus are presented in Chapter 4. The electronic spectra of several gas-phase protonated H^+PAHs at a rotational temperature of $\sim 10\,K$ constituted the first results of this apparatus and are presented in Chapter 5. These molecules were not studied with one of the two targeted methods, however, they were the firsts spectra obtained in the gas phase for such large cations for astronomical comparison. Also studying these five H^+PAHs allowed us to get a better handling of the setup and to solve experimental issues, as shown in Chapter 6. Chapter 7 presents the first results obtained using one of the targetted methods, the electronic spectra of coronene$^+$ and corannulene$^+$, extrapolated from the photodissociation (PD) spectra of their complexes with He. Chapter 8 addresses the case of protonated C_{60}, a project which has merely been started. Finally Chapter 9 concludes and gives an outlook about the general challenge of identifying large molecules in the ISM and CSEs.

2. SPECTROSCOPY AND LARGE UNIDENTIFIED MOLECULES IN THE ISM

In contrast to the many small molecules identified in dark clouds, there is evidence for the presence of large molecules in the ISM and CSEs. Molecules have been identified in dark clouds because the number of possible structures to be assessed is limited, and larger molecules have not been identified because the number of relevant structures is nearly unlimited. Strikingly, small molecules do not outnumber large ones in the ISM, and they tell more about our limited experimental means than about the true molecular population.

Almost all what we have learned of the Universe is through spectroscopy, with limited information coming from cosmic rays and meteorites.[16,17] For the observation of large molecules, the methods rely mostly on direct absorption through diffuse media and fluorescence from reflection nebulae at UV-Vis and IR wavelengths. Four main types of spectroscopical features, all bringing specific information, will be described in this Chapter. The anomalous microwave emission is not described, but the information it brings is mainly limited to the temperature and size distribution of the emitting grains or molecules.

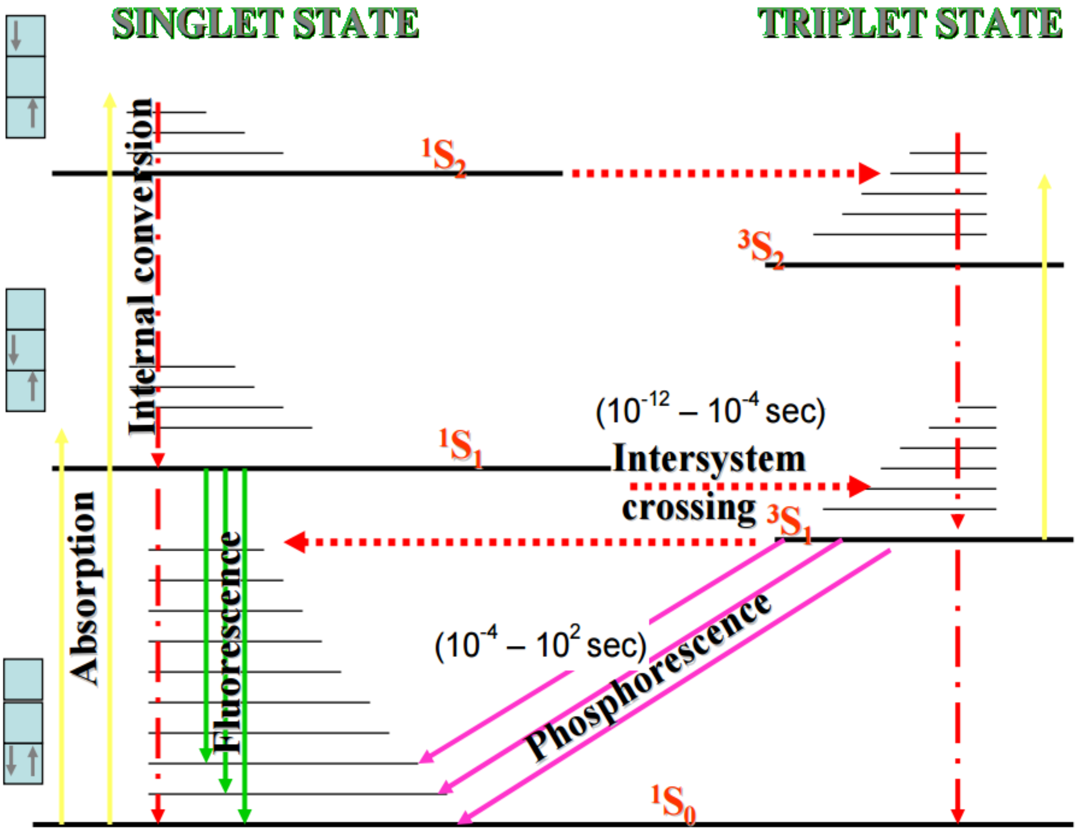

Fig. 2.1: A Jablonski diagram showing the possible outcomes after a molecule has absorbed a photon promoting it to an excited electronic state. Environmental effects (collisions) do not play a role in the case of the ISM given the low densities. The molecule will eventually get rid of its energy by emitting either IR (vibrational relaxation) or visible photons (fluorescence, phosphorescence).

2.1 Unidentified infrared bands (UIBs)

The most prominent astronomical features that show evidence of large molecules are mid-IR bands between 3.3 and 20 μm, lying on top of several broader emission features (plateaus). These emissions are observed in almost all kinds of interstellar environments,[19–21] except dark clouds on one hand, and extremely hot environments, on the other. In virtually all other types of gasses, galactic and extragalactic, including highly red-shifted galaxies,[22–24] these emissions are present. The nature of their carriers is debated, but it is clear that they arise from large carbon-based molecules excited by UV photons and fluorescing in the IR via vibrational transitions. Most of these transitions are assigned to specific vibrational modes, such as C-H and C-C

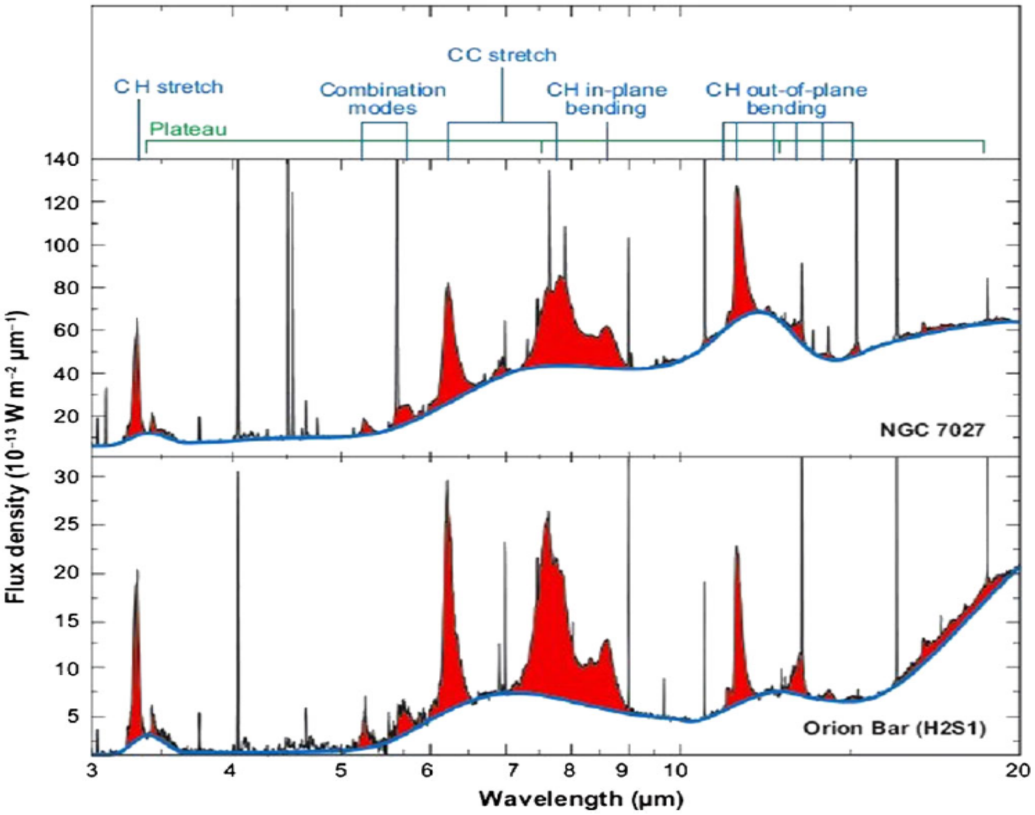

Fig. 2.2: Overview examples of the mid-IR emission features[18] in a planetary nebulae (NGC 7027) and a photodissociation region (Orion Bar). Both spectra will vary depending on the location within NGC 7027 and the Orion cloud. Specific vibrations are assigned to the main features, and the strengths of the C-C and C=C stretchings attest of the carbonaceous nature of the carriers.

bendings and stretchings, but no definite molecule or mixture of molecules or their structure have been identified to date. The main of these features are at 3.3, 6.2, 7.7, 8.6, 11.2, and 12.7 μm, and are assigned in Figure 2.2 to specific vibrational modes of hydrocarbons. Weaker emissions appear at 3.4, 5.2, 5.7, 6.0, 7.4, 12.0, 13.5, 14.2, 15.8, 16.4, 17.0, and 17.4 μm, and broader features around 7, 12 and 17 μm. The peak positions of the latter can vary with the sightline.

Infrared emission arise from fluorescence, that is, spontaneous photon emissions from a material which has been previously excited by another photon. The detection generally happens perpendicularly to the source flux to avoid saturating the detector with the much higher intensities from the source. This is the case of the UIB carriers, typically irradiated by a very luminous neighboring star, and re-emitting in all directions. The scheme for the UIB emissions is the absorption of a

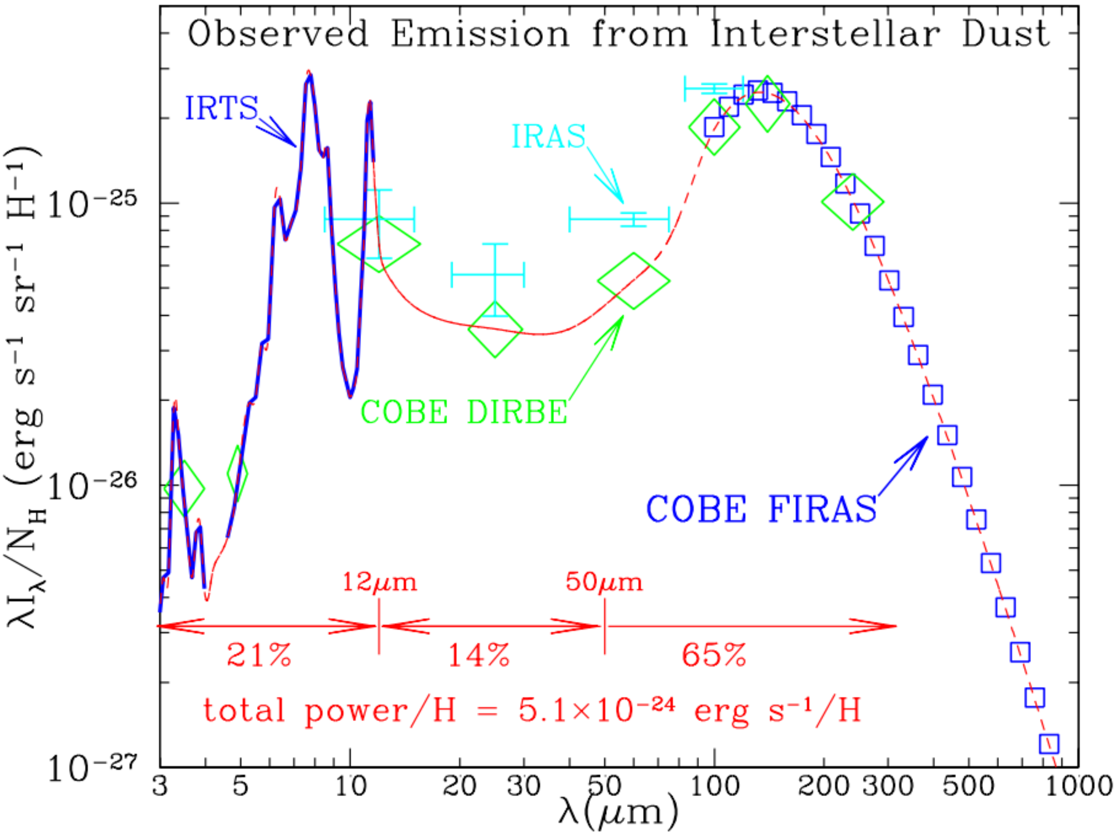

Fig. 2.3: Observed diffuse emissions in the infrared, normalized to the column density of hydrogen. Taken from the Infrared Astronomical Satellite (IRAS),[25] the Infrared Telescope in Space (IRTS),[26,27] Spitzer Space Telescope (Spitzer),[25] and Cosmic Microwave Explorer (COBE).[28,29]

UV-Vis photon promoting the molecule to an excited electronic state, followed by internal conversion to an excited vibrational state of the electronic ground state, followed by IR emission from vibrational de-excitation within the ground electronic state.[31,32] In Figure 2.1, it is represented by the yellow and dashed red arrow and does not involve electronic fluorescence (in green).

The color temperature of a theoretical blackbody emission peaking at 8 μm is 360 K. For the case of a photon energy of 8 eV, entirely going into the vibrations (since there is no electronic fluorescence), the number of vibrational modes (∼ 3 N) in the molecule is calculated as followed:[33]

$$3\,N \;=\; \frac{\Delta E}{k\,T} = \frac{8\,eV}{k\,360} = 257 \tag{2.1}$$

This is the number of modes which, excited by a 8 eV photon will bring 257 modes, or ∼ 86 atoms, to a temperature of 360 K. This is not necessarily the total number

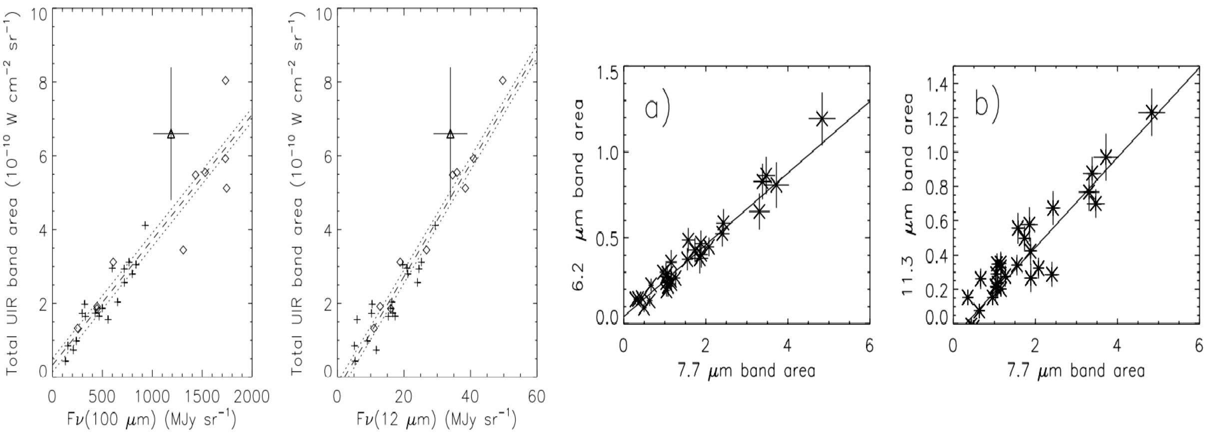

Fig. 2.4: The left two panels show the correlation of the mid-IR features with the continuum at 100 and 12 μm, and the right two panels show the correlation of the 7.7 μm emission with the 6.2 and 11.3 μm emissions.[30] The left two panels indicate a strong correlation of the mid-IR features with the dust emission, and the right two panels of the mid-IR features with themselves.

of modes of the particle. Only a portion of a large molecule or a grain may be the source of the IR emission. As such, this result gives a minimum. Also, given the wavelength range of the UIBs and that of the exciting photons, the expectable size range of the emitters is also very wide.

Dust continuum is a strong and smooth emission continuum at longer wavelengths, centered around 100 - 200 μm. The curve resembles a blackbody emission, strongly correlated with the mid-IR features,[30] as shown in the two left panels of Figure 2.4. Grains are heated by starlight and re-emit in the IR through vibrational relaxation. This process is thought to occur since these emissions show no polarization, as would be expected from scattering of starlight. These grains probably occasionally eject molecules or clusters formed on their surface, and these, now in the gas phase, will emit at discrete frequencies. Dust grains emit around 2/3 of the total power in the IR and large molecules around 1/3.

PAHs emissions. The 3.3, 6.2, 7.7, 8.6, 11.2 and 12.7 μm features are seen in most reflection and emission nebulae, i.e., diffuse molecular gasses subjected to relatively intense radiation from a nearby star. However, the radiation intensity seems not to be a critical parameter as these features are seen against a variety of star temperatures. Along with the various hypotheses on the nature of the carriers and the sightline dependent profiles, this seems to suggest a variety of carriers depending on the local conditions. Most hypotheses stand between the two following somewhat extreme cases. The first one is that only a few specific PAH structures of 50 - 100 atoms, very stable, maybe containing H, N, and O to some extent, survive and stand out of the crowd of possible PAHs and are responsible for these emissions.[18] The second hypothesis is that a mix of aromatic-aliphatic compounds, with no specific structure and a variety of sizes could be the origin of these emissions.[34] Intermediates include very small carbonaceous molecules[35] or hydrogenated amorphous carbon (HAC). Mid-IR features also have a high correlation with a high C/O ratio in the emitting gas.[36] This implies, as it was already thought, that the carriers are carbon-based molecules. A high C/O ratio (> 1), originating from so-called carbon stars, is not required to observe IR emissions, but is of great help for C not to be locked-up by O in the very abundant CO, and to form other compounds.

C_{60} and C_{70} emissions. The detection of C_{60} (via the 18.9 and 17.4 μm bands) and C_{70}[37] have raised a possible link to PAHs, and more generally, to the carriers of the mid-IR features. Some of the environments in which C_{60} and C_{70} vibrational emissions have been identified also show the mid-IR features and plateaus. However, some do not, and given the small number of C_{60} and C_{70} detections in comparison to the UIBs, a link is questionable.

Emission plateaus. There are three main emission plateaus centered around 7 - 8, 12 - 13, and 17 - 18 μm. The first two are identified as a superposition of modes in aromatic molecules containing aliphatic groups.[34] The last one has not been assigned, but could be due to CCC vibrations in aromatics. This plateau seems to be present in particularly harsh environments were fully aromatic structures are more likely to survive UV radiation than those containing aliphatic groups.

In conclusion, many experiments and calculations have been performed over the last two decades attempting at reproducing specific emission features[38, 39] or the whole ensemble[40, 41] using selected compounds or mixtures of compounds. However, none has conclusively disclosed the composition of the carriers, and 40 years after their discovery, several families of candidates still stand. One reason is the large variety of possible families of carriers, including PAHs, mixed aliphatic aromatic nanopaticles, dehydrogenated PAHs, PAHs with hetero-atoms, deuterium, protonation, and small specific carbonaceous molecules readily produced. Another reason is that the fluorescence yield is not proportional to the absolute amount of a specific emitter relatively to the others. It is likely that the UIBs will give us in the future a more global knowledge of the molecular population in these environments, and will not lead to the identification of distinct molecules, in contrast to the DIBs.

2.2 Red extended emission (ERE)

ERE can be seen as the electronic photoluminescence counterpart of the UIBs. They arise from dust particles or crystals, often in CSEs, absorbing a UV-Vis photon, and re-emitting several photons at shorter wavelengths. The carriers, still unknown, are probably different from the UIB carriers since there is no observational correlation between them. The emission spectrum peaking between 660 and 700 nm was first analyzed in a study[42] of HD 44179, in the red rectangle (RR). Since then, ERE has been observed in spectra of many reflection nebulae,[43,44] HII regions, in the Milky Way and other galaxies. More generally, it has been found to be a general feature of the dusty ISM.[45] Although to date, never as bright as in the spectrum of the RR.

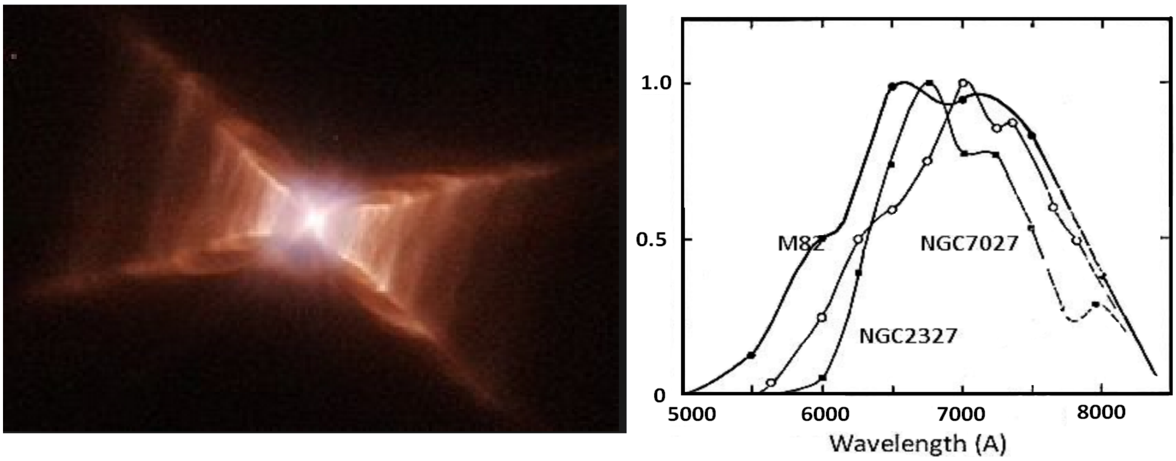

Fig. 2.5: (Left) Observed with Hubble space telescope, the RR was the first nebulae where ERE was detected and is still the brightest ERE source known. The nebula is created by a red giant carbon-rich star, coupled to a very hot white dwarf (HD 44179), both totally hidden behind their dusty ejecta. The hot white dwarf might be the reason for the strength of this ERE. (Right) ERE spectra from nearby galaxy M82 and two galactic nebulae. The general appearance of the feature is the same but the peak position and FWHM vary from source to source. These two characteristics vary as well within a specific nebula as respect to the distance from the central star.

Photo-luminescence from far-UV photons. The carriers are thought to absorb very energetic photon $\sim 10\,\mathrm{eV}$ and subsequently emit one to three red photons from low-lying electronic states. With a quantum efficiency of more than 100%, the process is based on the concept of inverse electronic relaxation.[46] The energy from a highly excited vibrational state of the electronic ground state is transferred to a low-lying electronic excited state, from which it fluoresces. In Figure 2.1 on the left, that would correspond to the dashed red arrow followed by the yellow arrow, and not the contrary. This is possible because the transition probabilities for vibrational modes are much lower than the ones for optical fluorescence transitions. Then, quantum efficiencies up to 300% are possible when ERE photon energies are around 2 eV and exciting photons energies $\sim 10\,\mathrm{eV}$. As long as no collisions with other particles occurs in the meantime. Photons of this energy and the diluted medium where ERE comes from, to avoid collisions, meet these requirements.

Observational constraints on the carriers. The ERE is strictly only created by far-UV photons because they are absent in reflection nebulae whose star's $T_{\mathrm{eff}} \leq 10^4\,\mathrm{K}$.[47] This contrasts with ordinary PL where the absorbed photon only needs to be slightly higher in energy compared to the emitted one and proves that the process relies on far-UV photons coming from the central star. An interesting finding from studies of different sources is that the ERE peak intensity shifts to longer wavelengths and its FWHM increases along with the density of far-UV photons from the source. Namely, as the UV density increases by six orders of magnitude, the integrated ERE intensity increases by four orders of magnitude, and its FWHM doubles. This strongly supports a whole family of carrier molecules shifting, as does a blackbody signature, from small ones in the case of a lower UV irradiation to larger ones. As the UV irradiation increases the smaller species get destroyed, leaving less numerous and larger species yielding a broader, proportionally fainter and red-shifted band. Fainter, maybe also because the conversion efficiency is lower for larger molecules. Another survey of 20 planetary nebulae comprising carbon and oxygen-rich stars found that only carbon-rich stars displayed ERE,[48] leading to a carbonaceous nature of the carriers. Finally, inside a given nebula, the ERE is not spatially correlated to the UIBs at 3.3, 8, 11.3, 12 and 22 μm. The ERE is situated close to the illuminating star whereas UIBs appear farther away indicating more stable structures as carriers of the ERE than the UIBs.

Proposed carriers. The original studies of the ERE suggested hydrogenated amorphous hydrocarbons (HAC) to be the responsible, with a varying extent of hydrogenation accounting for the shift in the peak wavelength.[44] When experimental

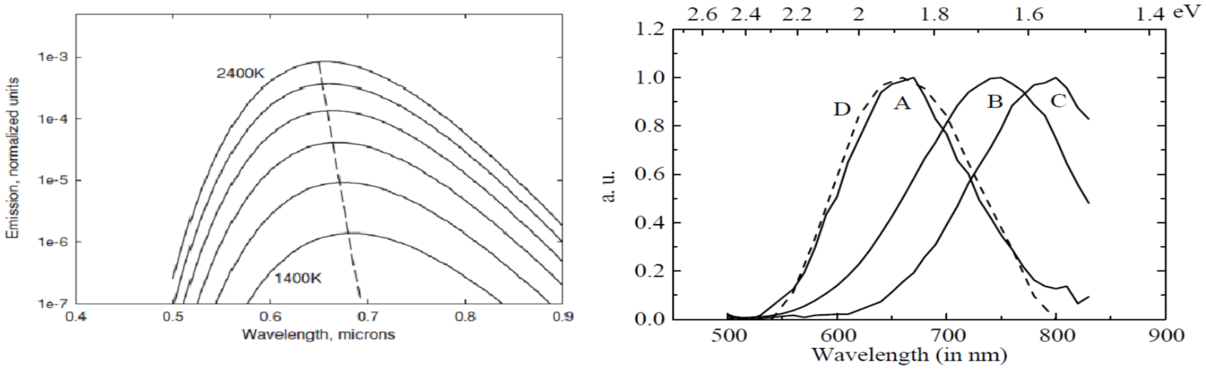

Fig. 2.6: On the left, thermal emission calculated for individual carbon nanoparticles heated to temperatures 1 400 to 2 400 K. For a molecule like C_{24}, T = 2 400 K corresponds to the absorption of a 13.6 eV photon, and T = 1 400 K to 8 eV. On the right, silicon nanoparticles photoluminescence spectra under excitation at 266 nm. Samples A, B, C have average particle sizes of 3.65, 3.92 and 4.95 nm, and efficiencies of 1, 1.2, and 1.6%, respectively.[49] The dashed curve represents the ERE from NGC 2023.[44]

studies of these candidates came, it turned out that HAC's PL efficiency is high when the band-gap is high (in the blue) and drops towards the red, discarding them as good candidates. Moreover, the discovery that silicate features are also present in carbon-rich circumstellar environments and the correlation between H_2 and the ERE further came against the HAC hypothesis. Large PAHs and fullerenes were also suggested, but the first ones have sharp absorption features in the blue which are not seen in astronomical spectra, and the second have a PL efficiency which is too low to explain the ERE. The first candidates which experimental PL spectrum and efficiency matched the ERE,[49,50] were Si nanoparticles SiO_x and pure porous Si particle, for which the variation of the size of the particle was shifting the peak wavelength. These particles should be in the size range of a couple of nm, and as both Si and O are abundant, the required total dust mass for the ERE strength was only a fraction of the available Si and O. More recently, nanodiamonds have been proposed as the carriers. Although the experimental spectra are not as strikingly similar to the ERE,[51] they have the advantage that C is more abundant than Si and that ERE is correlated with CSEs of carbon stars.

2.3 Diffuse interstellar bands (DIBs)

The DIBs are visible and near-IR absorption bands caused by gas-phase molecules present in diffuse ISCls. Among all astronomical features demonstrating the presence of large molecules, they were the first to be discovered. The first observation, at the Mont Wilson, dates back 1919,[2] and their first assignment to interstellar unidentified molecules dates back to 1936.[52] Then, Merrill stated: " four additional detached lines, whose approximate wavelengths are 5 780.4, 5 796.9, 6 283.9, and 6 613.9 Å and an other one, a vague feature near 4 427 Å is suspected. The chemical identification of these lines has not yet been made". Almost a hundred years later, their chemical identification and that of hundreds of other lines has not yet been made. These interstellar absorptions arise from electronic transitions in molecules whose number of atoms is, a priori, from a few, to dozens or possibly hundreds. For the assignment of any DIB to a specific molecule, a laboratory absorption spectrum of this molecule in the gas phase and at cold temperatures (to mimic interstellar conditions), must match with the DIB. Given the possibly large number of atoms that the may molecules contain, the number of possibilities is extremely high. A difficulty in finding the carriers is that each spectrum obtained in the laboratory comes at the expense of a considerable work.

In the middle of the 20th century, with the advent of IR astronomy, a good correlation between some of the strongest DIBs and the dust extinction was observed, and the theory flipped to dust grains as carriers of the DIBs.[54] Later, it was realized that dust grains had a number of weaknesses that gas-phase molecules do not have. These include varying absorption characteristics that should depend on the grain size, polarization effects from grains, and most importantly the realization that some molecules do form efficiently in harsh interstellar environments. Higher resolution spectra later showed that the contour of some DIBs can indeed be assigned to rotational profiles of electronic transitions in gas-phase molecules.

Absorption spectroscopy. The diffuse interstellar medium (DISM) is optically thin, that is, most of the visible light passes through. Following the Beer-Lambert law, the absorbance A of a molecule, unitless, is proportional to the number of absorbing species N, the absorption cross section σ, and the path length L.

$$A = \sigma N L \,(cm^2 \times cm^{-3} \times cm) \tag{2.2}$$

$$A_{molecule} = 10^{-15} \times 10^{-3} \times 10^{18} = 10^{-2} \tag{2.3}$$

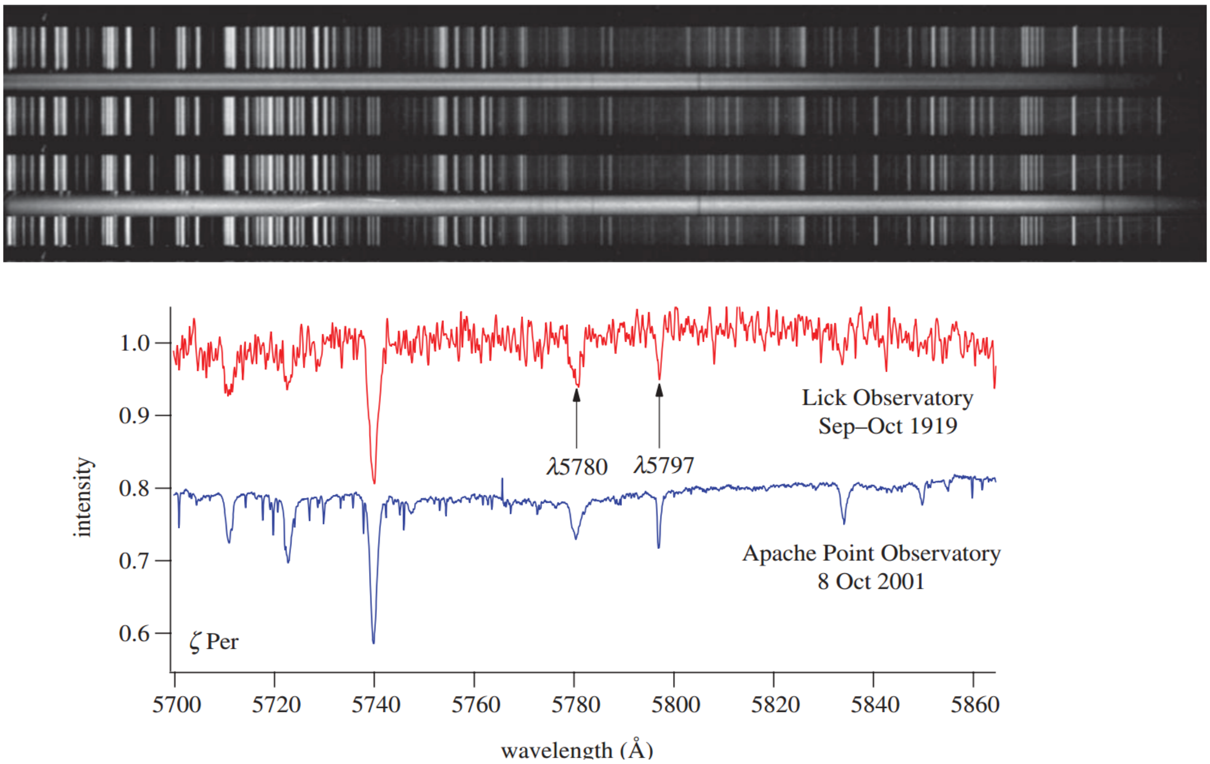

Fig. 2.7: On top, the two plates recorded by Mary Lea Heger at the Lick Observatory in 1919. Red spectrum is an average of the digitization of her plates,[53] and contend the two first DIB observed. Blue spectrum is a 2001 spectrum toward the same star, for comparison. Her observations of Zeta Persei aimed at measuring atomic lines, and very little attention was paid to these two unidentified bands until Merrill's work,[53] a decade later.

In the case of a typical diffuse cloud, the H density is around $10^2\,\mathrm{cm}^{-3}$, the C density is around $10^{-2}\,\mathrm{cm}^{-3}$, and the density of the most common molecules is around $10^{-3}\,\mathrm{cm}^{-3}$. With an absorption cross section of $10^{-16}\,\mathrm{cm}^2$ and a cloud of 1 ly depth, the absorption is around 0.1%. The starting numbers are extraordinarily different from terrestrial references, nevertheless, it is interessting to note that the resulting column density and absorption are comparable to that of a meter of polluted air on Earth.

There are three types of UV-Vis transitions, and they involve p, s, and n electrons, charge-transfer electrons, and d and f electrons. Absorption of UV-Vis photons in organic molecules is limited to chromophores that contain valence electrons, as shown in Figure 2.8. $\pi \rightarrow \pi^*$ are the transitions of interest since they have the strongest absorptions, typically in unsaturated organic compounds, thought to be

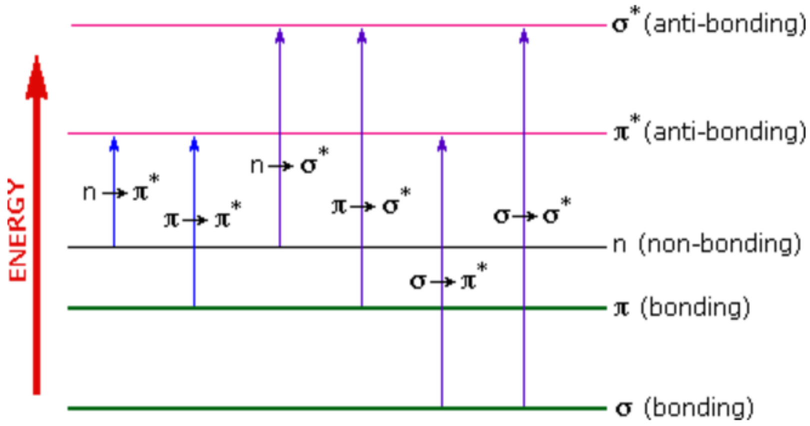

Fig. 2.8: Electronic transitions of π, σ, and n electrons in organic molecules.[55] They are responsible for the UV bump, the DIBs, and possibly the far-UV rise of extinction.

responsible for the DIBs. Charge-transfer absorptions are strong but less likely to be relevant for the ISM since they are often very broad, and hence, would be difficult to detect. Absorptions involving d and f electrons are also not very relevant for the case of molecules in the ISM since they require large atoms whose abundances are very low. Absorption spectroscopy can be done through a solid, liquid or gas-phase medium. Theoretically, it could also be done through an ion cloud, however, since ions keep far away from each others, extremely low sample densities make the technique impractical.

Observational constraints. Every candidate molecule for laboratory study has to be carefully selected, and observational constraints give the firsts criteria. DIBs are observed in other galaxies and extragalactic objects and are maybe revealing the largest reservoir of organic molecules in the universe. DIBs are not as apparent as other features assigned to organic molecules, as for instance the UIBs. DIBs are observed in absorption in the visible, and only optically thin sightlines in the visible are relevant targets. This constitutes a strong observational constraint meaning a high absolute quantity of the carriers.

One of the fundamental questions concerning the carriers is to find out whether they are built on grains' surfaces or via reactions in the gas phase (whether these occur in the diffuse clouds themselves or a long time before in circumstellar shells). It turns out that several DIBs among the strongest are well correlated with E(V - B), but that a majority of small DIBs are poorly correlated with E(V - B).[56,57] There

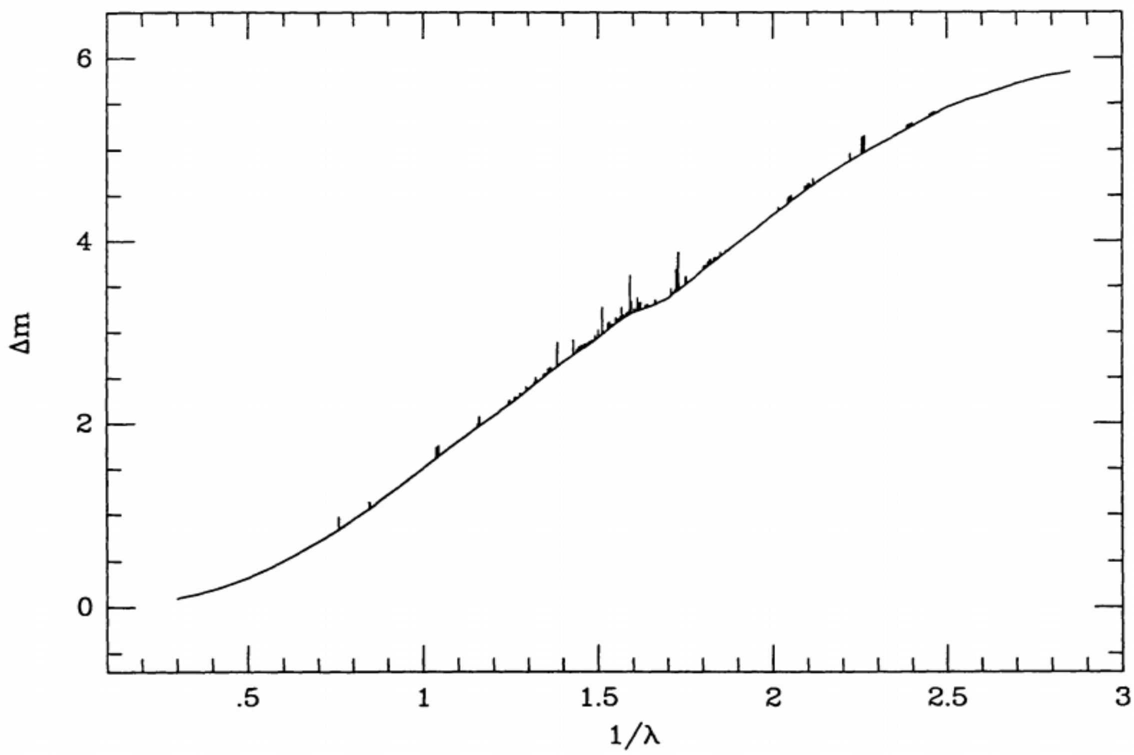

Fig. 2.9: The diffuse interstellar bands seen toward HD183143, on an inverted log scale. Electronic absorptions arising from interstellar molecules appear as little spikes.

even have been recently detected two DIBs with a negative correlation to dust extinction.[57]

Another fundamental aspect of the problem, assuming that DIBs arise from electronic transitions in gas-phase molecules, is to find if some of them arise from the same carriers, or even from the same electronic transition. Analysis of the correlations between individual DIBs has been widely performed, with machine learning now bringing a lot of information.[56,57] Several of them have been found to be strongly correlated and are probably due to the same carrier, however, a large majority of the DIBs actually display a poor correlation between each other, suggesting many different carriers. Although this constitutes a significant piece of information, it does not bode well for a long-term exhaustive assignment of the features. Nonetheless, several classes of carriers could be extracted (such as the C_2 DIBs) by correlating their strength to that of diatomic or atomic absorption lines.

The unique case of the Red rectangle. Since its identification in 1975, the red rectangle (RR) has probably been the most interesting astronomical object in terms of emission features suggesting the formation of complex molecules. It does constitute the only known source which displays the ERE, the UIBs, and a few DIBs together. Also, it is the only known source to feature the DIBs in emission, thus constituing a unique piece of information toward their identification.

It is not known why the RR is so unique, and why these features are not observed in other circumstellar or circumbinary nebulae. The central binary, HD 44179, is a C-rich post-asymptotic giant branch star coupled to a helium white dwarf, situated $\sim 710\,\mathrm{pc}$ from us.[58] An evolutionary scenario suggests that the stars were 2.3 and 1.9 solar masses ($M_\odot$) in their main sequence,[58] as seen in Figure 2.10. Now, the post-asymptotic giant branch star has a mass of $0.57\,M_\odot$, with $T = 7\,500\,\mathrm{K}$ and $L = 6\,000\,L_\odot$, while the white dwarf mass is $0.35\,M_\odot$ with $T = 60\,000\,\mathrm{K}$ and $L = 100\,L_\odot$. The presence of this much hotter companion may be the crucial factor giving to the RR its spectroscopic characteristics. The white dwarf blackbody spectrum is centered at 50 nm and produces a small HII region in the inner dense torus. What does it tell us about these major DIB carriers? (1) First, they are present in environments differing a lot from DISM. The biconical flow has densities of 5×10^5 particles.cm^{-3} 160 AU away fom the central star. The carriers seem to survive all the way from the center to the interstellar medium. (2) Such dense and irradiated environments may be the typical media where many DIB carriers form. Once released in the ISM, they would survive for millions of years in more sterile environments. DIB carriers may be produced from the strong UV irradiation from the white dwarf, around the HII region. Such irradiation does not occur in a common circumstellar nebula. (3) Finally, the RR has a very low observed metallicity. The dust formation from refractory elements seems to link the formation of these DIB carriers to dust grains.

In conclusion, the chemistry of the RR is fascinating; particularly the presence in emission of what is almost surely electronic transitions in the same molecules that cause the respective DIBs. However, the evolution of the binary system in the RR is a commonly observed scenario and raises the question of why its chemistry seems unique. It is possible that this specific timing in the evolution of the two stars is necessary to produce such a chemistry. Also, we are witnessing a very short-lived phenomenon, making it rare in terms of astronomical observation, but still significant since the molecules produced will probably soon seed the DISM.

Link with the ERE. The correlation between DIB and ERE carriers is difficult to assess because of the methods of observation. The DIBs are observed in

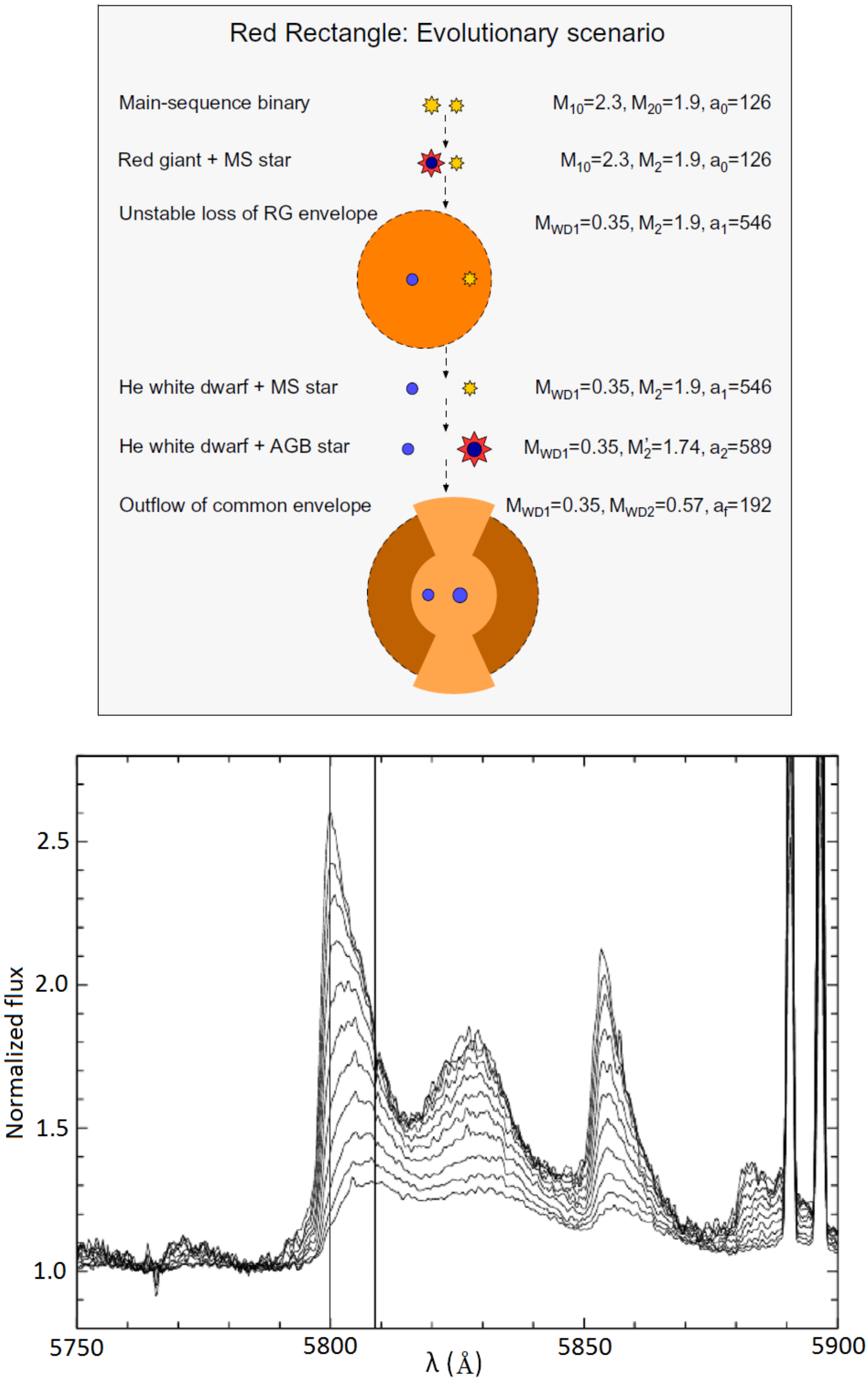

Fig. 2.10: On top, the evolutionary scenario for the binary system which gave rise to the RR.[58] On the bottom, ERE from the RR around 6 800 Å, recorded at various distances from the central binary. The measurements were done 2.9 arcseconds from the binary (bottom trace) to 5.6 arcseconds (top trace).[59] For a reference, the image from Hubble Figure 2.5 has a total angular view of ~ 25 arcseconds, where the feature converges to the narrow 5 797 DIB.

absorption toward distant stars whereas the ERE is observed in emission from closer objects. Both, however, yield similar families of possible carriers, namely stable carbon-based molecules[60] and nanoparticles. The spectral density of DIBs overlaps rather well with the ERE spectrum which suggests that the carriers might even overlap.

We can note the recent findings of DIB carriers seen in emission, apart of the RR. Emissions were found at 4 428 and 5 780 Å in the CSE of the fullerene-containing planetary nebulae Tc 1,[61] and at 6 613 Å in the diffuse ISM.[62] This does not only shows that some DIB carriers do fluoresce in the visible as the ERE carriers do, but also strongly suggest their circumstellar origin.

2.4 The 217.5 nm absorption (UV bump)

The UV bump is yet another ubiquitous interstellar absorption feature whose carriers are unidentified. It was discovered in 1965[64] and appears smoothly embedded in the UV interstellar extinction curve, peaking at 217.5 nm. Its average equivalent width is 130 Å,[65,66] two order of magnitude higher than the strongest DIBs. Its specificity, compared to other astronomical features, is that it has a constant peak wavelength but a width varying from 36 to 77 nm along different sightlines (Figure 2.11). Many models and experiments have tried to reproduce these characteristics, without any consensus on the carriers to date. However, it is generally agreed that (1) the carriers are different from the ones causing the interstellar extinction curve since their presence are not correlated. (2) They are carbon-based particles processed by the ISRF and containing a debated amount of hydrogen.[67] (3) Some DIBs tend to correlate with the UV bump height and anticorrelate with its width.[68] This could mean that the latter DIB carriers are strongly related with more UV-processed UV bump carriers, the ones causing a heigher and narrower feature. In other words, these DIB carriers would be end products of UV processing of the UV bump carriers. For instance, UV processed fulleranes responsible for the UV bump would give fullerenes for the DIBs.

Figure 2.12 shows the results from computations on nano-sized UV-processed hydrogenated amorphous carbon grains (top), and from direct absorption spectroscopy on the fullerane $C_{60}H_{36}$ in n-hexane (bottom). From 1998 and 2009, respectively, both fit remarkably well the astronomical data. Hence, it is still unknown

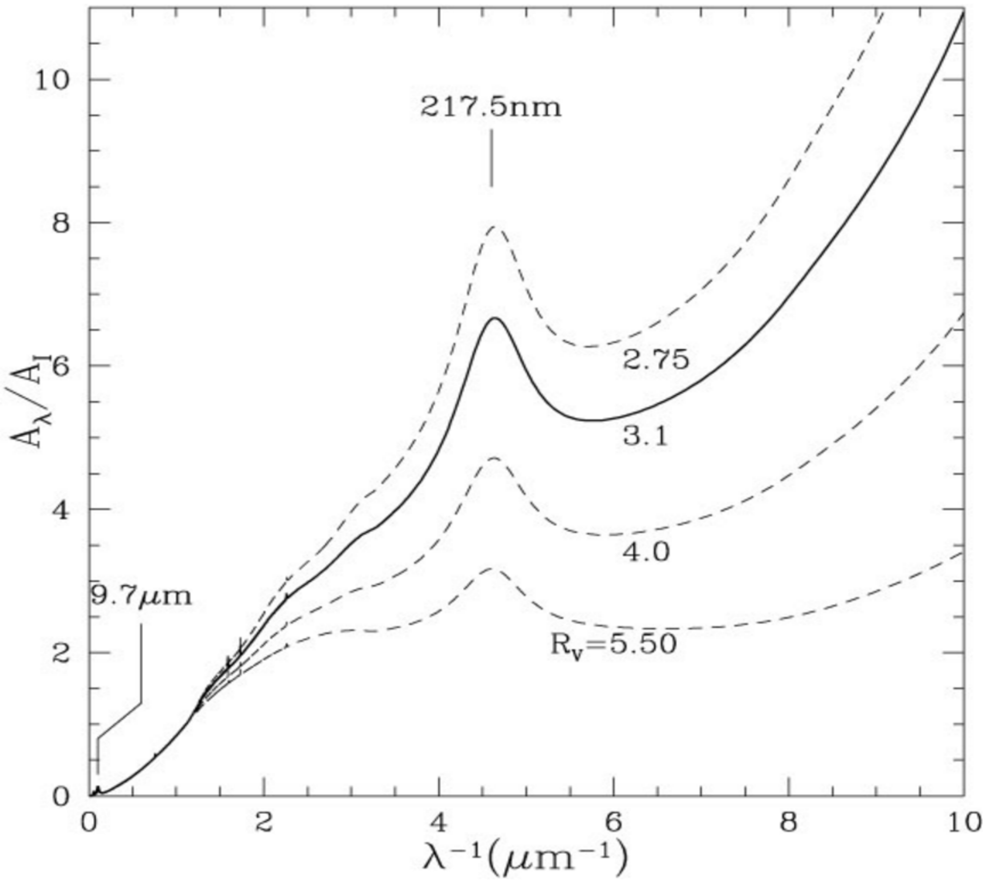

Fig. 2.11: The UV interstellar extinction curve recorded toward sightlines with extinctions from $R_v = 2.75$ to 5.5.[63] The absorption band has various widths and intensities but a constant peak wavelength. One can note the relative strength of the DIBs, barely visible.

whether the carriers are from a restricted group of molecules, like specific stable fulleranes,[71–74] or from a broader family of nano-sized carbonaceous particles more or less structured by UV radiation.[69, 75–77]

Fulleranes are almost surely present, to some extent, in the ISM because C_{60}, C_{70}, and C_{60}^+ have identified and because of the fast reaction of C_{60}^+ with the overwhelming H. Fulleranes have also been detected in meteorites[78] and constitute major candidates for astronomical detection in general. The degree of hydrogenation of fullerenes will, however, be limited by the fragility of the C-H bonds (2 to 3.5 eV). Hence, the balance between formation and destruction will subtly depend on the local conditions and on the accurate formation and destruction rates of the various fulleranes. Since all these are not known and will not be known accurately in the near future, the way to identify fulleranes in the ISM is through laboratory

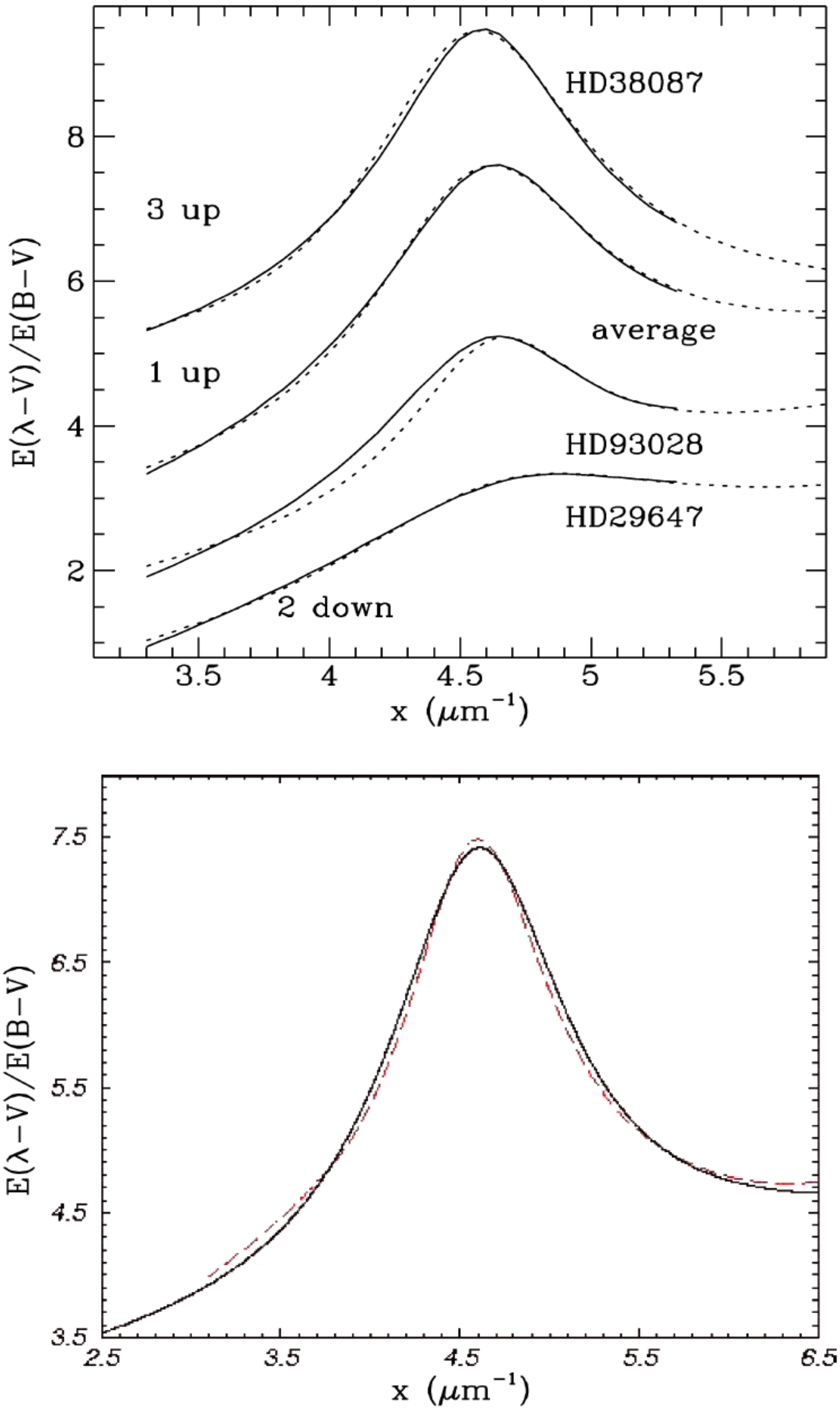

Fig. 2.12: On top, computational data (solid lines) fitting the UV bump (dotted lines). They are obtained from nano-sized, UV-processed hydrogenated amorphous carbon grains.[69] In this model, the variation of the width is obtain by varying the UV processing of the grains, and hence, their size distribution and hydrogenation. More processing leads to smaller grains with less hydrogen and a shaper feature. On the bottom, experimental data obtained from UV spectroscopy of the fullerane $C_{60}H_{36}$ in n-hexane.[70]

spectroscopy.

As for small carbonaceous particles, more recent experiments than the one shown Figure 2.12 were performed,[76] which confirm the conclusion, that irradiated HAC materials are candidate carriers of the UV bump. However, the estimated amount of carbon needed to produce the feature is higher than the C available for interstellar dust grains. To this regard, fulleranes need less material for the same absorption, and thus, do not suffer C availability.

2.5 Light scattering and the interstellar extinction

Interstellar extinction is mainly caused by dust particles and not by molecules and does not belong, strictly speaking, to this chapter. However, the boundary between large unidentified molecules and dust particles is not strict and light scattering could be seen as spectroscopy extended to extremely large molecules.

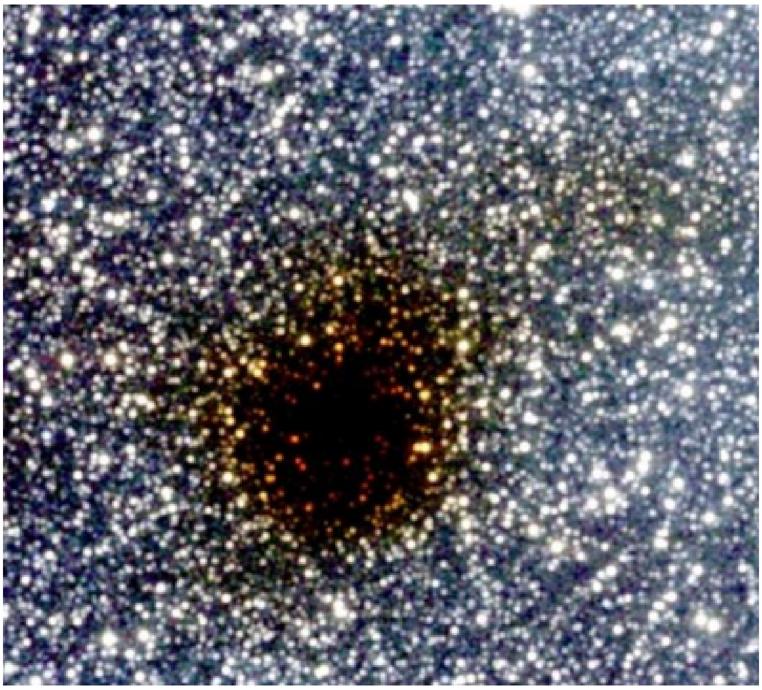

Fig. 2.13: A nearby interstellar cloud for which no star lies between us and the cloud. The effect of reddning is very apparent and related to the column density.

Within galaxies, the dust has a very important function despite its low share of the mass. First, light scattering by dust grains allows the gravitational collapse of dense clouds to protostars. By shielding the cloud's core from UV-Vis and by emitting far-IR radiation that can escape the cloud, dust grains create an antigreenhouse effect, which is vital for the formation of stars. Secondly, by protecting some interstellar regions, dust allows the production of molecules, mostly H_2, that could not form as efficiently otherwise. Finally, dust grain's surface is the catalyst and the cradle of a chemistry which would not happen in the gas phase. Many large unidentified molecules or their precursors probably form on their surface. On the spectroscopic point of view, dust particles cause interstellar extinction in the UV-Vis wavelengths (see Figure 2.11) and reradiate in the far-IR, in the form a blackbody spectrum, centered around 60 μm. Both the extinction and the blackbody spectrum, are telling us about the temperature and size distribution of the dust particles. It is, however, much more difficult to learn about their composition and structure.

Interstellar extinction has two components: absorption and scattering. Absorption is efficient for grains with sizes $a \leq \lambda$, while scattering is most efficient for $a \sim \lambda$. Thus, because the number density of grains is steeply increasing with decreasing size ($n \propto a^{-3.5}$),[79] so does the interstellar extinction with decreasing wavelengths (Figure 2.11). As early as in 1930, it was demonstrated that the extinction dependence on the wavelength can be approximated to λ^{-1}.[80] This dependence, though, varies from one dusty environment to the other.[81] The increase in extinction toward shorter wavelengths gives rise to the effect known as reddening. As seen in Figure 2.13, the dust component within the cloud lets preferentially longer wavelengths pass through. A measure of reddening is the "color excess":

$$E_{B-V} = A_B - A_V = (B - V) - (B - V)_0 \tag{2.4}$$

A_B and A_V denote the total extinctions at 450 and 550 nm, respectively. $(B - V)_0$ denotes the intrinsic value of the star, which is known if the star is well identified, and (B - V) the observed value.

3.1 Overview of the setup

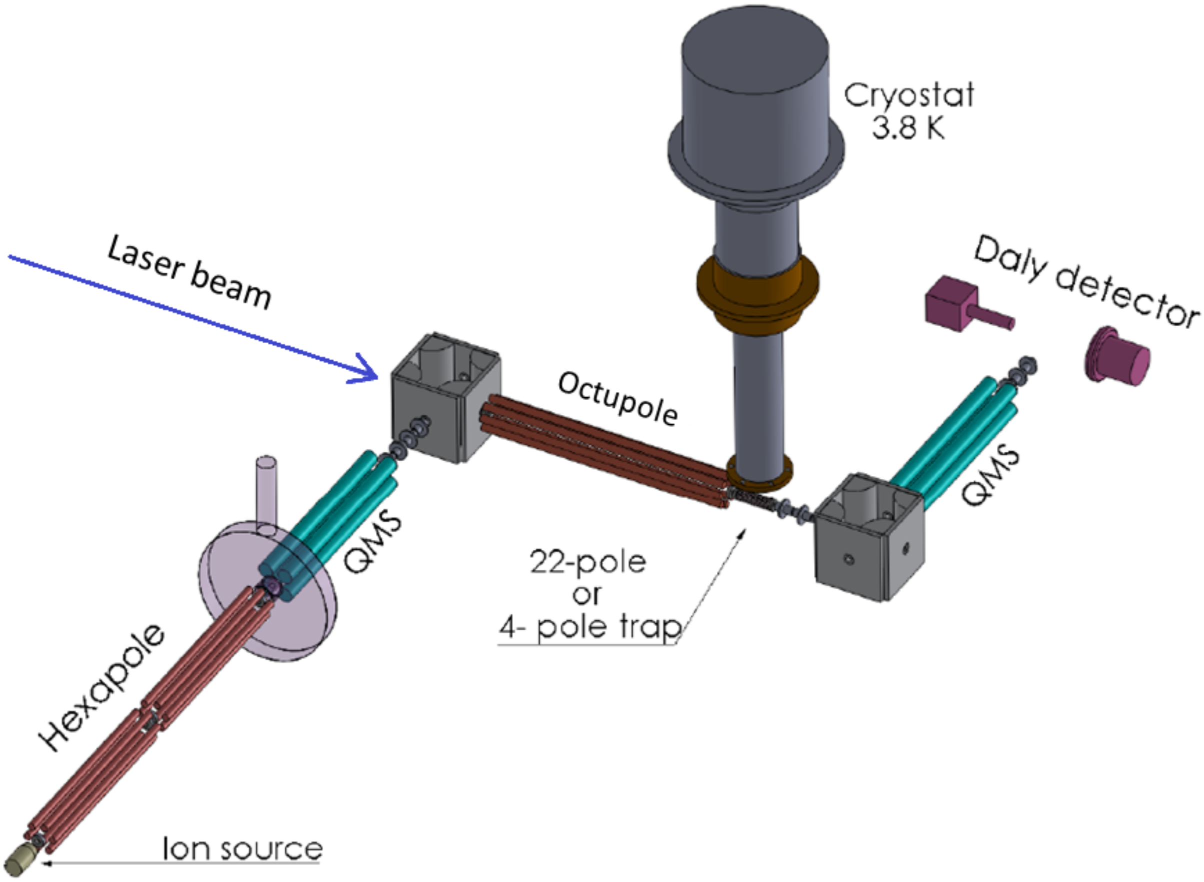

Fig. 3.1: Three-dimensional schematic of the experimental setup

Figure 3.1 displays the major components of the setup: an ion source, a hexapole ion guide (6-pole), a first quadrupole mass selector (QMS), an octopole ion guide leading to the cryogenic radiofrequency (RF) ion trap, a second QMS and a Daly detector. The general design adds some modifications to a setup previously described.[82] The ion source has been regularly changed, to allow the ionization of a variety of molecules, ranging in size from N_2O^+ to protonted C_{60}. All these elements were housed in ultra high vacuum chambers (UHV) and split into five differential pumping stages to ensure UHV in the trap and detector chambers. Six turbomolecular pumps (TMP) were used, four of $250\,\mathrm{L.s^{-1}}$ and two of $520\,\mathrm{L.s^{-1}}$ for the higher gas loads of the source and trap chambers. As TMP can only work against medium vacuum at least, all of them were connected to a screw pump providing 10^{-2} mbar when the source was operated. The vacuum could reach 10^{-9} mbar without loading and after several weeks of pumping.

Most experiments were synchronized at 10 Hz with the laser. The 100 ms of each cycle are devised as follows: ions from the source are being loaded in the trap during $\sim$30 ms, then cooled for around 65 ms, here the laser is triggered, and ions are extracted and detected during the last 5 ms. While ions are being cooled in the trap, the next are already accumulating in the 6-pole.

3.2 Ion production

Ions were produced with different sources depending on the precursors used. The setup embedded at the start a home-made electron-impact ionization (EI) source, and then commercial (EI) and chemical ionization (CI) sources from Agilent. They were exchanged, depending on the molecule targeted. Also, an electrospray ionization (ESI) source was tried for the tentative production of $\mathrm{H^+}$hexabenzocoronene or $\mathrm{H^+C_{60}}$, without success. Below, their principle and use are described.

$$\mathrm{M + e^- \rightarrow M^+ + 2e^-}$$

An EI source ionizes a compound present in the gas-phase. If the precursor is solid (or liquid) at room temperature, a vapor can be obtained by heating it until a sufficient vapor pressure is reached. The sample molecules are bombarded by 10 - 30 eV electrons, and ionized. In order to obtain a reasonable yield of ionization, the electron energy is set substantially higher than the ionization potential of the molecule. As an undesirable consequence, molecules may fragment. In some cases, however, the aim is to fragment the molecule and study a specific fragment of the precursor. It is the case in this thesis with $\mathrm{C_7H_3^+}$ (Appendix), for which $\mathrm{C_7H_8}$ vapor (toluene) was used as the precursor. Even though the energy used to produce the ions is controllable, EI is a harsh method of ionization. The energetic electrons are produced via thermionic emission from a hot filament on which an external negative

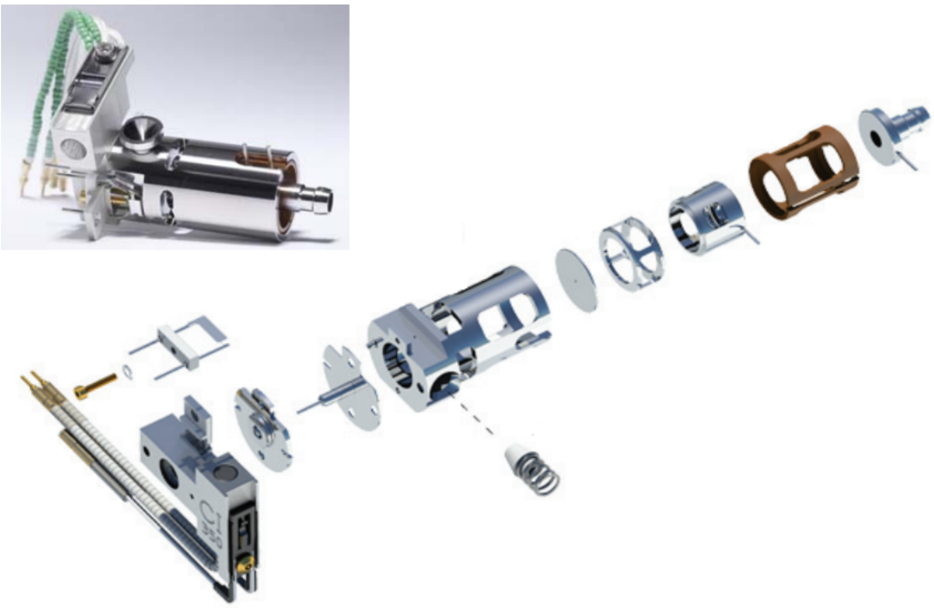

Fig. 3.2: Assembled and disassembled CI source. The main difference with the EI source are the tiny apertures for the electrons to come in and the cations to come out, to allow the pressure to build up.

voltage is applied to eject them with the exess kinetic energy. This filament is made out of a refractory metal such as tungsten or rhenium. Mostly rhenium was used as it is not as brittle as tungsten.

$$[\mathrm{R\text{-}H}] + e^- \rightarrow [\mathrm{R\text{-}H}]^+ + 2e^-$$
$$\mathrm{M} + [\mathrm{R\text{-}H}]^+ \rightarrow \mathrm{R} + [\mathrm{M\text{-}H}]^+$$

A CI source ionizes the reagent gas (R) and the sample (M) is only subjected to a proton transfer. In the case of a low proton affinity, a CI source is not a sensible choice. As in the EI source, sample and reagent are bombarded by 10-30 eV electrons ejected from the glowing filament. It has the same design as an EI source but all apertures of the inner reaction chamber are smaller to allow higher pressures to build up, up to ~ 1 mbar. With adjusting the pressure of the reagent, the partial pressure of the sample and the temperature of the filament, the proportion of protonated sample molecules can be optimized. As for the EI source, an oven can be plugged to it to sublimate solid samples. All five protonated species studied in this thesis were produced in a CI source. For all these rather large species, samples were solid and were heated in the oven to 90 °C for azatriphenylene ($C_{17}H_{11}N$), fluoranthene (Fluo) and pyrene (Pyr), 120 °C for corannulene (Cora), and 160 °C for coronene (Cor) to obtain a sufficient vapor pressure. This method is softer for the analyte, but it is indirect, yielding a lower ion count than the EI source.

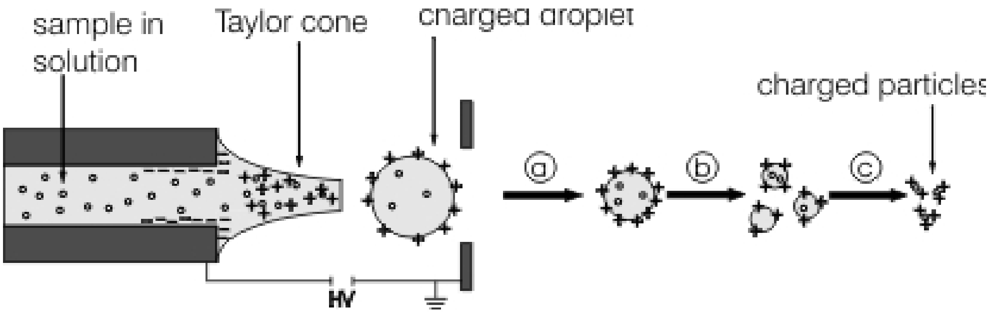

Fig. 3.3: Schematic of the electrospray ionization process.

ESI sources offer a much softer ionization as they do not make use of energetic particles. Electrospray ionization generates an aerosol from a liquid sample thanks to high voltages (HV). The tip of a thin capillary containing the dissolved sample (left in Figure 3.3) is exposed to a HV, typically 3 - 4 kV. A charge separation will occur at the tip, with negative charges accumulating on the tip of the capillary, and positive charges accumulating in the solution. These positive charges go away from the HV, hence stretching the liquid and producing a so-called Taylor cone. This cone, above a certain threshold voltage, surpasses the "Taylor angle", that is, gets thin enough to break down and a jet is formed. This jet is loaded with positive charges of around a mm escaping the HV. They will quickly decrease in size until they are reduced to bare ionized molecules. The starting solution consists of the analyte dissolved in a low boiling point solvent, to which is added an acid in minute amount. An amount of solid precursor of 1 mg can make around 10 ml of solutionand last several days of experimentation making this method much more economic than the EI and CI sources. For the PAH precursors used in this thesis, up to several mg could be used in only a single day. Then, expensive samples, such as large PAHs obtained in minute amounts, must be preferentially studied with an ESI source.

The 6-pole ion guide provides thermalization of the ions before the mass selection. The source is directly plugged onto the 440 mm long 6-pole. In the latter, ions will undergo collisions at room temperature with the gas leaking from the source, and be thermalized. The RF field had an amplitude of 60 to 120 V, a frequency of 3.5 MHz, and a DC offset of 5 to 15 V. The 6-pole is made of two parts, first a high-pressure cell, up to 10^{-2} mbar, and then a lower pressure cell where the buffer gas simply leaks from the first cell. Ions leaving the source have a wide range of translational energies. Ions internal temperatures do not matter at that point and will be cared of in the 22-pole trap, however, a broad distribution of translational energies decreases the efficiency of the ion guiding and the mass selection. Inelastic collisions with the buffer gas will reduce the translational and internal energies of the ions and provide a more efficient handling of the ions.[83]

$$l = \frac{R\,T}{\sqrt{2}\,\pi\,d^{\,2}\,N_{\,a}\,P} \tag{3.1}$$

Equation 3.1 gives the mean free path of a particle, depending on the pressure and temperature of the gas. With a pressure of 5×10^{-4} mbar at room temperature, a 0.3 nm molecule (such as pyrene) will have a mean free path of 0.5 m. We can see that the number of collisions will not even reach unity if the molecule only passes by the 6-pole. If the molecule stays in the 6-pole 40 ms, this corresponds to a travel of a He atom of ~ 50 m. If we consider a much slower molecule than He, 50 m leads to ~ 250 collisions in 40 ms. This number is rather low but the pressure in the 6-pole cannot be set much higher because of the neighboring QMS.

The 6-pole is separated from the QMS by a differential wall to prevent large amounts of gas from the source to come in. This is especially useful for the use of an ESI source. In the QMS, pressures above 10^{-2} - 10^{-3} mbar would create a discharge due to the high RF voltages on the rods. This differential wall consists of a gate valve which, when closed, enables to vent the source while leaving the rest of the apparatus under UHV. This gate valve allows to clean, fix, or refill the source, while the cryostat is still running, saving several hours.

3.3 Mass selection

The apparatus has two QMS, the first one selecting which ions from the source will be studied in the trap, and the second one selecting the photodissociation products to be counted. A QMS consists of four precisely set parallel rods (see Figure 3.4) on which a potential $\pm\,(\mathrm{U_0} + \mathrm{V_0}\cos(\omega.\mathrm{t}))$ is applied to opposite pairs of rods. $\mathrm{U_0}$ is a DC voltage and $\mathrm{V_0}$ the amplitude of the RF oscillations. These oscillations are necessary because a charged particle cannot be confined in space by constant potentials. This fundamental principle, stated mathematically, express that no global minimum of a potential energy surface (PES) can be created by any spatial arrangement of electric fields around a charged particle. The way around this limitation was found by W. Paul and H. Steinwedel in 1953 and is the use of oscillating electric fields.

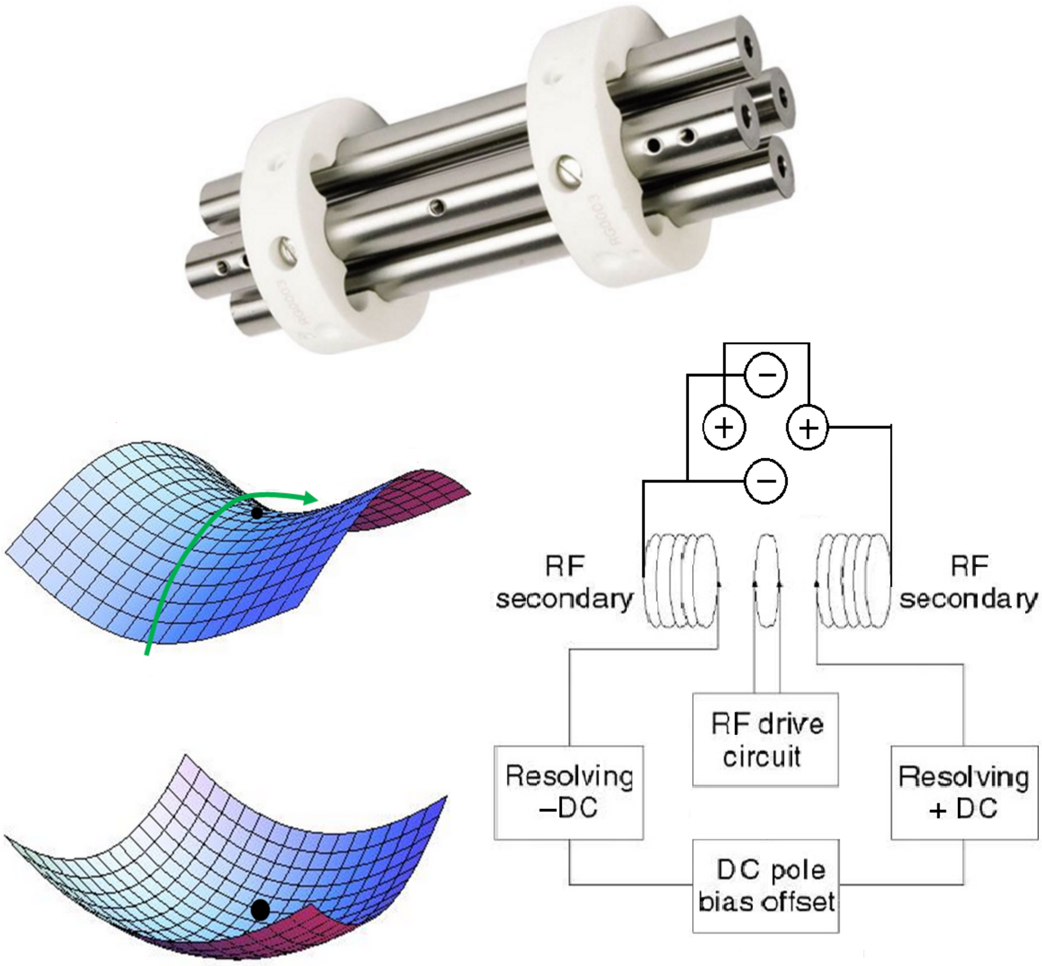

Fig. 3.4: Picture, PES, and electrical diagram of a QMS. The top PES is the instantaneous potential. The bottom PES is the effective potential created over time, which enables to confine the charge.

Effective potential. Oscillating electric fields still do not create a global minimum in the PES at an instant ”t” (top PES in Figure 3.4). However, the average over time does create an effective potential well (Bottom PES in Figure 3.4). If the inertia of the particle suits the amplitude and the frequency of the oscillations, the particle is confined. If the mass of the particle is too low, its inertia allows it to escape within a single oscillation of the field. Above a certain critical mass, particles are too slow to react, fall into the well, and are confined. The RF voltages act as an adjustable high-pass filter, the critical mass depending on the frequency. Now, to select a single mass, a low-pass filter has to be combined with the high-pass filter. To achieve this, opposite DC potentials are added to the RF to opposite pairs of rods (D-C source in the diagram of Figure 3.4). Negative DC voltages destabilize high masses, and positive ones, low masses. By adjusting the DC offsets, one can make the high-pass and low-pass filters overlap over the required range.

Resolution. In the description above, the particle has no initial radial and axial kinetic energy. The energy distribution is closely related to the most important quality of a QMS, the resolution. The ability of a QMS to differentiate two molecules with similar masses depends on the quality of the mechanical assembly of the rods, the rod surfaces, the electric fields, and as an external parameter, on the quality of the ion beam. The QMS does not operate the same way on particles of the same mass if they have different radial and axial initial speeds. In any apparatus containing a mass spectrometer, it will be important to obtain an ion beam with an energy distribution as narrow as possible.

Calibration. Figure 3.5 shows two mass spectra obtained from toluene vapor (top trace) and krypton gas (bottom trace) introduced in the EI source. These exemplify the calibration process. The QMS is able to separate molecules with different masses (1 amu separation between each in Figure 3.5), but the absolute position of the peaks must be reference at least once, with a compound producing a known mass spectrum. In top spectrum of Figure 3.5 we cannot tell, a priori, which is the mass peak of toluene among the several dissociation and recombination products. To do so, we identify the main peak of krypton spectrum at 81.8 amu, compare it to the literature, which says 84 amu, and we can realize that our mass spectrum is shifted by 2.2 amu toward lower masses. In consequence, the toluene peak is actually the second largest of the spectrum at 89.8 amu. This means, by the way, that most of the toluene molecules do not survive in the EI source with H-loss dominating the spectrum.

A QMS can be a simple ion guide as well when the DC voltages are not applied. To this regard, RF ion guides are a good solution to transport ions over a significant distance without much losses compared to a stack of electrodes of the same length.

3.4 Ion traps

Two ion traps were used during this thesis, a 22-pole trap for three years and a wire 4-pole trap during the last year. Figure 3.6 shows the two traps side by side. The ion trap is the heart of the setup, where the mass-selected ions will be cooled to a few kelvins and probed by the laser. Each cycle, the trap is filled with $\sim 100\,000$ ions.

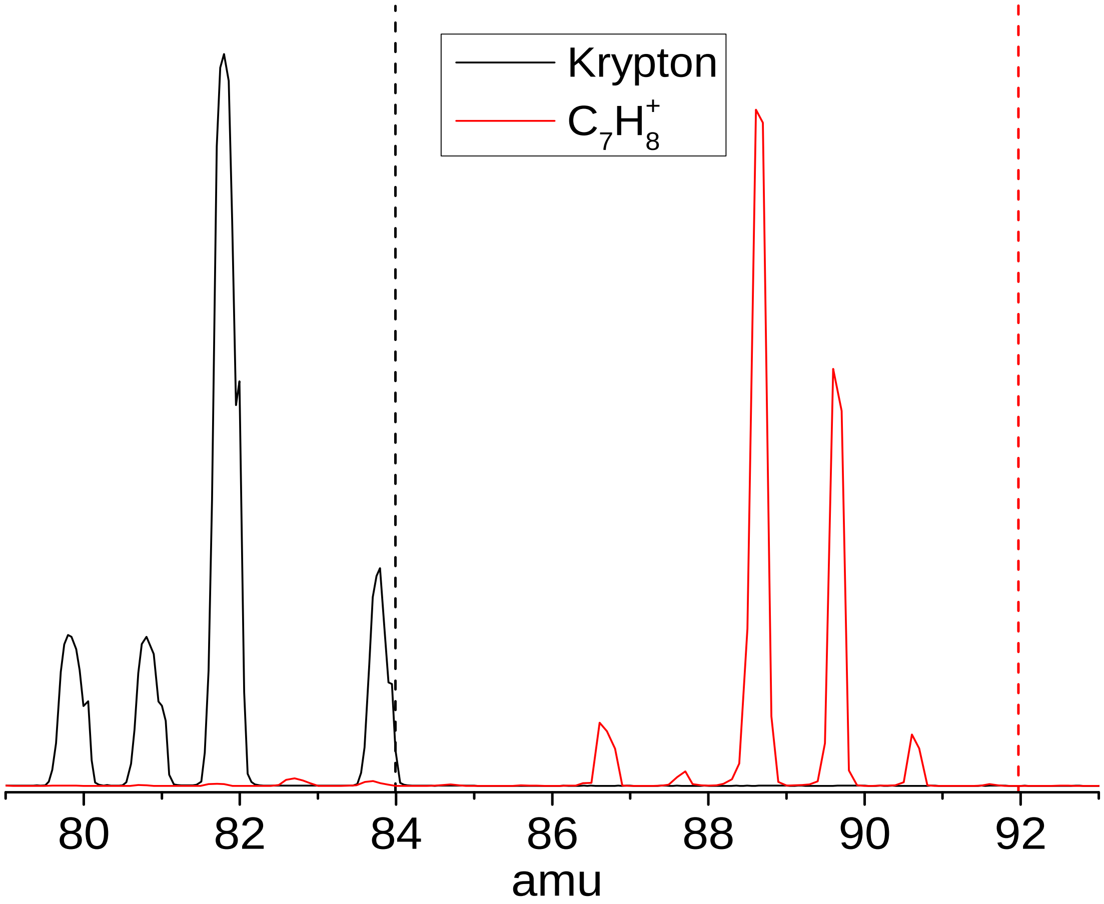

Fig. 3.5: A mass spectrum of krypton, in black, and toluene, in red, produced in the EI source. The main krypton isotope appears at 81.8 amu instead of 84 amu (dashed black line), indicating a systematic error in our mass spectra of -2.2 amu. When one shifts the mass spectrum of toluene of +2.2 amu, one realizes that toluene, now at the red dashed line, is not the main product of the source. EI is indeed not a soft method of ionization.

Ions are trapped radially by the oscillating field applied on the rods, and axially by the electrostatic potential of the entrance and exit electrodes. He is leaked in the trap and at the end of the trapping time, the laser is triggered. Shortly after, the voltage of the exit electrode is lowered by 2 V, and parent ions and laser induced dissociation (LID) products leave the trap to be mass selected (Figure 3.12).

The trap chamber is pumped by a TMP (685 l.s^{-1}). When the buffer gas is pulsed into the trap, the pressure reaches 10^{-5} mbar, and without, can go down to 10^{-9} mbar. The trap is mounted on the second stage of a closed cycle cryocooler achieving of 4 K and is enclosed in an aluminum shield which cooled to 30 K by the first stage of the cryostat. During the course of this project, the radiation

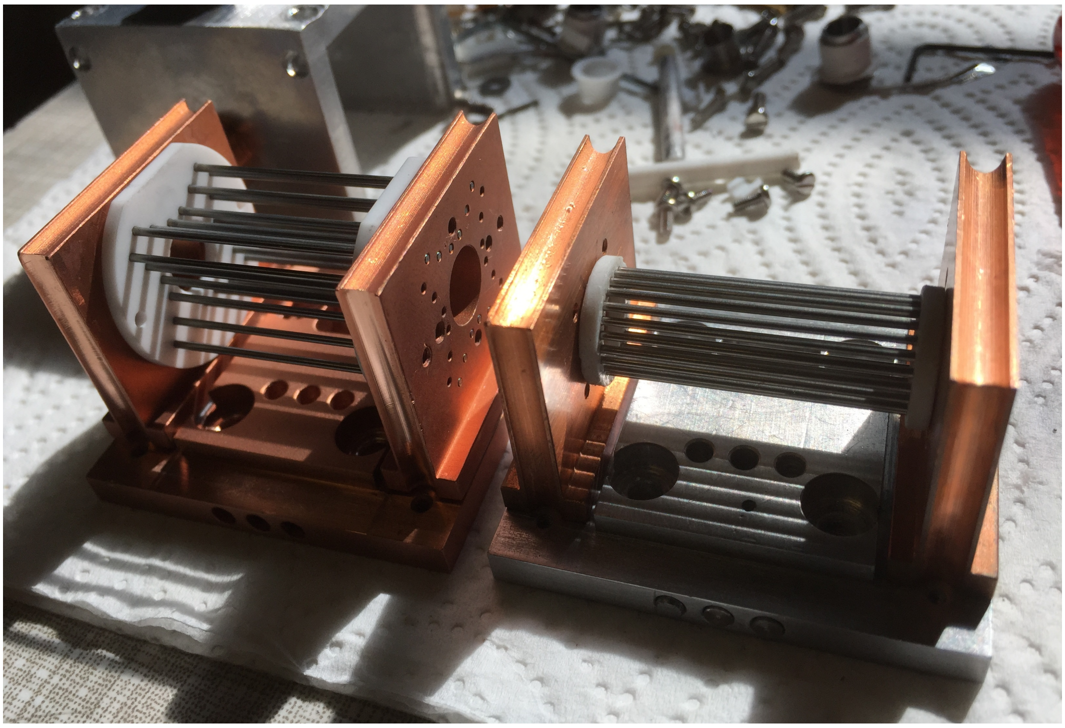

Fig. 3.6: The quadrupole wire trap (left), compared to the 22-pole trap (right).

shield surrounding the trap was replaced for a simpler design. The previous design was made of seven plates that had to be carefully assembled together with indium patches between them. Disassembling and assembling this shield turned out to be a laborious task when the trap needed regular maintenance. Figure 3.7 shows the current design made of an aluminum block and a closing plate, and the use of indium became unnecessary. Another aspect of the design is that the outer electrodes of the trap are now pressed in the shield itself. Before, the trap outer electrodes were set on the trap and exposed to the 300 K blackbody radiation. Now, the 300 K blackbody radiation is only affecting the radiation shield. Electrical wires to the trap are precooled along with the radiation shield, and 0.1 mm Kapton insulated wires are used to avoid heat to be transported to the trap. Two resistive heaters and three silicon diode temperature sensors are mounted on different parts of the trap to have an overview of the temperature between 4 and 315 K.

He buffer gas is introduced in the trap via a piezo valve. 10 V at 3.3 kHz is applied to resonate the piezo-element (Figure 3.8). The valve takes a couple of ms to be in resonance and opened. There exist, however, several ways of using these valves within the trapping cycle: One can leak the gas in continuous. This is the simplest method, not only because one just needs a leak valve, but also because the number

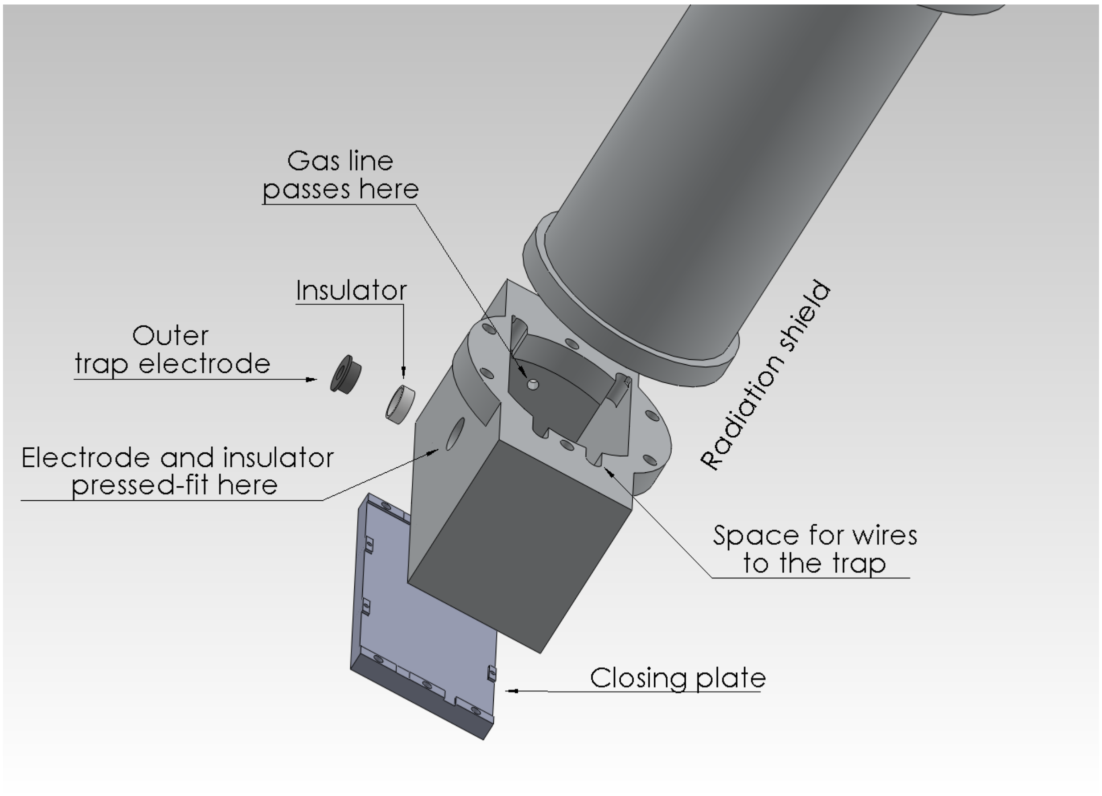

Fig. 3.7: Radiation shield with a simple design, allowing quicker maintenance on the trap. The shield does not require the ues of indium because it is mostly made of one block. Also, it can be removed without worrying about the wires to the trap since these pass in some grooves between the shield and the tube.

density in the trap is always known and easily characterized. As a consequence, the behavior of the ions is also easier to understand. One can also select within the trapping cycle, periods of time with gas and periods without gas. This leads to a finer monitoring of the number density depending on whether the ions are entering the trap, already cooled or exiting. This method was used because it allows cutting the gas before the extraction of the ions, avoiding collisions induced dissociations (CID). CID on the way to the detector false the results when PD is the method to detect the absorption. Also, higher He densities can be achieved compared to the continuous regime. One can also use a burst of gas by applying a short pulse of 100 - 300 V bending the piezo element. The advantage is to reach even higher number densities in the trap for a few ms for a more efficient cooling. Again, to avoid CID, a pump out period is necessary. This method can be complemented by resonating the piezo element after the burst.

An important aspect of buffer gas cooling is the number of collisions undergone

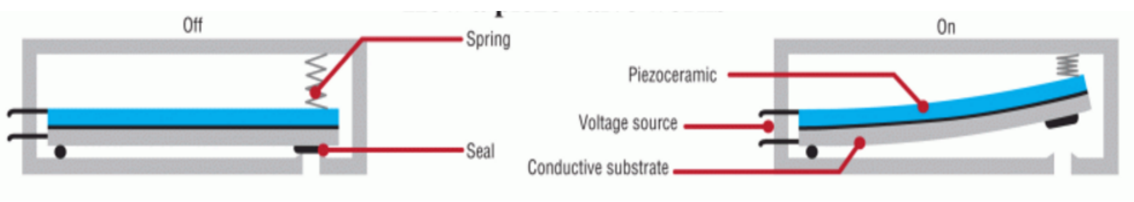

Fig. 3.8: Schematic of a piezo valve. It can be continuously opened with a high voltage, or resonated with low voltage at the resonance frequency of the piezo element.

by one molecule with He during the trapping. This number depends on (1) the axial and radial energy distributions of the incoming ion beam, ranging from 0.1 to 2 eV. Ideally, the ion beam has an energy distribution of ≤ 200 meV, but in practice, analysis of the ion beam around the trap area showed that this was rarely the case. (2) The mass-dependant secular and micro-motions caused by RF voltages. These are accurately known in theory for a 4-pole trap and a given ion mass. (3) The density and temperature of the He buffer gas. These are approximately known since we do not measure the pressure directly in the trap but only in the vacuum chamber. Also, we measure an average pressure when the He is actually pulsed and the He density in the trap varies over several orders of magnitude over a trapping cycle. Estimations using the pressure in the whole trap chamber and the flow conductance of the trap and TMP give a He density of 2 to $5 \times 10^{15}\,\mathrm{cm}^{-3}$ in the trap. (4) During the 30 ms of filling time, the ions can arrive at any time, which can be averaged to 15 ms. (5) The size and geometry of the molecule are known. As we can see, several of these parameters influencing the number of collisions are not well characterized. Assuming a He density of $5 \times 10^{15}\,\mathrm{cm}^{-3}$, a mean velocity of the He atoms of $190\,\mathrm{m.s}^{-1}$ at 6 K, a cross-section for Cor^{+} of $6 \times 10^{-19}\,\mathrm{m}^{-2}$ and motionless ions, we obtain $450\,000\,\mathrm{collision.s}^{-1}$. This calculation does not take into consideration both, the micro- and secular motions of the ions due to the RF, and the initial axial and radial speed of the ions. For this reason, the true number of collisions is probably significantly higher.

22-pole vs 4-pole ion trap. The 22-pole trap[84] is 36 mm × 10 mm with RF voltages of 40 to 80 V, f = 7.4 MHz, applied on the 2×11 stainless steel rods. The 4-pole wire trap[85] is 36 mm × 10 mm with RF voltages of 40 to 200 V, f = 2 MHz, applied to 2×2 pairs of poles. Each of the four poles of this trap is made of six wires that mimic a parabolic rod, making a total of 24 wires. These wires, which are

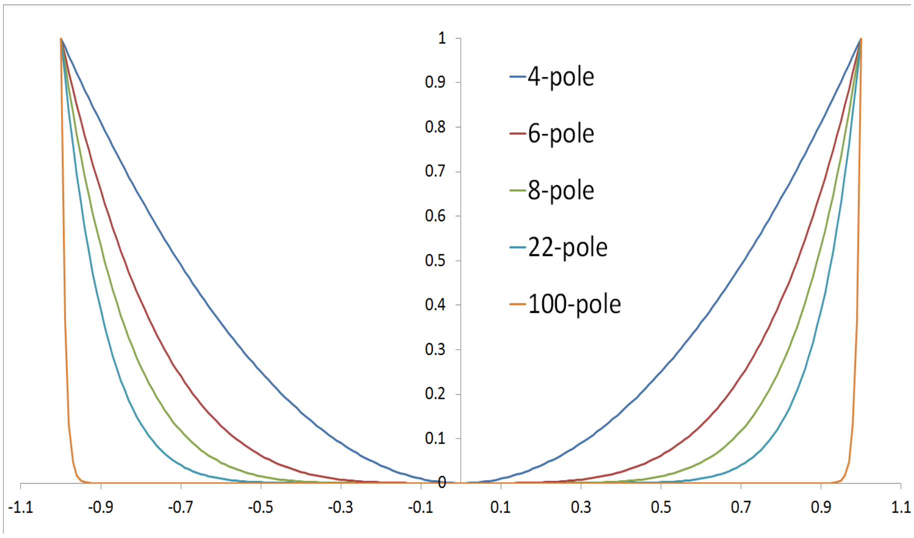

Fig. 3.9: Radial effective potentials created by the oscillating fields for different number of poles. The quadrupole has a much stronger, focusing effect. On the other hand, a high number of poles allows to store more ions, and have less interaction between the latter and the RF.

technically 1 mm rods, are used since it is easier to set six rods to form a parabolic shape than build such a solid rod, and the potential created is very similar. The main difference between the two traps is the effective potential built by each arrangement. The higher the number of poles, the wider the potential well created, and an infinite number of poles would theoretically create a uniform (square) trapping potential within the inscribed radius.

$$V_{\text{eff}} = \frac{q^2 n^2 V_0^2}{4 m \omega^2 R_0^2} (R/R_0)^{2n-2} \tag{3.2}$$

The effective potential of the 22-pole interacts less with the ions and allows more of them to be trapped than a 4-pole (as much as 40 times more) and is a sensible choice for very low ion internal temperatures. However, the 22-pole revealed to have a serious disadvantage. The ion cloud is much wider than the $\sim 1\,\text{mm}^2$ laser beam probing it. As a consequence, only a small percentage of the trapped ions are made useful each cycle. Even worse may happen, some ions may stay close to the rods due to patch potentials from hardware's imperfections. This can create some spatial mass selection that would bias the experiment. On the other hand, in a 4-pole, ions are tightly confined in a section $\leq 1\,\text{mm}^2$ and no such effects can happen, and most importantly, all ions are probed by the laser. The first experiment realized with the 4-pole wire trap was done with OC_4O^+, whose electronic spectrum had just been

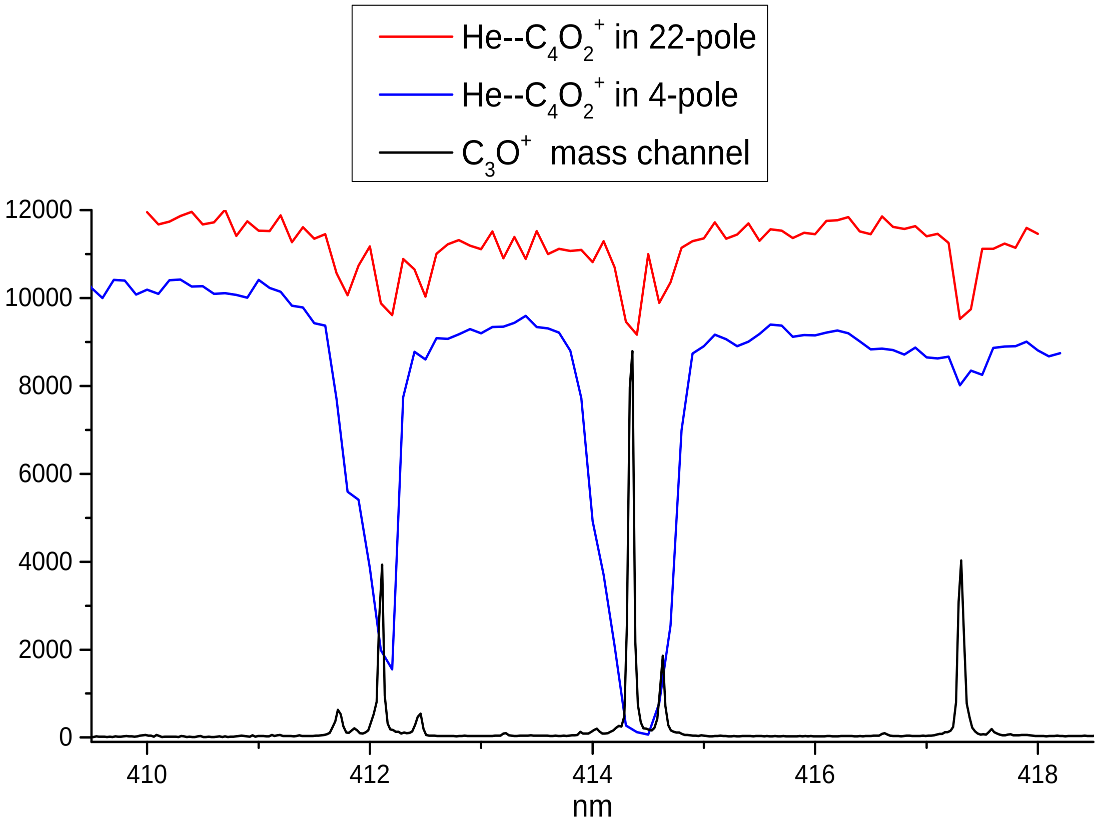

Fig. 3.10: Electronic transition of $C_4O_2^+$ recorded via the photodissociation of their He complexes in a 22-pole trap (red trace), and a 4-pole trap (blue trace). For reference, the spectrum recorded via photodissociation of the bare molecule, via the loss of CO, is shown in black. With enough laser power, the blue spectrum is saturated to zero and shows that all the ions in the 4-pole trap can be probed by the laser.

recorded by monitoring its photodissociation via CO-loss. This experiment proved that the 4-pole trap was more adapted to our needs (see Figure 3.10), since the ion cloud and the laser beam almost perfectly overlap.

As a note, RF heating effects, that is, increased micro and secular motions of the ions due to the RF, are higher in a 4-pole than in higher order multipoles. Hence, they could be seen as a limitation of the 4-pole trap for the purpose of obtaining He complexes. However, it has been shown that these effects only play a significant role at very low temperatures of $\leq 1\,\mathrm{K}$,[86] and hence, are not a concern.

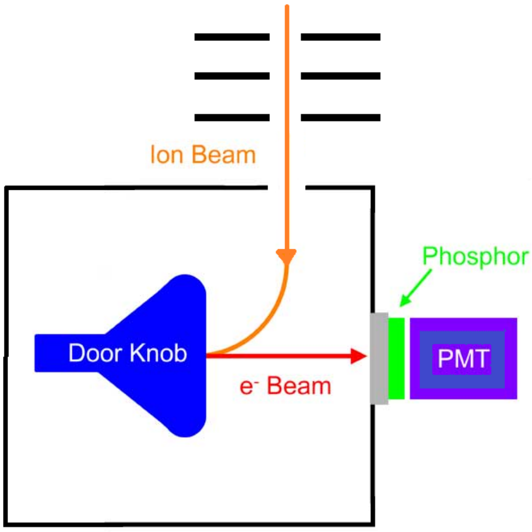

Fig. 3.11: Schematic of a Daly detector.

3.5 Detection and data correction

Mass-selected products of the photodissociation (PD) are collimated and accelerated by three electrodes into the Daly detector (Figure 3.11). Cations are directed toward the center of a polished stainless-steel surface set at -30 kV. The hit releases a shower of electrons which are accelerated away onto a scintillator. From these, the scintillator produces photons emitted toward a photomultiplier (PMT). The Daly detector can count ions at a rate of $10^8\,\mathrm{s}^{-1}$. This is observed experimentally as the signal saturates at around 90 million ions per second. Typically, such a strong signal is only attainable with a pure He or Ar ion beam guided from the source to the detector without trapping. Pulses from the PMT $> 5\,\mathrm{mV}$ are selected and amplified by a discriminator and counted by a 400 MHz frequency counter.

The Daly detector relies on a somewhat complicated cascade of events and simpler schemes for ion detection exist. However, the -30 kV of the Daly detector does not have an intrinsic mass selection and has a high count rate, whereas other types of detectors using much lower voltages have an undesirable lower sensitivity at higher masses, and count rates of around 10 MHz. Furthermore, ions only strike the dynode, allowing the whole detector to have a longer lifetime.

As shown in Figure 3.12, a Labview program sends some commands to the pump laser, piezo valve, and trapping electrodes, while acquiring the number of ions from the counter (Figure 3.12). This constitutes the raw signal, that is, the number of ions of a specific mass leaving the trap, per second.

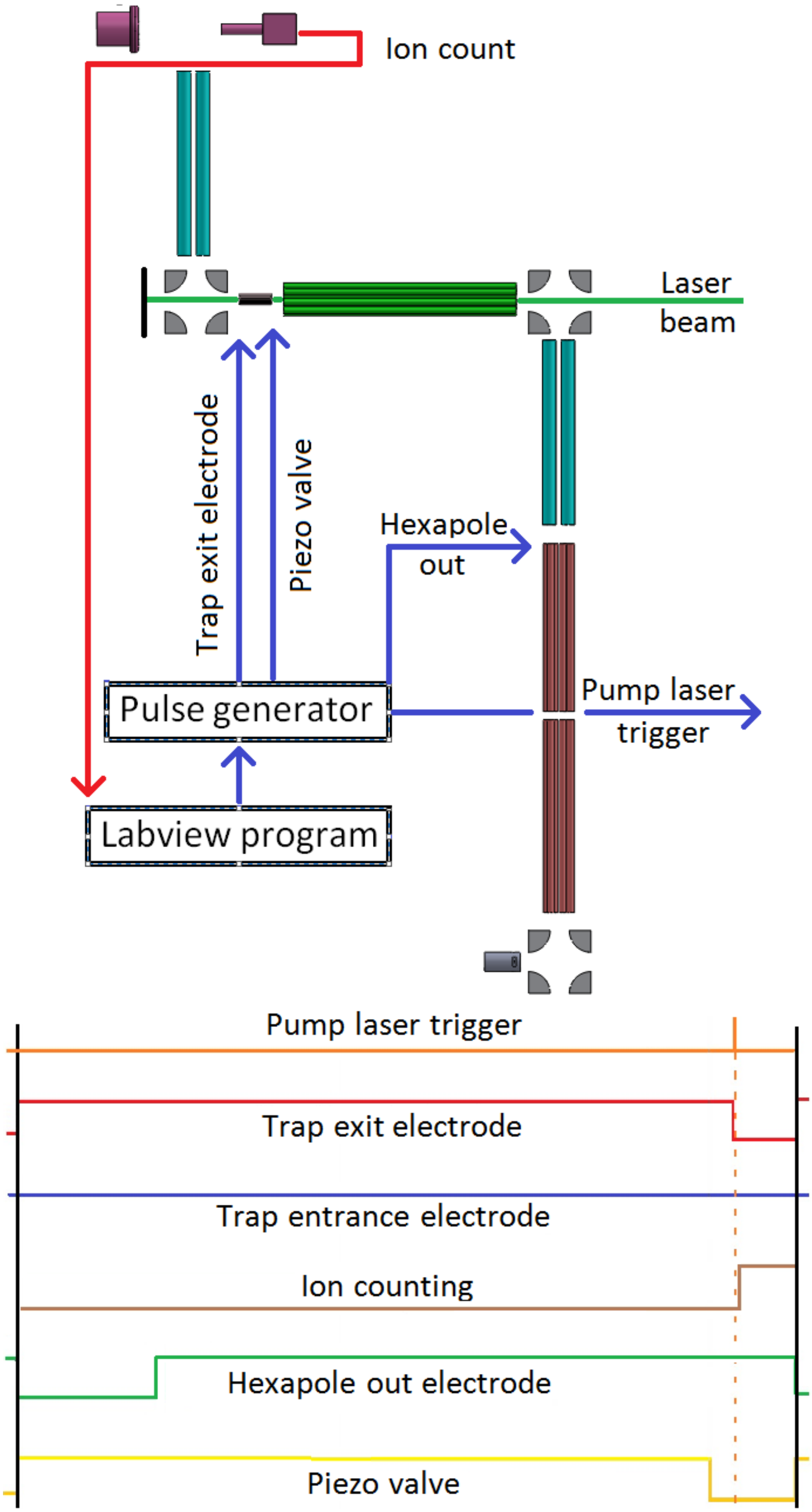

Fig. 3.12: Voltages involved in the trapping cycle and spectrum aqcuisition.

Not all the ions of the product mass are relevant. Some of them, the most energetic ones, may have passed over the voltage barriers of the trap, during the trapping time, and reach the detector without being trapped. In order to avoid taking them into account, only the ions exiting the trap during the 5 ms of extraction are counted. This latter count, recorded as a function of the laser wavelength, must be calibrated in wavelength (x-axis) and power-corrected (y-axis). The dye laser sets the wavelength by monitoring the position of the step motor tilting the gratings. This system does not give a reliable wavelength and a calibration is done with a wavemeter. Also, the power of the laser beam is not a constant function of the wavelength and will dramatically influence the PD efficiency. To account for this, the emission spectrum of the dye used is recorded and the spectrum of the molecule is corrected as follows. The dependence of the PD on the laser power is measured, as shown in Figure 3.13. If all molecules need only one photon to be dissociated within the millisecond scale of their exiting the trap, the power dependence will be linear. In Figure 3.13 it can be seen, by fitting the measurements to a polynomial function, that the power dependence is quadratic. This function is then applied to the emission curve of the dye used, as seen in the top of Figure 3.14. The raw signal can now be divided by the corrected dye emission curve. As seen in the bottom of Figure 3.14, the original data, in black, were distorted by the dye emission curve, which moreover, have a quadratic dependence on the PD.

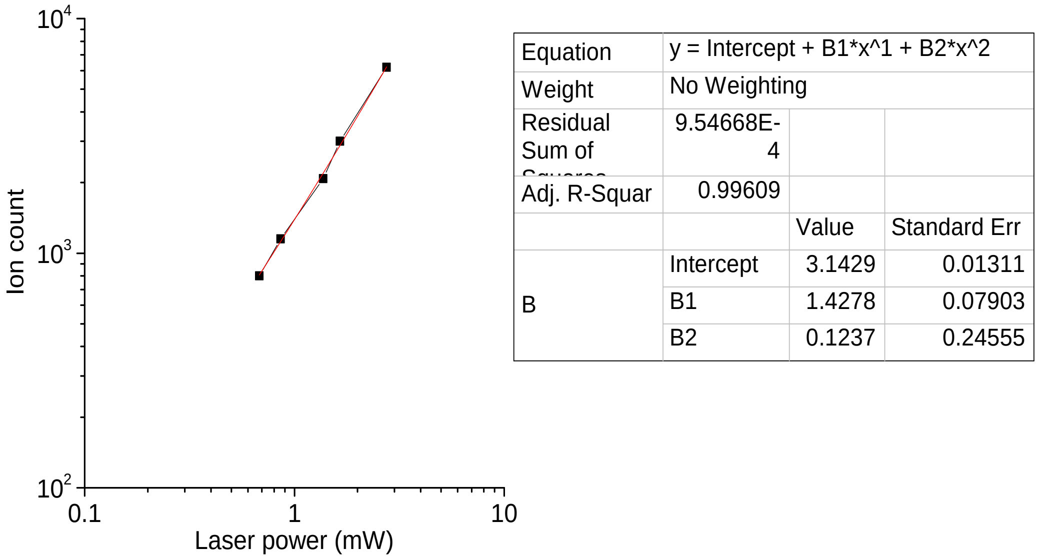

Equation	y = Intercept + B1*x^1 + B2*x^2		
Weight	No Weighting		
Residual Sum of	9.54668E-4		
Adj. R-Squar	0.99609		
		Value	Standard Err
B	Intercept	3.1429	0.01311
	B1	1.4278	0.07903
	B2	0.1237	0.24555

Fig. 3.13: Example of the power dependence of the PD on a logarithmic scale. The fit shows a quadratic dependence.

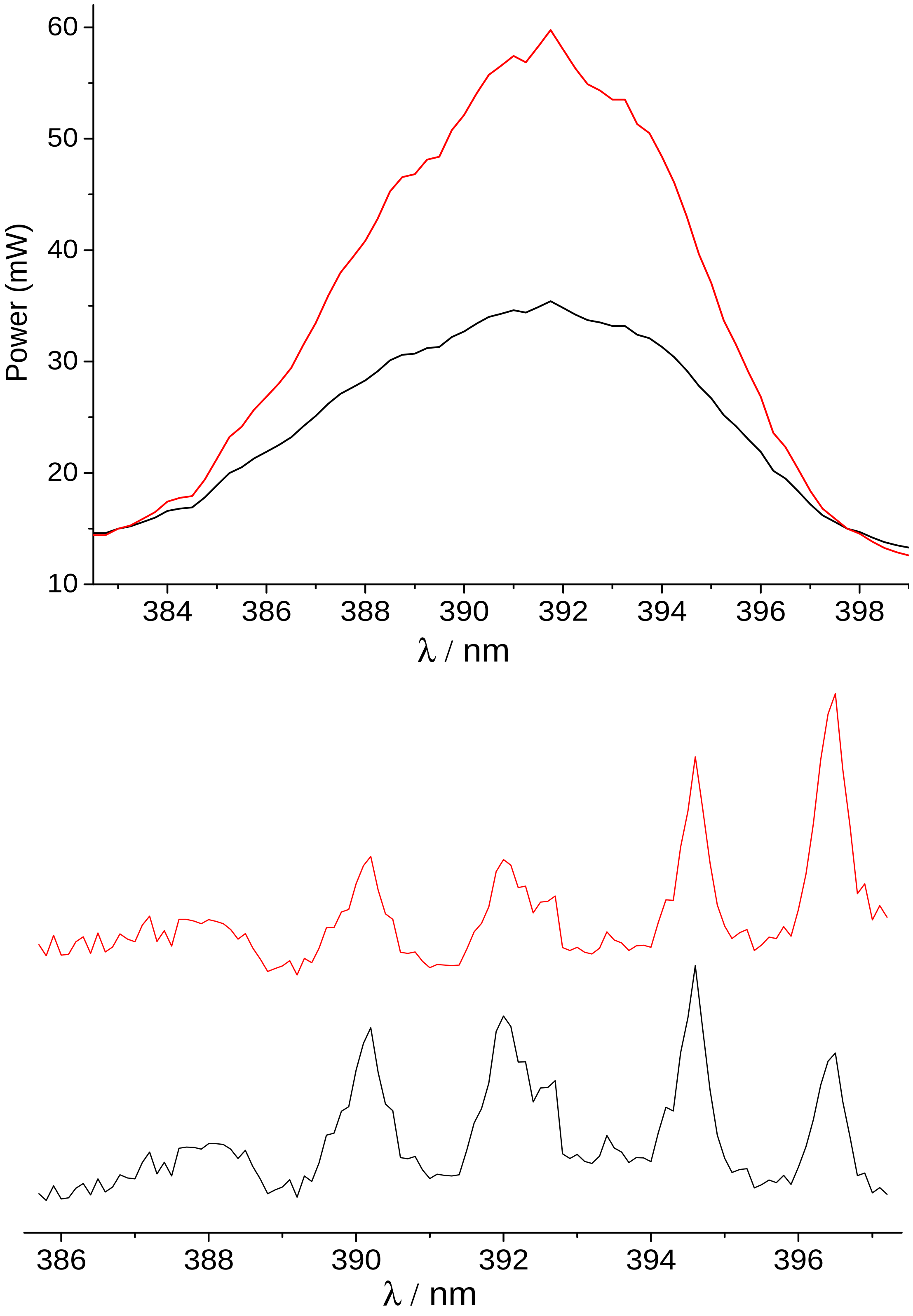

Fig. 3.14: On top, the dye emission curve before (black) and after (red) correction. The fit of the power dependence showed in Figure 3.13 is applied to the black curve, to account for the quadratic power dependence. On the bottom, the original spectrum (black) is divided by the corrected dye curve (red). The origin band, previously the less intense band, becomes the most intense.

4. TESTING THE SETUP

4.1 Some aspects of the newly built setup

The electrical reference. The apparatus was not referenced to the ground since it contained too much electrical noise for the experiment. Instead, all electrical potentials of the apparatus were referenced to a master potential (MP), with the exception of the two commercial QMS, which are not electrically floatable devices. This master potential was connected to the vacuum chambers. If the MP was 5 V, and a guiding electrode had 12 V, then, the voltage between this electrode and the surrounding vacuum chamber was 17 V. Ideally, by varying the MP, one could have more control over the translational energy of the ion beam. Raising the MP would slow down the ions and possibly stop them if the MP is higher than their initial kinetic energy. To be effective, the MP must absolutely be applied to every single device. However, the two QMS cannot be referenced to the MP, and made it lose its value.

Concerning the energy of the ions within the guiding elements, large pressure gradients, and hardware's imperfections likely render any estimation of the ion beam's behavior flawed. When significant gas loads are present such as around the source and the trap, the ion optics do not behave ideally anymore due to unknown pressure gradients and gas flows. Also, inhomogeneities in the electric fields of the electrodes, due to mechanical imperfections, or noise on the DC voltages, create unpredictable effects on the ions. Slight deviations from theoretical behavior in any part of the apparatus undergo a snowball effect downstream. A realistic simulation of the behavior of the ions need simulation tools taking accurately these phenomena into account, and not merely electrostatic effects.

In contrast to a theoretical approach, the method which did allow to control, to some extent, the ion beam was to track the ion current along the setup. Thanks to a very senstitive current meter (down to pico-ampere), we optimized the voltages upstream from where we measured the ion beam intensity. This has to be done for every potential one by one, starting from the source were it is straigthforward to "find" the ion beam, until the detector. This method is laborious but robust and allows to spot any malfunction along the way. We did this procedure every time we did a major modification or maintenance on the setup.

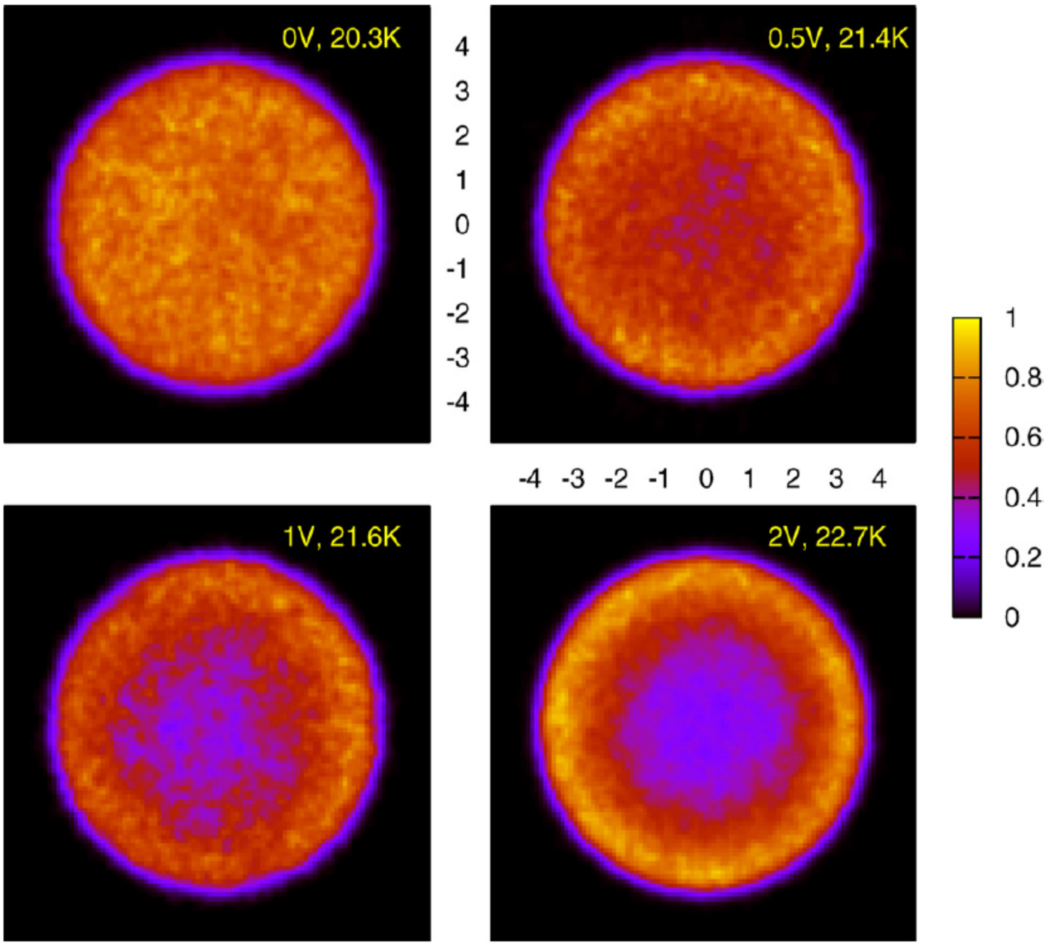

Fig. 4.1: Simulated and color-coded transversal probability distributions of ions in a 22-pole trap.[87] The trapping electrodes voltages was varied and resulted in small changes in the ion temperatures but in large changes in the cylindrical distribution of the ion cloud. With increasing electrode voltage, the ions are pushed closer to the RF rods.

Ion distribution in the 22-pole trap. A major issue encountered during the first experiments on H^+Pyr and H^+Cor was the absence of observed PD of the ions. We then realized that PD does appear when the laser is triggered during the filling or extraction periods, but does not appear when it is triggered during the trapping time. Probing the ions during the filling time is obviously wrong since the ions are not cold yet. For this reason, and before finding the cause of this issue, we triggered the laser during the extraction. We suspected the ion density in the center of the trap to be lower than that toward the rods, forming a cylindrical torus ion cloud. Geometrical imperfections, as well as increased voltages, do create distorted ion clouds. In particular, it has been demonstrated that in non-ideal situations, as seen in Figure 4.1, ions in a 22-pole trap tend to gather toward the rods.[87,88] In this simulation, the temperature increase is not as worrying as the distortion of the ion cloud.

On the other hand PD was observed when triggering the laser during filling or extraction because when the ions pass through the entrance or exit electrode, they concentrate in the center. There, they are along this axis and accessible to the laser beam. As a consequence, when using the 22-pole trap, we recorded the spectra of internally cold molecules by triggering the laser around 100 μs after that we lowered the exit electrode voltage. As it will be detailed in Chapter 6, the method consisted in a subtle adjustment of this timing, dependent on the trap voltages, so that the ions are probed ”on their way out” but still inside the trap to avoid collisions with the rest gas. With an increased experience of the apparatus and a better adjustments of the trapping parameters this issue has tended to wear off. Nevertheless, this ion cloud distortion, already significant at rather low voltages (see top right simulation, with 0.5 V, in Figure 4.1), constitutes a serious issue of the 22-pole trap, and will be further discussed in Chapter 6 and 7.

4.2 Internal temperature of N_2O^+

N_2O^+, whose gas-phase electronic spectrum had already been recorded at low temperatures,[89,90] was chosen to assess quantitatively the buffer gas cooling of the ions thanks to the analysis of the rotational profile of the bands. The $\tilde{A}\,^2\Sigma^+\,(2,0,0) \leftarrow \tilde{X}\,^2\Pi^+_{3/4}(0,0,0)$ transition of N_2O^+ had was recorded. The energy of one photon lies above the dissociation threshold. Figure 4.2 shows the experimental spectrum. Using Pgopher,[91] the rotational profile was simulated using the constants $A'' = 132\,\mathrm{cm}^{-1}$, $B'' = 0.412\,\mathrm{cm}^{-1}$, $D'' = 2.99 \times 10^{-7}\mathrm{cm}^{-1}$, $B' = 0.433\,\mathrm{cm}^{-1}$, and $D' = 2.86 \times 10^{-7}\,\mathrm{cm}^{-1}$. By comparison with simulated rotational profiles, it was concluded that the rotational temperature of N_2O^+ ions was 11 K. This constitutes a slight improvement compared to the 10 - 15 K of the latest experiment.[90]

A more qualitative way to assess the low internal temperature of the ions is to observe the formation of complexes with He. The formation of the complexes depends on the He density, the interaction time with the buffer gas, and the mass and geometry of the ions themselves. A measurement of the number of parent ions and complexes produced in the trap as a function of the trapping time is given Figure 4.3. More He attach to the ions as the interaction time is increased, but counteracting effects dissociating the complexes seem to be acting in the trap and prevent a complete conversion.

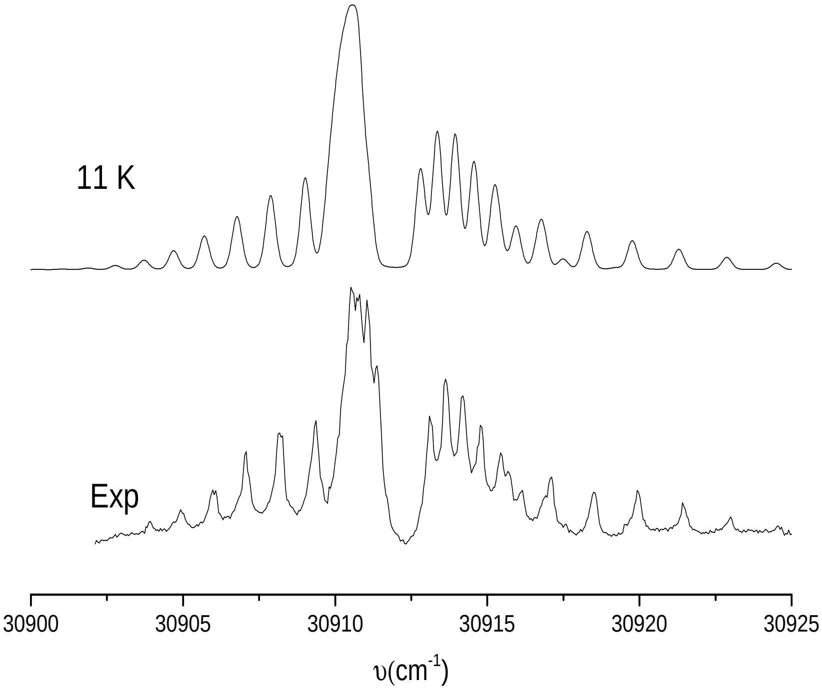

Fig. 4.2: The $\tilde{A}\,^2\Sigma^+$ (2,0,0) ← $\tilde{X}\,^2\Pi^+_{3/4}$(0,0,0) transition of N_2O^+ recorded by monitoring the number of NO^+ fragments exiting the trap, as a function of the laser wavelength. A simulated profile of the band at a rotational temperature of 11 K shows the best match with the experiment.

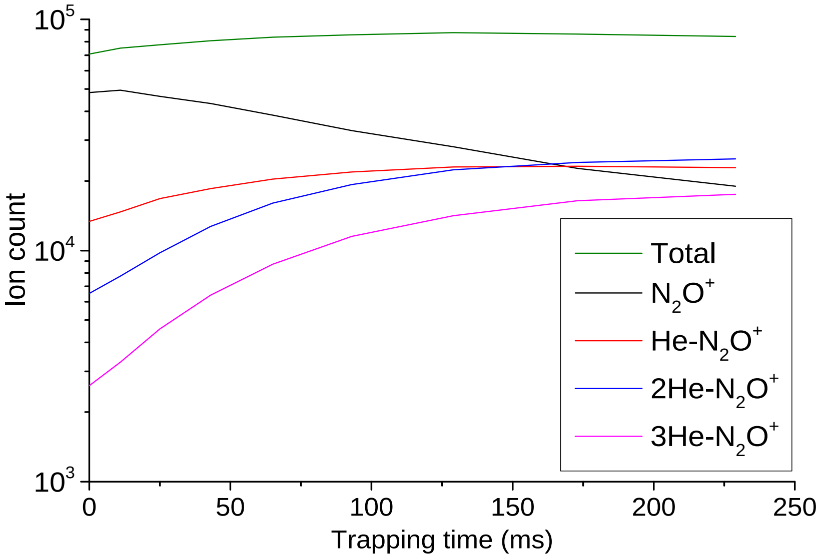

Fig. 4.3: Production of He - N_2O^+ complexes as a function of the trapping time. The longer the interaction time, the higher the conversion. Unknown effects in the trap were at play, causing a saturation of the conversion at higher trapping times.

5. MEDIUM-SIZED PROTONATED PAHS (H^+PAHS)

After that the setup was successfully tested with N_2O^+, medium-sized H^+PAHs were targeted, for two reasons. First, they were suggested as DIB carriers and this will be detailed in the next section. Also, they were easier targets in terms of photochemistry than other possible projects for this setup such as bare PAH or fullerene cations. The electronic spectra of medium-sized H^+PAHs can be recorded by monitoring their photodissociation via H-loss, following the absorption of only two visible photons. The reasons are their lower dissociation threshold and an IVR favorable to H-loss on the protonation site. In contrast, medium-sized PAHs or fullerenes do not fragment upon the absorption of two visible photons and require a more elaborate detection technique (see Chapter 7). Hence, before going for more challenging species, medium-sized H^+PAHs appeared as a good start for the setup.

The experimental setup has been described in Chapter 3. All five H^+PAHs were produced from a solid sample of the PAHs heated to ∼ 90 - 160 °C in a CI source. 90 °C for the smaller pyrene and fluoranthene molecules, 120 °C for azatriphenylene and corannulene, and 160 °C for coronene. The vapor created was bombarded with 20 - 50 eV electrons in the presence of toluene (C_7H_8) vapor. The proton affinity of C_7H_8 is 784 kJ mol^{-1} and is lower than that of all studied PAHs$^+$. These are 869, 861, 816, ∼ 950, 829 kJ mol^{-1},[92] for Pyr, Cor, Cora, $C_{17}H_{11}N$ and Fluo, respectively. The following protonation reaction is thus exothermic:

$$C_7H_9{}^+ + C_xH_y \rightarrow C_xH^+_{y+1} + C_7H_8$$

For all spectra, visible radiation from a tunable dye laser was used (0.07 cm^{-1} bandwidth with ≤ 1 mJ of energy per pulse). The electronic spectra measured were calibrated with a wavemeter, and the intensities of the recorded absorption features were power-corrected.

5.1 Introduction

Short timeline

- 1980s: PAHs are probably responsible for the UIBs, so they might also be responsible for the DIBs.[31, 93, 94]
- 1990s: Experimental electronic spectra of small PAHs: no match with the DIBs.[95] However, PAHs react with hydrogen, so H^+PAHs might populate the ISM.
- 2000s: H^+PAHs should have strong transitions in the visible.
- 2010 - 2012: Matrix and gas-phase electronic spectra of small protonated PAH-s.
  Results encourage the study of larger species.

50 years after the discovery of the first DIBs, a new kind of spectroscopic feature was observed, the UIBs. The UIBs are generally attributed to vibrational transitions in gas-phase molecules with aromatic and/or aliphatic structure. It was suggested in the 1990's that the elusive DIBs could also be due to PAHs.[31, 93, 94] Although, PAHs would be more likely in the cationic form in the DISM. The spectra of many small PAHs, cationic and neutral, were recorded in cryogenic rare gas matrices.[95] In 30 years of laboratory investigations, no match with any DIB was found. The attention was then brought toward protonated PAHs (H^+PAHs) when the reaction rates of some PAHs$^+$ with H, O and N atoms (mostly neutral in diffuse clouds) was measured.[96] It was estimated that H^+PAHs are likely to deplete PAHs$^+$ if the later are originally formed. Radiative association, photodissociation, photoionization, and electron recombination are the main physical processes competing in the ISM to produce PAHs in various charged and hydrogenation states. To know which specific members of this immense family to study in the laboratory, one must obtain first all the molecule specific reaction rates in the laboratory, as inputs of simulations of specific interstellar environments.

5.2 PAH^+ chemistry with H

The first estimates of the hydrogenation states of PAHs in diffuse clouds obtained in a selected ion flow tube gave significant reaction rates of Pyr^+ and $anthracene^+$ with H atoms,[96] and were confirmed by later studies,[96–100] as shown in Figure 5.1 for Cor^+. In the case of Pyr in a diffuse cloud, with $n_H \sim 10\,cm^{-3}$, $T \sim 100\,K$, and the derived rate coefficient $k = 3.1\times10^{-10}\,cm^3\,s^{-1}$, from the first study in the 1998, the hydrogenation timescale of Pyr^+ was estimated to be $t_H = 1/(n_H \times k)$ $= 1/(10\times3.1\times10^{-10}) = 10.2\,yr$, and similarly, the one of $anthracene^+$ was found to be 7.6 yr. Electron recombination timescale was found to be $t_e = t_H \times 6$. The authors then suggested that protonated species could dominate the PAH^+ population, however, they conclude that laboratory studies should focus on large H^+PAHs. Indeed, PD processes were omitted in these estimations, and some models had already predicted at the time that small species like anthracene would not survive the typical IRSF.[101]

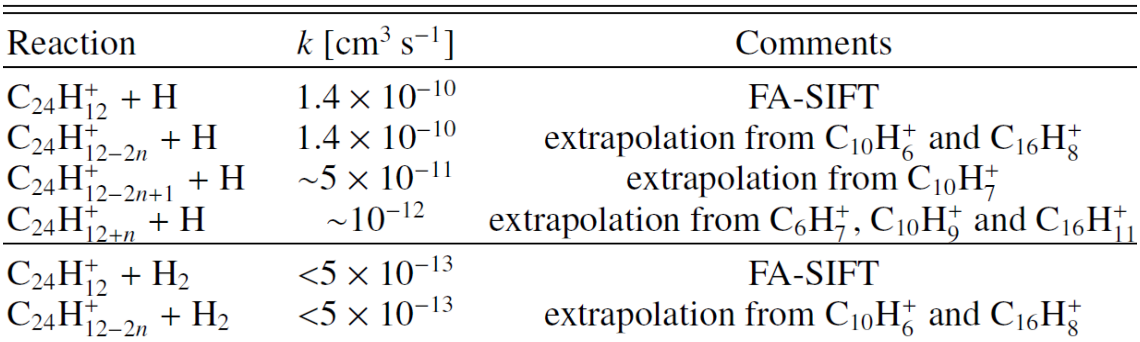

Reaction	k [$cm^3\,s^{-1}$]	Comments
$C_{24}H_{12}^+ + H$	1.4×10^{-10}	FA-SIFT
$C_{24}H_{12-2n}^+ + H$	1.4×10^{-10}	extrapolation from $C_{10}H_6^+$ and $C_{16}H_8^+$
$C_{24}H_{12-2n+1}^+ + H$	$\sim5 \times 10^{-11}$	extrapolation from $C_{10}H_7^+$
$C_{24}H_{12+n}^+ + H$	$\sim10^{-12}$	extrapolation from $C_6H_7^+$, $C_{10}H_9^+$ and $C_{16}H_{11}^+$
$C_{24}H_{12}^+ + H_2$	$<5 \times 10^{-13}$	FA-SIFT
$C_{24}H_{12-2n}^+ + H_2$	$<5 \times 10^{-13}$	extrapolation from $C_{10}H_6^+$ and $C_{16}H_8^+$

Fig. 5.1: Reaction rates of some small H^+PAHs with H, O and N measured in a selected ion flow tube experiment.[96–100]

The amount of H atoms covering PAHs is mostly a balance between UV-Vis induced fragmentation via H-loss and reactions with atomic H. Later models showed that, not only PD is a key process, but that the chemical state of a PAH is extremely sensitive to the H density and the ISRF. As a consequence, it is still currently impossible to accurately determine the charge and hydrogenation state of a specific PAH. However, general conclusions could be drawn, such that small PAHs like Pyr and anthracene will be destroyed,[102] and that much larger PAHs can be treated without taking into account PD, as they will be able to internally distribute the

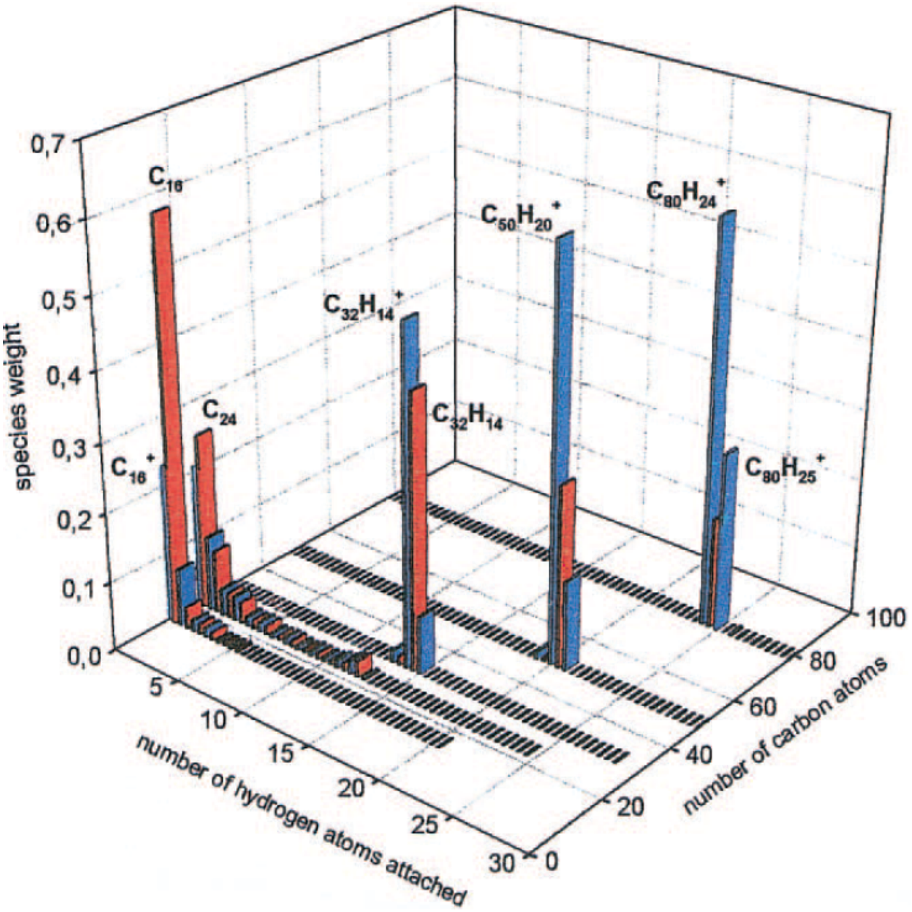

Fig. 5.2: Charge and hydrogenation states of five different PAHs sizes[102] ($C_{16}H_n$, $C_{24}H_n$, $C_{32}H_n$, $C_{50}H_n$, and $C_{80}H_n$). The environmental parameters for the diffuse cloud are $n_H = 100\,cm^{-3}$, $f = 0.5$, $T = 100\,K$, $n_e = 10^{-4} n_H\,cm^{-3}$.

photon energy, without even an H-loss. Figure 5.2 shows the results of the calculation applied for typical diffuse cloud conditions. Even a molecule like Cor will be dehydrogenated, and only around ~50 - 100 atoms, the protonated form of a PAH becomes appreciable.

5.3 H^+PAH expected transitions

Since no laboratory electronic spectra of isolated H^+PAH in the gas phase or rare gas matrices were reported at that time, calculations were performed on some H^+PAH. Closed-shell neutral PAHs and isoelectronic H^+PAHs have many of their electronic transitions falling in the UV. However, the case of coronene and ovalene have been studied theoretically,[103] and has shown that the protonation can lift electronic degeneracy and strong transitions in the visible are predicted for these medium-

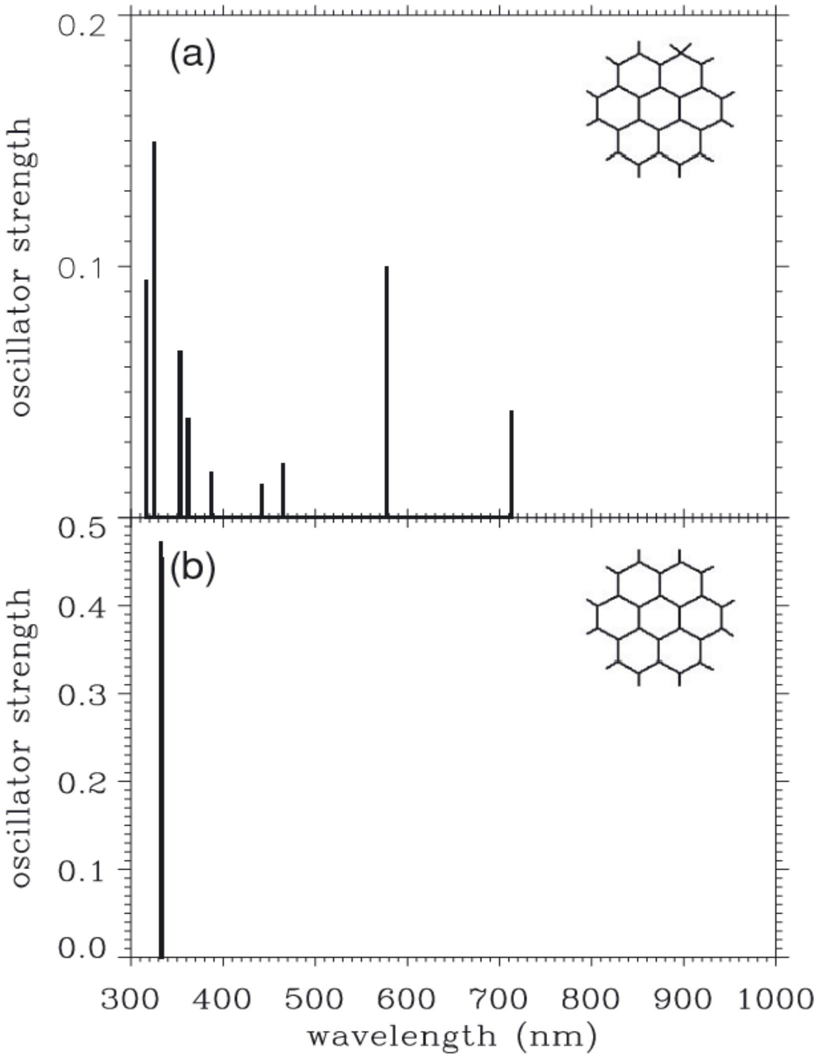

Fig. 5.3: TD-DFT absorption spectra for (a) protonated coronene and (b) neutral coronene.

sized H^+PAHs. Figure 5.3 shows the expected transitions of protonated and neutral coronene exemplifying the trend. The results were similar for ovalene, except that the protonated form has four isomers. The conclusion was that large H^+PAH are good candidate carriers of the DIBs and that efforts should be done to obtain experimental spectra. The first experimental spectrum showing the absorption in the visible of a H^+PAH was done on naphthalene.[104] The spectrum contained dozens of absorption bands around 500 nm and did not match any DIB, but this is one of the smallest PAHs and the work was asking for the spectra of larger species. The H^+PAH hypothesis has weaknesses even for candidates containing around 60 - 100 carbon atoms. Protonation weakens, in two ways, the intensity of the electronic transitions. First, protonated species appear in several isomeric structures in most cases, and also, by decreasing the symmetry of the molecule, protonation often distributes the absorption over more vibrational modes, as seen Figure 5.3 for H^+Cor. Astronomical detection becomes then much less likely than for bare PAHs$^+$, given that most DIBs show little correlation which each other.

The spectra of medium-sized H^+PAHs presented in the next sections were, in view of the above-mentionned constraints, already largely doomed in terms of astronomical identification, however, their obtention does not only constitute an experimental validation of the models, but also a necessary step if one wants to be able to obtain the spectra of even larger and more challenging species.

For all H^+PAH studied in this thesis, a direct absorption spectrum had already been obtained in a rare gas matrix. These spectra were complemented by theoretical calculations for the assignment of the absorptions features to the different isomers potentially present in the matrix. These matrix data made the task of obtaining the spectrum in the gas phase much easier since the positions and strengths of the absorption bands were known, but also the structural assignment was done.

5.4 Protonated pyrene (H^+Pyr)

The absorption is monitored by a one-color two-photon process; the $1\,^1A' \leftarrow X\,^1A'$ electronic transition (Figure 5.4) of H^+Pyr is resonant with the first photon. The excited electronic state lies below the threshold for the H-loss, and thus, the absorption of a second photon is used to bring the system to the fragmentation continuum. The excess energy is sufficient such that H-loss is fast enough and the residual $C_{16}H_{10}^+$ is detected. Visible radiation from a tunable dye laser (R ~ 270 000, with ~ 3 mJ energy per pulse) was used.

According to the data obtained in the 6 K neon matrix,[105] the most stable isomer of H^+Pyr is the one shown in Figure 5.4, and its $1\,^1A' \leftarrow X\,^1A'$ allowed electronic transition has an origin band around 487.5 nm. The absorption in the gas phase was found on the basis of these data, and other less stable isomers were not detected. In the spectra obtained, the relative intensities are likely distorted from a linear measurement. PD is dependent on the specific vibrational mode excited since some of them will lead to faster H-loss than others, and artificially increase the intensity of specific bands. However, the extent of this distortion can be assessed to some extent by comparing the gas phase and matrix spectra.

In the bottom spectrum, obtained first, the bands are broader and hot bands can be seen ~ 1.3 nm to the red of the strongest absorptions. A low energy vibrational mode of the ground electronic state was populating almost 10% of the ions. In the top spectrum of Figure 5.4, all transitions originate from the lowest vibrational level of the ground electronic state. A narrowing of the bands also reveals colder ions.

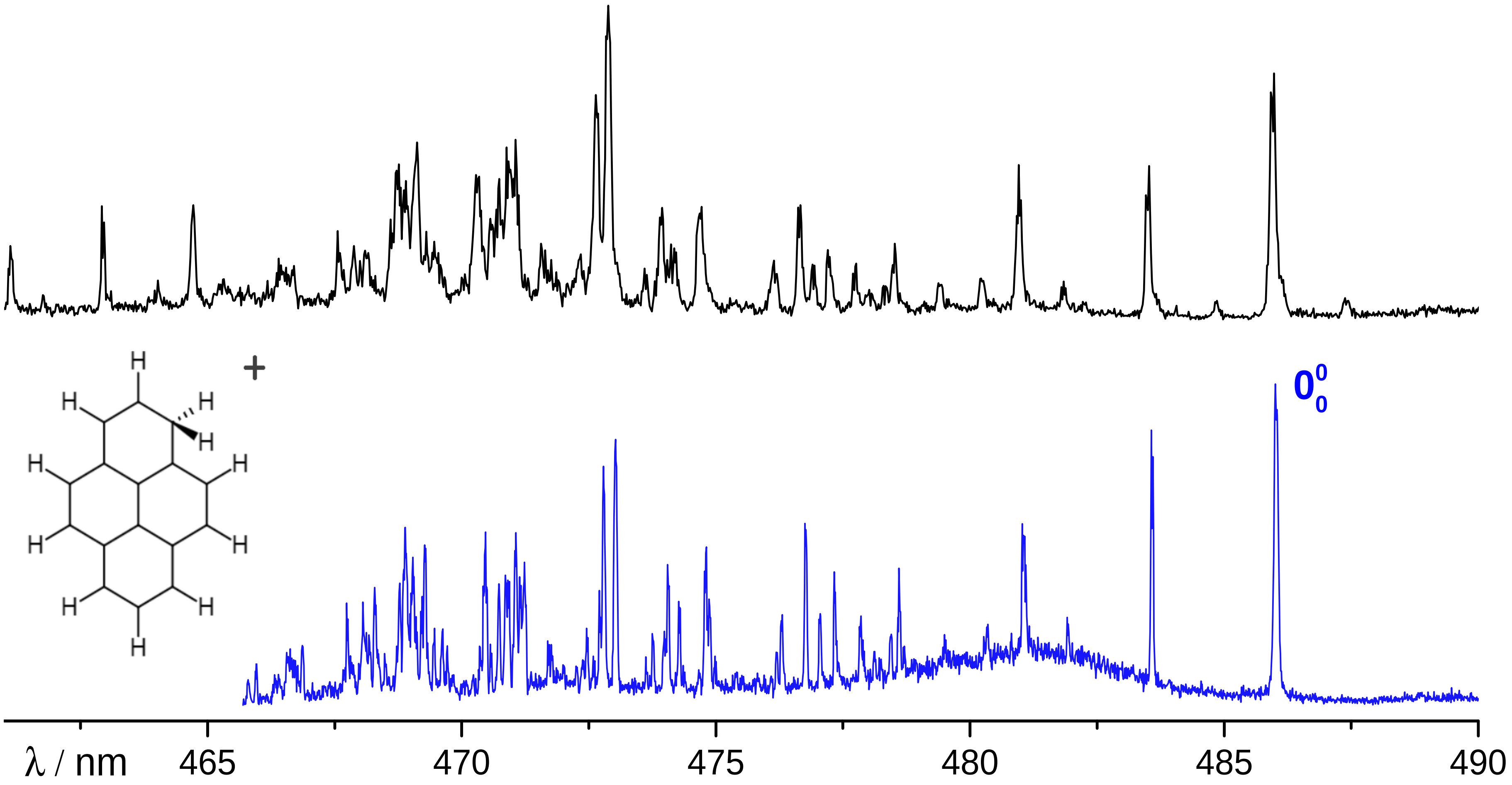

Fig. 5.4: The $1\,^1A' \leftarrow X\,^1A'$ electronic system was measured by a one-color, two-photon excitation/dissociation technique using a pulsed dye laser with R ∼ 270 000. The top trace was recorded at a rotational temperature of ∼ 15 K and the bottom trace at ∼ 100 K.

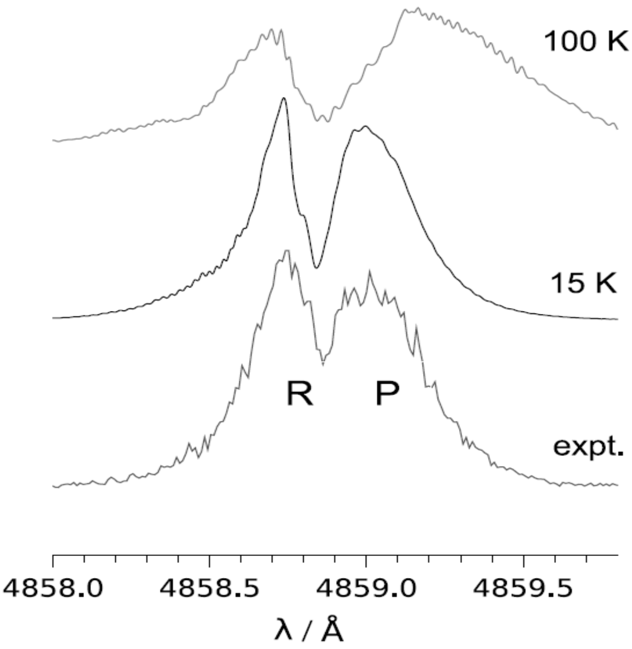

Fig. 5.5: Absorption profile of the origin band in the $1\,^1A' \leftarrow X\,^1A'$ electronic transition of protonated pyrene (bottom) and the simulated profile at 15 K (middle) and 100 K (top).

To assess experimentally the temperature of the ions, the origin band was recorded with a resolution of 0.001 nm and compared to simulated spectra at different temperatures (Figure 5.5). Simulating the rotational contour of the origin requires knowing the rotational constants of the ground and electronic states. Since these are not known for the excited state, a procedure used for large molecules is followed.[106] The molecular constants of the $1\,^1A'$ ground state were calculated using B3LYP/ccpVTZ theory (Gaussian 09[107]) yielding $A'' = 0.03383\,\mathrm{cm}^{-1}$, $B'' = 0.01817\,\mathrm{cm}^{-1}$ and $C'' = 0.01185\,\mathrm{cm}^{-1}$. In the calculation, these values were fixed and the values for the ^{1}A' were varied along with the temperature. Assuming a Boltzmann distribution and parallel b-type transition, the simulation is fitted to the experimental profile. The best agreement is obtained with the following values: $A' = 0.0348\,\mathrm{cm}^{-1}$, $B' = 0.0168\,\mathrm{cm}^{-1}$, $C' = 0.0118\,\mathrm{cm}^{-1}$, $\tilde{\nu}_{00} = 20575.35\,\mathrm{cm}^{-1}$, and a rotational temperature of 15 K. The most significant change between the $1\,^1A'$ and $^1A'$ states is for the B constant (8%), and indicates a decrease in the CH_2 bond angle at the protonation site. Also, the shoulder to the red of the origin band is comparable for the simulation at 100 K and the bottom spectrum in Figure 5.4, giving an estimate of the temperature for the later. Given the accuracy of the fit, one can also confirm the assignment of the spectrum to the isomer shown in Figure 5.4.

5.5 Protonated coronene, (H^+Cor)

Coronene protonation sites on the peripheral C are all equivalent. Isomers with inner H^+ addition are energetically higher by $\sim 65\,\mathrm{kJ\,mol_1}$ and are not expected in the CI source.[108,109] The $(1)\,^1A' \leftarrow X\,^1A'$ symmetry-allowed transition of H^+Cor was first observed in a 6 K neon matrix. The transition was sought in the gas phase on the basis of these data and is presented Figure 5.6. The origin band is measured at 695.22 nm, 0.4 nm blue-shifted from the matrix. The $(1)\,^1A'$ excited state lies ~ 2.5 eV below the thermodynamic threshold for H-loss; therefore, two or more photons are required to bring H^+Cor to the fragmentation continuum.

Protonated coronene is of Cs symmetry and has 105 vibrations, 70 of a$'$ and 35 of a$''$ symmetry. Band positions and suggested assignments are given in Table 5.1. The experimental values assigned are in agreement with the calculated excited-state frequencies (B3LYP/cc-pVTZ level of theory), except in the lowest vibration ν_{105}; theory predicts it to be at $64\,\mathrm{cm^{-1}}$, whereas the experiment gives $55\,\mathrm{cm^{1}}$, which is deduced from double quanta excitations. The intensity ratio of the $2\nu_{105}$ to the origin band suggests that the fragmentation pathway goes through the CH_2 rocking, leading to H-loss. This dissociation is the lowest energy channel for all smaller H^+PAHs[110] except for protonated benzene,[111] where H_2 loss dominates. Molecular hydrogen loss is not observed for H^+Cor. As for H^+Pyr, the relative intensities of the bands in Figure 5.6 are probably distorted due to the PD processes, involving two to three photons.

The excitation of the in-plane a$'$ modes in the $(1)\,^1A'$ state is observed at +347.9, +357.7, +369.8, and $+373.8\,\mathrm{cm^{-1}}$. They are attributed to the ν70, ν69, ν68, and ν67 modes, respectively, listed in Table 5.1. In the neon matrix spectrum, the excitation of the vibrational mode ν69 (ring deformation) in the excited state is observed at $+361\,\mathrm{cm^{-1}}$, which is comparable to the gas-phase recording at $+357.7\,\mathrm{cm^{-1}}$. There are more distinct absorption bands in the $(1)\,^1A' \leftarrow X\,^1A'$ transition of H^+Cor in the gas phase than in a neon matrix. In crystalline neon, low-frequency bending modes are not pronounced because their larger amplitudes are hindered, and solid-state effects broaden the spectrum.

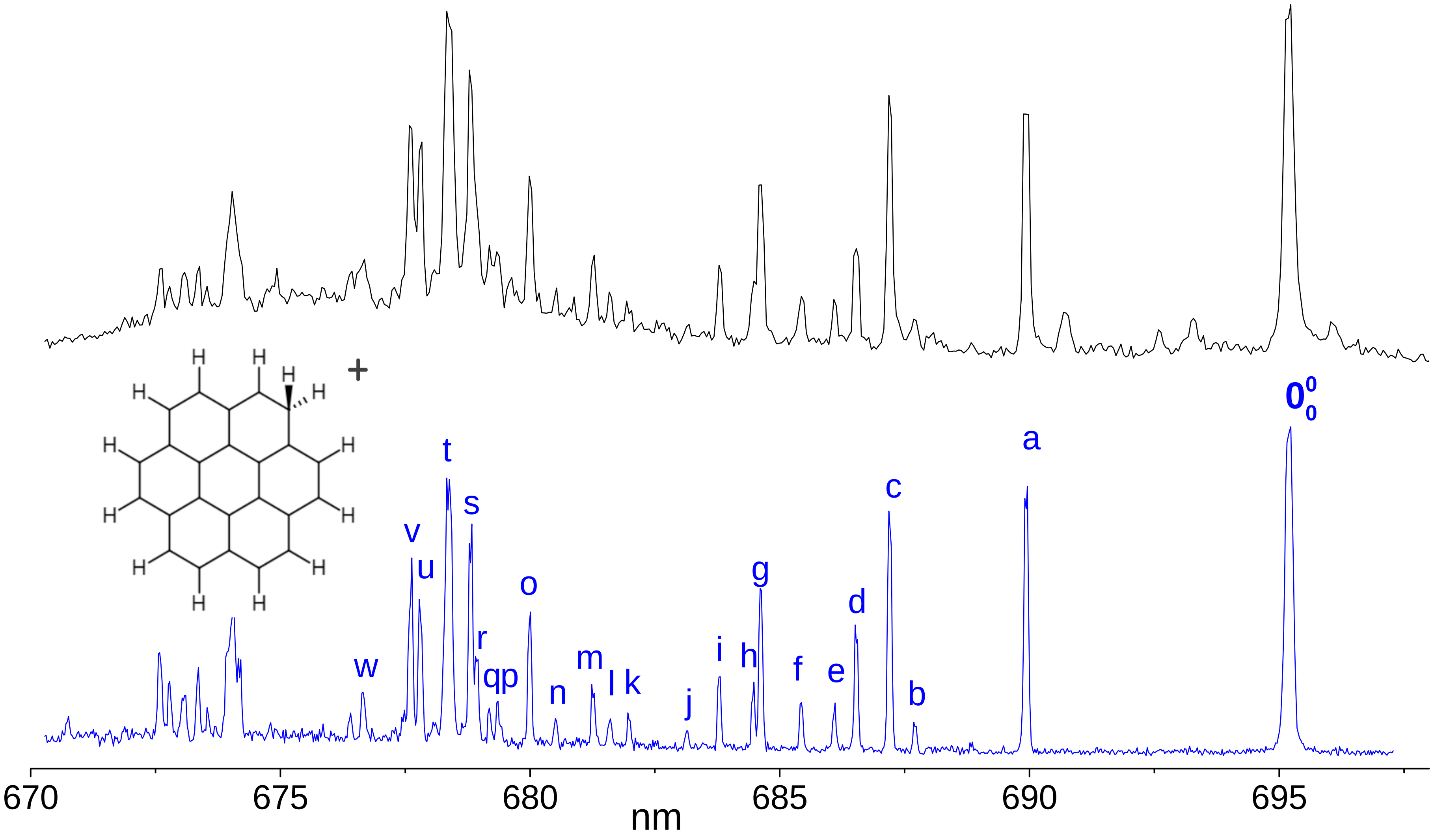

Fig. 5.6: The (1) $^1A' \leftarrow X\,^1A'$ electronic transition of H^+Cor measured with a 0.07 cm^1 laser bandwidth using a resonant one-color multiphoton fragmentation scheme. The absence of hot bands in the lower trace indicates rotational and vibrational temperatures of at most 15 K.

Tab. 5.1: Band Maxima (± 0.2 cm^{-1}) and suggested assignments of the vibrational bands in the $(1)\,^1A \leftarrow X\,^1A$ electronic transition of H^+Cor in Figure 5.6

Label	λ/nm	$\tilde{\nu}$/cm^{-1}	$\Delta\tilde{\nu}$/cm^{-1}	Assignment
0_0^0	695.22	14 383.8	0	0_0^0
a	689.93	14 494.2	110.4	$2\times\nu_{105}$
b	687.71	14 541.1	157.3	$\nu_{105}+\nu_{104}$
c	687.20	14 551.8	168.0	$2\times\nu_{104}$
d	686.53	14 565.9	182.1	$\nu_{105}+\nu_{103}$
e	686.10	14 575.2	191.4	$\nu_{105}+\nu_{102}$
f	685.43	14 589.4	205.6	$\nu_{104}+\nu_{103}$
g	684.61	14 606.8	223.0	$4\times\nu_{105}$
h	684.46	14 610.0	226.2	$\nu_{104}+\nu_{102}$
i	683.79	14 624.4	240.6	$2\times\nu_{103}$
j	683.15	14 638.1	254.3	$\nu_{103}+\nu_{102}$
k	681.98	14 663.2	279.4	$2\times\nu_{105}+2\times\nu_{104}$
l	681.60	14 671.4	287.6	?
m	681.25	14 678.8	295.0	$\nu_{105}+\nu_{100}$
n	680.52	14 694.7	310.9	$\nu_{102}+\nu_{101}$
o	679.99	14 706.0	322.2	$\nu_{104}+\nu_{100}$
p	679.34	14 720.2	336.4	$6\times\nu_{105}$
q	679.18	14 723.7	339.9	$4\times\nu_{104}$
r	678.93	14 729.1	345.3	$2\times\nu_{105}+2\times\nu_{103}$
s	678.81	14 731.7	347.9	ν_{70}
t	678.36	14 741.5	357.5	ν_{69}
u	677.80	14 753.6	369.8	ν_{68}
v	677.62	14 757.6	373.8	ν_{67}
w	677.46	14 761.1	377.3	$2\times\nu_{105}+2\times\nu_{102}$

5.6 Protonated corannulene, (H^+Cora)

Cora$^+$ possesses three non-equivalent protonation sites: rim, spoke, and hub, from the outer to the inner C of the structure.[112] According to DTF/PBE0 and ri-MP2 calculations, the lowest energy $C_{20}H_{11}^+$ structure is the *hub*-isomer. The *rim* is located only 7 and 20 kJ mol^{-1} above the *hub* by these methods. This difference is too small to exclude the *rim* isomer. On the other hand, the calculations exclude the *spoke* isomer.

A weak electronic transition around 520 nm and a much stronger one starting at 396.55 nm were detected (Table 5.3). The $3\,^1$A excited state lies below the ~ 2.5 eV thermodynamic threshold for H-loss. Therefore, one photon promotes $C_{20}H_{11}{}^+$ to the $3\,^1$A state and a second into the fragmentation continuum. The 520 nm feature (Figure 5.7) is broad and no vibrational structure in the $3\,^1\mathrm{A} \leftarrow X\,^1\mathrm{A}$ electronic transition is discernible. The relationship between the bandwidth and the excited state lifetime τ is given by $\Delta\nu = 1/2.\pi.\tau$, with $\Delta\nu$ in Hz. The whole absorption has FWHF of ~ 50 nm, however, if the main bands which are blended within this absorption are significantly separated in wavelength, the true natural bandwidth will not be revealed. This absorption, however, fits to a Lorentzian function of 53 nm FWHM (blue dotted trace in Figure 5.7), and the lifetime in the $3\,^1$A state is ~ 3 fs, a particularly extrem value.

The 397 nm system is compared with the spectrum of *rim*-H^+Cora measured in a 6 K neon matrix (Figure 5.8). The origin of the $4\,^1\mathrm{A} \leftarrow X\,^1\mathrm{A}$ electronic transition in the gas phase is blue shifted by $\sim 140\,\mathrm{cm}^{-1}$ with respect to the position in a neon matrix. The gas-phase to matrix shift is within the expected 1 % energy range of the electronic transition.[113] Excess excitation energy of $4\,^1$A state was sufficient for PD; however, two photons were absorbed so that $C_{20}H_{10}{}^+$ was detectable on a μs timescale. The origin band of the $4\,^1\mathrm{A} \leftarrow X\,^1\mathrm{A}$ electronic transition of $C_{20}H_{11}{}^+$ was scanned with a dye laser; however, no rotational structure was apparent. A ~ 0.2 ps lifetime in the $4\,^1$A state is inferred by the width of the origin band.

A well-resolved vibrational structure is seen for the $4\,^1\mathrm{A} \leftarrow X\,^1\mathrm{A}$ electronic transition of $C_{20}H_{11}{}^+$ in the gas phase. The next most intense absorption lies $123\,\mathrm{cm}^{-1}$ to higher energy of the origin band. In the matrix spectrum, a weak shoulder $127\,\mathrm{cm}^{-1}$ to the blue of the origin is present. This band is assigned to the CH_2 rocking mode ν_{87} of the protonation site on the basis of the vibrational frequencies calculated with

Tab. 5.2: Excitation energies in eV and oscillator strengths of *hub*- and *rim*-isomers of H^+Cora calculated with TDDFT, SAC-CI, and CC2 methods using ground state equilibrium structures obtained from DFT/PBE0 and *ri*-MP2.

hub-$X\,^1\mathrm{A}'$				
	TDDFT/PBE0	SAC-CI/PBE0	SAC-CI/MP2	CC2/MP2
$1\,^1\mathrm{A}'$	2.67 0.09	1.80 0.1	1.77 0.1	2.53 0.1
$2\,^1\mathrm{A}'$	3.74 0.03	3.34 0.05	3.22 0.04	3.61 0.06
$3\,^1\mathrm{A}'$	3.89 0.02	3.52 0.01	3.56 0.005	3.90 0.005
$4\,^1\mathrm{A}'$	4.22 0.2	3.94 0.3	3.80 0.3	4.13 0.3
$1\,^1\mathrm{A}''$	2.32 0.004	1.75 0.03	1.77 0.06	2.35 0.02
$2\,^1\mathrm{A}''$	2.66 0.05	1.82 0.04	1.79 0.0	2.54 0.05
$3\,^1\mathrm{A}''$	3.96 0.2	3.82 0.2	3.57 0.2	3.88 0.2
$4\,^1\mathrm{A}''$	4.66 0.0	4.47 0.04	4.61 0.05	4.57 0.02
rim-$X\,^1\mathrm{A}$				
	TDDFT/PBE0	SAC-CI/PBE0	SAC-CI/MP2	CC2/MP2
$1\,^1\mathrm{A}$	1.88 0.003	1.19 0.003	1.15 0.003	1.78 0.007
$2\,^1\mathrm{A}$	2.14 0.007	1.54 0.01	1.46 0.01	2.11 0.01
$3\,^1\mathrm{A}$	2.60 0.09	1.94 0.08	1.88 0.08	2.46 0.1
$4\,^1\mathrm{A}$	3.47 0.1	3.03 0.2	3.01 0.2	3.37 0.2
$5\,^1\mathrm{A}$	3.78 0.02	3.64 0.02	3.50 0.02	3.81 0.03

the DFT method. The calculated energy of this mode is $127\,\mathrm{cm}^{-1}$. This excited-state frequency of ν_{87} is more than double in H^+Pyr and H^+Cor for a similar nuclear motion.[114,115] This is due to the tertiary structure of $C_{20}H_{11}{}^+$. Double quanta excitation of ν_{87} in the $4\,^1$A state is also observed at $25\,464\,\mathrm{cm}^{-1}$. The ν_{87}, $2\nu_{87}$, ν_{81} and ν_{77} vibronic bands in the $4\,^1$A excited state have $50-90\,\%$ of the intensity of the origin and are stronger than these observed in the neon matrix. This reflects a dependence of the dissociation rate on the excess excitation energy supplied to the cation. Photofragmentation takes place from a highly excited vibration in the ground state of H^+Cora and leads to the formation of Cora$^+$ and H. This is similar for protonated pyrene and coronene.[114,115] The band maxima of the $4\,^1\mathrm{A} \leftarrow X\,^1\mathrm{A}$ transition are given in Table 5.3.

Tab. 5.3: Observed band maxima in the $3, 4\,^1\mathrm{A} \leftarrow X\,^1\mathrm{A}$ transitions of the rim-isomer of H^+Cora, in the gas phase.

λ/nm	$\tilde{\nu}$/cm^{-1}	$\Delta\tilde{\nu}$/cm^{-1}	Assignment
521	19 200	0	$3\,^1\mathrm{A} \leftarrow X\,^1\mathrm{A}$
396.53	25 219	0	$4\,^1\mathrm{A} \leftarrow X\,^1\mathrm{A}$
394.60	25 342	123	ν_{87}
392.7	25 464	245	$2 \times \nu_{87}$
392.0	25 510	291	ν_{81}
390.20	25 628	409	ν_{77}

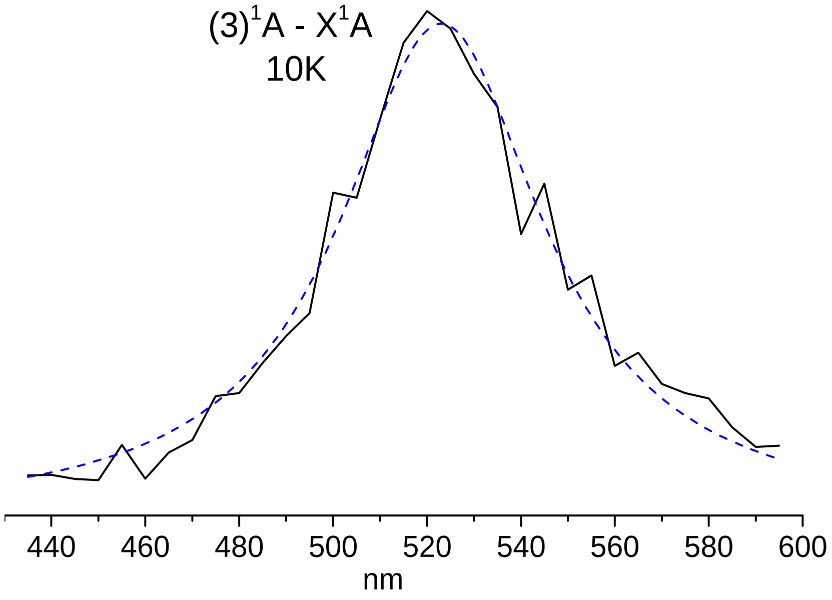

Fig. 5.7: Absorption assigned to the $3\,^1\mathrm{A} \leftarrow X\,^1\mathrm{A}$ transition of H^+Cora. In dotted blue is a Lorentzian fit demonstrating a natural broadening of 53 nm FWHM due to a 3 fs lifetime of the $3\,^1\mathrm{A}$ state.

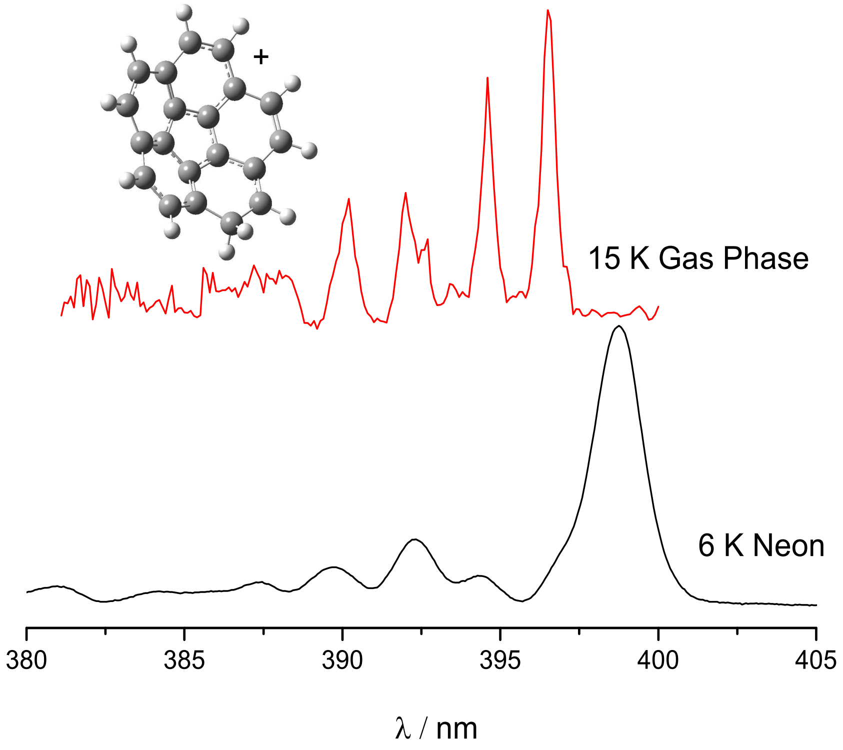

Fig. 5.8: $4\,^1\mathrm{A} \leftarrow X\,^1\mathrm{A}$ electronic transition of H^+Cora detected in a 6 K neon matrix (black trace) and the spectrum in the gas phase at 15 K (red trace).

5.7 Protonated fluoranthene, (H$^+$Fluo)

As it is the case of Cora$^+$, Fluo$^+$ share a similarity with C_{60} by possessing a five-membered ring. H$^+$Fluorene electronic spectrum has already been recorded[116] and H$^+$Fluo is a step toward large species. The study of H$^+$Fluo in a neon matrix,[117] along with quantum chemical calculations, assigned all three visible absorption systems to the most stable of the five isomers of H$^+$Fluo (shown in Figure 5.10). Of these (2, 3, 4) $^1A' \leftarrow X\,^1A'$ transitions, only the (2, 3) $^1A' \leftarrow X\,^1A'$ were sought for in the gas phase. The 4^{th} transition is the weakest, and being around 380 nm, is less relevant for an astronomical comparison.

In Figure 5.9, a comparison of the 6 K neon matrix and gas-phase spectra of the $2\,^1A' \leftarrow X\,^1A'$ transition is presented. The origin band at 558.28 nm is blue-shifted by 1 nm from that in solid neon. The line widths of the gas-phase spectrum are narrower than in the matrix, however, the main absorption features are similar in both. There is a large change in geometry in the $2\,^1A'$ excited state, as seen by the rich vibrational progressions in the gas-phase spectrum (Figure 5.9, red trace). The origin band has a half width of $\sim 4\,\mathrm{cm}^{-1}$, corresponding to a lifetime in the $2\,^1A'$ state of around 1 ps. Sometimes fluorescence is observed in solid neon because the caged environment rapidly quenches the low-frequency modes in contrast with the gas phase. In Figure 5.10, the $3\,^1A' \leftarrow X\,^1A'$ electronic transition of H$^+$Fluo in the gas-phase is shown along with the absorption spectrum in a 6 K neon matrix. The origin band at 474.92 nm is blueshifted to the matrix spectrum by 1.4 nm. The Franck-Condon envelope of the $3\,^1A' \leftarrow X\,^1A'$ transition of H$^+$Fluo is less pronounced than that of the $2\,^1A' \leftarrow X\,^1A'$ one. This is most likely due to the fact that there is a slight geometry change in the $3\,^1A'$ state and therefore fewer vibrational excitations will be prevalent within this electronic transition and the transition will constitute a better reference for astronomical comparison.

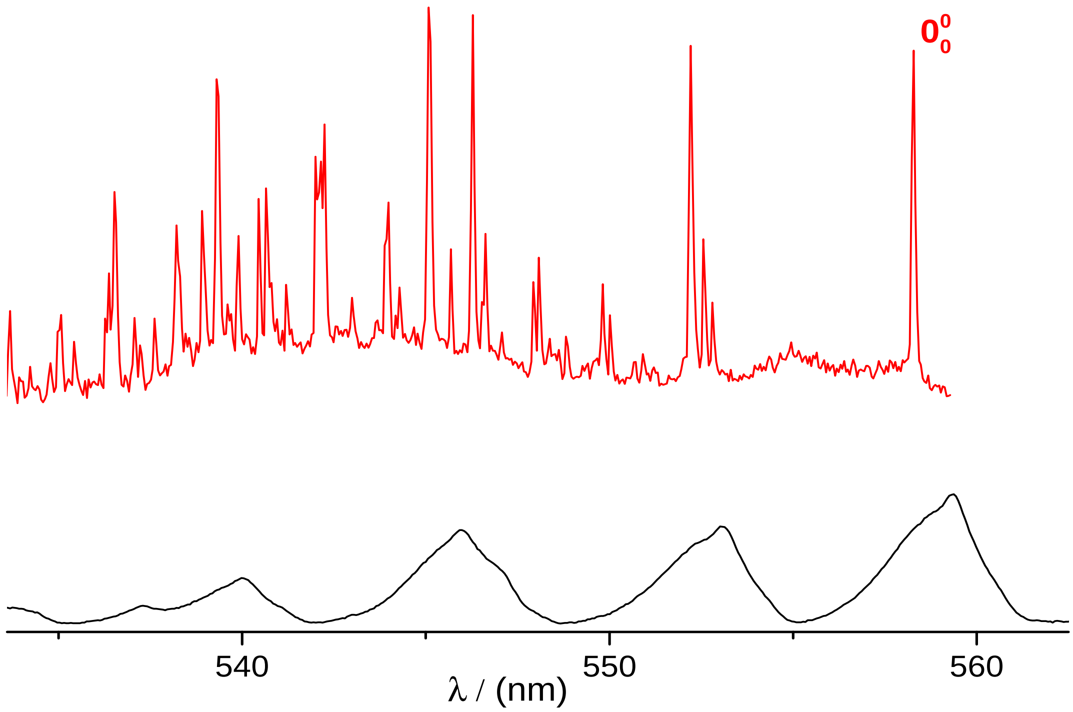

Fig. 5.9: Matrix (black) and gas-phase (red) spectra of the $2\,^1A' \leftarrow X\,^1A'$ transition of H^+Fluo.

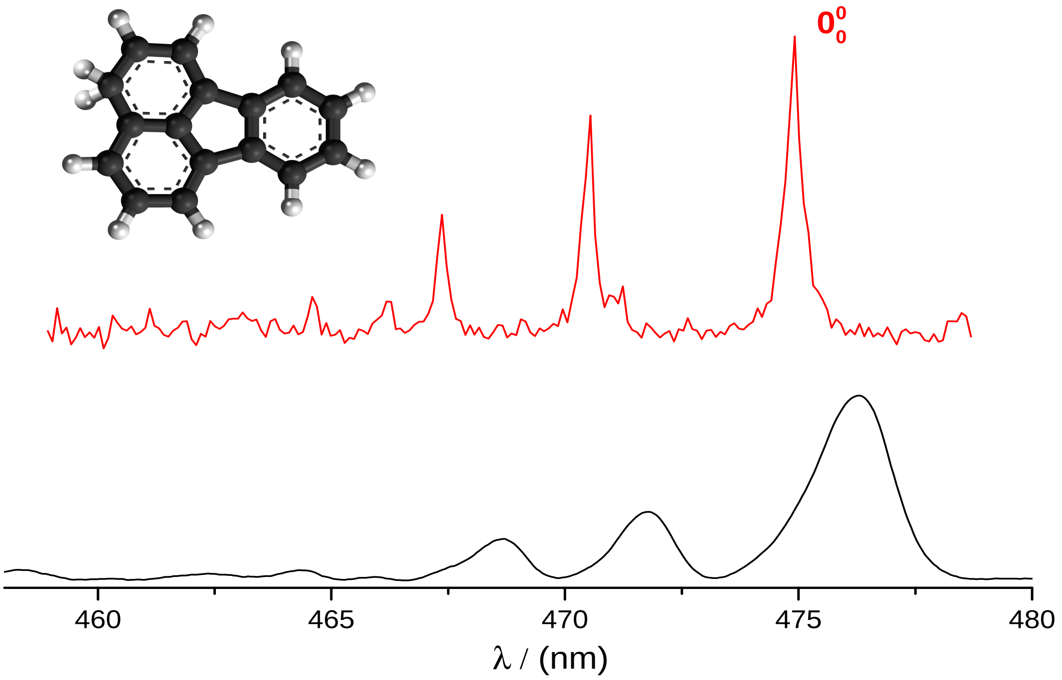

Fig. 5.10: Matrix (black) and gas-phase (red) spectra of the $3\,^1A' \leftarrow X\,^1A'$ transition of H^+Fluo.

5.8 $C_{17}H_{11}N^+$

Azatriphenylene, $C_{17}H_{11}N^+$, has C_s symmetry when triphenylene ($C_{18}H_{12}$) has D_{3h}. Because of the N substitution, it also has all non-equivalent protonation sites. The proton affinity of 1-azatriphenylene is assumed to be similar to that of pyridine (930 kJ mol^{-1}) and acridine (973 kJ mol^{-1}), which are both relatively high compared to that of toluene (784 kJ mol^{-1}). 12 different protonation sites of $C_{17}H_{12}N^+$ were calculated at the B3LYP/cc-pVDZ level to determine on which atom the additional H is chemically bound. Theoretically, the lowest energy isomer of $C_{17}H_{12}N^+$ is protonated on the N and the next highest one is at 134 kJ mol^{-1} (Table 5.4). All other structures on the ground state potential energy surface are stable, but would not be produced in a CI source. No inner C were considered to be protonated because these isomers would be energetically higher.

Tab. 5.4: Relative energies of the X ^{1}A$'$ ground states of protonated azatriphenylenes calculated at the B3LYP/ccpVDZ level of theory and their computed proton affinity. Labeling of atoms is given Figure 5.11 a

atom labeling	E/kJ mol^{-1}	PA/kJ mol^{-1}	atom labeling	E/kJ mol^{-1}	PA/kJ mol^{-1}
1	0	1009	9	151	858
2	181	828	10	146	864
3	154	855	13	134	875
4	197	813	14	148	862
7	151	859	15	137	872
8	147	863	16	142	868

Protonated azatriphenylene was initially considered to be the absorbing species of the three electronic transitions in the visible because azatriphenylene was the precursor used in the CI source. However, as the calculated excitation energies (gray column in Table 5.5) for the electronic transitions differ by > 1 eV with the observed spectra, it was concluded that a different isomeric structure was responsible for the absorptions. The protonation in the CI source can deposit excess energy into 1H$^+$-1-Azat and dissociate one of the bonds, causing a ring-opening in the conjugated Π-system or H-loss. Therefore, bond cleaving mechanisms, based on the 1H$^+$-1-Azat

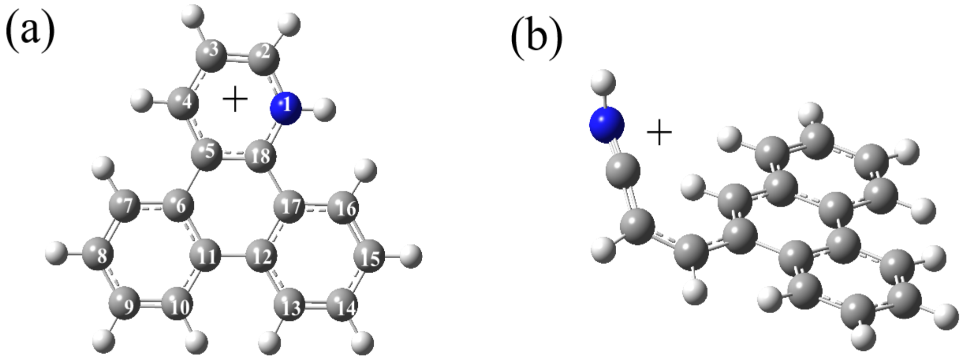

Fig. 5.11: Optimized geometry structures of the open-ring isomer (left) of $C_{17}H_{12}N^+$ and protonated azatriphenylene (right).

Mulliken charge distribution were investigated. Two mechanisms, having the same m/z as $1H^+$-1-Azat, were considered, one in which the (18)CNH bond is broken (Figure 5.11 b) and the other being between (2)CNH (labeling of the atoms is given in Figure 5.11 a). In case 1, the geometry of $C_{17}H_{12}N^+$ is that seen in Figure 5.11 b. There is H migration from (2)C to (18)C, making a cyanoethyl-substituted phenanthrene. In case 2, the calculated structure is not a minimum on the potential energy surface, and converges to $1H^+$-1-Azat. The recorded electronic transitions were finally assigned to the structure shown in Figure 5.11 b. Theoretical vertical excitation energies are 1.92, 2.21, and 3.17 eV for the 1, 2, and $3\,^1A \leftarrow X\,^1A$ electronic transitions and 1.80, 2.00, and 2.92 eV for the experimental data (Table 5.5). The theoretical oscillator strengths for the $1\,^1A \leftarrow X\,^1A$ and $2\,^1A \leftarrow X\,^1A$ transitions are approximately 1:6, also similar to the relative intensities in the recorded spectrum (Figure 5.12).

$1\,^1A' \leftarrow X\,^1A'$ electronic transition. The $1\,^1A' \leftarrow X\,^1A'$ electronic transition of $C_{17}H_{12}N^+$ (Figure 5.12) has an origin at $14\,519 \pm 30\,\mathrm{cm}^{-1}$. The 0^0_0 band is broad, having a FWHM of $158 \pm 15\,\mathrm{cm}^{-1}$ and no rotational structure. From this, the excited state lifetime of the $1\,^1A'$ system is inferred to be ~ 30 fs.

There is a vibrational structure within the $1\,^1A' \leftarrow X\,^1A'$ electronic transition of $C_{17}H_{12}N^+$; however, all absorptions are lifetime broadened. Three distinct features (Figure 5.12) are observed in the spectrum at 15 292, 15 509, and $15\,721\,\mathrm{cm}^{-1}$, having a similar FWHM as the assigned origin band. The absorption maxima are collected in Table 5.6.

$2\,^1A' \leftarrow X\,^1A'$ electronic transition. A stronger, broader absorption is

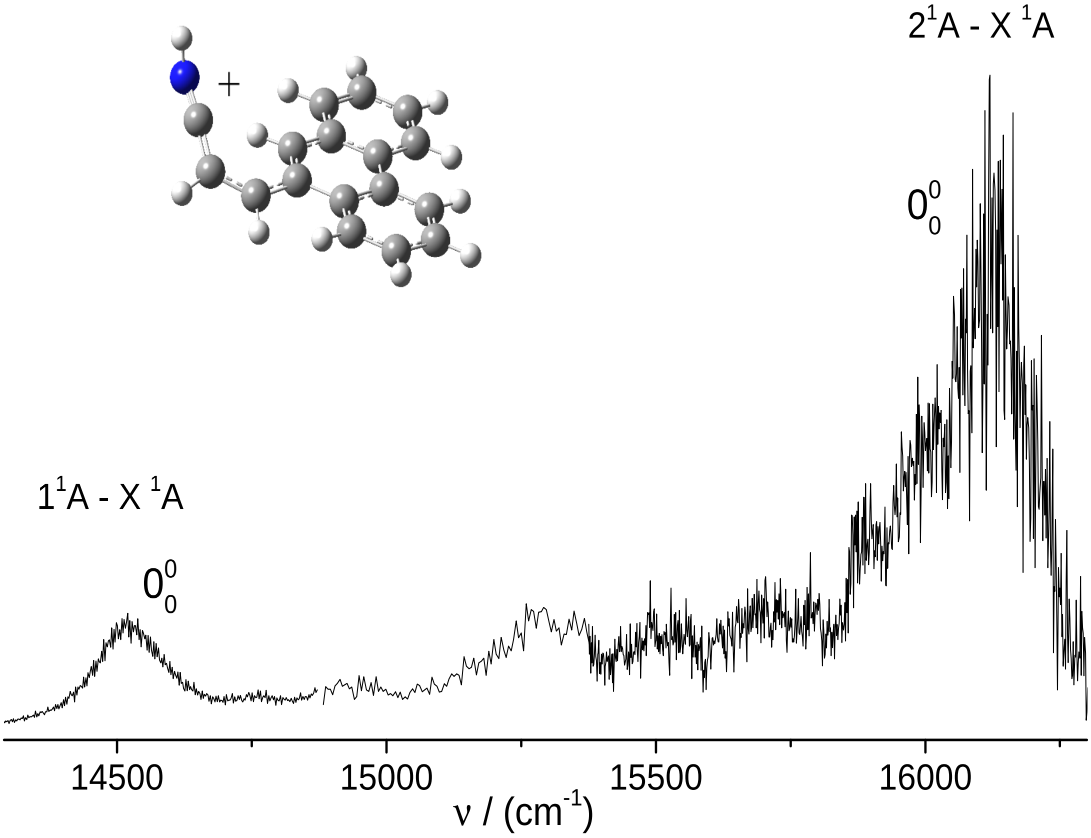

Fig. 5.12: $1\,^1$A ← X ^{1}A and $2\,^1$A ← X ^{1}A electronic transitions of $C_{17}H_{12}N^+$ measured with a 0.07 cm^{-1} bandwidth laser.

blueshifted by ∼ 1600 cm^{-1} relative to the 0^0_0 band of the $1\,^1A' \leftarrow X\,^1A'$ electronic transition. This feature has a larger FWHM of 307 cm^{-1} compared to the one observed at 14 519 cm^{-1} and is assigned to the origin of the $2\,^1A' \leftarrow X\,^1A'$ transition. It is most probable that the $1\,^1A'$ excited state vibrations also absorb in this region of the visible, causing a wider, structureless feature to be observed. From the FWHM of the 0^0_0 band, a $2\,^1A'$ excited state lifetime of 17 fs is extracted.

$3\,^1A' \leftarrow X\,^1A'$ electronic transition. The $3\,^1A' \leftarrow X\,^1A'$ electronic transition of $C_{17}H_{12}N^+$ is observed in the optical in the 23 500 – 24 600 cm^{-1} region, having an origin at 23 586 ± 1 cm^{-1}. The 0^0_0 band has a FWHM of 7 cm^{-1}, corresponding to an excited state lifetime of ∼ 750 fs.

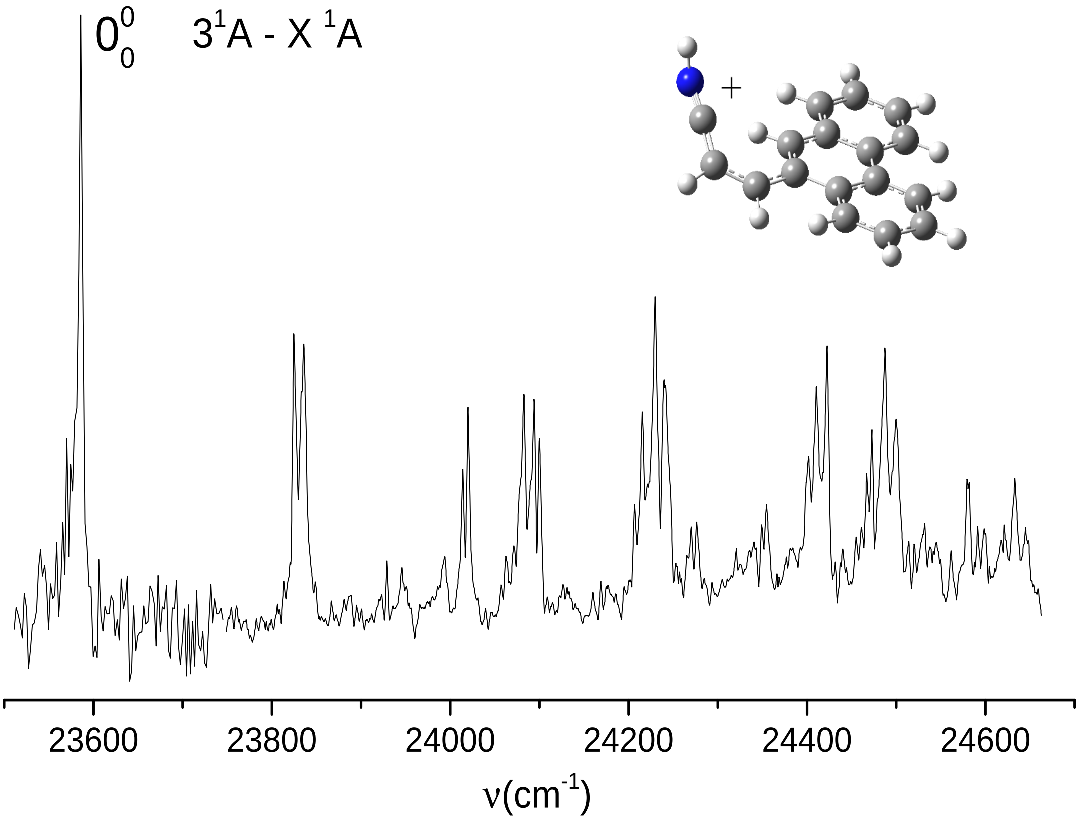

Fig. 5.13: $3\,^1\mathrm{A} \leftarrow \mathrm{X}\,^1\mathrm{A}$ electronic transition of $C_{17}H_{12}N^+$. Vibrational bands within the $3\,^1\mathrm{A}$ excited state are listed in Table 5.6.

Tab. 5.5: Vertical excitation energies SAC-CI/cc-pVDZ and B3LYP compared to experimental values. Results in gray were performed on protonated azatriphenylene (Figure 5.11 a), which was thought at the start to be the carrier of the absorptions. Protonated azatriphenylene does not match the experimental results, however, cyanoethyl-substituted phenanthrene does.

	SAC-CI*		SAC-CI	B3LYP		Exp.
transition	E/eV	f	E/eV	E/eV	f	E/eV
(1) $^1A' \leftarrow X\,^1A'$	3.14	0.04	1.81	1.92	0.02	1.80
(2) $^1A' \leftarrow X\,^1A'$	3.33	0.17	1.89	2.21	0.13	2.00
(3) $^1A' \leftarrow X\,^1A'$	4.12	0.14	3.20	3.17	0.25	2.92
(4) $^1A' \leftarrow X\,^1A'$	4.28	0.10	4.46	3.54	0.06	
(5) $^1A' \leftarrow X\,^1A'$	4.64	0.19	4.58	3.83	0.01	

Tab. 5.6: Band maxima of the $3\,^1A' \leftarrow X\,^1A'$ transition of $C_{17}H_{12}N^+$.

	$\tilde{\nu}/\mathrm{cm}^{-1}$	$\Delta\tilde{\nu}/\mathrm{cm}^{-1}$	assignment
	14 519	0	0^0_0 $1\,^1A' \leftarrow X\,^1A'$
	15 292	773	
	15 509	990	
	15 721	1202	
	16 120	0	0^0_0 $2\,^1A' \leftarrow X\,^1A'$
	23 586	0	0^0_0 $3\,^1A' \leftarrow X\,^1A'$
a	23 825	239	ν_{61}
b	23 836	250	ν_{60}
c	24 014	428	ν_{59}
d	24 020	434	ν_{58}
e	24 083	497	ν_{57}
f	24 094	508	
g	24 100	514	
h	24 207	621	
i	24 215	629	ν_{55}
j	24 230	644	ν_{54}
k	24 240	654	ν_{53}
l	24 402	816	ν_{51}
m	24 411	825	ν_{50}
n	24 422	836	
o	24 467	881	
p	24 473	887	
q	24 487	901	
r	24 500	914	

5.9 Discussion

Upper limit of the column density. All spectra with sufficiently narrow bands were compared to both astronomical spectra toward HD 183143 and HD 204827. None of them showed a match with any DIB and an upper limit of the column density can be estimated. In the case of optically thin media:

$$N(cm^{-2}) = 1.13 \times 10^{20} \frac{EW(A)}{f \,.\, \lambda(A)^2} \tag{5.1}$$

Table 5.7 summarizes the estimations, assuming 5 mA equivalent width (EW) as a minimum for a detectable DIB toward HD 183143 and HD 204827.

Tab. 5.7: Upper limits of the column densities for the five H$^+$PAHs studied. f values were computed along with the matrix spectra that allowed the gas-phase study. For each transition, the origin band was taken, and its share of the f value was estimated from the spectrum.

Molecule	transition used	f value	0^0_0	Col. density (cm^{-2})
H-Pyr$^+$	$1\,^1A' \leftarrow X\,^1A'$	0.18	10%	$\leq 10^{12}$
H-Cor$^+$	$1\,^1A' \leftarrow X\,^1A'$	0.11	10%	$\leq 2.10^{12}$
$C_{17}H_{11}N^+$	$3\,^1A' \leftarrow X\,^1A'$	0.25	5%	$\leq 10^{12}$
H-Cora$^+$	$4\,^1A \leftarrow X\,^1A$	0.09	10%	$\leq 2.10^{12}$
H-Fluo$^+$	$3\,^1A' \leftarrow X\,^1A'$	0.20	25%	$\leq 4.10^{11}$

Astronomical relevance of H$^+$PAHs. These results show that medium-sized H$^+$PAHs, and likely as well medium-sized hetero-H$^+$PAH, are not major constituents of the diffuse ISM. The spectra obtained for $C_{17}H_{11}N^+$ are less relevant for astronomy because of the structure inferred by the calculations. However, the opening of the azatriphenylene structure upon protonation rules out the isomers were the N is replacing one of the outer C. Even if protonation does not occur in diffuse clouds for medium-sized PAHs, the strong UV flux will likely have an even worse effect. However, this does not extend to the more stable isomers with N located on the central benzene ring. It has been shown for example that N-substitution of PAHs gives consistent results for reproducing the UIBs,[118,119] and N heterocycles have been identified in meteorites.[120] Then, in the case of diffuse clouds, if the molecule contains 60 or more C, N-substitution seems a very reasonable option. Nevertheless, in the case of the present work, if medium-sized H^+PAH are ruled out, medium-sized H^+NPAH can also safely be ruled out.

Larger protonated species, such as hexabenzocoronene and ovalene, were considered since the method was working well. An ESI source was borrowed and their production was attempted, without success. No stable or reproducible ion beam from the ESI source could be introduced in the 6-pole and guided through the machine. After several modifications, such as testing other skimmers (100 and 200 μm), needles and capillaries, the project was casted-off. From this point onward, we targeted the PD of He complexes for the study of species that do not fragment easily, such as medium-sized PAHs$^+$ or fullerenes$^+$.

6. THE ELECTRONIC SPECTRUM OF H^+COR AS AN EXPERIMENTAL PLAYGROUND.

Although only the two or three most relevant spectra have presented in the publications on H^+Py and H^+Cor, a large number of them have been obtained along the project. These two molecules were the first ones to be studied, and the influence of many parameters on the electronic spectra was tentatively assessed to have better control over the apparatus. Among the amount of data accumulated, some are of interest and are presented here.

For the purpose of comparing the spectrum of a molecule to astronomical data, a spectrum at a rotational temperature of $\approx 20\,\mathrm{K}$ is satisfying. However, electronic spectra of molecules in the gas phase are often recorded at temperatures as low as possible, as it is the case in this thesis, close to 10 K. The reason for this has nothing to do with astronomy but with spectroscopy. The effect of increasing the temperature of a molecule is to populate more vibrational and rotational levels in the electronic ground state. By greatly increasing the number of possible transitions, the effect of higher temperatures on the electronic spectrum is to congest it and broaden the bands, as shown by blue and magenta traces in Figure 6.1. The colder the molecule, the easiest it is to assign the few bands that it will be made of. In Figure 6.1, the hot bands (HBs) present in the red spectrum obtain at 20 K could be confused with a vibrational mode in the excited state. Then, it is important for the reliability of the assignment of the vibrations to obtain spectra of ions as cold as possible.

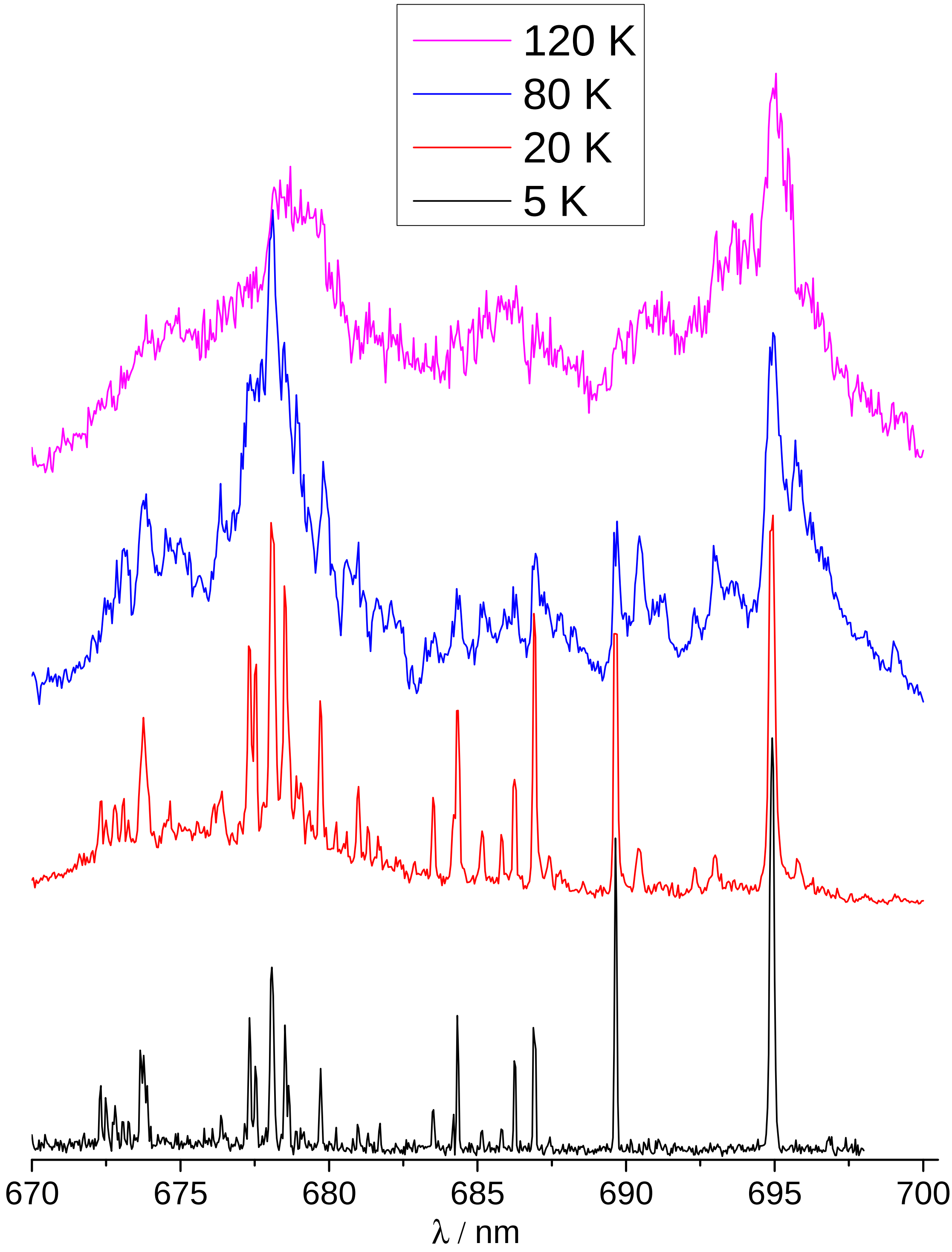

Fig. 6.1: Electronic spectra of H$^+$Cor recorded with trap temperatures of 5, 20, 80, and 120 K. The power on the trap heater was varied while keeping the cryostat on, and an equilibrium could be reached. The disappearance of any HBs in the black spectrum, which makes easier the assignment of the vibrational bands, shows the importance of obtaining spectra as cold as possible.

6.1 Collision-induced heating

The spectra of the H^+PAHs obtained during the first two years of this thesis consistently contained undesired HBs. Undesired, not only from the spectroscopic point of view mentioned above but also from the experimental point of view showing that the cooling of the molecules was not proper. At a temperature of $\approx 10\,\mathrm{K}$, no vibrational state should be populated. First, the length of the trapping period was invoked to explain the phenomenon, and longer trapping periods would cool molecules of this size. However, it became apparent with the time that molecules of this size can be cool very fast, and that HBs had nothing to do with the length of the trapping period. Figure 6.2 shows the spectra of H^+Cor recorded with different "filling + trapping" (F+T) periods. For the various timings, no difference is seen, and multiplying F+T by 100 does not seem to cool any further the ions. Besides this, the black trace in Figure 6.2 shows that ions, virtually just passing by the trap, can be cooled already decently.

Collision induced heating. The reason why the timings seem made no difference in Figure 6.2 was because the ions were probed "on their way out" of the trap, and not inside the trap. The reason for this was given in Chapter 4. The low ion density in the center of the 22-pole trap forced us to trigger the laser when the ions were passing through the exit electrode. A side effect was that the ions had time to collide with the rest gas before being probed by the laser. Hence, care should be taken not to probe the ions too late on their way out, not to give them time to collide with the rest gas. In Figure 6.3 presented three spectra for which only the timing of the laser trigger was varied. When the laser is triggered too late, ions are already out of the trap, subjected to room temperature rest gas. With a precise adjustment of the timing (ions released $\approx 100\,\mu\mathrm{s}$ before that the laser is triggered), which depends on the trapping voltages, the ions are concentrated toward the axis, but not yet out of the trap. In conclusion, the spectra in Figure 6.2 are from ions which were cooled properly but later heat up out of the trap just before being probed. The problem had nothing to do with the cooling efficiency. Moreover, ions of this size can be cooled in a couple of ms with a reasonable He density of $\approx 4.10^{15}\mathrm{cm}^{-3}$.

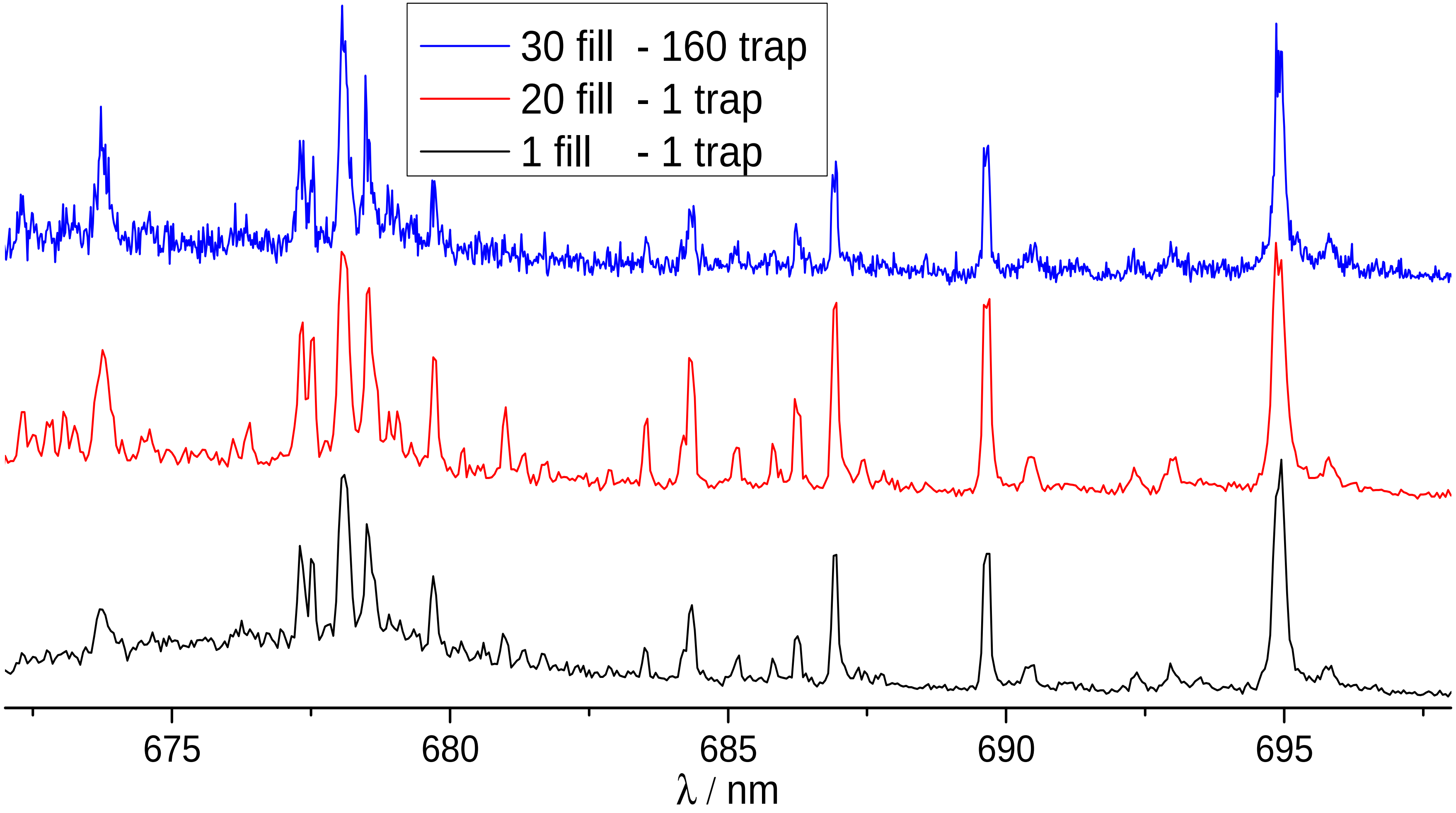

Fig. 6.2: Electronic spectra of H$^+$Cor recorded with "filling + trapping" time (F+T) indicated in ms. Contrarily to what was expected, the spectra always contained HBs, regardless of the timing.

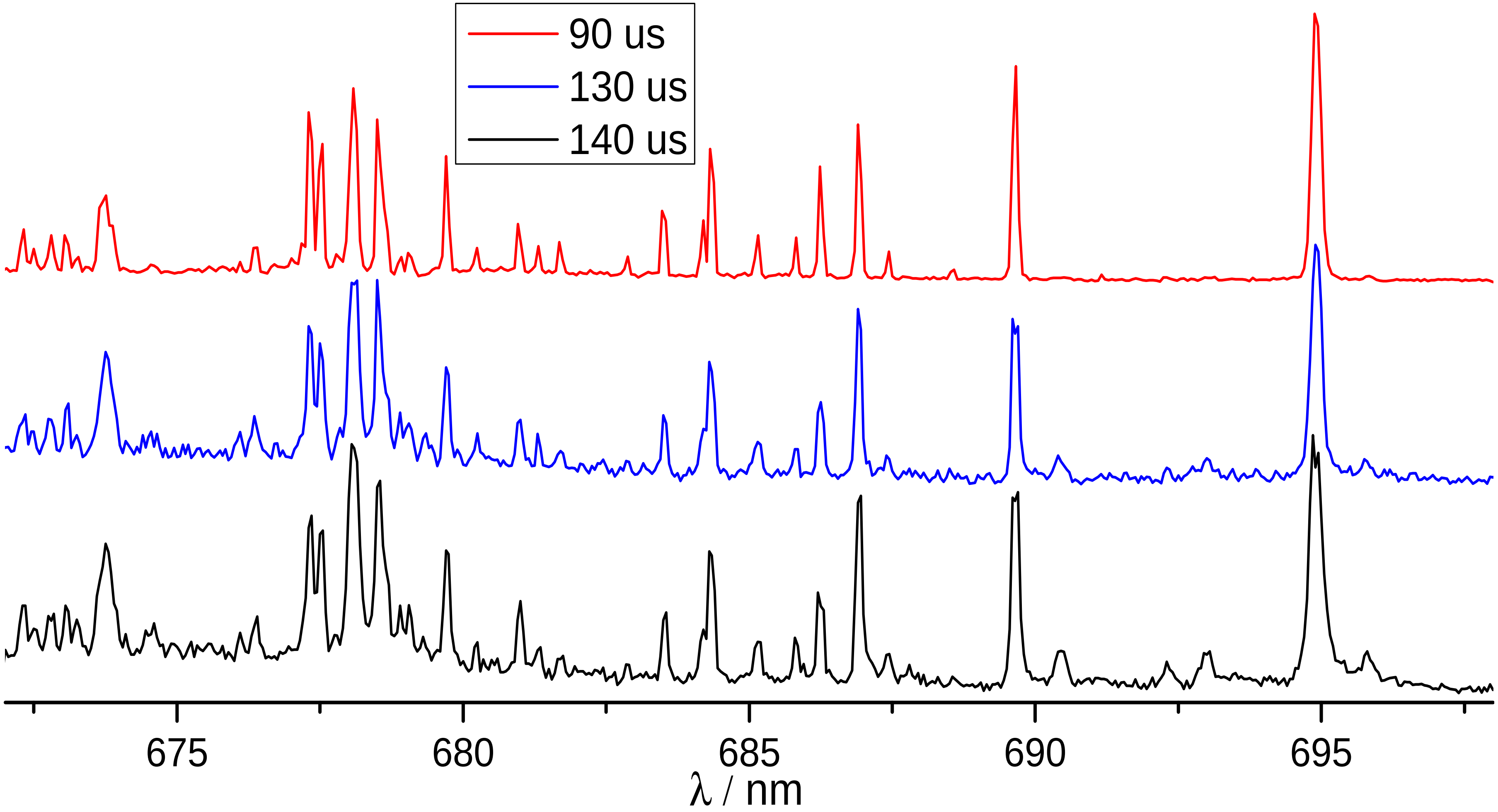

Fig. 6.3: Electronic spectra of H$^+$Cor recorded with only varying the laser trigger timing, in reference to the lowering of the voltage of the exit electrode. Put simply, the ions need around 100μs to leave the trap; if they are given more they will collide with the rest gas, unless a long pump-out period is set.

6.2 Isotopic substitutions

D^+Cor for an easier mass selection. One difficulty in obtaining the electronic spectrum of the protonated form of large molecules is to resolve the two mass peaks separated by only one amu. Only the protonated form should go in the trap to have the advantage of a background-free experiment. In chapter 9, it has been shown to be a real issue with H^+C_{60}. Most of the signal was cut away when applying a good mass selection between 720 and 721 amu. One way around this problem is the use of deuterium. The mass selection issue is still not negligible, but much less serious than before. The first electronic transition of D^+Cor was recorded to observe the effect of the deuteration and is shown in Figure 6.4. The two main effects are a shift of the spectrum by ≈ 0.8 nm to the red, and a large increase in the number of vibrational bands. As much as this spectrum can be a rich source of information on the molecular level, it has, from the astronomical point of view, a debatable importance. That is, the cosmic D/H ratio ($\approx 2.5\times10^{-5121}$) is very low, however, D seems to accumulate in some interstellar environments due to some widespread but subtle processes working more efficiently with one of the isotopes. For this reason, it is not known to which extent D substituted species must be considered.

$H^+C^{13}_xC_{24-x}H_{12}$ electronic spectra and their astronomical implications. The bigger a carbon-based molecule, the most likely it will contain one or more C^{13}. This is as much inevitable in the lab as it is the ISM, and one should mind this isotopic substitution when recording spectra of large PAHs and fullerenes. The ratio C^{12}/C^{13} is 0.011 and a significant proportion of molecules containing several dozens of carbon atoms will have at least one isotopic substitution. For the case of the DIBs, this means that the influence of this substitution on the electronic spectra should be carefully considered. Isotopic substitution of C is supposed to bring only very small changes on the electronic structure of H^+Cor since it does not break the C_s symmetry. This contrasts with the D substitution. Although the variations should be imperceptible, the spectra will represent a superposition of all configurations of C substitutions within the molecule. In Figure 6.5 are presented four spectra of $H^+C^{13}_xC_{24-x}H_{12}$, with $x = 0, 1, 2, 3$. All spectra are recorded by monitoring an H-loss. The substitution does not modify the general aspect of the spectrum. However, as shown in Figure 6.6, which is a zoom-in of Figure 6.5 on the origin band, isotopic substitution does slightly shift the spectrum. It has been suggested in the past that isotopic substitution of C-bearing molecules can explain the substructure of some DIB such as λ6614.[122] A later model has shown that a superposition of peaks following an isotopic distribution reproduces the latter DIB.[123] However, this hypothesis does not explain the variations from sightlines to sightlines of the respective strengths and widths of the subpeaks. On the other hand, rotational contour in molecules with varying temperatures[124,125] explains very well the observations and isotopic shifts were ruled out. Nevertheless, in the laboratory, if the electronic spectrum is recorded from a specific mass, e.g. 301 amu for H^+Cor, it will inevitably yield narrower and shifted bands compared to astronomical data which represent the true, whole isotopic distribution of the molecule. This fact should be considered when comparing laboratory and astronomical spectra of sufficiently large molecules.

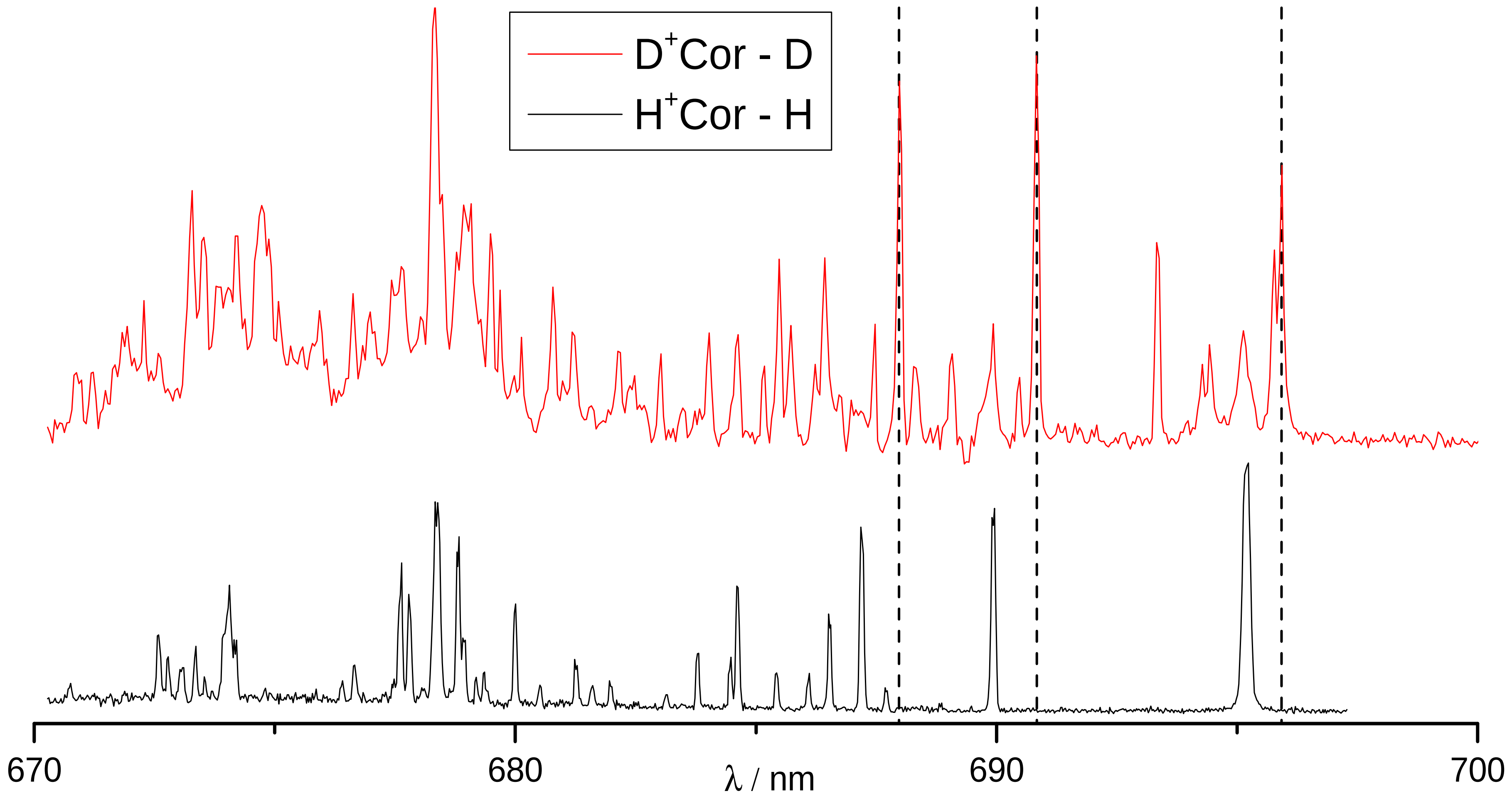

Fig. 6.4: (1) ^{1}A′ ← X ^{1}A′ transition of H$^+$Cor, in black, compared to its D substituted counterpart. The spectra were recorded by monitoring H-loss and D-loss. A red shift is apparent and many more vibrational bands due to the loss of the planar symmetry in D$^+$Cor.

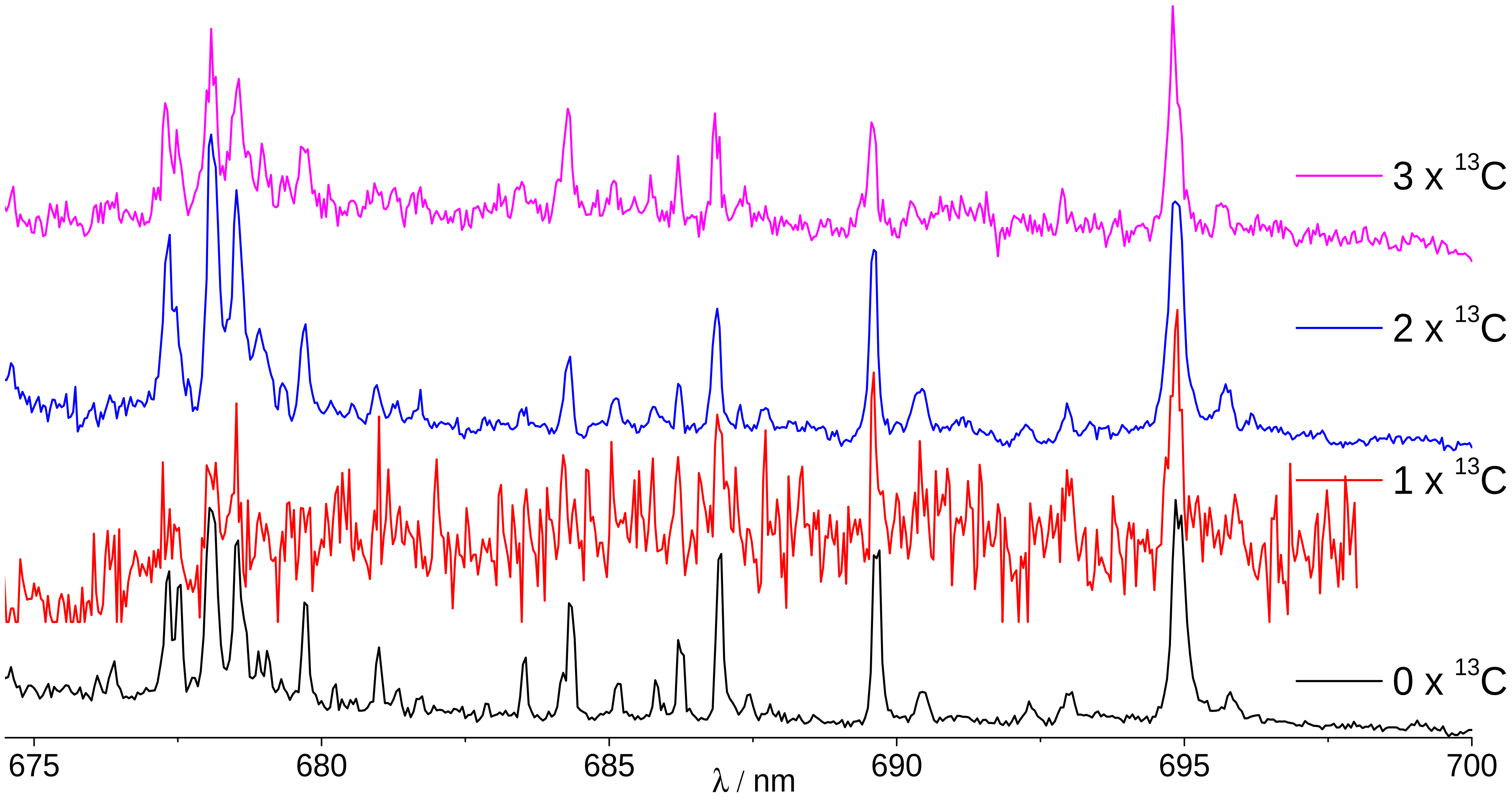

Fig. 6.5: Spectra of $H^{+}C^{13}_{x}C_{24-x}H_{12}$, with x = 0, 1, 2, 3. In contrast to the substitution of H on the protonation site, the substitution of one or more carbon atoms does not change the electronic spectrum at first sight.

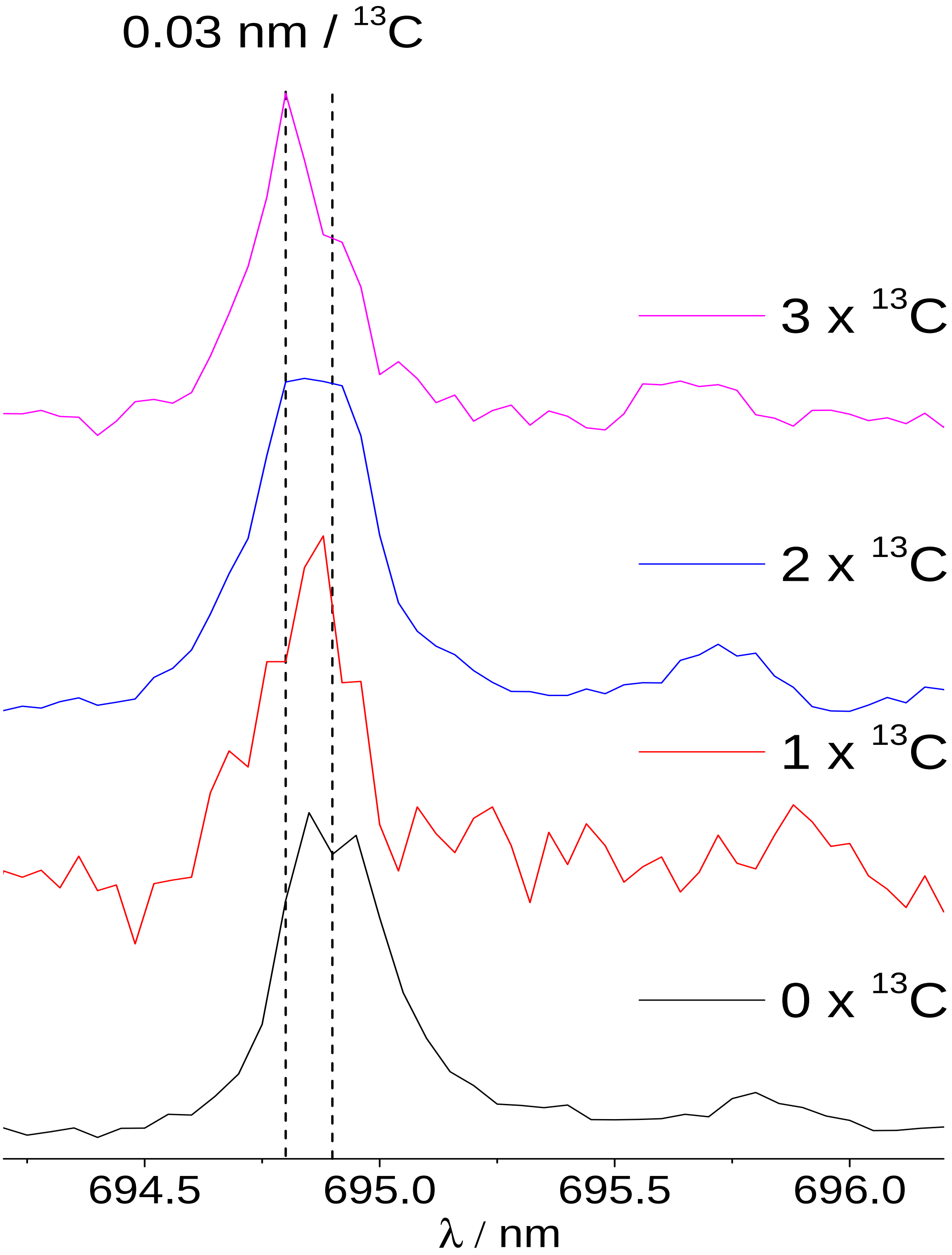

Fig. 6.6: A detailed view on the origin band of the spectra of $H^+C^{13}_xC_{24-x}H_{12}$, with x = 0, 1, 2, 3. The isotopic shift is now visible and increases with the number of substituted C atoms. The shift is ≈ 0.03 nm per C substitution for the origin band, and ≈ 0.04 nm for the HB on the right.

7. CORONENE$^+$ AND CORANNULENE$^+$ (COR$^+$ AND CORA$^+$)

Following the exchange of the 22-pole trap to a 4-pole trap, the gas-phase electronic spectra of He-Cor$^+$, He-Cora$^+$, and 2He-Cora$^+$ complexes have been recorded by monitoring their photodissociation. He-Cor$^+$ spectrum displays two strong features, belonging to the $D_1 \leftarrow D_0$ and $D_9 \leftarrow D_0$ electronic transitions, at 9 436 and 4 570 Å, respectively. Cora$^+$ has two Jahn-Teller structures in its electronic ground state, leading to the $(3)\,^2A' \leftarrow X\,^2A''$ and $(3)\,^2A'' \leftarrow X\,^2A'$ transitions, with origin bands at 5 996.15 Å and 5 882.65 Å, respectively, in a region where many diffuse interstellar bands (DIBs) lie. Also, the spectrum of 2He-Cora$^+$ was recorded to estimate the perturbation brought by the He.

7.1 Long-standing DIB candidates

Since the diffuse interstellar bands (DIBs) are attributed to interstellar gas-phase molecules, polycyclic aromatic hydrocarbons (PAHs) have been among the major candidates.[31, 93, 126] Some reasons include the tendency of carbon to form large molecules such as PAHs, the cosmic abundance of carbon, and the stability of PAHs regarding UV photodissociation. Also, the unidentified infrared emission bands, generally assigned to vibrational de-excitation of aromatic and aliphatic compounds,[33, 96, 127] show that PAHs$^+$ could be widespread in interstellar media.

For the identification of a specific molecule as a DIB carrier, its electronic absorption spectrum is usually obtained in a rare gas matrix, and subsequently, in the gas phase at cold temperatures. For this purpose, over the last decades, such spectra have been recorded for dozens of carbon chains and rings in the gas phase, mostly neutral and cationic, without any match with the DIBs.[128] A number of medium-sized neutral PAHs have also been studied in supersonic expansions, finding no match with DIBs.[95, 129, 130] Large PAHs$^+$, have only been studied in rare gas matrices[131] and remain a challenge for gas-phase laboratory measurements.[132, 133] Gas-phase electronic spectra are generally recorded by monitoring the photofragmentation of the molecule as a function of the wavelength. However, a molecule is a good candidate carrier of the DIBs, if it is photo-resistant to the UV-Vis flux of the interstellar medium, making the laboratory detection via photofragmentation as inefficient as the molecule is a good candidate. For this reason, no gas-phase electronic spectrum could be recorded so far for large or even medium-sized PAH$^+$.[132] H$^+$PAHs were also proposed as candidates, but have been ruled out by models and experiments.

A method to obtain the electronic spectrum of larger molecules consists in attaching a rare gas atom to the cold molecule and monitoring the photodissociation of the complex.[134] A number of electronic spectra were obtained using Ar as a tag atom, but the shift and broadening of the absorption bands, induced by Ar, are too large to make a reliable comparison with astronomical spectra. In this regard, the attachment of a He atom brings significantly less disruption.[135,136] These complexes have binding energies from hundreds cm^{-1} with He to thousands cm^{-1} with Ar. The efficient production of He complexes requires the use of an ion trap to increase the interaction time with the buffer gas.[137,138]

Cor ($C_{24}H_{12}$) and Cora ($C_{20}H_{10}$) are two major members of the PAH family. Cor is a typical highly symmetric PAH (D_{6h}), while Cora (C_{5v}), presents some unique properties in terms of astronomical detection. Cora has a high symmetry and a dipole moment of 2.1 D.[139] Structurally, Cora is the smallest PAH having a curved shape, given by its central five-membered ring, relating it to C_{60}. Recently, laboratory spectra[140] confirmed that gas-phase C_{60}^+ is a DIB carrier, making Cora$^+$ of special interest.

7.2 Experiemental

Ions were created in the EI source from a solid Cor or Cora sample heated to ~150 °C. Ions from the source are then mass selected and guided to the trap. Efficient production of He complexes is best achieved in an ion trap,[137,138] as compared to supersonic expansions. However, the 22-pole trap is not suitable for such an experiment as shown in Chapter 3 with $C_4O_2^+$. That is, since the PD of complexes is not background-free, a good SNR requires a 4-pole trap. The wire 4-pole trap[85] that was used is described in chapter 3. Figure 7.1 shows two mass spectra recorded with and without laser radiation at 5 996.15 Å. Most Cora$^+$ are tagged by one or more He, and a significant proportion of He-Cora$^+$ is depleted. It has not been clearly understood why the complexes with one He have always been preferentially depleted. The broadening of the bands due to the successive additions of He atoms may be one reason because it weakens the absorption at a specific wavelength.

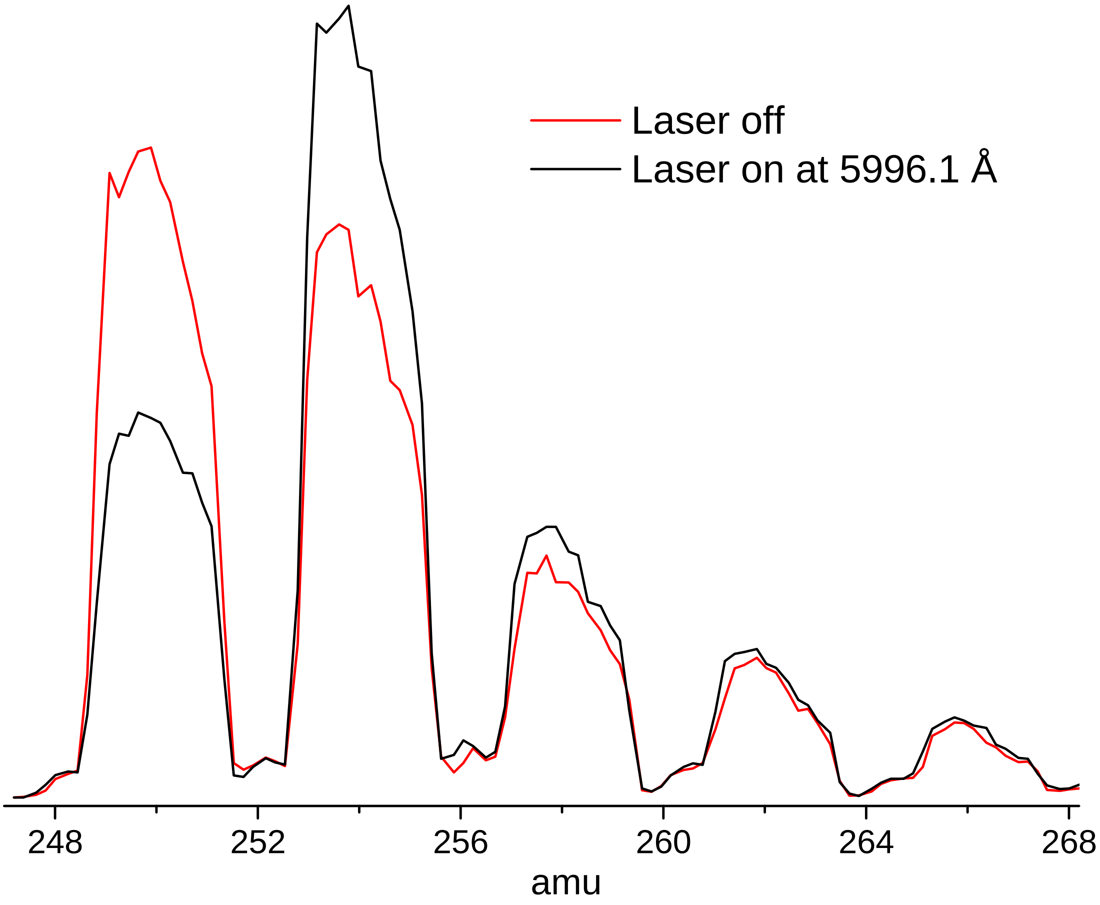

Fig. 7.1: Mass spectra of He$_x$Cora$^+$, x = 0...4. The absorption of 5 996.15 Å photons deplete the complexes.

The sequence was 200 ms for filling the cations into the trap, followed by ~800 ms of cooling, and a few ms to extract the ions. The laser was continuously triggered at 10 Hz, submitting the ions to 8 - 10 shots per trapping cycle, while He-Cor$^+$ or He-Cora$^+$ complexes were continuously produced by interactions with the buffer gas. Toward the end of the 1 s cycle, the buffer gas was pumped out before that the ions were ejected and counted. A piezo-valve introduced helium buffer gas into the trap from the beginning of the filling period, achieving after a few ms a helium density of $\sim 4 \times 10^{15}$ cm^{-3}. The depletion of the complexes is monitored as a function of the laser wavelength to record the electronic spectrum.

7.3 Results

The electronic spectrum of Cor$^+$ in the 4 000 - 10 000 Å region was first recorded as far back as 1992 in a 4 K neon matrix,[141] and showed two sharp absorptions at 4 590 Å and 9 465 Å with respective oscillator strengths of 0.012 and 0.0018. Cor$^+$ was later investigated in an FT-ICR cell,[142] however, the spectrum is broad ($\sim$150 Å) because of the multi-photon dissociation technique heating up the ions during the process. Using the photodissociation of He-Cor$^+$ complexes, we provide a gas-phase electronic spectrum at temperatures below 10 K. The spectra are presented Figure 7.2 (black traces). The spectrum of the $D_9 \leftarrow D_0$ electronic transition consists mainly of one broad feature at 4 575 Å, blue-shifted 0.15 Å compared to the neon matrix. A vibrational band, weaker, is visible at 4 525 Å. There is almost no difference in width between the matrix and the gas-phase spectra ($\sim$20 Å), indicating an excited state lifetime of $\sim$50 fs. The $D_1 \leftarrow D_0$ transition consists of one band at 9 436 Å, blue-shifted 29 Å to the neon matrix. It has a width $\sim$5 Å, likely due to the laser bandwidth, indicating an excited state lifetime $\geq$0.2 ps. The red trace on the left panel of Figure 7.2 was recorded by monitoring the depletion of the complexes, and the black trace was recorded by monitoring the parent ions, Cor$^+$. The two features at 9 436 Å and 4 575 Å do not match with any DIB in the lines of sight of HD 183143 and HD 204827,[143, 144] confirming that Cor$^+$ is not a carrier.

The electronic spectrum of Cora$^+$ in the 6 000 Å region was recently recorded in a 6 K neon matrix, after mass selected deposition.[145] The gas-phase electronic spectrum, recorded by monitoring the photodissociation of their complexes with He, is presented Figure 7.4. Cora$^+$ has two Jahn-Teller structures in its electronic ground state leading to the two origin bands and vibrational progressions. The spectrum is similar to the one recorded in the neon matrix, from which the two origin bands, at 5 996.15 and 5 882.65 Å, are blue-shifted by 16 Å. The weakness of the complex bonding, the predicted 0.2 oscillator strength, and the use of a 4-pole trap, allows a strong depletion, and a good SNR was achieved.

To estimate the influence of He on Cora$^+$, the spectrum with 2 He attached was also recorded with a resolution of 0.05 Å (Figure 7.3). For the origin band at 5 882.65 Å the full width at half maximum (FWHM) increases from 0.45 to 0.7 Å with no significant shift. For the origin band at 5 996.15 Å the FWHM increases from 0.5 to 0.55 Å with a red shift of 0.1 Å. We can expect the positions of the

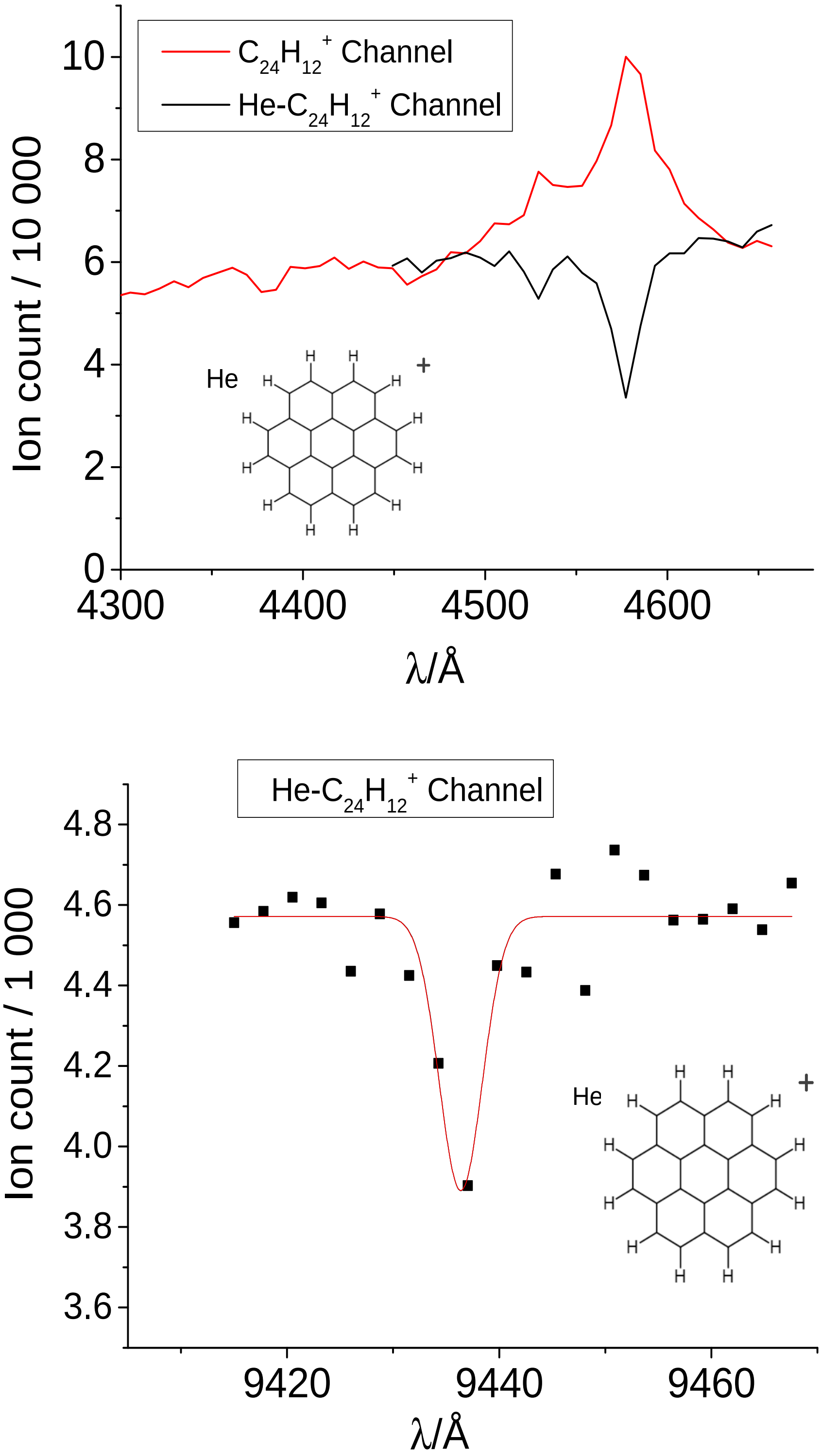

Fig. 7.2: Gas-phase electronic spectra of He-Cor$^+$ recorded with a laser of 1 Å bandwidth in the visible, and 10 Å bandwidth in the infrared. On the left panel, the absorptions induced ∼ 50% depletion of the He-Cor$^+$ (black traces). Red trace was recorded by monitoring the mass-channel of the bare ion, $C_{24}H_{12}{}^+$. On the right panel, a single-peak Gaussian fit is overlayed to the spectrum.

origin bands of the bare Cora$^+$ to be ~0.1 Å to the blue, and ~0.1 - 0.2 Å narrower compared to the measurements with one He attached. These results are sufficient for a comparison to astronomical data. The band A is similar in position and width to the around 5 995.9 Å (DIB 104[144]). However, a comparison of band B and other less intense bands to the astronomical spectra shows that this is merely a coincidence. Thus, Cora$^+$ is not a carrier of the DIBs.

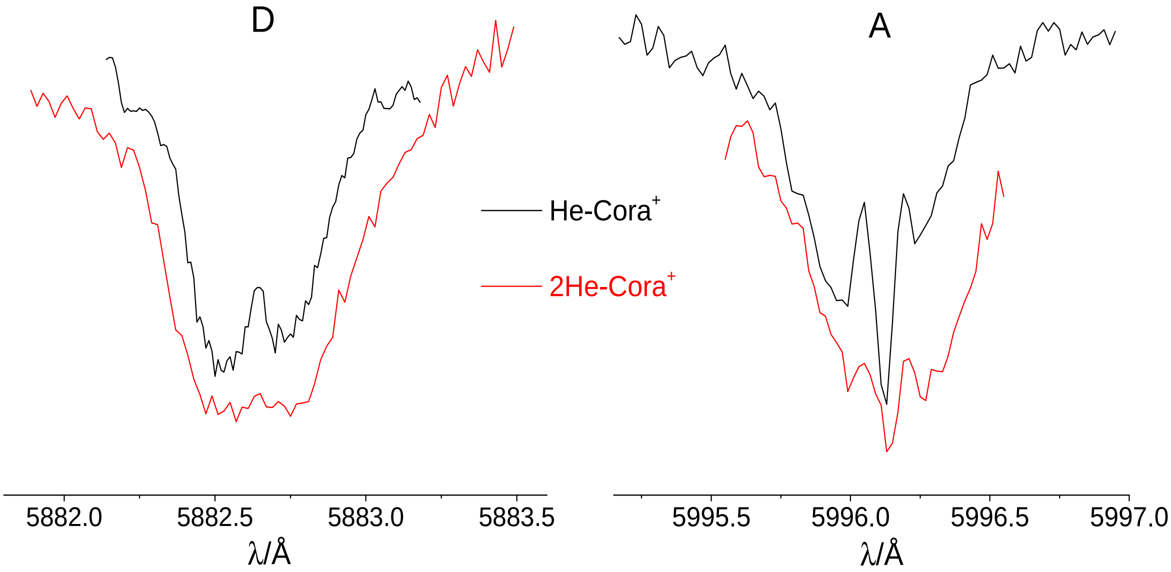

Fig. 7.3: The bands A and D of Figure 7.4, recorded with a laser power of 50 μJ / pulse and a resolution of 0.01 Å (black traces). Red traces were recorded with two He attached on Cora$^+$.

The power dependence of the contour of the band "C" have been recorded with a laser power as low as the experiment allowed. Figure 7.5 shows the spectra measured with laser powers of 400, 100, 50, and 20 μJ/pulse. Because the band seems power-broadened even with 20 μJ/pulse, the inferred FWHM is $\leq$ 0.45 Å and indicates an excited state lifetime $\geq$ 60 ps.

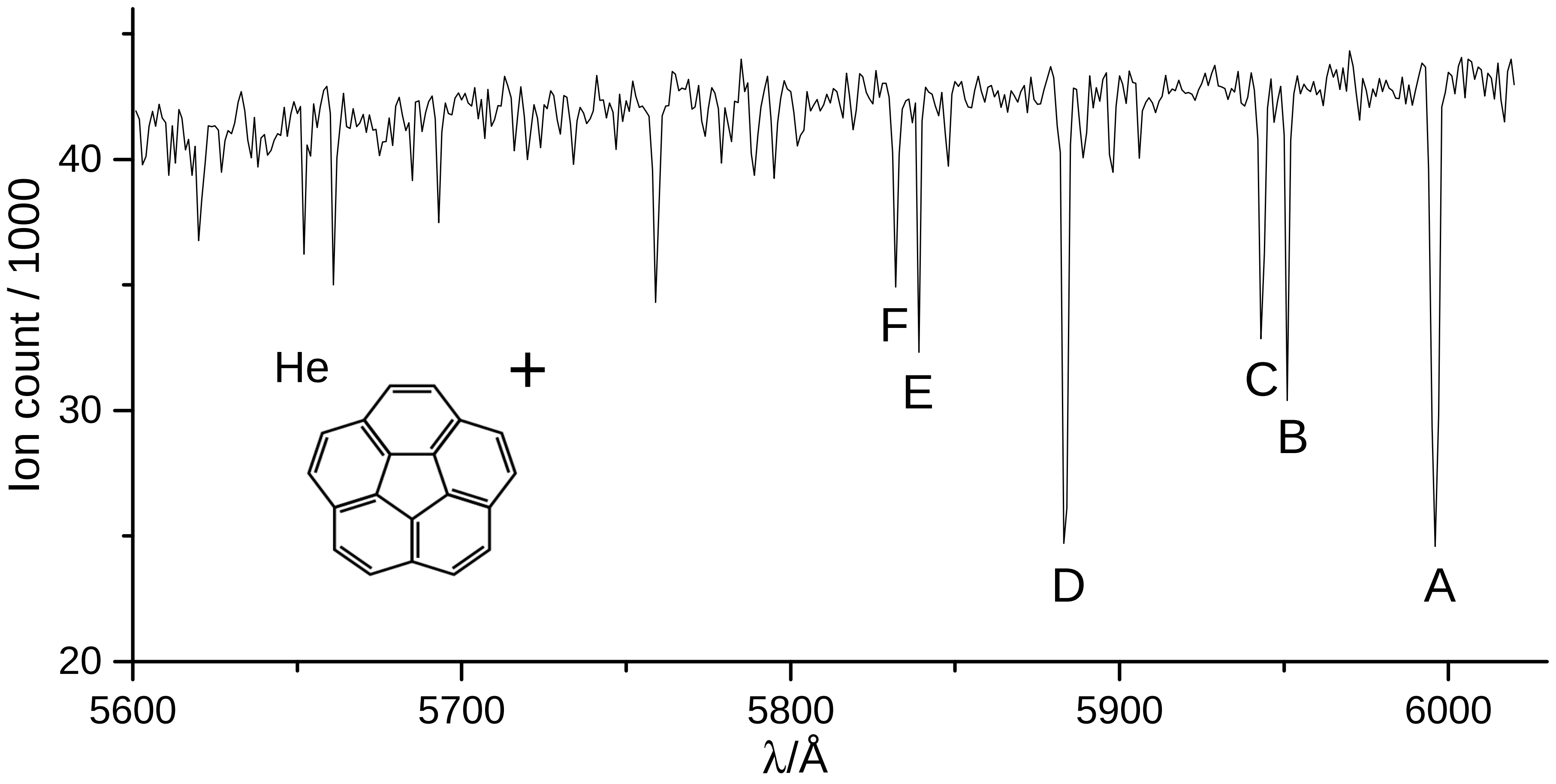

Fig. 7.4: Gas-phase electronic spectrum of He-Cora$^+$ recorded with a laser of 1 Åbandwidth (200 μJ/pulse). The two Jahn-Teller structures in the electronic ground state of Cora$^+$ lead to the $(3)\,^2\mathrm{A}' \leftarrow \mathrm{X}\,^2\mathrm{A}''$ and $(3)\,^2\mathrm{A}'' \leftarrow \mathrm{X}\,^2\mathrm{A}'$ transitions.

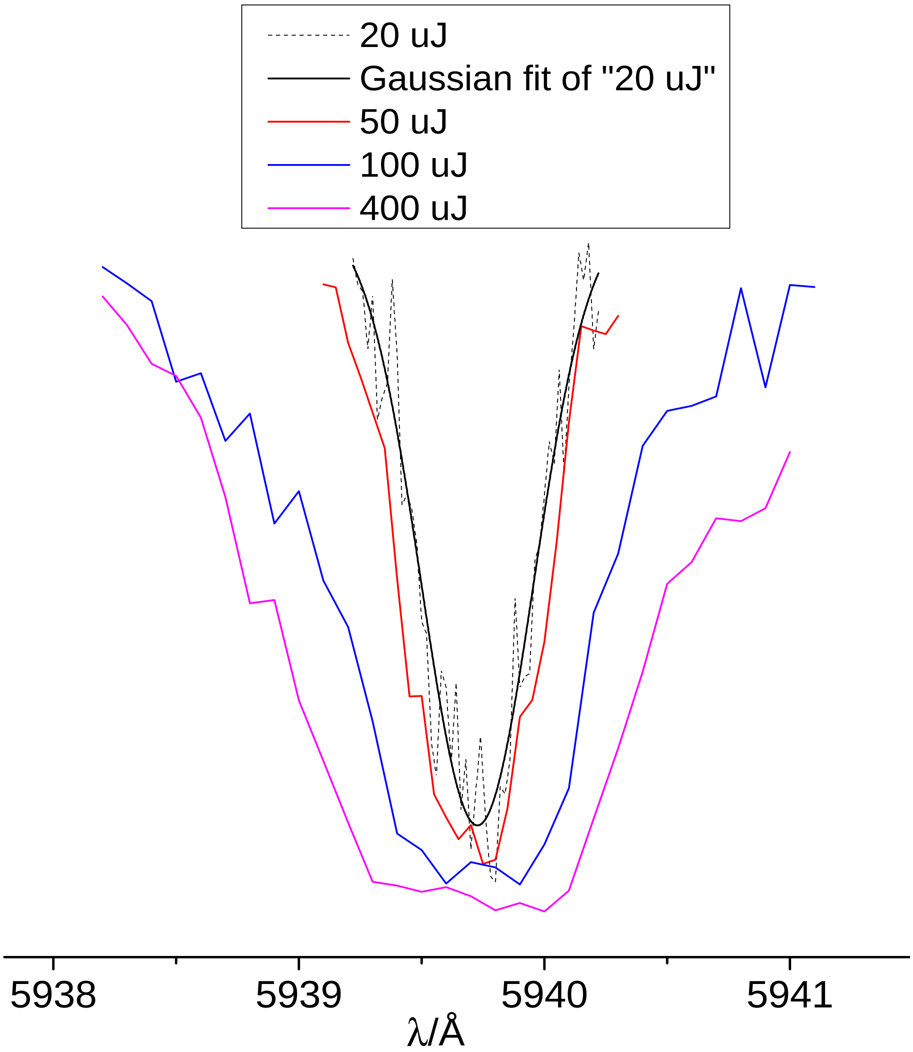

Fig. 7.5: Band "C" from Figure 7.4 recorded with different laser powers.

7.4 Conclusion

The electronic spectra of He-Cor$^+$, He-Cora$^+$ and 2He-Cora$^+$ have been recorded in the gas-phase. Because the technique requires He to bind to the sample ions, the spectra obtained are inherently the ones of cold ions. The method does not provide the genuine spectra of Cor$^+$ and Cora$^+$ but is sufficient for astronomical comparison. For the case of Cora$^+$, the shifts of the origin bands caused by the second He are ≤ 0.1 Å, and the broadenings ≤ 0.25 Å. Comparison to astronomical spectra shows that neither Cor$^+$ nor Cora$^+$ is a carrier of any DIBs. Models predict PAHs$^+$ of this size to be dehydrogenated in diffuse clouds.[102] The method used here can be utilized to obtain the spectra of larger PAHs$^+$, fullerenes$^+$, or dehydrogenated PAHs$^+$.

8. PROTONATED C_{60} (H^+C_{60})

The last project targeted C_{58}^+ and H^+C_{60}. The two cations were investigated through the photodissociation of C_{58}^+ - He and H^+C_{60} - He. No visible absorption was found for C_{58}^+ - He, and no reliable electronic spectrum was obtained for H^+C_{60} - He, nevertheless, since such project will likely be followed in the near future, it is worth mentioning what has been obtained so far. As a note, many other species could be observed in the mass spectra, such as C_{60}^{2+}, C_{60}^{3+}, C_{70}^+, C_{70}^{2+}, C_{56}^+, $(H_2O)_nC_{60}^+$ (n = 1 .. ≈ 20), $N_2C_{60}^+$, $O_2C_{60}^+$. The latter complexes formed because of the presence of rest gas in the trap chamber.

8.1 Introduction

Fullerenes have a unique history in molecular science since they were discovered on Earth thanks to research attempting at finding the composition of the ISM.[146] Later studies made us realize that fullerenes are naturally present in many different environments such as soots on Earth, meteorites,[78] and in the gas phase in the DISM[140,147] and CSEs.[37] Despite a seemingly serendipitous discovery, the original experiment could not perform better since the class of molecules they produced did provide, as of today, the best candidate carriers for many interstellar features. Actually, in three decades, fullerenes and fulleranes have been proposed as possible carriers of virtually all unidentified spectrocopic interstellar features, from anomalous microwave emission, to the UIBs, the ERE, the DIBs (especially the 4 430AA feature[71]), the UV bump, and to the interstellar extinction.[125,148–155] The only obstacle to their assignment in the ISM is the lack of conclusive experimental data. In this regard, electronic spectroscopy of the cold molecules, in the gas phase, stands out from other techniques as it can provide unambiguous assignments. It includes, however, the difficult choice of the relevant species among a large number of possibilities, and the luck related to the rather unpredictable strength of their electronic transitions.

8.2 Challenging production of C_{60}^+ and H^+C_{60}

At the start, no protonation could be obtained in the CI source, despite a proton affinity of C_{60} of 857 kJ.mol^{-1}.[156,157] The reason is not known for sure but is probably because the sample of C_{60} had to be heated to around 550 °C to obtain a sufficient ion signal. In principle, 300 °C should already provide an efficient sublimation, and in previous experiments, strong and stable signal of Pyr$^+$ and Cor$^+$ were obtained with 90 and 160 °C, respectively. The significant internal energy of the C_{60} molecules exiting the oven at 550 °C may have prevented the protonation reaction, despite the relatively high pressure in the CI source ($\approx$0.1 mbar). Several protonation agents were tried, such as toluene, methane, H_2, without success. Additionally, the high temperatures needed to obtain C_{60}^+ caused significant troubles since the source is not built for such temperatures. To obtain a good signal with lower oven temperatures, a new design of the CI source was made, and is presented Figure 8.2.

In the CI source (presented Figure 8.1), the electrons from the filament, entering

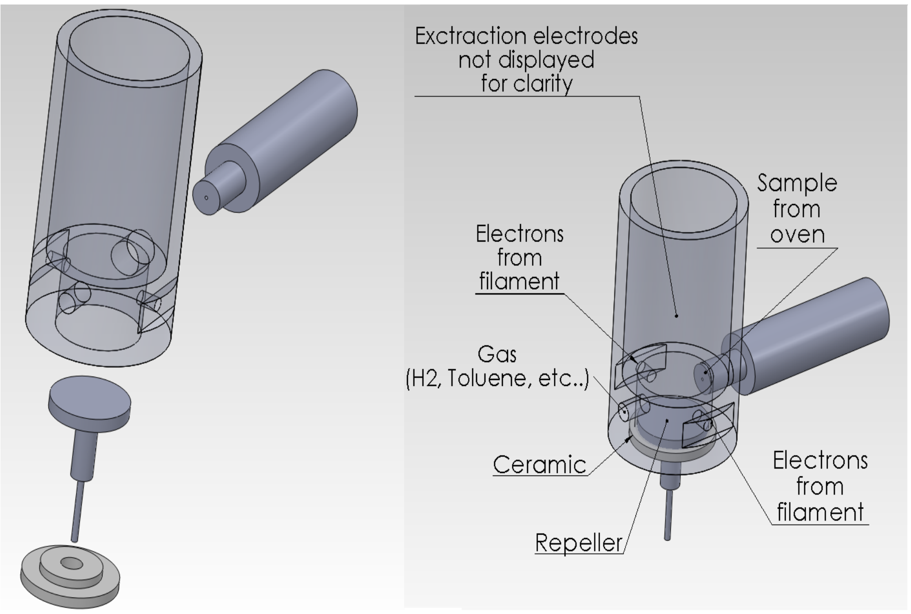

Fig. 8.1: Original design of the CI source reproduced on Solidworks. A workable C_{60}^+ signal could not be obtained unless heating the sample to around 550 °C. Electrons are directed toward the repeller plate, without crossing the zone where the sample density is the highest, at the exit of the oven.

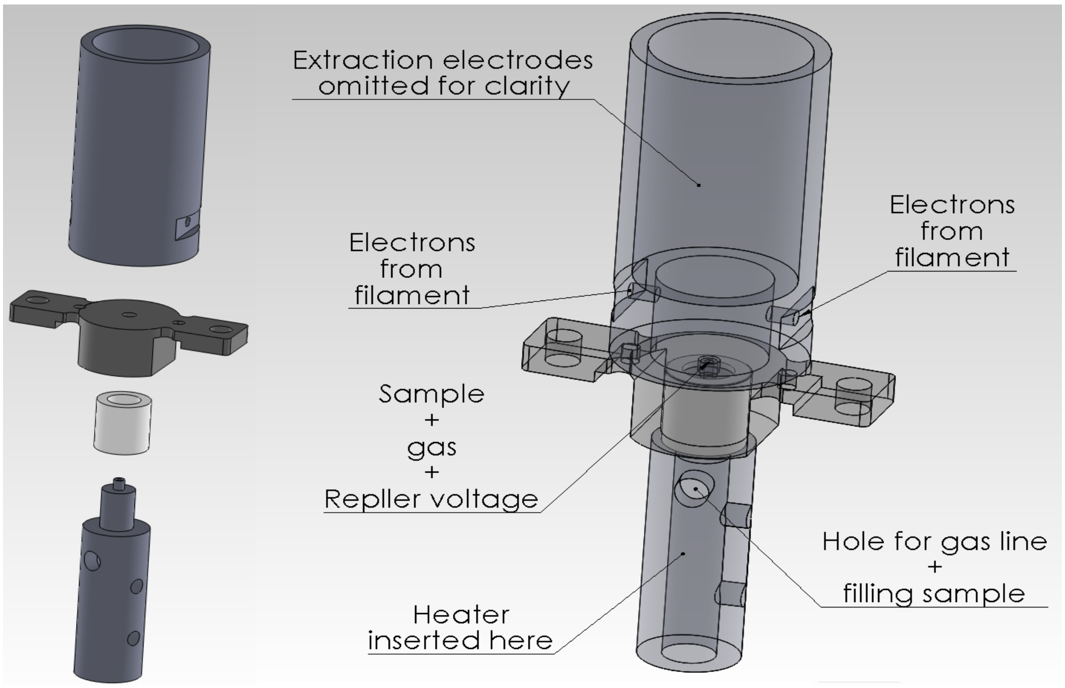

Fig. 8.2: Re-designed CI source to obtain C_{60}^+ with reduced temperatures, and protonation. The electrons are directed toward the sample and the gas. The repeller is no more a plate but a tip with a 1 mm hole. Around this tip, the electrons, the gas, and the sample densities are all much higher than in the previous design.

the reaction chamber, are attracted by the repeller. The purpose of the repeller is to push away the newly formed cations toward the extraction electrodes. However, attracting the electrons is an undesirable side effect since they do not meet efficiently the sample molecules coming out perpendicularly from the oven. If there is no repeller, as in the source bought from Agilent and presented in Chapter 3, the electrons would just fly anywhere in the reaction chamber of the source, or be directed toward some possible patch potentials. In any case they do not interact very efficently with the sample.

In the new design (Figure 8.2), the heated sample molecules and the carrier gas, both come out of the repeller itself. The intention was to direct precisely the electrons toward the sample and the gas. The repeller is not a plate anymore but a tip with a 1 mm hole, from which the vapor comes out. Around this tip, the electrons, the gas, and the sample all meet idensities are all much higher than in the commercial design. The repeller now consists in an oven, with a little container for the sample, and is electrically insulated by a ceramic. This ceramic has the additional advantage of thermally insulating the rest of the source from the oven. This design proved immediately successful. Not only a workable signal of C_{60}^+ could be obtained at only 300 °C, but also the protonation of C_{60}^+ with CH_4 and H_2.

8.3 H^+C_{60}-He around 700 nm

Ever since fullerenes were discovered, fulleranes have been considered as a likely component of the ISM[153, 158, 159] and, in the context of this thesis, as a possible carrier of the DIBs .[158, 160, 161] The reasons for this being the overwhelming presence of H in the ISM and a barrierless reaction of C_{60} with H.[162] However, with an average binding energy of 2.6 eV per H atom in $C_{60}H_{36}$,[162, 163] fulleranes will be efficiently dissociated in the DISM. Accurate rate coefficients and binding energies of H onto $H_n^+C_{60}$ are not known, so that currently, even rough estimates on the fullerane population in the ISM cannot be done.[161, 164]

H^+C_{60} was chosen since it is the first on the list and was the main fullerane produced in the newly modified source. It also has the advantage of having only one isomer. To our knowledge, no spectroscopy of any kind has been performed on singly hydrogenated or protonated C_{60} alone. For this experiment, once H^+C_{60} was readily produced, the main obstacle was the mass selection in the first QMS, which

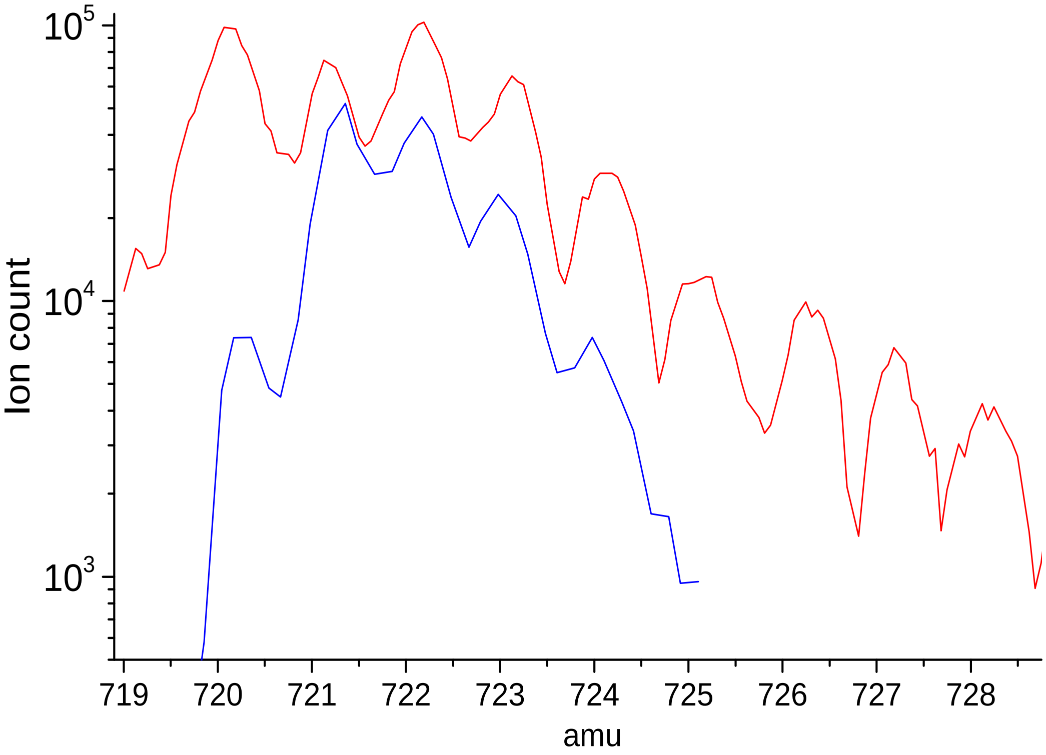

Fig. 8.3: In black, a mass spectrum obtained by heating C_{60} to 300 °C without reagent, showing its normal isotopic distribution. In red, a mass spectrum obtained in the presence of D_2. This mass spectrum shows 50% conversion. In blue, a mass spectrum obtained in the presence of H_2. This mass spectrum shows 90% conversion. For all, the first QMS is in guide mode.

was had to select the peak at 721 amu, among the isotopic distribution of C_{60}. When this mass selection was done properly, the resulting ion count was very low. The pronounced isotopic distribution of C_{60} makes the experiment more difficult than with smaller molecules. To help with the mass selection, deuterium can be used instead, as shown in the mass spectrum Figure 8.3.

The photodissociation of H^+C_{60}-He was recorded around 700 nm and is shown Figure 8.4. This PD is strongly correlated with the dye emission. Nevertheless, it indicates a very broad absorption in this region. Particularly around 705 nm onward, since there the dye emission decreases more that the PD. This observation is consistent with calculations predicting an absorption with onset around 728 nm (indicated by the dashed line on Figure 8.4). Further experiments are on the way, notably on expected near IR transitions expected to be sharper.

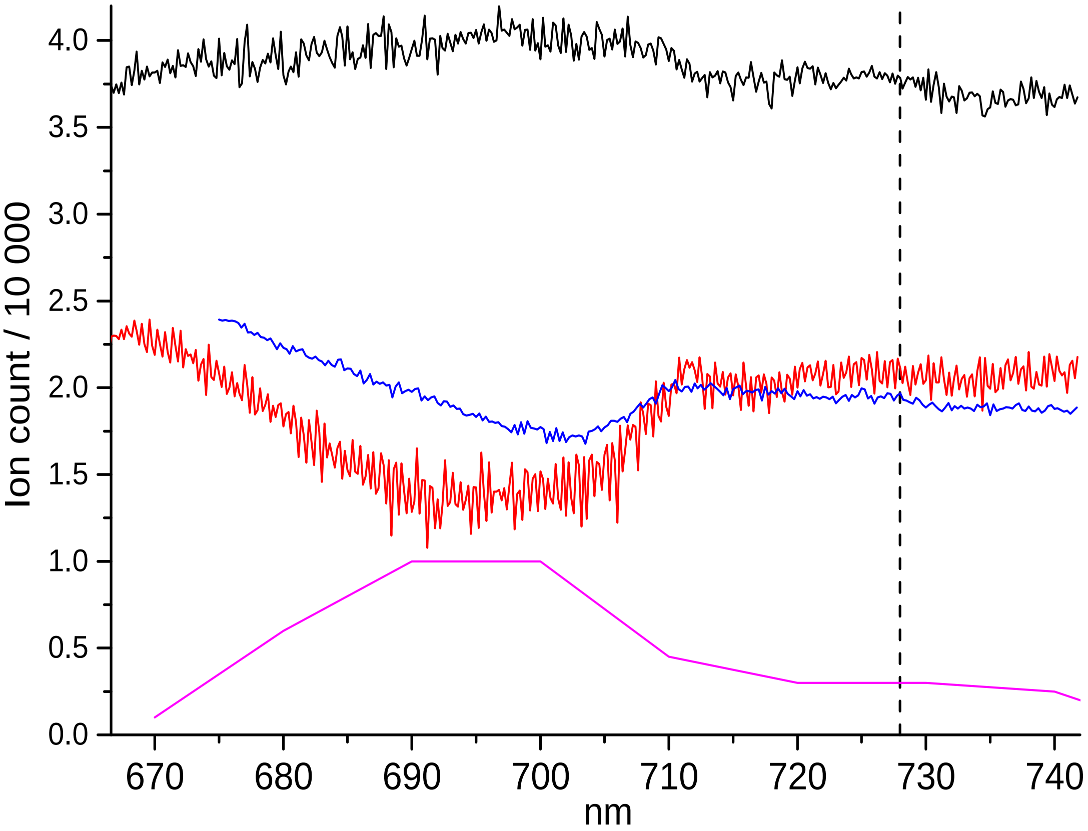

Fig. 8.4: PD of H^+C_{60}-He recorded with a dye laser around 700 nm. In black is the count of H^+C_{60}, in red and blue, two different scans showing the count of H^+C_{60}-He. In purple, is the recorded emission curve the dye which was used for these scans, Styryl 1. The strong correlation between the dye emission and the complexes dissociation indicates that the red and blue traces are not genuine spectra of H^+C_{60}-He. However, they do indicate broad absorptions in this region.

9. CONCLUSION AND OUTLOOK

As part of the project of identifying the carriers of the DIBs, we recorded the electronic spectra of cold medium-sized H^+PAHs and PAHs$^+$ in the gas phase. The setup used was a tandem mass spectrometer, centered on a cryogenic ion trap. In a first phase, we assembled the apparatus, and tested it by recording the already known gas-phase electronic spectrum of N_2O^+. In a second phase, we recorded the visible electronic spectra of five medium-sized H^+PAHs and estimated their rotational temperature to 10 - 15 K. In a third phase, we recorded the visible electronic spectra of He-Cor$^+$ and He-Cora$^+$ by monitoring the photodissociation of their complexes with He. We also recorded the spectrum of 2He-Cora$^+$ to estimate the influence of the He and extrapolate the spectrum of Cora$^+$. Using the same method, we started a project to obtain the electronic spectra of H^+C_{60} and C_{58}^+. All the spectra were compared to astronomical spectra, and since none showed a match, upper limits of their respective column density were inferred.

Medium-sized H^+PAHs and PAHs$^+$ have been dismissed by astrochemical models as candidate carriers of the DIBs. The results obtained in this thesis confirm experimentally that the major members of medium-sized H^+PAHs and PAHs$^+$ are not among the carriers. Such species are expected to be dissociated by the UV radiation present in the DISM, and a large number of carbon atoms ($\geq \sim 60$) is currently thought to be necessary for such molecules not to be dehydrogenated. The technique used for obtaining the spectra of Cor$^+$ and Cora$^+$ can be employed to study virtually any molecular cation that would be a candidate.

The two next sections of this Chapter present (1) what could be obtained in the near future by simplifying the experimental setup, and (2) what approach seems to be the most promissing for the long term assignment of the large molecules present in the ISM.

9.1 Simplified experimental setup

An experimental setup is suggested with the goal of reducing the time needed for performing an experiment and the amount of troubleshooting and maintenance. It consists of three components: an ion trap, a QMS, and a micro-channel plate (MCP) detector (see top setup of Figure 9.1). The main feature of this design is that the sample ions are produced directly in the trap. A UV laser, focused inside a conical cavity, made in the back trapping electrode itself, will vaporize and ionize the sample (see top setup of Figure 9.2). The sample is simply coated on the surface of the cone. The ions produced will automatically fall in the tapping potential, while being cooled by the buffer gas entering the trap via this cone. The method for the obtention of the electronic spectrum remains the PD of complexes with He, followed by mass selection and detection.

The main limitation of the top setup of Figure 9.1 is the lack of mass selection of the ions produced. However, some experiments can be performed with pure PAH, and fullerene samples, especially when very little amounts are needed. In this case mass selection is not a requirement, and the experiment is performed on the whole isotopic distribution of the molecule. If a mass selection is necessary for a specific experiment, the bottom setup Figure 9.1) can be used. In this setup, the products of the ion source will be mass selected before being introduced in the trap. The spectrum acquisition is the same. Although the UV laser and the dye laser have to be carefully aligned, the overall experiment rely on a very limited amount of parameters. That is, around three times less than to the current setup. Each element of a setup represents as many possible electrical and mechanical issues occurring during an experiment or maintenance. This design allows concentrating on the one thing of interest, the cold ions in the trap.

Introducing the buffer gas and the sample from the same cavity allows the newly produced ions to be automatically immersed in a high density buffer gas. The conical cavity, with a volume of $\sim 10\,\mathrm{mm}^2$, allows remarquably high number densities, while keeping the whole trap and vacuum chamber under reasonable pressures. This somewhat "surgical" buffer gas cooling might allow to obtain a full conversion of the sample to He complexes almost instantly. Obtaining a full conversion provides a background free experiment. With He density of $10^{17}\,\mathrm{cm}^{-3}$, in the cavity at 5 K, gives a mean free path of He in respect to a 3 nm molecule of 300 nm. With a He speed of 100 m.s^{-1} at 5 K, a sample molecule will undergo $\sim 3 \times 10^5$ collisions in a single ms. At this rate, a few ms are enough to cool any molecule, and the pressure in a 10 L vacuum chamber will only be $\sim 10^{-6}$ mbar.

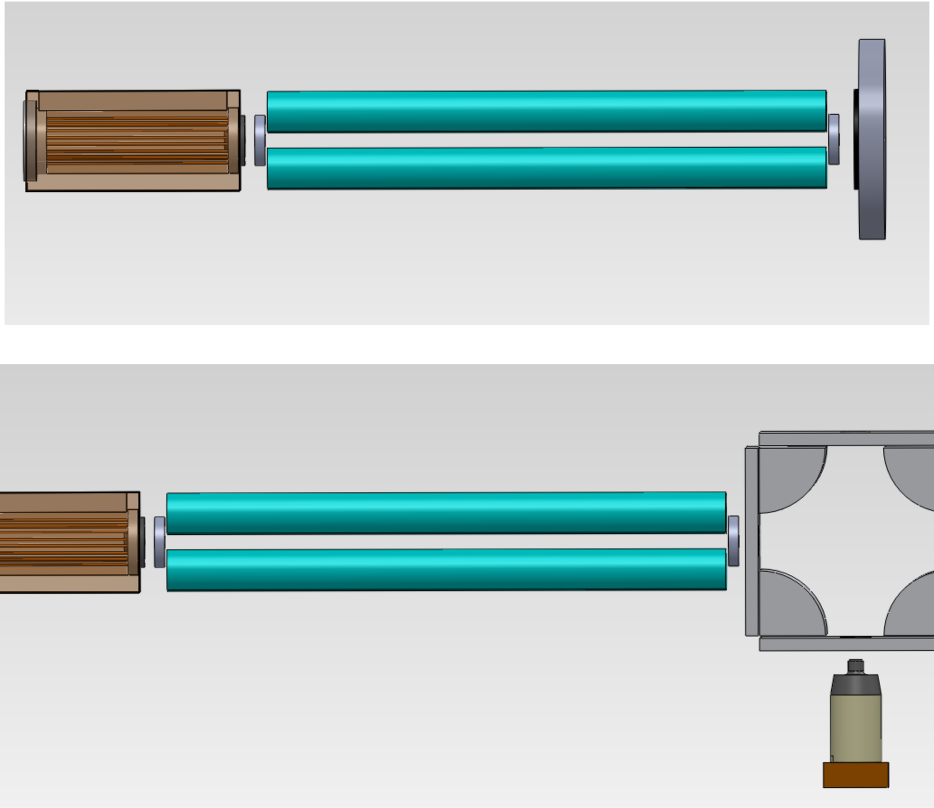

Fig. 9.1: 3-D overview of two experimental setups for the obtention of the cold electronic spectra of gas-phase cations. The top setup consists of a 4-p trap, a QMS, a 4-pole bender, an ion source, and an MCP detector. The bottom setup consists of a 4-p trap, a QMS, and an MCP detector. If ions cannot be produced by laser vaporisation-ionization inside the trap back electrode (see Figure 9.2), they can be produced in a separated ion source (setup 1).

Molecules obtainable with decent purity would constitute a target for the setup without prior mass selection, provided a suitable UV radiation for ionizing the sample without excessive fragmentation in the trap. By adjusting the laser power, the beam focus, and the He density in the cone, the number of ionized molecules should be set ideally to as little as required for the experiment, that is, between 1 000 and 100 000 per cycle.

Dehydrogenated PAHs$^+$ could be obtained if the amount of UV radiation irradiating the sample and the amount being in the axis of the trap can be tuned. For

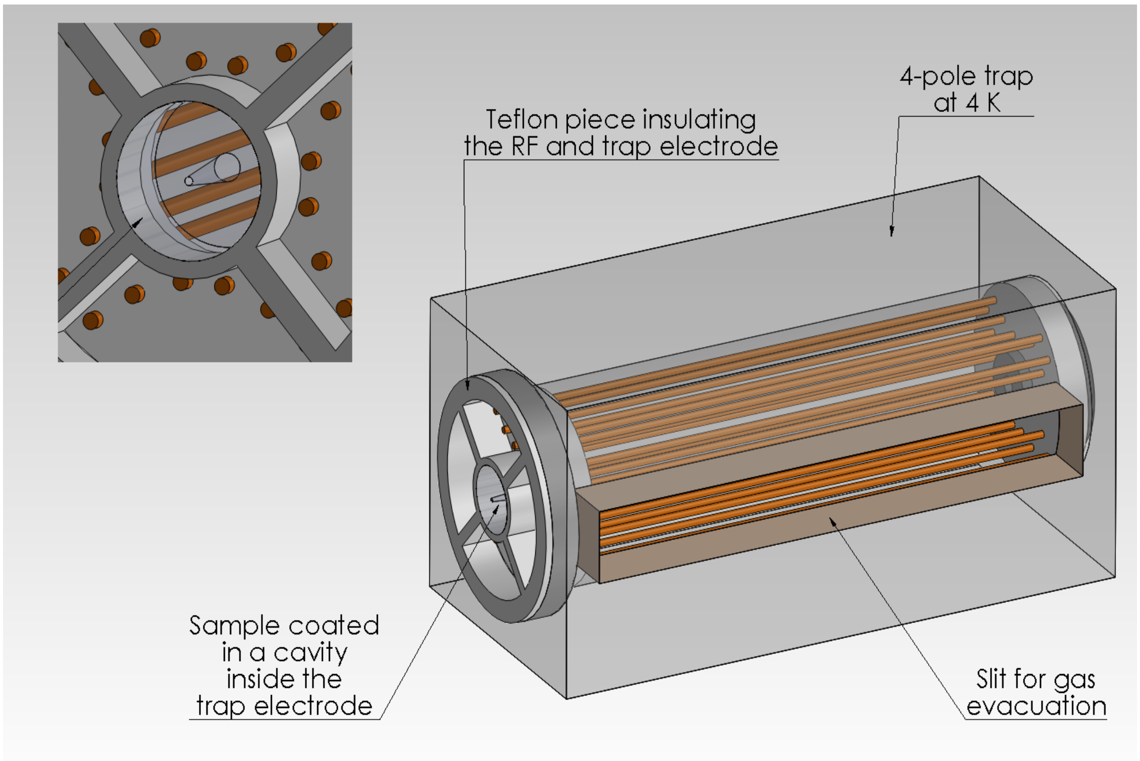

Fig. 9.2: A view of the 4-pole trap. The back trapping electrode is made transparent for the cone inside it to be visible. The housing of the trap is very compact to decrease to the minimum the unnecessary volume outside the trap. A large slit facing the pump and a 1 mm aperture in the exit electrode ensure that small amounts of buffer gas go to the QMS. The inset shows the conical cavity from which the buffer gas enters the trap, and in which the sample is coated.

instance, if the laser beam, tightly focused onto the 1 mm ion cloud, would mostly be in a 1 mm^2 section in the axis of the cone, the ion cloud would be highly irradiated while the sample not. The way to tune the proportion of UV radiation going to the sample, and to the ion cloud, could be by varying with the laser beam diameter. Following the absorption of a few UV photons, the PAHs^+ would deyhdrogenate will being kept cold by the He buffer gas.

Hydrogenated fullerenes$^+$ might be obtained with a mixture of H_2 and He at 20 K as buffer gas. Some H_2 molecules would be dissociated by the UV laser beam, provided a suitable laser radiation. H atoms could bind to the fullerene ions, continuously cooled by the buffer gas, while H_2 would not bind. By tuning the H_2 / He ratio, the power of the UV beam, and the density of the buffer gas, various degrees of hydrogenation might be reached. Spectroscopy could be done through the photodissociation of the produced fulleranes. Also, this experiment could give an insight into the production and destruction of fulleranes in the ISM, although free electrons would be missing in the picture.

Over the four years of this thesis we have experienced that the biggest obstacle for the obtention of the results we were aiming at, was not the difficulty of the method itself, but the regular occurrence of issues with the hardware. The setup suggested in this section must surely be more thought of. However, all efforts put into designing a setup which is as simple and technically elegant as possible could be highly rewarding during the course of its use.

9.2 The challenge of identifying large molecules in space

Many unidentified spectroscopical features, observed since several decades, show the presence of large molecules in the ISM and CSEs. They appear in a wide energy range, from microwave emissions to VUV absorptions. Despite considerable experimental, observational, and theoretical efforts put into identifying the responsible molecules, the carriers remain extremely elusive. However, seeing that already the identification of new molecules in dark clouds remains a challenge despite candidates containing only five to ten atoms, the identification of much larger molecules can be expected to be highly challenging. The method for the identifying small molecules in dark clouds and large molecules in the DISM and CSEs is essentially the same. It is a top-down approach using laboratory spectra of selected molecules, compared to astronomical spectra for a match or a fail. Since every other attempt is successful for molecules of a few atoms, one can expect a very low success rate for molecules of dozens of atoms.

Although being a significant discovery, the case of C_{60}^+ is a good illustration of this issue. The hint of the presence of this molecule in the DISM was given 20 years ago by a spectrum obtained in a neon matrix.[165] Many experiments and calculations were performed on other fullerenes and derivatives[166,167] such the molecule was an outstanding candidate. One could think that the confirmation of C_{60}^+ as a DIB carrier would trigger a chain reaction in which some derivatives would be identified as well. It is not the case. Not because no major derivatives could be studied since,[166] but because the ones which have been studied, unfortunately, did not match, the same way than dozens of exciting candidates did not match in the past. We see ourselves facing the same issue than when C_{60}^+ was not identified, that is, an

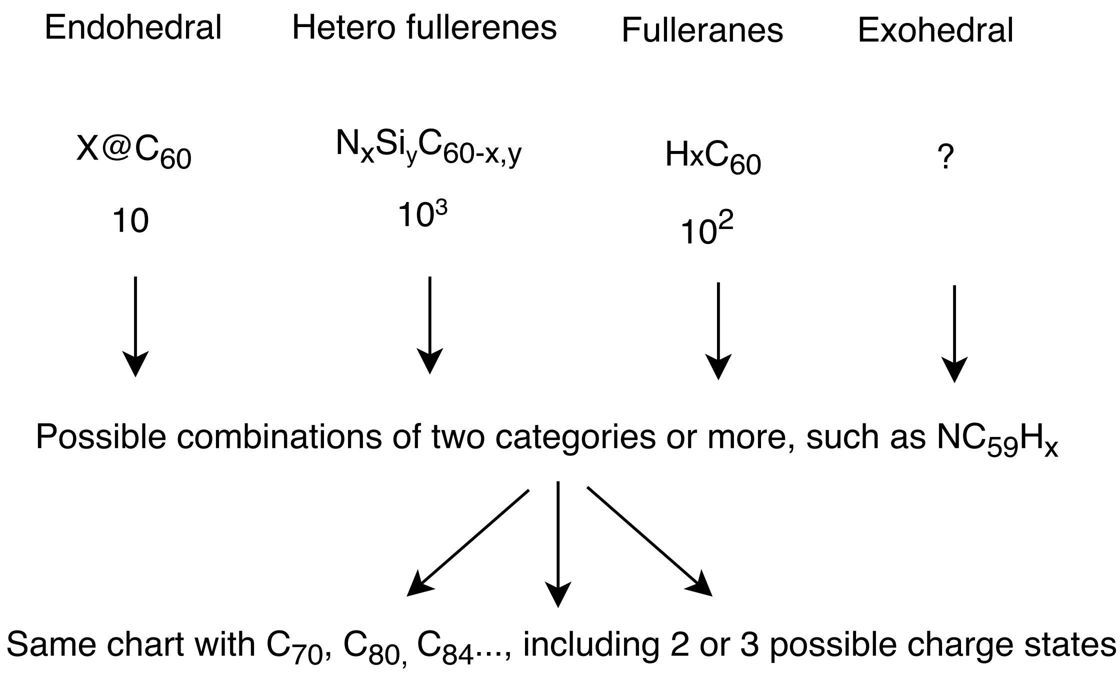

Fig. 9.3: Expectable fullerene derivatives in interstellar and circumstellar environments. For a single fullerene in a specific charge state, such as C_{60}, an order of magnitude of the number of relevant structures is given, for each type of derivative. For instance, $C_{60}H_x$ has much more than 100 isomers, but if we only take into account some of the most relevant fulleranes like $C_{60}H_2$, $C_{60}H_4$, $C_{60}H_{18}$ and $C_{60}H_{36}$, the number of isomers is in the order of a hundred. Each of these molecules would have a specific electronic spectrum which would require a dedicated laboratory experiment.

overwhelming number of candidates.[161] Figure 9.3 shows the families of fullerenes derivatives with an estimate of the number of the most probable structures. For instance, the single family of $N_xSi_yC_{60-x-y}$, for the most important, counts a few dozen of possibilities. This number, already high in terms of experimental validation of a candidate, becomes incommensurable when isomers, combinations with other derivatives, and charge states are included. Ironically, the unique starting point that is C_{60}^+ shows that when we deal with such large molecules, and unless the conditions where they exist are accurately described, the chances of guessing a right carrier molecule is very low. It might be early to draw such a conclusion concerning the case of C_{60} derivatives since the discovery is rather recent. However, it is probably not too early to draw this conclusion concerning the general case of large unidentified molecules in the ISM. For a more global understanding of the chemistry leading to these molecules, and an exhaustive assignment of the strong DIBs in the long term, a bottom-up approach simulating the conditions seems to be the most promising.

Surface chemistry on dust grains is a key to disclose the identity of most large gas-phase molecules, whether these are in reflection nebulae, CSEs, or the DISM. As fo the DISM, one could argue that there is a lack of significant correlation between many DIBs and dust extinction.[57,168] This is because the precursors of the carriers are likely formed in CSEs,[61] and the carriers themselves merely surviving in the DISM, hence the lack of correlation. On the other hand, these precursors may themselves very well be processed on dust grains in CSEs.

An approach to this chemistry consists in irradiating so-called "interstellar ice analogs"[169–174] (IIAs) or hydrogenated amorphous carbon[76,174,175] (HAC) with UV photons representing the ISRF. The detection of the product of this UV-induced cold surface chemistry can be achieved through a combination of temperature programmed desorption of the ice sample and mass spectroscopy or IR spectroscopy on the ice sample. It is shown that complex molecules are efficiently synthesized. Among these, stable species may regularly be desorbed to become a part, at least temporarily, of the gas-phase budget. However, these experiments are done on thermostated substrates, which would somehow mimic extremely large dust grains. Therefore, these IIAs or HAC samples may not be very realistic. In contrast, chemistry and desorption processes on the small and much more abundant "gas-phase dust grains" might be significantly different. Besides, the end products of these experiments are not detectable in astronomical spectra since the focus is on the solid phase. A complete bottom-up approach would not only reveal which molecules are most produced on and desorbed from dust particles, but also which of them survive the circumstellar and/or ISRF.

The DIB carriers are likely formed in CSEs subsequently diluting in the ISM, and probably little chemistry occurs later DISM. As a consequence, the problem can be divided into two experimental parts. First, a simulation of the formation and desorption of large molecules from grains occurring in denser media and high UV-Vis flux. Then, a simulation of the survival of the latter molecules in more diffuse media under the ISRF. The grains formed in CSEs are processed along the way, and their surface composition and size range is always evolving, depending on the local conditions. Positively charged dust grains could be grown and irradiated within ion traps. The setup presented in the previous section could perfom such experiments since it allows a production within the trap. The formation of the grains and that of the molecules which desorb from them could be studied under VUV irradiation. The first experiments may not mimic accurately interstellar conditions but the refinment with the time of such experimental simulations may be the most promissing approach for eventually identifying many large species, along with understanding the key processes occuring on dust grains.

BIBLIOGRAPHY

[1] M. L. Heger. The occurrence of stationary d lines of sodium in the spectroscopic binaries,[beta] scorpii and [delta] orionis. *Lick Observatory Bulletin*, 10:59–63, 1919.

[2] M. L. Heger. Further study of the sodium lines in class b stars. *Lick. Obs. Bull.*, 10:141–145, 1922.

[3] N.A.S.A. Voyager enters solar system's final frontier. 2005.

[4] E. Marsch, H.-J. Fahr, and K. Scherer. The outer heliosphere: The next frontiers. *Technology and Engineering*, 2000.

[5] M. S. Stiavelli. From first light to reionization. 2009.

[6] E. E. Barnard. On a nebulous groundwork in the constellation taurus. *The Astrophysical Journal*, 25, 1907.

[7] E. E. Barnard. On the dark markings of the sky, with a catalogue of 182 such objects. *Astrophys. J.*, 49:1–24, 1919.

[8] H. S. P. Muller, F. Schloder, J. Stutzki, and G. Winnewisser. The cologne database for molecular spectroscopy, cdms: a useful tool for astronomers and spectroscopists. *J. Mol. Struc.*, 742(1):215–227, 2005.

[9] D. P. Cox. The three-phase interstellar medium revisited. *Annu. Rev. Astron. Astrophys.*, 43:337–385, 2005.

[10] E. Orlando and A. Strong. Cosmic rays: interstellar gamma-ray and radio emission. *Nuclear Physics B-Proceedings Supplements*, 239:64–69, 2013.

[11] J. S. Mathis, P. G. Mezger, and N. Panagia. Interstellar radiation field and dust temperatures in the diffuse interstellar matter and in giant molecular clouds. *Astron. Astrophys.*, 1983.

[12] T. P. Snow and B. J. McCall. Diffuse atomic and molecular clouds. *Annu. Rev. Astron. Astrophys.*, 44:367–414, 2006.

[13] T. Dunham. *American Scientific Publisher*, 49:26, 1937.

[14] A. McKellar. Evidence for the molecular origin of some hitherto unidentified interstellar lines. *Publ. Astron. Soc. Pac.*, 52(307):187–192, 1940.

[15] S. Weinreb, A. H. Barrett, M. L. Meeks, and J. C. Henry. Radio observations of oh in the interstellar medium. *Nature*, 200(4909):829–831, 1963.

[16] W. G. B., Meinschein and D. J. Hennessy. Mass spectroscopic analysis of the orgueil meteorite: Evidence for biogenic hydrocarbons. *Annals of the New York Academy of Sciences*, 1961.

[17] J. W. Aerts, A. Elsaesser, W. F. M. Rling, and P. Ehrenfreund. A contamination assessment of the ci carbonaceous meteorite orgueil using a dna-directed approach. *Meteoritics and Planetary Science*, 2016.

[18] A. G. G. M. Tielens. The molecular universe. *Reviews of Modern Physics*, 85(3):1021, 2013.

[19] R. W. Russell, B. T. Soifer, and S. P. Willner. The 4 to 8 micron spectrum of ngc 7027. *Astrophys. J.*, pages L149–L153, 1977.

[20] F. Galliano, S. C. Madden, A. G. G. M. Tielens, E. Peeters, and A. P. Jones. Variations of the mid-ir aromatic features inside and among galaxies. *Astrophys. J.*, 679(1):310, 2008.

[21] K. Sellgren, K. I. Uchida, and M. W. Werner. The 15-20 m spitzer spectra of interstellar emission features in ngc 7023. *Astrophys. J.*, 659(2):1338, 2007.

[22] D. Lutz, E. Sturm, L. J. Tacconi, E. Valiante, M. Schweitzer, H. Netzer, R. Maiolino, P. Andreani, O.Shemmer, and S. Veilleux. Pah emission and star formation in the host of the z 2.56 cloverleaf qso. *Astrophys. J. lett.*, 661(1):L25, 2007.

[23] L. Armus, V. Charmandaris, J. Bernard-Salas, H. W. W. Spoon, J. A. Marshall, S. J. U. Higdon, V. Desai, H.I. Teplitz, L. Hao, D. Devost, B. R. Brandl,

Y. Wu, G. C. Sloan, B. T. Soifer, J. R. Houck, and T. L. Herter. Observations of ultraluminous infrared galaxies with the infrared spectrograph on the spitzer space telescope. ii. the iras bright galaxy sample. *Astrophys. J.*, 656(1):148, 2007.

[24] D. A. Riechers, A. Pope, E. Daddi, L. Armus, C. L. Carilli, F. Walter, J. Hodge, R.-R. Chary, G. E. Morrison, M. Dickinson, H. Dannerbauer, and D. Elbaz. Polycyclic aromatic hydrocarbon and mid-infrared continuum emission in a z ¿ 4submillimeter galaxy. *Astrophys. J.*, 786(1):31, 2014.

[25] F. Boulanger and M. Perault. Diffuse infrared emission from the galaxy. i-solar neighborhood. *Astrophys. J.*, 330:964–985, 1988.

[26] I. Yamamura, T. Onaka, T. Tanabe, T. L. Roellig, and L. Yuen. Mid-infrared spectral observations of point sources by irts. *Publications of the Astronomical Society of Japan*, 48(5):L65–L69, 1996.

[27] H. Murakami, M. M. Freund, K. Ganga, H. Guo, T. Hirao, N. Hiromoto, M. Kawada, A. E. Lange, S. Makiuti, H. Matsuhara, et al. The irts (infrared telescope in space) mission. *Publications of the Astronomical Society of Japan*, 48(5):L41–L46, 1996.

[28] D. P. Finkbeiner, M. Davis, and D. J. Schlegel. Extrapolation of galactic dust emission at 100 microns to cosmic microwave background radiation frequencies using firas. *Astrophys. J.*, 524(2):867, 1999.

[29] E. Dwek and R. G. Arendt. A tentative detection of the cosmic infrared background at 3.5 μm from cobe/dirbe observations. *Astrophys. J.l*, 508(1):L9, 1998.

[30] J. Kahanpää, K. Mattila, K. Lehtinen, C. Leinert, and D. Lemke. Unidentified infrared bands in the interstellar medium across the galaxy. *Astron. Astrophys.*, 405:999–1012, 2003.

[31] A. Leger and L. d'Hendecourt. Are polycyclic aromatic hydrocarbons the carriers of the diffuse interstellar bands in the visible? *Astron. Astrophys.*, 146:81–85, 1985.

[32] A. Léger, L. d'Hendecourt, P. Boissel, and F.-X. Desert. Photo-thermo-dissociation. i-a general mechanism for destroying molecules. *Astron. Astrophys.*, 213:351–359, 1989.

[33] K. Sellgren. The near-infrared continuum emission of visual reflection nebulae. *Astrophys. J.*, 277:623–633, 1984.

[34] S. Kwok. Complex organics in space from solar system to distant galaxies. *The Astronomy and Astrophysics Review*, 24(1):1–27, 2016.

[35] L. S. Bernstein and D. K. Lynch. Small carbonaceous molecules, ethylene oxide (c-c2h4o) and cyclopropenylidene (c-c3h2): Sources of the unidentified infrared bands? *Astrophys. J.*, 704(1):226, 2009.

[36] M. Cohen, L. Allamandola, A. G. G. M. Tielens, J. Bregman, J. P. Simpson, F. C. Witteborn, D. Wooden, and D. Rank. The infrared emission bands. i - correlation studies and the dependence on c/o ratio, 1986.

[37] J. Cami, J. Bernard-Salas, E. Peeters, and S. E. Malek. Detection of c60 and c70 in a young planetary nebula. *Science*, 329(5996):1180–1182, 2010.

[38] M. Steglich, C. Jäger, F. Huisken, M. Friedrich, W. Plass, H.-J. Räder, K. Müllen, and T. Henning. The abundances of hydrocarbon functional groups in the interstellar medium inferred from laboratory spectra of hydrogenated and methylated polycyclic aromatic hydrocarbons. *Astrophys. J. Sup.*, 208(2):26, 2013.

[39] W. W. Duley, V. I. Grishko, J. Kenel, G. Lee-Dadswell, and A. Scott. Laboratory and theoretical simulation of 3.4 μm spectra of hydrocarbons in interstellar sources. *Astrophys. J.*, 626(2):933, 2005.

[40] C. Jager, S. Krasnokutski, A. Staicu, F. Huisken, H. Mutschke, T. Henning, W. Poppitz, and I. Voicu. Identification and spectral properties of polycyclic aromatic hydrocarbons in carbonaceous soot produced by laser pyrolysis. *Astrophys. J. Sup.*, 166(2):557, 2006.

[41] A. Ricca, C. W. Bauschlicher Jr., C. Boersma, A. G. G. M. Tielens, and L. J.Allamandola. The infrared spectroscopy of compact polycyclic aromatic hydrocarbons containing up to 384 carbons. *Astrophys. J.*, 754(1):75, 2012.

[42] G. D. Schmidt, M. Cohen, and B. Margon. Discovery of optical molecular emission from the bipolar nebula surrounding hd 44179. *Astrophys. J. lett.*, 239:L133–L138, 1980.

[43] A. N. Witt, R.E. Schild, and J. B. Kraiman. Photometric study of ngc 2023 in the 3500 a to 10000 a region-confirmation of a near-ir emission process in reflection nebulae. *Astrophys. J.*, 281:708–718, 1984.

[44] A. N. Witt and T. A. Boroson. Spectroscopy of extended red emission in reflection nebulae. *Astrophys. J.*, 355:182–189, 1990.

[45] K. D. Gordon, A. N. Witt, and Brian C. F. Detection of extended red emission in the diffuse interstellar medium. *Astrophys. J.*, 498(2):522, 1998.

[46] A. Nitzan and J. Jortner. Theory of inverse electronic relaxation. *JCP*, 71(8):3524–3532, 1979.

[47] S. Darbon, J.-M. Perrin, and J.-P. Sivan. Observational constraints on the ere interpretation. *Astron. Astrophys.*, 1999.

[48] D. G. Furton and A. N. Witt. Extended red emission from dust in planetary nebulae. *Astrophys. J.*, 386:587–603, 1992.

[49] G. Ledoux, M. Ehbrecht, O. Guillois, F. Huisken, B. Kohn, M. A. Laguna, I. Nenner, V. Paillard, R. Papoular, D. Porterat, et al. Silicon as a candidate carrier for ere. *Astron. Astrophys.*, 333:L39–L42, 1998.

[50] A. N. Witt, K. D. Gordon, and D. G. Furton. Silicon nanoparticles: Source of extended red emission? *Astrophys. J. lett.*, 501(1):L111, 1998.

[51] H.-C. Chang, K. Chen, and S. Kwok. Nanodiamond as a possible carrier of extended red emission. *Astrophys. J. lett.*, 639(2):L63, 2006.

[52] P. W. Merrill. Stationary lines in the spectrum of the binary star boss 6142. *Astrophys. J.*, 83:126, 1936.

[53] B. J. McCall and R. E. Griffin. On the discovery of the diffuse interstellar bands. In *Proc. R. Soc. A*, volume 469, page 20120604. The Royal Society, 2013.

[54] G. H. Herbig. The diffuse interstellar bands. iv-the region 4400-6850 a. *Astrophys. J.*, 196:129–160, 1975.

[55] Michigan State University online content: Visible and Ultraviolet Spectroscopy. https://www2.chemistry.msu.edu/faculty/reusch/virttxtjml/spectrpy/uv-vis/spectrum.htm.

[56] J. Kos, T. Zwitter, R. Wyse, O. Bienaymé, J. Binney, J. Bland-Hawthorn, K. Freeman, B. K. Gibson, G. Gilmore, E. K. Grebel, et al. Pseudo–three-dimensional maps of the diffuse interstellar band at 862 nm. *Science*, 345(6198):791–795, 2014.

[57] D. Baron, D. Poznanski, D. Watson, Y. Yao, N. L. J. Cox, and J. X. Prochaska. Using machine learning to classify the diffuse interstellar bands. *Mon. Not. R. Astron. Soc.*, 451:332–352, 2015.

[58] A. B. Men'shchikov, D. Schertl, P. G. Tuthill, G. Weigelt, and L. R. Yungelson. Properties of the close binary and circumbinary torus of the red rectangle. *Astron. Astrophys.*, 393:867–885, 2002.

[59] H. Van Winckel, M. Cohen, and T. R. Gull. The ere of the red rectangle. *Astron. Astrophys.*, 390(1):147–154, 2002.

[60] S. M. Scarrott, S. Watkin, J. R. Miles, and P. J. Sarre. Evidence for a link between the more prominent optical emission bands in the red rectangle and some of the diffuse interstellar absorption bands. *Mon. Not. R. Astron. Soc.*, 255(1):11P–16P, 1992.

[61] J. J. Díaz-Luis, D. A. García-Hernández, N. K. Rao, A. Manchado, and F. Cataldo. A search for diffuse bands in fullerene planetary nebulae: evidence of diffuse circumstellar bands. *Astron. Astrophys.*, 573:A97, 2015.

[62] T. B. Williams, P. J. Sarre, K. Spekkens, R. Kuzio de Naray, and C. C. M. Marshall. Diffuse interstellar bands in emission. 2015.

[63] R. A. Meyers and S. N. Shore. Encyclopedia of astronomy and astrophysics. 1, 1989.

[64] T. P. Stecher. Interstellar ectinction in the ultraviolet. *Astrophys. J.*, 142:1683, 1965.

[65] T. P. Stecher. Interstellar extinction in the ultraviolet. ii. *Astrophys. J.*, 157:L125, 1969.

[66] K. Nandy, G. I. Thompson, C. Jamar, A. Monfils, and R. Wilson. Studies of ultraviolet interstellar extinction with the sky-survey telescope of the td-1 satellite. i-results for three galactic regions. *Astron. Astrophys.*, 44:195–203, 1975.

[67] J. H. Hecht. A physical model for the 2175 a interstellar extinction feature. *Astrophys. J.*, 305:817–822, 1986.

[68] F.-X. Desert, P. Jenniskens, and M. Dennefeld. Diffuse interstellar bands and uv extinction curves. the missing link. *Astron. Astrophys.*, 303:223, 1995.

[69] V. Mennella, L. Colangeli, E. Bussoletti, P. Palumbo, and A. Rotundi. A new approach to the puzzle of the ultraviolet interstellar extinction bump. *Astrophys. J. lett.*, 507(2):L177, 1998.

[70] F. Cataldo and S. Iglesias-Groth. On the action of uv photons on hydrogenated fulleranes c60h36 and c60d36. *Mon. Not. R. Astron. Soc.*, 400(1):291–298, 2009.

[71] R. V. Bensasson, E. Bienvenue, J.-M. Janot, S. Leach, P. Seta, D. I. Schuster, S. R. Wilson, and H. Zhao. Photophysical properties of three hydrofullerenes. *Chem. Phys. Lett.*, 245(6):566–570, 1995.

[72] C. Carraro, R. Maboudian, and C. R. Stoldt. Infrared and ultraviolet spectra of fulleranes: Hreels studies and implications for the interstellar medium. In *Fulleranes*, pages 27–37. Springer, 2010.

[73] H. Wang, Y. He, Y. Li, and H. Su. Photophysical and electronic properties of five pcbm-like c60 derivatives: spectral and quantum chemical view. *J. Phys. Chem. A*, 116(1):255–262, 2011.

[74] F. Cataldo, D. A. García-Hernández, A. Manchado, and S. Iglesias-Groth. Spectroscopy of fullerenes, fulleranes and pahs in the uv, visible and near infrared spectral range. *Proceedings of the IAU*, 9(S297):294–296, 2013.

[75] S. Tomita, M. Fujii, and S. Hayashi. Defective carbon onions in interstellar space as the origin of the optical extinction bump at 217.5 nanometers. *Astrophys. J.*, 609(1):220, 2004.

[76] K. A. K. Gadallah, H. Mutschke, and C. Jäger. Uv irradiated hydrogenated amorphous carbon (hac) materials as a carrier candidate of the interstellar uv bump at 217.5 nm. *Astron. Astrophys.*, 528:A56, 2011.

[77] L. Gavilan, I Alata, K. C. Le, T. Pino, A. Giuliani, and E. Dartois. Vuv spectroscopy of carbon dust analogs: contribution to interstellar extinction. *Astron. Astrophys.*, 586:A106, 2016.

[78] L. Becker and T. E. Bunch. Fullerenes, fulleranes and polycyclic aromatic hydrocarbons in the allende meteorite. *Meteoritics & planetary science*, 32(4):479–487, 1997.

[79] J. S. Mathis, W. Rumpl, and K. H. Nordsieck. The size distribution of interstellar grains. *Astrophys. J.*, 217:425–433, 1977.

[80] R. J. Trumpler. Absorption of light in the galactic system. *Publ. Astron. Soc. Pac.*, 42(248):214–227, 1930.

[81] K. D. Gordon, G. C. Clayton, K. A. Misselt, A. U. Landolt, and M. J. Wolff. A quantitative comparison of the small magellanic cloud, large magellanic cloud, and milky way ultraviolet to near-infrared extinction curvespartially based on observations made with the nasa/esa hubble space telescope, obtained at the space telescope science institute, which is operated by the association of universities for research in astronomy, inc., under nasa contract nas 5-26555. these observations are associated with proposal 8198. *Astrophys. J.*, 594(1):279, 2003.

[82] V. Rudnev, C. A. Rice, and J. P. Maier. electronic spectrum of nccn in the gas phase. *JCP*, 129:134315, 2008.

[83] D. Gerlich. The study of cold collisions using ion guides and traps, chapt 3 in: Low temperatures and cold molecules. *Imperial College Press*, 2008.

[84] D. Gerlich. Ion-neutral collisions in a 22-pole trap at very low energies. *Physica Scripta*, 1995(T59):256, 1995.

[85] J. Jasik, J. Zabka, J. Roithova, and D. Gerlich. Infrared spectroscopy of trapped molecular dications below 4 k. *IJMSp*, page 354355, 2013.

[86] V. L. Ryjkov, X. Zhao, and H. A. Schuessler. Simulations of the rf heating rates in a linear quadrupole ion trap. *Phys. Rev. A*, 71(3):033414, 2005.

[87] O. Asvany and S. Schlemmer. Numerical simulations of kinetic ion temperature in a cryogenic linear multipole trap. *Int. J. Mass Spectrom.*, 279(2):147–155, 2009.

[88] R. Otto, P. Hlavenka, S. Trippel, J. Mikosch, K. Singer, M. Weidemuller, and R. Wester. How can a 22-pole ion trap exhibit ten local minima in the effective potential? *J. Phys. B*, 42(15), 2009.

[89] A. Dzhonson. *An apparatus for the measurement of the electronic spectra of cold ions in a radio-frequency trap.* PhD thesis, University of Basel, 2007.

[90] S. Chakrabarty. *Electronic spectroscopy of cold cations in a 22-pole trap by indirect methods.* PhD thesis, University_of_Basel, 2013.

[91] C. Western. Pgopher, a program for simulating rotational structure. 2010.

[92] E. P. L. Hunter and S. G. Lias. Evaluated gas phase basicities and proton affinities of molecules: an update. *Journal of Physical and Chemical Reference Data*, 27(3):413–656, 1998.

[93] G. P. Van der Zwet and L. J. Allamandola. Polycyclic aromatic hydrocarbons and the diffuse interstellar bands. *Astron. Astrophys.*, 146:76–80, 1985.

[94] F. Salama, E. L. O. Bakes, L. J. Allamandola, and A. G. G. M. Tielens. Assessment of the polycyclic aromatic hydrocarbon–diffuse interstellar band proposal. *Astrophys. J.*, 458:621, 1996.

[95] R. Gredel, Y. Carpentier, G. Rouill, M. Steglich, F. Huisken, and Th. Henning. Abundances of pahs in the ism: confronting observations with experimental results. *Astron. Astrophys.*, 530:A26, 2011.

[96] T. P. Snow, V. Le Page, Y. Keheyan, and V. M. Bierbaum. The interstellar chemistry of pah cations. *Nature*, 391(6664):259–260, 1998.

[97] V. Le Page, Y. Keheyan, T. P. Snow, and V. M. Bierbaum. Gas phase chemistry of pyrene and related cations with molecules and atoms of interstellar interest. *Int. J. Mol. Spec.*, 185:949–959, 1999.

[98] V. Le Page, Y. Keheyan, T. P. Snow, and V. M. Bierbaum. Reactions of cations derived from naphthalene with molecules and atoms of interstellar interest. *J. Am. Chem. Soc.*, 121(40):9435–9446, 1999.

[99] V. Le Page, T. P. Snow, and V. M. Bierbaum. Hydrogenation and charge states of pahs in diffuse clouds. i. development of a model. *Astrophys. J. Sup.*, 132(2):233, 2001.

[100] N. B. Betts, M. Stepanovic, T. P. Snow, and V. M. Bierbaum. Gas-phase study of coronene cation reactivity of interstellar relevance. *Astrophys. J. lett.*, 651(2):L129, 2006.

[101] T. Allain, S. Leach, and E. Sedlmayr. Photodestruction of pahs in the interstellar medium. ii. influence of the states of ionization and hydrogenation. *Astron. Astrophys.*, 305:616, 1996.

[102] V. Le Page, T. P. Snow, and V. M. Bierbaum. Hydrogenation and charge states of polycyclic aromatic hydrocarbons in diffuse clouds. ii. results. *Astrophys. J.*, 584(1):316, 2003.

[103] A. Pathak and P. J. Sarre. Protonated pahs as carriers of diffuse interstellar bands. *Mon. Not. R. Astron. Soc.: lett.*, 391(1):L10–L14, 2008.

[104] I. Alata, R. Omidyan, M. Broquier, C. Dedonder, O. Dopfer, and C. Jouvet. Effect of protonation on the electronic structure of aromatic molecules: naphthaleneh+. *Phys. Chem. Chem. Phys.*, 12(43):14456–14458, 2010.

[105] I. Garkusha, J. Fulara, P. J. Sarre, and J. P. Maier. Electronic absorption spectra of protonated pyrene and coronene in neon matrixes. *J. Phys. Chem. A*, 115(40):10972–10978, 2011.

[106] C. Cossart-Magos and S. Leach. Polycyclic aromatic hydrocarbons as carriers of the diffuse interstellar bands-rotational band contour tests. *Astron. Astrophys.*, 233:559–569, 1990.

[107] M. J. Frisch, G. W. Trucks, H. B. Schlegel, G. E. Scuseria, M. A. Robb, J. R. Cheeseman, G. Scalmani, V. Barone, B. Mennucci, G. A. Petersson, H. Nakatsuji, M. Caricato, X. Li, H. P. Hratchian, A. F. Izmaylov, J. Bloino, G. Zheng, J. L. Sonnenberg, M. Hada, M. Ehara, K. Toyota, R. Fukuda, J. Hasegawa, M. Ishida, T. Nakajima, Y. Honda, O. Kitao, H. Nakai, T. Vreven, J. A. Montgomery, Jr., J. E. Peralta, F. Ogliaro, M. Bearpark, J. J. Heyd, E. Brothers, K. N. Kudin, V. N. Staroverov, R. Kobayashi, J. Normand, K. Raghavachari, A. Rendell, J. C. Burant, S. S. Iyengar, J. Tomasi, M. Cossi, N. Rega, J. M. Millam, M. Klene, J. E. Knox, J. B. Cross, V. Bakken, C. Adamo, J. Jaramillo, R. Gomperts, R. E. Stratmann, O. Yazyev, A. J. Austin, R. Cammi, C. Pomelli, J. W. Ochterski, R. L. Martin, K. Morokuma, V. G. Zakrzewski, G. A. Voth, P. Salvador, J. J. Dannenberg, S. Dapprich, A. D. Daniels, . Farkas, J. B. Foresman, J. V. Ortiz, J. Cioslowski, and D. J. Fox. Gaussian09 Revision E.01. Gaussian Inc. Wallingford CT 2009.

[108] M. Hirama, T. Tokosumi, T. Ishida, and J.-I. Aihara. Possible molecular hydrogen formation mediated by the inner and outer carbon atoms of typical pah cations. *Chem. Phys.*, 305(1):307–316, 2004.

[109] M. Bahou, Y.-J. Wu, and Y.-P. Lee. Infrared spectra of protonated pyrene and its neutral counterpart in solid para-hydrogen. *J. Chem. Phys. Lett.*, 4(12):1989–1993, 2013. PMID: 26283241.

[110] H. Knorke, J. Langer, J. Oomens, and O. Dopfer. Infrared spectra of isolated protonated polycyclic aromatic hydrocarbon molecules. *Astrophys. J. lett.*, 706(1):L66, 2009.

[111] W. Jones, P. Boissel, B. Chiavarino, M. E. Crestoni, S. Fornarini, J. Lemaire, and P. Maitre. Infrared fingerprint of protonated benzene in the gas phase. *Angew. Chem. Int. Ed.*, 42(18):2057–2059, 2003.

[112] S. N. Spisak, A. V. Zabula, A. S. Filatov, A. Y. Rogachev, and M. A. Petrukhina. Selective endo and exo binding of alkali metals to corannulene. *Angew. Chem. Int. Ed.*, 50(35):8090–8094, 2011.

[113] M. E. Jacox. Vibrational and electronic energy levels of polyatomic transient

molecules. supplement a. *Journal of Physical and Chemical Reference Data*, 27(2):115–393, 1998.

[114] F.-X. Hardy, O. Gause, C. A. Rice, and J. P. Maier. Absorptions in the visible of protonated pyrene collisionally cooled to 15 k. *Astrophys. J.*, 778(2):L30, 2013.

[115] C. A. Rice, F.-X. Hardy, O. Gause, and J. P. Maier. (1) 1a x 1a electronic transition of protonated coronene at 15 k. *J. Chem. Phys. Lett.*, 5(6):942–945, 2014.

[116] I. Alata, M. Broquier, C. Dedonder, C. Jouvet, and E. Marceca. Electronic excited states of protonated aromatic molecules: Protonated fluorene. *Chem. Phys.*, 393(1):25–31, 2012.

[117] A. Chakraborty, C. A. Rice, F.-X. Hardy, J. Fulara, and J. P. Maier. Electronic spectra of protonated fluoranthene in a neon matrix and gas phase at 10 k. *J. Phys. Chem. A*, 2016.

[118] D. M. Hudgins, C. W. Bauschlicher Jr, and L. J. Allamandola. Variations in the peak position of the 6.2 μm interstellar emission feature: A tracer of n in the interstellar polycyclic aromatic hydrocarbon population. *Astrophys. J.*, 632:316, 2005.

[119] H. A. Galué, O. Pirali, and J. Oomens. Gas-phase infrared spectra of cationized nitrogen-substituted polycyclic aromatic hydrocarbons. *Astron. Astrophys.*, 517:A15, 2010.

[120] O. Botta and J. L. Bada. Extraterrestrial organic compounds in meteorites. *Surveys in Geophysics*, 23(5):411–467, 2002.

[121] M. Pettini and R. Cooke. A new, precise measurement of the primordial abundance of deuterium. *Mon. Not. R. Astron. Soc.*, 425(4):2477–2486, 2012.

[122] A. Webster. A possible isotope shift in the spectrum of a diffuse interstellar band. *Mon. Not. R. Astron. Soc.*, 282(4):1372–1382, 1996.

[123] G. A. H. Walker, D. A. Bohlender, and J. Krełowski. Further evidence for carbon isotopic structure in the $\lambda\lambda$5797 and 6614 diffuse interstellar bands. *Astrophys. J.*, 530(1):362, 2000.

[124] J. Cami, F. Salama, J. Jiménez-Vicente, G. A. Galazutdinov, and J. Krełowski. The rotational excitation temperature of the λ6614 diffuse interstellar band carrier. *Astrophys. J. lett.*, 611(2):L113, 2004.

[125] J. P. Sarre. The diffuse interstellar bands: A major problem in astronomical spectroscopy. *J. Mol. Spectr.*, 238:1 – 10, 2006.

[126] M. Steglich, J. Bouwman, F. Huisken, and T. Henning. Can neutral and ionized polycyclic aromatic hydrocarbons be carriers of the ultraviolet extinction bump and the diffuse interstellar bands? *Astrophys. J.*, 742(1):2, 2011.

[127] C. J. Mackie, E. Peeters, C. W. Bauschlicher Jr., and J. Cami. Characterizing the infrared spectra of small, neutral, fully dehydrogenated polycyclic aromatic hydrocarbons. *Astrophys. J.*, 799(2):131, 2015.

[128] L. N. Zack and J. P. Maier. Laboratory spectroscopy of astrophysically relevant carbon species. *Chem. Soc. Rev.*, 43:4602–4614, 2014.

[129] A. Staicu, G. Rouillé, O. Sukhorukov, Th. Henning, and F. Huisken*. Cavity ring-down laser absorption spectroscopy of jet-cooled anthracene. *Mol. Phys.*, 102(16-17):1777–1783, 2004.

[130] F. Salama, G. A. Galazutdinov, J. Kreowski, L. Biennier, Y. Beletsky, and In-Ok Song. Polycyclic aromatic hydrocarbons and the diffuse interstellar bands: A survey. *Astrophys. J.*, 728(2):154, 2011.

[131] A. L. Mattioda, D. M. Hudgins, and L. J. Allamandola. Experimental near-infrared spectroscopy of polycyclic aromatic hydrocarbons between 0.7 and 2.5 μm. *Astrophys. J.*, 629(2):1188, 2005.

[132] F. Salama and P. Ehrenfreund. A critical review of pahs as dib carriers-progress and open questions. *Proceedings of the IAU*, 9(S297):364–369, 2013.

[133] T. Pino, G. Féraud, P. Bréchignac, E. J. Bieske, and T. W. Schmidt. Laboratory spectroscopy of pahs. *Proceedings of the IAU*, 9(S297):247–257, 2013.

[134] A. Patzer, M. Schutz, C. Jouvet, and O. Dopfer. Experimental observation and quantum chemical characterization of the s 1 s 0 transition of protonated naphthalene–argon clusters. *J. Phys. Chem. A*, 117(39):9785–9793, 2013.

[135] E. J. Bieske, A. M. Soliva, A. Friedmann, and J. P. Maier. Electronic spectra of n+2(he)n (n=1, 2, 3). *JCP*, 96(1):28–34, 1992.

[136] N. Chalyavi, K. J. Catani, J. A. Sanelli, V. Dryza, and E. J. Bieske. Gas-phase electronic spectrum of the indole radical cation. *Mol. Phys.*, 113(15-16):2086–2094, 2015.

[137] J. Roithov, A. Gray, E. Andris, J. Jak, and D. Gerlich. Helium tagging infrared photodissociation spectroscopy of reactive ions. *Accounts of Chemical Research*, 49(2):223–230, 2016.

[138] C. J. Johnson, A. B. Wolk, J. A. Fournier, E. N. Sullivan, G. H. Weddle, and M. A. Johnson. Communication: He-tagged vibrational spectra of the sarglyh+ and h+(h2o)2,3 ions: Quantifying tag effects in cryogenic ion vibrational predissociation (civp)spectroscopy. *J. Chem. Phys.*, 140(22), 2014.

[139] F. J. Lovas, Rl J. McMahon, J.-U. Grabow, M. Schnell, J. Mack, L. T. Scott, and R. L. Kuczkowski. Interstellar chemistry: a strategy for detecting polycyclic aromatic hydrocarbons in space. *J. Am. Chem. Soc.*, 127(12):4345–4349, 2005.

[140] E. K. Campbell, D. Gerlich, M. Holz, and J. P. Maier. Laboratory confirmation of c60+ as the carrier of two diffuse interstellar bands. *Nature*, 523:322–323, 2015.

[141] P. Ehrenfreund, L. d'Hendecourt, L. Verstraete, A. Léger, W. Schmidt, and D. Defourneau. Search for the 4430 a dib in the spectra of coronene cation and neutral ovalene. *Astron. Astrophys.*, 259:257–264, 1992.

[142] F. Useli-Bacchitta, A. Bonnamy, G. Mulas, G. Malloci, D. Toublanc, and C. Joblin. Visible photodissociation spectroscopy of pah cations and derivatives in the pirenea experiment. *Chem. Phys.*, 371(1):16–23, 2010.

[143] L. M. Hobbs, D. G. York, T. P. Snow, T. Oka, J. A. Thorburn, M. Bishof, S. D. Friedman, B. J. McCall, B.Rachford, P. Sonnentrucker, and D. E. Welty. A catalog of diffuse interstellar bands in the spectrum of hd 204827. *Astrophys. J.*, 680(2):1256, 2008.

[144] L. M. Hobbs, D. G. York, J. A. Thorburn, T. P. Snow, M. Bishof, S. D. Friedman, B. J. McCall, T. Oka, B. Rachford, and P. Sonnentrucker. Studies of the diffuse interstellar bands. iii. hd 183143. *Astrophys. J.*, 705(1):32, 2009.

[145] C. A. Rice, J. Fulara, I. Garkusha, Á. Nagy, F.-X. Hardy, O. Gause, and J. P. Maier. Electronic spectra of corannulenic cations and neutrals in neon matrices and protonated corannulene in the gas phase at 15 k. *Zeitschrift für Physikalische Chemie*, 229(10-12):1709–1728, 2015.

[146] H. W. Kroto, J. R. Heath, S. C. O'Brien, R. F. Curl, R. E. Smalley, et al. C 60: buckminsterfullerene. *Nature*, 318(6042):162–163, 1985.

[147] G. A. H. Walker, D. A. Bohlender, J. P. Maier, and E. K. Campbell. Identification of more interstellar c60+ bands. *Astrophys. J. lett.*, 812(1):L8, 2015.

[148] K. Dongho, Minyung L., Y. Doug S., and K. S. Keun. Observation of fluorescence emission from solutions of c60 and c70 fullerenes and measurement of their excited-state lifetimes. *J. Am. Chem. Soc.*, 114(11):4429–4430, 1992.

[149] J. Catalan and J. Elguero. Fluorescence of fullerenes (c60 and c70). *J. Am. Chem. Soc.*, 115(20):9249–9252, 1993.

[150] G. H. Herbig. The diffuse interstellar bands. *Annu. Rev. Astron. Astrophys.*, 33:19–74, 1995.

[151] A. Webster. The interstellar extinction curve and the absorption spectra of two fulleranes. *Mon. Not. R. Astron. Soc.*, 288(1):221–224, 1997.

[152] S. Iglesias-Groth. Fullerenes and buckyonions in the interstellar medium. *Astrophys. J. lett.*, 608(1):L37, 2004.

[153] S. Iglesias-Groth. Electric dipole emission by fulleranes and galactic anomalous microwave emission. *Astrophys. J. lett.*, 632(1):L25, 2005.

[154] J. Cami. Can fullerene analogues be the carriers of the diffuse interstellar bands? *Proceedings of the IAU*, 9(S297):370–374, 2013.

[155] Y. Zhang, S. Kwok, and S. Sadjadi. Fullerenes and fulleranes in circumstellar envelopes. In *J. Phys.: Conference Series*, volume 728, page 052004. IOP Publishing, 2016.

[156] T. J. Millar. The chemistry of pah and fullerene molecules in interstellar clouds. *Mon. Not. R. Astron. Soc.*, 259(1):35P–39P, 1992.

[157] M. Sala, M. Hodoscek, S. Arulmozhiraja, and T. Fujii. Complete set of critical points on the c60h+ potential energy surface. *J. Phys. Chem. A*, 113(13):3223–3226, 2009.

[158] A. Webster. Comparison of a calculated spectrum of c60h60 with the unidentified astronomical infrared emission features. *Nature*, 1991.

[159] J. J. Díaz-Luis, D. A. García-Hernández, A. Manchado, and F. Cataldo. A search for hydrogenated fullerenes in fullerene-containing planetary nebulae. *Astron. Astrophys.*, 589:A5, 2016.

[160] A. Webster. On the carriers of the diffuse interstellar bands. *Mon. Not. R. Astron. Soc.*, 263(2):385–393, 1993.

[161] A. Omont. Interstellar fullerene compounds and diffuse interstellar bands. *Astron. Astrophys.*, 590:A52, 2016.

[162] T. T. Vehviläinen, M. G. Ganchenkova, L. E. Oikkonen, and R. M. Nieminen. Hydrogen interaction with fullerenes: From c 20 to graphene. *Phys. Rev. B*, 84(8):085447, 2011.

[163] S. M. Pimenova, S. V. Melkhanova, V. P. Kolesov, and A. S. Lobach. The enthalpy of formation and ch bond enthalpy of hydrofullerene c60h36. *J. Phys. Chem. B*, 106(9):2127–2130, 2002.

[164] S. Petrie, H. Becker, V. I. Baranov, and D. K. Bohme. Repeated addition of atomic hydrogen to fullerene cations, dications and trications. *IJMSI*, 145(1):79–88, 1995.

[165] J. Fulara, M. Jakobi, and J. P. Maier. Electronic and infrared spectra of c+ 60 and c- 60 in neon and argon matrices. *Chem. Phys. Lett.*, 211(2):227–234, 1993.

[166] F. Cataldo, S. Iglesias-Groth, and A. Manchado. On the radical cation spectra of fullerenes and fulleranes. part 1: C60, c70, c76, c78 and c84. *Fullerenes, Nanotubes and Carbon Nanostructures*, 20(8):656–671, 2012.

[167] B. Kern, D. Strelnikov, P. Weis, A. Bottcher, and M. M. Kappes. Ir, nir, and uv absorption spectroscopy of c602+ and c603+ in neon matrixes. *J. Chem. Phys. Lett.*, 5(3):457–460, 2014.

[168] D. Baron, D. Poznanski, D. Watson, Y. Yao, and J. X. Prochaska. Dusting off the diffuse interstellar bands: Dibs and dust in extragalactic sloan digital sky survey spectra. *Mon. Not. R. Astron. Soc.*, 447(1):545–558, 2015.

[169] G. M. Caro Munoz, A. Jiménez-Escobar, J. A. Martin-Gago, C. Rogero, C. Atienza, S. Puertas, J. M. Sobrado, and J. Torres-Redondo. New results on thermal and photodesorption of co ice using the novel interstellar astrochemistry chamber (isac). *Astron. Astrophys.*, 522:A108, 2010.

[170] M. S. Gudipati and R. Yang. In-situ probing of radiation-induced processing of organics in astrophysical ice analogsnovel laser desorption laser ionization time-of-flight mass spectroscopic studies. *Astrophys. J. lett.*, 756(1):L24, 2012.

[171] G. Danger, F.-R. Orthous-Daunay, P. de Marcellus, P. Modica, V. Vuitton, F. Duvernay, L. Flandinet, L. Le Sergeant dHendecourt, R Thissen, and T Chiavassa. Characterization of laboratory analogs of interstellar/cometary organic residues using very high resolution mass spectrometry. *Geochimica et Cosmochimica Acta*, 118:184–201, 2013.

[172] A. Boogert, P. Gerakines, and D. Whittet. Observations of the icy universe. 2015.

[173] M. J. Abplanalp, M. Förstel, and R. I. Kaiser. Exploiting single photon vacuum ultraviolet photoionization to unravel the synthesis of complex organic molecules in interstellar ices. *Chem. Phys. Lett.*, 644:79–98, 2016.

[174] E. Dartois, A. Jallat, I. Alata, L. Gavilan, G. A. Cruz-Diaz, M. Chabot, K. Beroff, and G. M. Muñoz Caro. Uv photolysis of hydrogenated amorphous carbons of astrophysical interest. *Polycyclic Aromatic Compounds*, pages 1–11, 2016.

[175] I. Alata, G. A. Cruz-Diaz, G. M. Caro Muñoz, and E. Dartois. Vacuum ultraviolet photolysis of hydrogenated amorphous carbons-i. interstellar h2 and ch4 formation rates. *Astron. Astrophys.*, 569:A119, 2014.

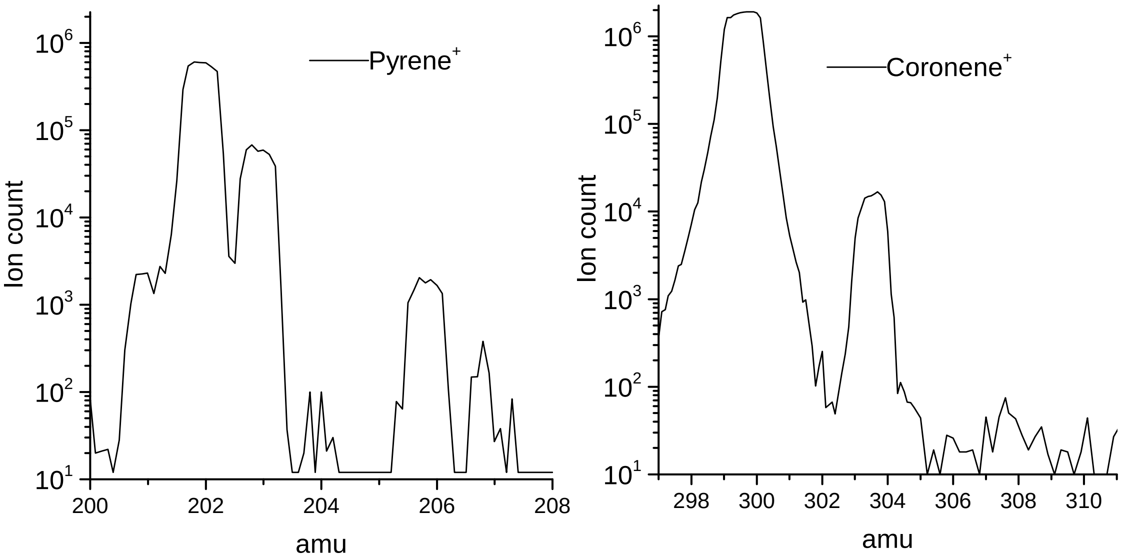

Fig. 10.1: On the left, a mass scan of Pyr^+ (202 amu) and $He\text{-}Pyr^+$(206 amu) isotopic distributions. On the right, a mass scan of Cor^+ (300 amu) and $He\text{-}Cor^+$ (304 amu). From $\approx 10^6$ parent ions in the trap, only $\approx 10^3$ - 10^4 complexes were detected.

After that medium-sized H^+PAHs have been studied, the best-suited candidates had now to be agreed on. The family of bare $PAHs^+$ was one of the main objectives of this apparatus. To obtain their electronic spectra, and since these do not fragment following the absorption of 1 - 2 visible photons, a method of choice is to monitor the PD of their complexes with He. However, the production of He complexes in the trap was not efficient. As seen in Figure 10.1, only a few thousands of complexes were formed at a trap temperature of ≈ 5.5 K. In itself, a few thousand ions is almost enough to perfom an experiment, however, in light of the results obtained with N_2O^+ (chapter 4), a much more efficient production of complexes is expected. Also, for recording the above mass spectra, the second QMS is not switched on. When it is switched on for an experiment, the overall signal significantly decreases. Later, modifications on the trap were done, and the trap temperature went down to 3.5 - 4 K, and the production of complexes was back to normal, at $\approx 50\,\%$ conversion. Nevertheless, these two degrees of difference are not enough to explain such a decrepancy, and the reason for the inefficient production shown in Figure 10.1 is still not completely understood.

Modifications in the trap region are, a priori, often time-consuming and risky maneuvers. Thus, other candidates were found ($C_7H_3^+$, OC_4O^+ and $C_6H_2O^+$) and that could be studied with the current technique, before attempting some improvements on the setup.

The Astrophysical Journal, 824:9 (6pp), 2016 June 10 doi:10.3847/0004-637X/824/1/9

OPTICAL ABSORPTIONS OF OXYGENATED CARBON CHAIN CATIONS IN THE GAS PHASE

F.-X. Hardy, C. A. Rice, A. Chakraborty, J. Fulara, and J. P. Maier
Department of Chemistry, University of Basel, Klingelbergstrasse 80, CH-4056 Basel, Switzerland; j.p.maier@unibas.ch

Received 2015 December 22; accepted 2016 March 24; published 2016 June 3

ABSTRACT

The gas-phase electronic spectra of linear OC_4O^+ and a planar $C_6H_2O^+$ isomer were obtained at a rotational temperature of ≈10 K. Absorption measurements in a 6 K neon matrix were followed by gas-phase observations in a cryogenic radiofrequency ion trap. The origin bands of the $1\ ^2\Pi_u \leftarrow X\ ^2\Pi_g$ transition of OC_4O^+ and the $1\ ^2A_2 \leftarrow X\ ^2B_1$ of $HCCC(CO)CCH^+$ lie at 417.31 ± 0.01 nm and 523.49 ± 0.01 nm, respectively. These constitute the first electronic spectra of oxygenated carbon chain cations studied under conditions that are relevant to the diffuse interstellar bands (DIBs), as both have a visible transition. The recent analysis of the 579.5 nm DIB indicates that small carriers, five to seven heavy atoms, continue to be possible candidates (Huang & Oka 2015). Astronomical implications are discussed regarding this kind of oxygenated molecules.

Key words: astrochemistry – line: identification – methods: laboratory: molecular – techniques: spectroscopic

1. INTRODUCTION

Oxygen does not make as complex molecules as carbon, but is the most abundant heavy element in the interstellar medium (ISM); oxides of the most common elements were identified in dense clouds or circumstellar envelopes through pure rotational transitions (Bujarrabal et al. 1994; Furuya et al. 2003; Tenenbaum et al. 2007; Tenenbaum & Ziurys 2009; Kamiński et al. 2013). Silicates such as olivine and pyroxene were also found as a component of circumstellar dust in oxygen-rich stars (Molster & Kemper 2005; Aller et al. 2014). Nevertheless, the chemistry in the latter is not as complex as in their carbon-rich counterparts, where unidentified features having a molecular origin are still present. This constrains the possibility for oxygen to be incorporated into gas-phase molecules when the envelope is ejected into interstellar space. However, these silicates and metal oxides are not present in large enough quantities in either dense or diffuse media to deplete elemental oxygen (Li & Draine 2001; Jenkins 2009; Whittet 2010), which is almost an order of magnitude more abundant than silicon, iron, and magnesium combined. An estimated 20% to 40% of oxygen appears to be unaccounted for in dense and diffuse clouds (Whittet 2010). An unknown reservoir of oxygen in the diffuse ISM is suggested to be larger grains composed of either O-bearing carbonaceous matter or amorphous silicates, both of which are opaque to infrared radiation (Hincelin et al. 2011). The substantial uncertainty of its identity leaves a possibility for other oxygenated-compounds. Moreover, if the role of oxygen is to terminate a carbon chain, availability should not be a problem.

In the context of the diffuse interstellar bands (DIBs; Snow & McCall 2006), molecules could desorb from oxygenated carbonaceous dust under the UV flux present in the diffuse ISM. It has been shown that large aliphatic/aromatic structures are possible carriers of the unidentified infrared emissions (Kwok & Zhang 2013) and better fits of the 11.3 μm feature are obtained when oxygen was included in the PAH mixture (Sadjadi et al. 2015). As particulate matter is in the diffuse ISM, oxygenated molecules could be candidates of the DIBs if these species are readily produced on grains.

Few DIBs allow for a rotational contour analysis; however, a study of the 579.71 nm DIB led to the conclusion that the most likely carrier is a molecule with five to seven heavy atoms (Huang & Oka 2015). In the past two decades, electronic spectra of a number of small carbon chains and their ions with visible and near-infrared electronic transitions were obtained in the gas phase at low temperatures, 10 to 30 K (Zack & Maier 2014). It could be shown that systems comprising up to a dozen or so carbon atoms are not responsible for the strongest DIBs. Electronic spectra of cyano-polyacetylene cations were also recorded in the gas phase with no matches found with any DIBs (Zack & Maier 2014). Therefore, a search began for systems which may have been omitted from laboratory measurements until now, such as the cumulenic species $H_2C_7H^+$ (Rice et al. 2015). Also absent from the list of studied molecules are oxygen-containing chains.

Electronic absorptions in the visible were recorded for two oxygen-containing carbon chain molecules: OC_4O^+, a linear species, and planar $HCCC(CO)CCH^+$. In this article the approach adopted to obtain gas-phase spectra under conditions as in diffuse interstellar clouds with vibrational and rotational degrees of freedom equilibrated to ≈10 K is described and then the laboratory data are compared with the astronomical observations. Measurements involve the use of a radio-frequency (rf) trap, collisional cooling with 5 K helium, and a laser excitation-dissociation scheme.

2. METHOD

The strategy for obtaining the gas-phase electronic spectrum of an astrophysically relevant molecular ion consists in recording initally the absorptions of mass-selected species in a 6 K neon matrix, supported by theoretical calulations to identify the geometric structures. Once the main characteristics, such as the wavelength of the transitions and oscillator strengths are known, the gas-phase spectrum can be measured for a direct comparison with astronomical data.

2.1. Matrix Isolation

2.1.1. Experimental

The experimental approach is a combination of mass spectrometry and matrix-isolation (Nagy et al. 2013). OC_4O^+ ions were produced in a hot-cathode source from carbon suboxide, C_3O_2,

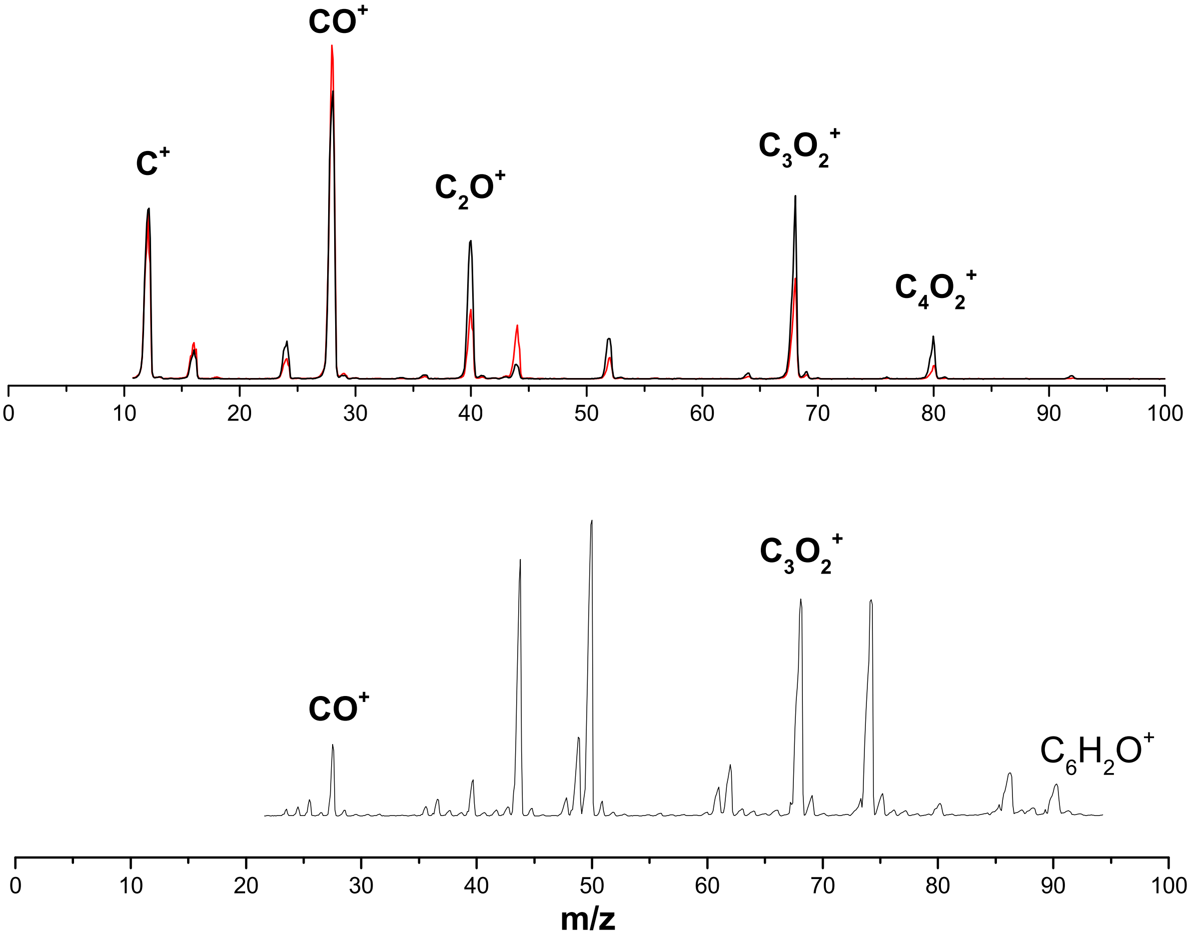

Figure 1. Mass spectra of carbon suboxide in a hot-cathode source (the top trace) and from carbon suboxide mixed with diacetylene (the bottom trace). The top overlays two spectra recorded with different pressures and the higher of which (black) produces OC_4O^+ more efficiently.

in helium. Positive species were guided, deflected 90° by an electrostatic bender to eliminate neutrals, and transported to a quadrupole mass selector (QMS). Cations ($m/z = 80$) are co-deposited with neon onto the matrix substrate, a rhodium-coated sapphire plate held at 6 K. CH_3Cl in a 1:30,000 ratio with neon undergoes dissociative electron capture and reduces space-charge effects. After a three to four hr deposition, a typical thickness of the matrix was 100 to 150 μm. Absorption spectra were measured from 250 to 1100 nm in a wave-guide arrangement by passing broadband radiation from halogen and xenon arc lamps. Light was passed through the 20 mm length of the matrix, transmitted to a spectrograph via optical-fibers, wavelength dispersed, and recorded by a CCD camera.

2.2. *Gas Phase*

The experimental setup (Hardy et al. 2015) is a tandem mass spectrometer in which ions are cooled and probed in a cryogenic 22-pole rf ion trap. The OC_4O^+ and $C_6H_2O^+$ isomers were produced by electron impact from C_3O_2 and a mixture of C_3O_2 and HC_4H, respectively. Cations from the source were guided to a hexapole and cooled to room temperature by collisions with background gas. A first QMS selected the mass of interest, and after passing through an einzel lens, a 90° deflector, and an rf-only octupole, ions arrived in a 22-pole rf ion trap. The latter was held at 4 K by a closed-cycle helium cryostat, where ions underwent collisions with helium. After a couple of milliseconds, a helium density of $4 \times 10^{15} \mathrm{cm}^{-3}$ was achieved via a piezo valve. The trap was loaded for 30 ms, whereby positive species were thermalized with cold helium and axially and radially confined. At the end of one period, a 5 ns pulsed-dye laser, having 0.002 nm bandwidth, was triggered. Sequentially, the exit electrode was lowered by 2 V for 5 ms to release both photoproducts and parent ions. To record an electronic spectrum, a second QMS monitored the photodissociation yield as a function of the laser wavelength, and selected cations were transported to a Daly detector. The entire experiment was synchronized at a repetition rate of 10 Hz.

2.2.1. *Computational*

The linear structure OC_4O^+ was optimized with density functional theory (DFT) at the B3LYP/cc-pVTZ level (Becke 1988; Lee et al. 1988) and the equilibrium coordinates were employed to calculate the excited-state energies with multi-state complete active space perturbation theory (MS-CASPT2; Andersson et al. 1990, 1992) implemented in Molcas (Aquilante et al. 2010). In CASPT2, an active space was constructed from 11 electrons distributed over 12 orbitals. Previous theoretical predictions for $HCCC(CO)CCH^+$ are from Chakrabory et al. (2015).

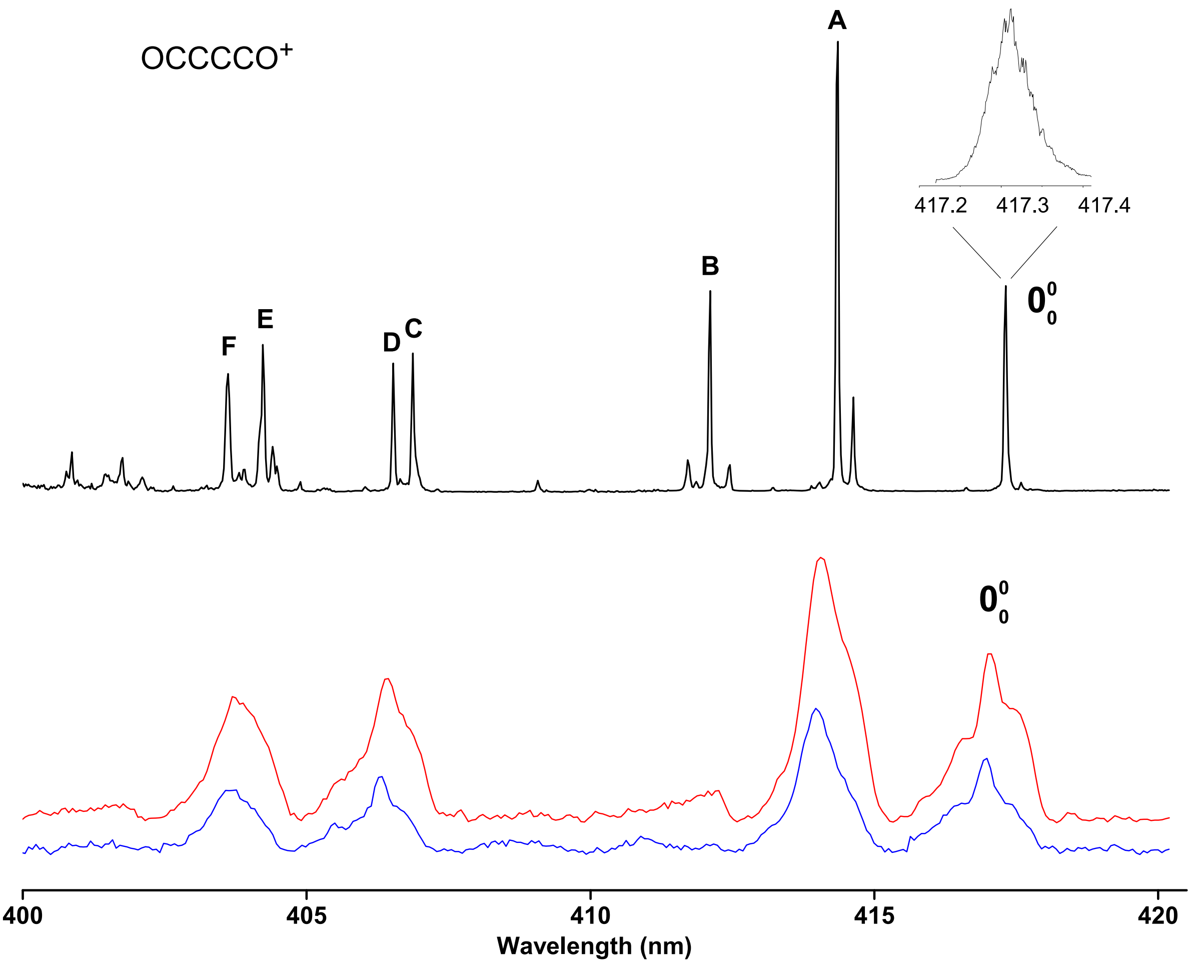

Figure 2. Gas-phase absorption spectrum of the 1 $^2\Pi_u \leftarrow X\ ^2\Pi_g$ transition of OC_4O^+ (the top trace) compared with the matrix recording (the middle trace). The bottom spectrum was recorded after 17 minutes UV (<270 nm) irradiation of the matrix and the decrease in band intensity indicates a cation.

3. RESULTS

A mass spectrum was first recorded with gaseous carbon suboxide and then one of carbon suboxide mixed with diacetylene (Figure 1) using a hot-cathode discharge source. Peaks due to OC_4O^+ and $C_6H_2O^+$ are indicated. Both oxygenated species are made in the plasma and OC_4O^+ forms through an ion-molecule reaction of C_2O^+ with C_2O. This is inferred from the four-fold increase of $m/z = 80$ when the pressure within the source is doubled from 0.02 to 0.04 mbar.

3.1. Electronic Spectrum of OC_4O^+

The absorption spectrum was first recorded in a 6 K neon matrix after mass-selected deposition of $C_4O_2^+$ and revealed several transitions in the 370 to 420 nm region (Figure 2, the middle trace). Thereafter, the matrix was exposed to photons with wavelengths below 270 nm photons causing electron detachment from Cl^-. After UV-irradiation of the matrix, a decrease in the absorption intensities demonstrates the cationic origin of the absorber because of electron recombination (Figure 2, the bottom trace). A proportional decrease of all bands indicates that they arise from a single electronic transition with an onset at 417.0 nm.

Other ground-state geometries were unstable on the potential energy surface compared with the linear form. Vertical excitation energies of OC_4O^+ were calculated. OC_4O^+ was optimized at the M06-2X/cc-pVTZ level and these coordinates were used for the MS-CASPT2 method (Table 1). According to CASPT2, OC_4O^+ possesses a visible transition 1 $^2\Pi_u \leftarrow X\ ^2\Pi_g$ at 3.19 eV with an oscillator strength of 0.004, in agreement with the observation at 2.97 eV (417 nm). In Figure 2 every two adjacent peaks are separated by 150 to 170 cm^{-1}, indicating a Franck-Condon active bending mode in the excited state.

Table 1
Electronic Excitation Energies E_{cal} (eV) and Oscillator Strength f of the Dipole-allowed Electronic Transitions for OC_4O^+ Calculated by the MS-CASPT2 Method

Transition	E_{cal}	f	E_{exp}
1 $^2\Pi_u \leftarrow X\ ^2\Pi_g$	3.19	0.004	2.97
2 $^2\Pi_u \leftarrow X\ ^2\Pi_g$	3.24	0.000	⋯
3 $^2\Pi_u \leftarrow X\ ^2\Pi_g$	3.78	0.000	⋯
4 $^2\Pi_u \leftarrow X\ ^2\Pi_g$	4.04	0.001	⋯

The gas-phase spectrum of the 1 $^2\Pi_u \leftarrow X\ ^2\Pi_g$ electronic transition of OC_4O^+ is shown in Figure 2 (the top trace). The origin band at 417.31 nm (Figure 2, inset), redshifted 0.31 nm compared with the absorption in the matrix, has a FWHM of 0.06 nm due to a short excited-state lifetime of ≈1 ps. The

Table 2

Electronic Absorption Band Maxima of the 1 $^2\Pi_u \leftarrow X\ ^2\Pi_g$ Transition of OC_4O^+ and 1 $^2A_2 \leftarrow X\ ^2B_1$ of $HCCC(CO)CCH^+$

	λ/nm	$\tilde{\nu}$/cm^{-1}	$\Delta\tilde{\nu}$/cm^{-1}	Assignment	A/cm^{-1}	B/cm^{-1}	C/cm^{-1}
OC_4O^+							
	417.31	23,956	0	0_0^0	⋯	⋯	⋯
A	414.33	24,128	172	$2 \times \nu_{13}$ (π_u)	⋯	⋯	⋯
B	412.11	24,265	309	$2 \times \nu_{12}$ (π_u)	⋯	⋯	⋯
C	406.87	24,571	615	$4 \times \nu_{12}$ (π_u)	⋯	⋯	⋯
D	406.52	24,592	636	⋯	⋯	⋯	⋯
E	404.23	24,667	711	⋯	⋯	⋯	⋯
F	403.62	24,769	813	$2 \times \nu_{13} + 4 \times \nu_{12}$	⋯	⋯	⋯
$HCCC(CO)CCH^+$							
	523.49	19,103	0	0_0^0	0.101	0.079	0.045
A	521.62	19,171	69	⋯	0.101	0.078	0.044
B	509.33	19,238	135	⋯	⋯	⋯	⋯
C	503.37	19,282	179	$\nu_8(a_1)$	⋯	⋯	⋯
D	503.37	19,634	531	$\nu_7(a_1)$	0.102	0.079	0.044
E	503.37	19,656	553	⋯	⋯	⋯	⋯
F	503.37	19,702	599	⋯	⋯	⋯	⋯
G	503.37	19,727	624	⋯	⋯	⋯	⋯
H	503.37	19,748	645	⋯	⋯	⋯	⋯
I	503.37	19,772	669	$\nu_6(a_1)$	⋯	⋯	⋯
J	503.37	19,814	701	⋯	⋯	⋯	⋯
K	503.37	19,866	761	$\nu_5(a_1)$	0.102	0.078	0.044

Note. Ground-state vibrations were calculated at the MP2/cc-pVDZ level of theory for OC_4O^+. Rotational constants in the 1 $^2A_2$ state of $HCCC(CO)CCH^+$ are from the simulations, whereas those for $X\ ^2B_1$ are taken from M06-2X/cc-pVTZ calculations. A, B, C, etc. correspond to the labels in Figures 2 and 3.

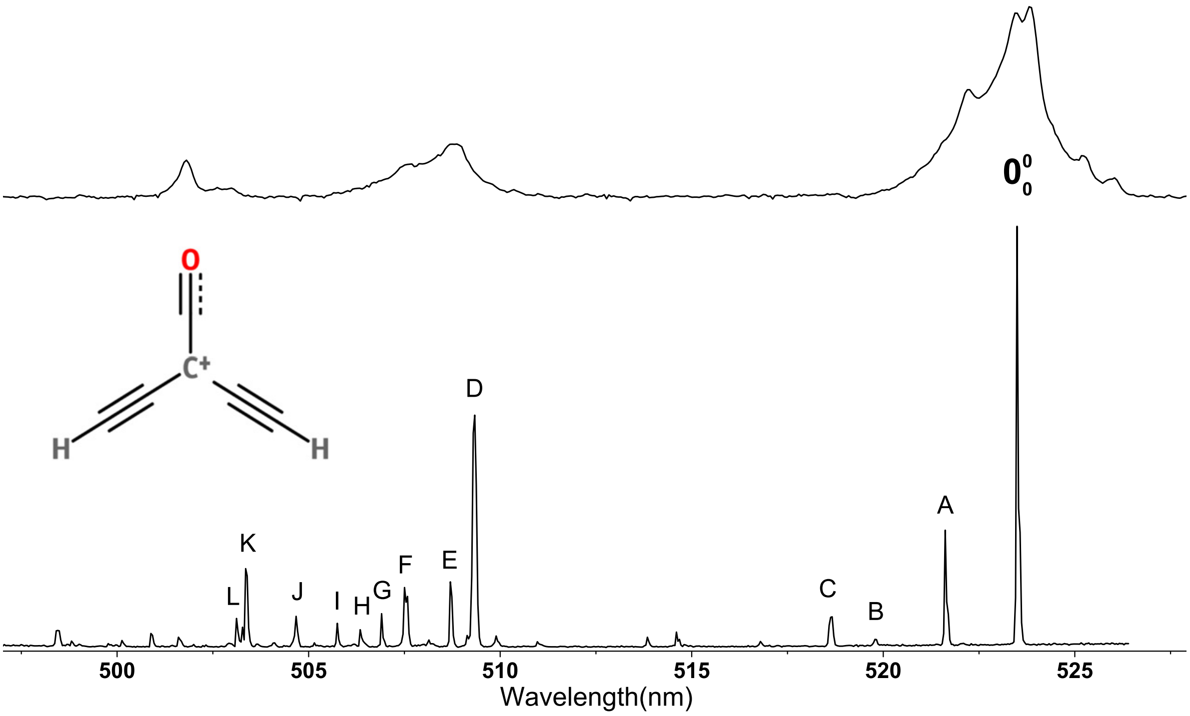

Figure 3. Electronic spectra of the 1 $^2A_2 \leftarrow X\ ^2B_1$ transition of $C_6H_2O^+$ recorded in a 6 K neon matrix (top) and the gas phase (bottom) at 10 K with a 0.002 nm laser bandwidth. The top trace is redshifted 4 nm for comparison.

thermodynamic dissociation threshold of OC_4O^+ via CO loss is 3 to 3.6 eV, and a laser power of ≈20 μJ/pulse had to be used to prevent saturation effects. The vibrational progression in the excited state is similar to the one recorded in the matrix, with one band 155 cm^{-1} from the origin, arising from a low-frequency bending mode with double-quanta excitation of π_u symmetry. A tentative assignment of the vibrational transitions in the absorption spectrum of OC_4O^+ is given in Table 2.

3.2. Electronic Spectrum of $C_6H_2O^+$

The absorption spectrum of mass-selected $C_6H_2O^+$ in a 6 K neon matrix was recorded together with theoretical calculations of different isomers (Chakrabory et al. 2015). The study revealed two structures with visible absorptions. The 2-ethynylbut-3-yn-1-enone-1-ylide isomer (C_{2v} symmetry and previously labelled F^+) has the $1\ ^2A_2 \leftarrow X\ ^2B_1$ electronic transition starting around 528 nm ($f = 0.11$), and the (2-ethynylcycloallyl) methanone cation (C_s symmetry and labelled B^+), around 497 nm ($f = 0.024$), the latter being broader and weaker. Only F^+ was chosen for a gas-phase measurement because its electronic transition is in the 400–900 nm region with a dominant origin band and larger oscillator strength.

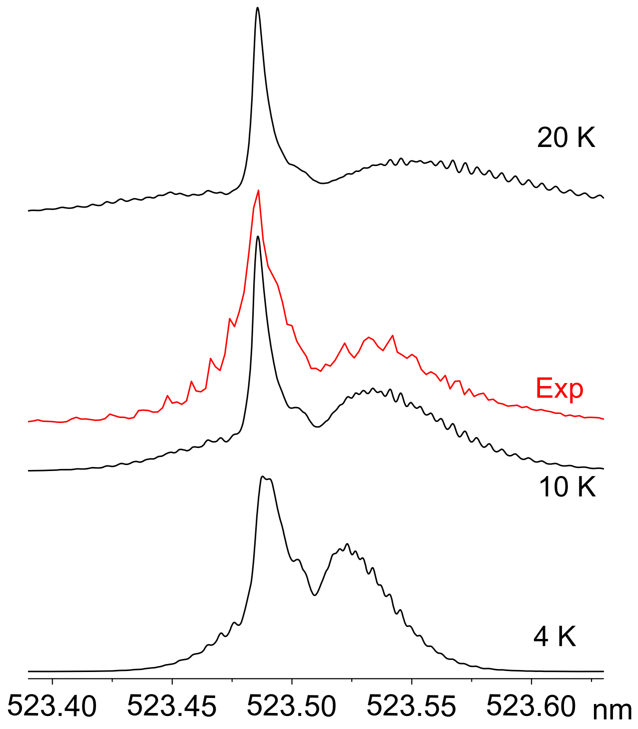

Figure 4. Origin band of the $1\ ^2A_2 \leftarrow X\ ^2B_1$ electronic transition of $C_6H_2O^+$ in the gas phase (in red) and simulated profiles at rotational temperatures of 4, 10, and 20 K using a 0.002 nm Gaussian linewidth.

The electronic spectrum (Figure 3) was produced by monitoring the CO loss from $C_6H_2O^+$. The origin band of the $1\ ^2A_2 \leftarrow X\ ^2B_1$ transition at 523.49 nm has a FWHM of 0.07 nm. Vibrational progressions in the $1\ ^2A_2$ excited state are similar to those observed in the absorption spectrum in a neon matrix (Chakrabory et al. 2015). These are slightly more intense in the dissociation spectrum as the fragmentation process used for detection can distort the intensities in comparison with a direct absorption technique. Moreover, the solid neon environment can hinder nuclear motion, especially bending vibrations, yielding discrepancies in relative intensities in the two spectra. Nevertheless, the gas-phase spectrum, blueshifted ≈5 nm from the neon value, can be attributed without doubt to the isomer observed in the matrix study.

The origin band at 523.49 nm was recorded with a 0.002 nm bandwidth laser and is compared with simulated profiles (Figure 4). The $X\ ^2B_1$ ground-state rotational constants $A'' = 0.100\ \mathrm{cm^{-1}}$, $B'' = 0.089\ \mathrm{cm^{-1}}$, and $C'' = 0.047\ \mathrm{cm^{-1}}$ were used from DFT calculations and the temperature along with the spectroscopic parameters for the $1\ ^2A_2$ excited state were varied. As expected from previous studies (Rice et al. 2015), the best fit was with $T_{\mathrm{rot}} \approx 10$ K. The molecular constants in the $1\ ^2A_2$ excited state are $A' = 0.101\ \mathrm{cm^{-1}}$, $B' = 0.079\ \mathrm{cm^{-1}}$, and $C' = 0.045\ \mathrm{cm^{-1}}$. The most intense vibrational bands (Table 2) in the $1\ ^2A_2$ excited state lie at $+69\ \mathrm{cm^{-1}}$, $+532\ \mathrm{cm^{-1}}$, and $+764\ \mathrm{cm^{-1}}$ from the origin band and show similar P- and R-branches. They were also recorded (Figure 4) with 0.002 nm resolution and compared with simulations. The profiles confirm that the isomeric structure F^+ inferred in the matrix study (Chakrabory et al. 2015) is also the one observed in the gas phase. The rotational constants indicate a substantial change of geometry in the excited electronic state, with $B'' > B'$ differing by more than 10%.

A change of the angle between the two acetylenic side-chains in the lower and upper state from 127.5° to 119.5° is evident based on theoretical calculations at the M06-2X/cc-pVTZ level. This corresponds to a rotational transformation of the internal A- and B-axes. The low-frequency totally symmetric a_1 modes are assigned in the spectrum shown in Figure 3 and given in Table 2. When higher-resolution recordings of bands

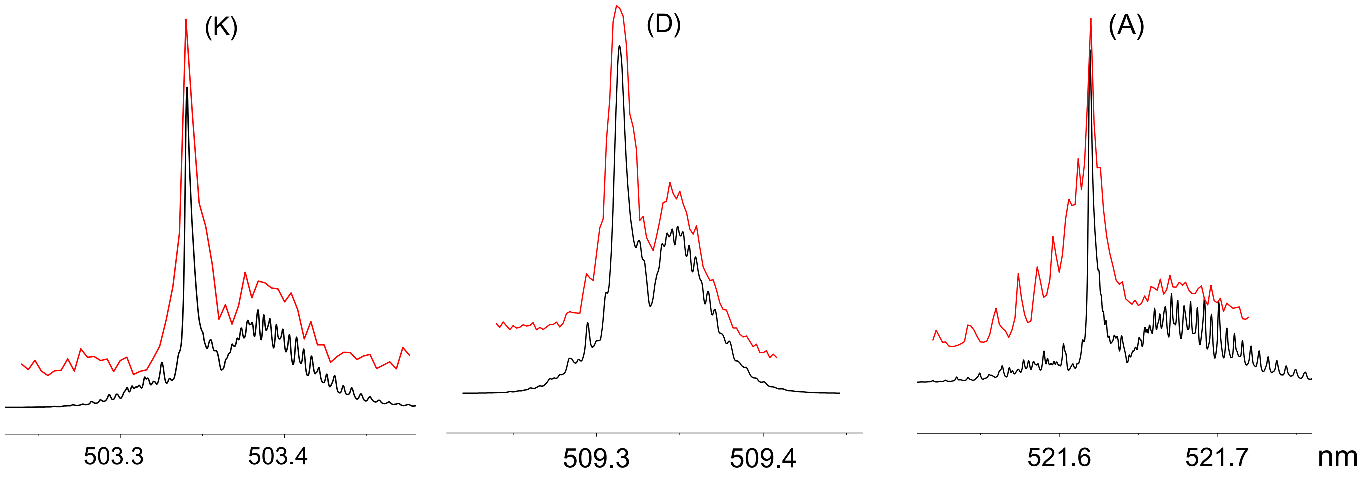

Figure 5. Rotationally resolved vibrational bands in the $1\ ^2A_2 \leftarrow X\ ^2B_1$ electronic transition of $HCCC(CO)CCH^+$ in the gas phase with band maxima at (A) 521.62 nm, (D) 509.33 nm, and (K) 503.37 nm. Molecular constants used for the contour fit are given in Table 2. A, D, and K are labelled in Figure 3.

involving ν_7 and ν_8 (a_1 symmetry) excitations are examined (Figure 5), the profiles have a similar contour to that of the origin band and thus have comparable A, B, and C rotational constants.

Higher-resolution spectra (Figure 5) are affected by saturation even when recorded with 10 μJ/pulse as indicated by narrower FWHM with lower laser fluence. Below this power, a decent quality spectrum could not be recorded. The thermodynamic threshold for the molecule via CO loss is $\approx$2 eV, much less than the 5 eV for H-loss, indicating that a single photon (528 nm, 2.3 eV) can lead to dissociation. Upon 528 nm radiation, H-loss, leading to HC_6O^+, was also detected, but two to three orders of magnitude weaker than CO fragmentation. This is, however, a multiphoton process and the probability is less likely given a lower laser fluence.

4. CONCLUSION

The $1\ ^2\Pi_u \leftarrow X\ ^2\Pi_g$ and $1\ ^2A_2 \leftarrow X\ ^2B_1$ electronic transitions of linear OC_4O^+ and a planar $HCCC(CO)CCH^+$ were recorded in the gas phase with a rotational temperature of $\approx$10 K, following absorption measurements in 6 K neon matrices. The study was motivated by the fact that no electronic spectra of oxygen containing carbon chain cations are available for comparison with astronomical data and that both molecules have a visible transition. However, neither the origin band of $HCCC(CO)CCH^+$ nor OC_4O^+ show a match with known DIBs (Hobbs et al. 2008, 2009). Upper limits of the column densities can be estimated using $N(\mathrm{cm}^{-2}) = 1.13 \times 10^{20}(\mathrm{EW}(\text{Å}))/(\lambda(\text{Å})^2 \times f)$. The f-value of the A band of OC_4O^+ (Figure 2) is approximated by 20% of the theoretically calculated 0.004 for the whole electronic transition. Taking a 10 mÅ equivalent width as the value of a detectable DIB around 400 nm leads to $N(OC_4O^+) < 7 \times 10^{13}\ \mathrm{cm}^{-2}$, and with $f = 0.11$ at 528 nm, $N(HCCC(CO)CCH^+) < 2 \times 10^{12}\ \mathrm{cm}^{-2}$.

Under near-UV/visible irradiation, these two radical cations undergo photodegradation. The thermodynamic threshold for CO loss is approximately 2–3.3 eV. Faster dissociation rates are achieved with larger excess energy due to multiphoton absorption and can cause other fragmentation pathways to be accessible. The strength of the CO-unit constrains small oxygenated species more than small hydrocarbons when the stability to photodestruction is considered as a criterion in the ISM. Thus, despite the possible presence in diffuse interstellar environments of oxygen-containing hydrocarbon dust particles, such small molecules with a bound $C \equiv O$ group are unprobable gas-phase DIB candidates. However, structures, such as cumulenic $H_2C_{2n+1}O^+$ or $OC_{2n+1}O^+$ $n = 2,3,\ldots$, are more likely to have a higher photofragmentation threshold and redistribute energy into the vibrational degrees of freedom after electronic excitation.

This work was supported by the European Research Council (ERC-AdG-ElecSpecIons:246998) and the Swiss National Science Foundation (project no. 200020-140316/1).

REFERENCES

Aller, M. C., Kulkarni, V. P., York, D. G., et al. 2014, ApJ, 785, 36
Andersson, K., Malmqvist, P.-A., Roos, B. O., et al. 1990, JPhCh, 94, 5483
Andersson, K., Malmqvist, P.-A., & Roos, B. O. 1992, JChPh, 96, 1218
Aquilante, F., De Vico, L., Ferre, N., et al. 2010, JCoCh, 31, 224
Becke, A. D. 1988, PhRvA, 38, 3098
Bujarrabal, V., Fuente, A., & Omont, A. 1994, A&A, 285, 247
Chakraborty, A., Fulara, J., & Maier, J. P. 2015, JPCA, 119, 50
Furuya, R. S., Walmsley, C. M., Nakanishi, K., et al. 2003, A&A, 409, L21
Hardy, F.-X., Rice, C. A., Gause, O., & Maier, J. P. 2015, JPCA, 119, 1568
Hincelin, U., Wakelam, V., Hersant, F., et al. 2011, A&A, 530, A61
Hobbs, L. M., York, D. G., Snow, T. P., et al. 2008, ApJ, 680, 1256
Hobbs, L. M., York, D. G., Thorburn, J. A., et al. 2009, ApJ, 705, 32
Huang, J., & Oka, T. 2015, MolPh, 113, 2159
Jenkins, E. B. 2009, ApJ, 700, 2
Kamiński, T., Gottlieb, C. A., Menten, K. M., et al. 2013, A&A, 551, A113
Kwok, S., & Zhang, Y. 2013, ApJ, 771, 5
Lee, C., Yang, W., & Parr, R. G. 1988, PhRvB, 37, 785
Li, A., & Draine, B. T. 2001, ApJL, 550, L213
Molster, F., & Kemper, C. 2005, SSRv, 119, 3
Nagy, A., Garkusha, I., Fulara, J., & Maier, J. P. 2013, PCCP, 15, 19091
Rice, C. A., Hardy, F.-X., Gause, O., & Maier, J. P. 2015, ApJL, 812, L4
Sadjadi, S. A., Zhang, Y., & Kwok, S. 2015, ApJL, 807, 95
Snow, T. P., & McCall, B. J. 2006, ARA&A, 44, 367
Tenenbaum, E. D., Woolf, N. J., & Ziurys, L. M. 2007, ApJL, 666, L29
Tenenbaum, E. D., & Ziurys, L. M. 2009, ApJL, 694, L59
Whittet, D. C. B. 2010, ApJ, 710, 1009
Zack, L. N., & Maier, J. P. 2014, Chem. Soc. Rev., 43, 4602

The Astrophysical Journal Letters, 812:L4 (3pp), 2015 October 10 doi:10.1088/2041-8205/812/1/L4

ELECTRONIC SPECTRUM OF $C_7H_3^+$ IN THE GAS PHASE AT 10 K

C. A. Rice, F.-X. Hardy, O. Gause, and J. P. Maier
Department of Chemistry, University of Basel, Klingelbergstr. 80, CH-4056 Basel, Switzerland; j.p.maier@unibas.ch
Received 2015 August 22; accepted 2015 September 15; published 2015 October 2

ABSTRACT

The analysis of the λ5797.1 diffuse interstellar band (DIB) by Huang & Oka concludes that the carrier is a chain-like molecule with five to seven heavy atoms with a large oscillator strength, $f \approx 1$, for the electronic transition. The spectra of carbon chains of this size with transitions in the visible have been obtained in the gas phase, but the *f*-values are too small. We have now found that certain carbon-chain cations with transitions in the DIB range have large *f*-values. An example is the origin band at 4387.7 Å of the $1\,^1A_1 \leftarrow X\,^1A_1$ electronic transition of the $H_2C_7H^+$ chain with $f \approx 0.3$. This could be measured in the gas phase at 10 K in an ion trap. Astrophysical relevance of such cations is discussed.

Key words: ISM: general – ISM: lines and bands – ISM: molecules – methods: laboratory: molecular – techniques: spectroscopic

1. INTRODUCTION

In the discussion of the likely molecules that could be responsible for the diffuse interstellar bands (DIBs), carbon chains came to prominence for two reasons. First, polar carbon chains were detected by radioastronomy in dense clouds (Kroto 1981), and second, Douglas (1977) indicated that bare carbon chains may have electronic transitions in the visible and their photophysical properties could lead to line broadenings comparable to DIB widths. The latter often have asymmetric absorption profiles, and some have several peak structures reminiscent of unresolved rotational contours of larger molecules (Kerr et al. 1996). A major development in this area has been the identification of the two DIBs at 9632 and 9577 Å due to C_{60}^+ (Campbell et al. 2015). It remains a quest to discover other carriers.

Our initial strategy was to choose species already identified in dense interstellar clouds by radioastronomy, e.g., C_6H and C_8H (Suzuki et al. 1986; Cernicharo & Guélin 1996), which are open-shell systems and have electronic transitions in the visible. This was then extended to related non-polar molecules, e.g., C_4 and C_5, and ionic species, such as C_7^- and HC_6H^+ (Rice & Maier 2013). The successful concept adapted was to locate the electronic transitions initially in 6 K neon matrices using mass selection, followed by gas-phase measurements using several techniques, cavity ring-down absorption spectroscopy, resonant two-photon ionization on neutral radicals, and cation radiofrequency (rf) traps. Though gas-phase spectra could be obtained for many such carbon-containing systems and directly compared with astronomical measurements, results were negative, except for C_3 detection (Maier et al. 2001), and only upper limits of the column densities could be inferred, generally $<10^{11}$–$10^{12}\,\mathrm{cm}^{-2}$ (Motylewski et al. 2000).

The important conclusion from these studies was that only species that possess electronic transitions with much larger oscillator strength, $f > 0.5$, remain as potential candidates in order to be consistent with a reasonable column density ($\approx 10^{12}\,\mathrm{cm}^{-2}$), as well as possessing the EW of the stronger DIBs (Maier et al. 2004). Identified among these were the longer carbon chains, C_{15}, C_{17}, C_{19},…, with very strong absorptions in the visible. These pure carbonaceous species have been measured in neon matrices; however, gas-phase spectra could not yet be obtained. Along with these arguments, other much larger molecules are being brought into consideration, primarily because the some of the electronic transitions could be intense and lie in the visible.

A recent development has been the analysis of the apparent rotational profile of the λ5797.1 DIB by Huang & Oka (2015). Their conclusion is that a linear or linear-like molecule comprising five to seven heavy atoms is the most probable carrier. However, in this category, the electronic spectra of a number of carbon chains were obtained in the gas phase, e.g., C_6H, C_7^-, HC_6H^+, HC_5N, but they have no match with the DIBs (Motylewski et al. 2000) and possess $f < 0.1$ values. Thus, the question arises whether certain molecular types have hitherto been neglected.

During our studies of the absorption spectra of hydrocarbon radicals and their cations in neon matrices, various isomeric structures could be identified via their electronic transitions combined with theoretical calculation. For example, in the investigation of $C_5H_3^+/C_5H_3$ (Fulara et al. 2015) and $C_7H_3^+/C_7H_3$ (Chakraborty et al. 2014) species, several isomers were produced in an ion source, the mass-selected ions then deposited in a 6 K neon matrix, and the absorptions measured. Those of the neutrals were obtained through neutralization of the ions by the release of electrons in the neon solid. Theoretical calculations of the possible structural isomers enabled the assignment of the electronic absorptions. The significant result is that some of the cation isomers have large oscillator strengths (range 0.1–1) for their lowest-energy electronic transitions, an order of magnitude larger than the neutrals. Thus, such species would fulfill the criteria from the analysis of the 5797.1 Å DIB (Huang & Oka 2015)—five to seven heavy atoms and large *f*-values.

The $C_7H_3^+$ isomer, with the structure given in Figure 1, is an example. The origin band of the $1\,^1A_1 \leftarrow X\,^1A_1$ electronic transition in a neon matrix lies at 4413 Å. It is the most intense in the absorption system, and the oscillator strength of the origin band is around 0.3. The present article reports the successful recording of this absorption in the gas-phase spectrum at 10 K, and the results are discussed in relation to the DIB aspects. The approach used for the measurement is based on mass selection of $C_7H_3^+$ and a radiofrequency (rf) ion trap, where the rotational and vibrational degrees of freedom are equilibrated to around 10 K by collisions with cryogenically

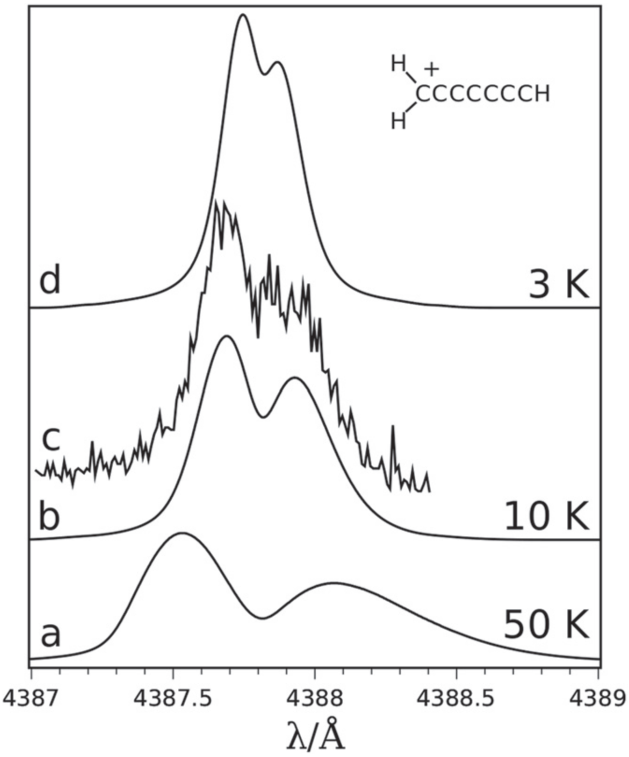

Figure 1. Origin band of the 1 $^1A_1 \leftarrow X$ $^1A_1$ electronic transition of $H_2C_7H^+$ measured with a 0.02 Å laser bandwidth in the gas phase (trace c). The simulated profiles shown are at the indicated rotational temperatures.

cold helium atoms. Thus, as in space, relaxation to a low temperature is achieved. The electronic spectrum is obtained by laser excitation of the transition followed by fragmentation.

2. EXPERIMENTAL METHOD

The experimental setup has been described by Hardy et al. (2015). Ions created in an electron impact source from a 1:1 mixture of diacetylene and propyne are injected into a 440 mm long hexapole composed of two parts. Positive species are confined within the second 6-pole and cooled for 50 ms by collisions with helium, narrowing the kinetic energy distribution of cations from the source. The exit electrode potential is then lowered, and the ions released into a quadrupole mass selector (QMS), which selects $m/z = 87$ with a resolution of ±0.5 u. The ion beam is turned 90° by a quadrupole deflector (QB), injected into an rf-only octupole ion guide, and transported to a 22-pole trap.

A $36 \times 10\,\mathrm{mm}^2$ 22-pole rf trap (Gerlich 1992) was filled with $\approx 10^5$ ions per cycle. The sequence is 40 ms for filling the trap, then 50 ms confinement, followed by laser irradiation and the release of the ions for detection of the photofragmentation products. The 22-pole is mounted on a closed-cycle cryostat at 3.2 K. Helium buffer gas is leaked into the trap via a piezo-valve, achieving a density of $\approx 4 \times 10^{15}\,\mathrm{cm}^{-3}$ after a few ms and leading to approximately one collision with $C_7H_3^+$ per microsecond. After exiting the trap, ions are collimated by several electrodes and deflected 90° by a QB into a second QMS. The latter selects $C_7H_2^+$ fragments, products of photodissociation. The ion beam is then focused by an einzel lens and counted via a Daly detector. The experiment is synchronized with a dye laser (resolving power = 240,000 at 4400 Å) at a repetition rate of 10 Hz.

3. ABSORPTION OF $C_7H_3^+$ IN THE VISIBLE

The electronic spectrum of $H_2C_7H^+$ in the 4400 Å region was first observed in a 6 K neon matrix after mass-selected deposition (Chakraborty et al. 2014). Its structure was inferred to be the cumulenic form $H_2CCCCCCCH^+$ of C_{2v} symmetry. The origin band of the 1 $^1A_1 \leftarrow X$ $^1A_1$ electronic transition of $H_2C_7H^+$ in the gas phase is observed at 4387.7 Å, blueshifted from the neon matrix value at 4413 Å. The spectrum has a dominant origin band. The transitions to higher energy, corresponding to the excitation of vibrations in the upper 1 $^1A_1$ electronic state, are weaker by more than an order of magnitude.

In Figure 1, the origin band profile measured with a resolving power of 240,000 is shown. The two broad features, peak width ≈1.2 Å, are unresolved *P*- and *R*-branches. Saturation effects were avoided by reducing laser power until the FWHM of the origin band did not change. Because the electronic transition is not rotationally resolved, it is necessary to rely on calculations to obtain information concerning the spectroscopic properties of the excited states. Time-dependent density functional theory at the M06–2X/cc-pVTZ level was carried out (Dunning 1989; Zhao & Truhlar 2008; Frisch et al. 2013). This predicts a dipole-allowed electronic transition at 4092 Å. When the transition moment is along the internuclear axis *A*, the selection rule for the *K* quantum number is $\Delta K = 0$. No *K* structure is seen for parallel bands; however, with the laser bandwidth and possible lifetime broadening, the *Q*-branch would not be observed. For a perpendicular one, *K* components should be identifiable even at ≈15 K. Therefore, the origin band observed in the spectrum is assigned as 1 $^1A_1 \leftarrow X$ $^1A_1$, a parallel *a*-type transition.

The spectrum of an asymmetric top is characterized by the rotational constants *A*, *B*, and *C* in the ground and excited states, the transition energy, temperature, spin-statistical weights, and FWHM of Gaussian line shapes. The ground state molecular constants $A'' = 9.581\,\mathrm{cm}^{-1}$, $B'' = 0.0276\,\mathrm{cm}^{-1}$, and $C'' = 0.0275\,\mathrm{cm}^{-1}$ were fixed to the results from the DFT calculation; the transition frequency was taken from the experimental data; and the rotational temperature was varied. In Figure 1, simulations with 3, 10, and 50 K are used. As the temperature is decreased, the *P*- and *R*-branches start to merge together, having an FWHM of approximately 0.3 Å. At 50 K, the band maximum of the *R*-branch is at 4387.5 Å blueshifting from that at 3 K by 0.2 Å. The most probable rotational temperature of the $C_7H_3^+$ ions in the trap is 10 K, which is inferred by comparing the experimental and simulated spectra. The spectroscopic constants obtained from the best fit to the experimental band profile for the $^1A_1$ excited state are $A' = 9.616\,\mathrm{cm}^{-1}$, $B' = 0.0273\,\mathrm{cm}^{-1}$, and $C' = 0.0272\,\mathrm{cm}^{-1}$.

The lowest-energy electronic transition of the $H_2C_{2n+1}H^+$ series shows a redshifting pattern as a function of carbon-chain length, similar to the $H_2C_{2n}H^+$ polyacetylenic chains (Dzhonson et al. 2007). If the origin band wavelength maximum in the electronic absorption spectrum in 6 K neon matrices is plotted as a function of *n* ($n = 1, 2, 3$), a linear fit can be applied to the data: $E_n/\text{Å} = n \times (870 \pm 30)/\text{Å} + (1790 \pm 60)/\text{Å}$, where *n* is an integer and E_n is the transition energy. For $n = 3$–8, this lies in the 4000–9000 Å region, the DIB range. Also, the oscillator strength of these transitions increases as the conjugated

π-system gets longer. The calculated *f*-value for these electronic transitions of $H_2C_5H^+$ and $H_2C_7H^+$ is 0.2 and 0.3, respectively.

4. ASTRONOMICAL CONSIDERATIONS

The measurement of the gas-phase electronic spectrum of $H_2C_7H^+$ was motivated by the conclusions drawn by Huang & Oka (2015) on the likely carrier of λ5797.1 DIB. Because the electronic spectra of many of the "evident" carbon-chain molecules, such as C_6H, HC_6H^+, and HC_5CN^+, have already been measured in the gas phase with no match to known DIBs and the oscillator strength of the transitions is moderate, ≈0.05, other candidates were sought.

The cumulenic cation $H_2C_7H^+$ has been found to have the generally correct characteristics, a transition in the DIB range, a dominant origin band at 4387.7 Å, and an *f*-value around 0.3. Unfortunately, this transition overlaps with a He I line, and one cannot discern if a DIB is present there. Assuming that the maximum column density of $H_2C_7H^+$ in the diffuse clouds is 10^{12} cm^{-2}, the EW of the DIB at 4387.7 Å would be ≈50 mÅ.

The cations $H_2C_{2n+1}H^+$, which include $H_2C_7H^+$ studied here, are isoelectronic with the cumulenes H_2C_{2n+1}. The latter are well characterized by millimeter-wave spectroscopy, and the $n = 1, 2, 3$ members have been identified in dense clouds (Thaddeus & McCarthy 2001). These types of molecules were suggested by Huang & Oka (2015) to be among the candidates for the λ5797.1 DIB carrier. Their lowest allowed electronic transitions have comparably larger oscillator strengths than the $H_2C_{2n+1}H^+$ species, but the absorptions for the ones comprising five to seven heavy atoms lie toward the UV. This has been measured in the gas phase for H_2C_5 at ≈3000 Å with $f \approx 0.1$ (Steglich et al. 2015). That of H_2C_7 and H_2C_9 are expected in the 4000–5000 Å region. On the other hand, the strong transitions of $H_2C_9H^+$ will lie in the 5300 Å region. The measurement of the absorptions of these types of molecules in the gas phase should be pursued.

This work was supported by the European Research Council (ERC-AdG-ElecSpecIons:246998) and the Swiss National Science Foundation (Project No. 200020-140316/1).

REFERENCES

Campbell, E. K., Holz, M., Gerlich, D., & Maier, J. P. 2015, Natur, 523, 322
Cernicharo, J., & Guélin, M. 1996, A&A, 309, L27
Chakraborty, A., Fulara, J., Dietsche, R., & Maier, J. P. 2014, PCCP, 16, 7023
Douglas, A. E. 1977, Natur, 269, 130
Dunning, T. H. 1989, JChPh, 90, 1007
Dzhonson, A., Jochnowitz, E. B., & Maier, J. P. 2007, JPCA, 111, 1887
Frisch, M. J., Trucks, G. W., Schlegel, H. B., et al. 2013, Gaussian 09, Revision D.01 (Wallingford, CT: Gaussian, Inc.)
Fulara, J., Chakraborty, A., Nagy, A., et al. 2015, JPCA, 119, 2338
Gerlich, D. 1992, AdChP, 82, 1
Hardy, F.-X., Rice, C. A., Gause, O., & Maier, J. P. 2015, JPCA, 119, 1568
Huang, J., & Oka, T. 2015, MolPh, 113, 2159
Kerr, T. H., Hibbins, R. E., Miles, J. R., et al. 1996, MNRAS, 283, L105
Kroto, H. W. 1981, IRPC, 1, 309
Maier, J. P., Lakin, N. M., Walker, G. A. H., & Bohlender, D. A. 2001, ApJ, 553, 267
Maier, J. P., Walker, G. A. H., & Bohlender, D. A. 2004, ApJ, 602, 286
Motylewski, T., Linnartz, H., Vaizert, O., et al. 2000, ApJ, 531, 312
Rice, C. A., & Maier, J. P. 2013, JPCA, 117, 5559
Steglich, M., Fulara, J., Maity, S., et al. 2015, JChPh, 142, 244311
Suzuki, H., Ohishi, M., Kaifu, N., et al. 1986, PASJ, 38, 911
Thaddeus, P., & McCarthy, M. C. 2001, AcSpA, 57, 757
Zhao, Y., & Truhlar, D. G. 2008, Theor. Chem. Acc., 120, 215

11. ACKNOWLEDGEMENTS

This manuscript, the work it represents, and the results it presents were carried out at the University of Basel. None would have been possible without a large number of people. I would like to thank Prof. John P. Maier for this opportunity of a lifetime. I would like to thank him for giving me the choice of the experiment I wanted to work on when I joined the group. It has been very challenging and I am happy about it. I would like to thank him for giving me the opportunity of working on what is the state-of-the-art in ion trapping techniques and mass spectrometry, and for the great motivation I felt every time I left his office after a discussion.

Prof. Markus Meuwly is thanked for kindly accepting to be the co-referee of my thesis and Prof. Wolfgang Meier for accepting to chair my defense. I would like to thank Dr. Corey A. Rice for everything; from his introducing me to the number of experimental abilities needed to run such a setup, including the joys of long periods of troubleshooting, to his patience when answering a large number of questions (in a raw) about spectroscopy or various other experimental techniques that he had an extensive knowledge of, to the generous and hearty person he is. I would like to thanks Dr. Oliver Gause for implementing his pragmatic way of thinking the experiment which has been crucial for the obtention of the results presented in this thesis.

The support of Dr. A. Johnson with the lasers was a luxury we had. Also indispensable for the group were G. Holderied for quick and tailor-made electronics, and Jacques for providing us with exotic molecules. Grischa Martin, Philipp Knpfel and Dieter Wild of the mechanical workshop are thanked for providing us with many high quality parts. Daniela Tischhauser and Maya Greuter are deeply thanked for taking care of administrative matters. I would like to thank all members of the group and persons I interacted with in the university and in Basel for participating in making these five years unforgettable and a personal success. Finally, I thank my parents for supporting me during these hectic but worthy 15 years of study.

Francois-Xavier Hardy

Doctor in physical chemistry

135 Riehenring, 4058 Basel (CH)
☎ *+41 (0)7 74 82 57 65*
✉ *fxhardy@unibas.ch*
B residency permit
08/06/1983

Education

2011-2016 **Ph.D. in physical chemistry, group of Prof. J. P. Maier, Basel University**.

- electronic spectra of molecules of interest regarding the diffuse interstellar bands
- results obtained with a tandem mass spectrometer centered on an ion trap cooled to 4 K
- publications in The Astrophysical Journal and The Journal of Physical Chemistry A
- achievement: implementation of He tagging technique to obtain electronic spectra of photostable molecules, with a resolution suitable for astronomical comparison.

2008–2011 **Master degree in Physics, Rennes University, France**.
Including training period in Cologne university (2010)

- Detection of vibrational hot bands of the $\nu5$ vibration of linear C7.
- In a supersonic expansion, the C7 molecule was produced from a laser ablated graphite rod and probed through direct (multi-pass) absorption by a high resolution infrared laser system.

2007 **Bachelor degree in Physics, Rennes University, France**.
Including a training periods in Madrid university (2008)

2006 **Admission to "ENSAM" engineer school after national competitive exams, Paris**, Quit after the 1st year for bachelor in physics.

Professional experience

2011-2016 **"Teaching assistant" for undergraduate students, Basel University**.

2010 **Internship at the Laboratory of Experimental Astrophysics**.
Cologne University (Prof. Dr. Thomas Giesen)

2000-2011 **Student jobs**, Maths teacher, construction worker, cashier, etc....

Others

Languages French: mother tongue
English: professional proficiency
Spanish: social proficiency
German: social proficiency

Programmes Solidworks, LaTeX, Office, Origin.

Interests Skydiving, wingsuit flying, chess, theater.

References

Prof. Dr. John P. Maier, F.R.S..
Universität Basel, Departement Chemie, j.p.maier@unibas.ch

Additional references can be provided during an interview..

Publications

2016 **F.-X. Hardy, C. A. Rice, and J. P. Maier**, Gas-phase electronic spectra of coronene and corannuelene cations.
Submitted to The Astrophysical Journal

F.-X. Hardy, C. A. Rice, A. Chakraborty, J. Fulara, and J. P. Maier, Optical absorptions of oxygenated carbon chain cations in the gas phase.
The Astrophysical Journal 824.1 (2016): 9

Arghya Chakraborty, Corey A. Rice, François Xavier Hardy, Jan Fulara, and John Paul Maier, Electronic Spectra of Protonated Fluoranthene in a Neon Matrix and Gas Phase at 10 K.
The Journal of Physical Chemistry A (2016)

2015 **C. A. Rice, F.-X. Hardy, O. Gause, and J. P. Maier**, Electronic spectrum of C7H3+ in the gas phase at 10 K.
The Astrophysical Journal Letters 812.1 (2015): L4.

Corey A. Rice, Jan Fulara, Iryna Garkusha, Ádám Nagy, François-Xavier Hardy, Oliver Gause, John P. Maier, Electronic Spectra of Corannulenic Cations and Neutrals in Neon Matrices and Protonated Corannulene in the Gas Phase at 15 K.
Z. Phys. Chem., 229(10-12), 1709-1728, 2015

F.-X. Hardy; Rice, C. A.; Gause, O.; Maier, J. P., Gas-Phase Electronic Transitions of C17H12N+ at 15K.
The Journal of Physical Chemistry A (2015)

2014 **C. A. Rice , F.-X. Hardy , O. Gause , and J. P. Maier**, (1)1A’- X1A’ Electronic Transition of Protonated Coronene at 15 K.
The Journal of Physical Chemistry A (2014)

2013 **F.-X. Hardy, O. Gause, C. A. Rice, and J. P. Maier**, Absorptions in the Visible of Protonated Pyrene Collisionally Cooled to 15 K.
The Astrophysical Journal Letters 778.2 (2013): L30.

2010 **J. Krieg, V. Lutter, F.-X. Hardy, S. Schlemmer, and T. F. Giesen**, The v5 antisymmetric stretching mode of linear C7 revisited in high resolution.
Journal of Chemical Physics 132.22 (2010): 224306